2017-06-01

In Situ Characterization of Voids During Liquid Composite Molding

Brock Don Zobell
Brigham Young University

In Situ Characterization of Voids During

Liquid Composite Molding

Brock Don Zobell

A thesis submitted to the faculty of
Brigham Young University
in partial fulfillment of the requirements for the degree of

Master of Science

Andrew R. George, Chair
David T. Fullwood
Michael P. Miles

School of Technology

Brigham Young University

ABSTRACT

In Situ Characterization of Voids During
Liquid Composite Molding

Brock Don Zobell
School of Technology, BYU
Master of Science

Global competition is pushing the composites industry to advance and become more cost effective. Liquid Composite Molding or LCM is a family of processes that has shown significant promise in its potential to reduce process times and cost while maintaining high levels of part quality. However, the majority of research and information on composite processes have been related to prepreg-autoclave processing which is significantly different than LCM. In order for LCM processes to gain large scale implementation, significant research is required in order to model and simulate the unique nature of the resin infusion process.

The purpose of this research is to aid in the development of *in situ* void measurement and characterization during LCM processing, particularly for carbon fiber composites. This will allow for the gathering of important empirical data for the validation of models and simulations that aid in the understanding of void formation and movement during LCM. For such data to be useful, it needs to include details on the formation, mobility and evolution of the void over time during infusion.

This was accomplished by creating a methodology that allowed for *in situ* images of voids to be captured during the infusion process. A clear mold was used to visually monitor infusions during RTM with UV dye and lighting to enhance contrast. Consecutive images were acquired through the use of macro lens photography. This method proved capable of yielding high quality images of a variety of *in situ* voids during infusions with carbon fiber composites. This is believed to be the first instance where this was accomplished.

A second methodology was then developed for the analysis of the collected images. This was done by using ImageJ software to analyze and process the acquired images in order to identify and characterize the voids. Success was found in quantifying the size and circularity of a wide range of micro and macrovoids in both a satin weave and double bias NCF woven fabrics.

To facilitate the burden of collecting large amounts of data, this process was made to be automated. A user generated macro script could be applied to large sets of images for rapid processing and analysis. This automated method was then evaluated against manually processed images to determine its overall effectiveness and accuracy as tool for validating void theory.

Keywords: Brock Zobell, composites, liquid composite molding, image analysis, void formation, *in situ,* void measurement, out-of-autoclave, resin infusion, carbon fiber

TABLE OF CONTENTS

LIST OF TABLES

LIST OF FIGURES

1 INTRODUCTION

The use of composites continues to grow in popularity as manufacturers and consumers recognize their benefits in superior strength and weight characteristics. The typical two components in a composite material are a matrix (typically a polyester or epoxy resin) that surrounds a fiber reinforcement (i.e. glass, carbon or aramid). The composite's strength comes from the fiber reinforcement, but the matrix plays a key role in transferring and distributing loads to the fibers. One of the key factors in a quality composite part is low void content. A void occurs when gas or air bubbles become trapped in the matrix material and remain after final cure of the part. Voids reduce the matrix's ability to transfer loads and create failure points within the structure of the part. In order for a composite part to achieve the mechanical properties of its design intent, a minimal void content is required.

Voids occur during processing of the matrix material or manufacturing of the part itself. The aerospace industry has become a leader in developing and processing composite parts. They have created methods that are capable of achieving minimal void content. This is often accomplished by using costly materials, called prepregs, where the matrix and fibers have already been combined. The material is cut and stacked to create the desired part geometry, then placed inside of a pressurized oven, called an autoclave, for curing. While effective, this method of manufacturing requires the use of expensive equipment and materials, and has slow processing times. This type of processing may not be practical in many other industries. Even in

the aerospace industry, global competition is forcing companies to reevaluate their processing methods. This has led researchers to focus on developing manufacturing methods that can produce quality parts at reduced costs and cycle times.

One method that has shown promise is liquid composite molding or LCM. In such a process, liquid resin is injected into the mold to infuse the fiber preform with the matrix material. LCM is a family of processes including resin transfer molding (RTM) and vacuum infusion (VI). In RTM, a dry fiber preform is placed inside of a two-piece mold and the flow is driven by pressure which is often assisted by additional vacuum pressure applied to the vent. In VI, one mold side is rigid while the other is a flexible membrane such as a vacuum bag, and the flow is driven solely by vacuum pressure. The composite part is then cured inside or on the mold. The curing process may be enhanced with heat and pressure. LCM has shown promise in its ability to create high quality parts with low void content without the expensive material and equipment costs used in prepreg-autoclave processing. It is also capable of producing parts in a fraction of the time, when compared to traditional autoclave processing.

Despite its promise, LCM has some disadvantages. It has not seen the amount of time or research that has been given to prepreg-autoclave processing. The nature of void formation and optimization techniques in this method are vastly different than with LCM. Additionally, accepted and established knowledge on prepregs is not always applicable to infusion processing. LCM processing adds the challenge of flow engineering, i.e. fluid dynamics, to the process science already used in prepreg processing. Currently, comprehensive modeling and simulation techniques for LCM are not ready for industry use. These tools are under development and their realization would allow manufacturers to build better parts, optimize processing parameters, and bring products to market much faster. Void modeling and simulation for infusion processes such

as LCM is a critical step in finding a composites processing solution that can meet current demands for reduced material and equipment costs, with faster cycle times. These capabilities would likely make LCM a more viable process for a wider variety of industries.

1.1   Problem Statement

Like most other composite processes, the voids created during LCM are a result of gas or air bubbles that have become trapped within the matrix material. The most common cause of void formation in LCM is the mechanical entrapment of air during the resin infusion process. The mechanical entrapment of air in LCM is complex with unique variables that do not exist in other composite processes, thus necessitating that new models be developed.

Such tools are under development, but the complex and dynamic nature of voids has made the work difficult. The models must not just predict how voids are formed, but describe how the voids flow and change throughout the preform during processing. This "in process" nature is often referred to as *in situ*. As researchers make progress on creating models for *in situ* void formation and evolution, their work needs to be validated with experimental data. There is a significant amount of data on the final void content and distribution as measured in already-cured laminates, but little data exists for the characterization of voids during infusion. This data has proven difficult to obtain as most current methodologies for obtaining images of *in situ* voids during infusion require the use of fiberglass reinforcements due to the easier imaging associated with this material's transparency. This is problematic because most advanced processes will require the use of carbon fibers, for which, there is no current method to acquire images of voids during infusion. Once images are acquired, large numbers will need to be analyzed in order to properly validate models. Data regarding the size, morphology and location of the voids as they

progress through the infusion process will need to be pulled out of each image. An automated image analysis procedure would greatly facilitate this time consuming process. Ultimately, the collection of such information would serve as an important tool in working towards the validation of models and simulation techniques that are currently under development, but in need of empirical data.

1.2   Motivation for Research

The purpose of this research is to develop a methodology for the *in situ* characterization of voids during LCM processing. This will include a method for capturing images of *in situ* voids and also an automated method for analyzing the captured images. This is meant to contribute to the development of void simulation models for LCM processing. Having accurate simulation models will help industry setup, optimize and bring infusion processes to market more quickly and effectively and also aid in optimal part designs.

1.3   Hypotheses

In situ void formation and movement in LCM with the use of carbon fiber reinforcements can be observed and captured by using clear molds and placing high end macro photography equipment directly over the tooling during the resin infusion process.

The size, morphology and movement of the voids may then be measured through automated image analysis. This data could then be useful as a tool for aiding in the development and confirmation of void simulation and modeling theories.

1.4 Overview of Research

For empirical data to be useful for validating models in void theory, it should include the following capabilities and characteristics:

- Image Acquisition

    o Yield clear and detailed images capable of identifying bubbles in the range of $0.5 \times 10^{-4} - 10.0 \text{ mm}^2$, both within and between fiber bundles.

    o Provide proper contrast between the fibers, matrix material and bubbles.

    o Allow for the use of carbon fiber materials.

    o Allow for the acquisition of consecutive images over time.

- Image Analysis

    o The ability to accurately determine the size, morphology and location of the bubble.

    o The ability to accurately determine overall void content.

    o Yield a high level of accuracy in identifying all voids within the images while avoiding false identifications.

    o Ease of processing by using automated macro scripts.

During this research, two methodologies were developed in order to meet these needs. For image acquisition, a methodology derived from previous work and techniques was developed that allowed for the collection of high quality images depicting *in situ* void formation and evolution within carbon fiber composites. This was accomplished by using clear tooling in RTM processing. A test oil was used instead of a thermoset resin to facilitate processing and cleanup. UV dye and lighting were also used to enhance visibility and contrast between the bubble and composite materials. During infusions, images were collected by using a digital

camera equipped with a macro lens and remote shutter release that were placed directly over the mold. Consecutive images were acquired at a high right of approximately 12 per second. Two different preform weaves were used during experimentation in order to produce a general variety of test conditions and bubble formations.

For the image analysis methodology, a public domain image analysis software called ImageJ was used for both image processing and analysis. The images that were studied and analyzed during this research where adjusted within the software in order to further optimize the contrasts between the voids and composite materials. ImageJ was also used to perform a particle analysis which identified the voids and provided data that was used to calculate the size and circularity of each one. The particle analysis process is also able to quantify the overall void content of each image.

Another reason for using ImageJ is that it is capable of rapidly processing images through the use of user generated macro scripts. In order to further facilitate the image analysis process, it was attempted to create a level of automation to this method where one of these macro scripts could be applied to a set of images in order to rapidly collect large data sets. This method was tested and compared against manually processed images in order to determine the overall accuracy and capabilities of the automated process.

1.5   Delimitations and Assumptions

While fiber type and preform orientation can have a significant impact on void formation and evolution, it was chosen to limit this research to certain specific materials that were readily available and used in other related experiments (see Appendix B for details). The bulk of this research was performed using four harness satin weave and double bias NCF carbon fiber preforms. These materials provide good variety in weave pattern, permeability and fiber

orientation. While there are many options of candidate materials, it was determined that results from these would provide a general replication of most applications and allow for universal insights into void phenomena that occurs in a variety of fiber types and configurations.

This study is also limited to one test fluid. The fluid used was a canola oil that was chosen because it displayed similar viscosity and surface tension to the typical epoxy resin systems used in LCM. This was used instead of a thermoset matrix resin for ease of processing and clean up. It is possible that this could introduce variation from true processing conditions using typical thermoset matrices, but the differences have been generally deemed acceptable in other similar research projects on void characterization (Patel, 1995; Gourichon, 2006; Labat, 2001).

Additionally, the preform geometry and ply counts were also controlled to optimize visibility and create manageable conditions. This was accomplished by using rectangular shapes and limiting the ply count to one or two. Shape and ply count may have an influence on void formation and motion, but it is impossible to encompass all combinations. Such limitations do not permit the visualizations of voids that may occur between plies, but this would not be possible using a visual technique with the use of carbon fiber reinforcements anyways. Despite this limitation, the voids observed in the top layer should provide valuable information towards the validation of models. This practice has been found to be common in other similar research projects (Patel, 1995; Lundström, 1994; Labat, 2001).

Processing conditions were limited to the use of resin transfer molding without additional vacuum assistance. The infusion pressure was kept within a range of 0.5 to 1.5 bar in order to eliminate variation and establish consistent results. Typical volume fractions were between 42 – 55%.

1.6   Definitions and Terms

Autoclave – An oven that is capable of creating a vacuum sealed pressurized environment for curing composite parts.

Cure – A process in which the resin (matrix material) is catalyzed into a chemical reaction that transforms the resin from a liquid into a solid material.

Dry Fiber – Fiber reinforcement material that has not been pre-coated with a matrix material.

Fiber Reinforcement – A component of a composite designed to give the material strength. Typical fiber materials are glass, carbon and aramid. These fibers can be oriented in specific directions or patterns to maximize strength as needed.

Flow Front – The front of the matrix material as it advances through the tooling and preform material during the infusion process.

Infusion – The process of permeating a fiber preform with a matrix material through pressure and/or vacuum assistance.

In situ – Dynamic nature that occurs during the infusion process before the matrix cures.

Liquid Composite Molding (LCM) – A family of composite processes where a fiber preform is placed on or within a mold and the matrix material is infused using pressure and vacuum assistance. The part remains on or in the mold under pressure until it has fully cured, sometimes with the assistance of heat. Two common LCM processes are resin transfer molding (RTM) and vacuum infusion (VI).

Macrovoid – A void created in the channel between fiber tows or rovings.

Matrix – The material that is responsible for holding the fiber reinforcements together and transferring loads to the fibers. This is typically a thermoset resin system. Polyester and epoxy are two popular matrix materials.

Microvoid – A void created within the fiber tow or roving.

Preform – An assembly of dry fibers either stacked in plies or mechanically woven into the shape or geometry of the final part.

Prepreg – A composite material where the fibers have already been pre-impregnated with the matrix material.

Roving – A bundle of fibers, typically referring to glass.

Tow – A bundle of fibers, typically referring to carbon.

Void Content – The remainder of the total volume minus the resin and fiber volumes.

2   LITERATURE REVIEW

2.1   Introduction

Void content has long been an important topic of research in the composites industry. Initial studies focused on what variables led to their formation and what effect they had on the final mechanical properties of the part. Now, researchers are striving to develop models that will help them simulate and predict void content in order to cut costs and bring products to market faster for the various methods of composite manufacturing. Significant amounts of information and studies related to prepreg-autoclave processing methods exist, but much of this material is not directly applicable to liquid composite molding or LCM.

The intent of this literature review is to provide background information on the effect of voids on mechanical properties, their dynamic nature during the resin infusion process, current modeling and simulation techniques used to predict void content and distribution, and methods of gathering experimental data that have been established through prior research to determine post cure and *in situ* void content. The primary focus will be in regards to LCM and in what areas further research is still needed. This knowledge will aid in understanding the critical need to control voids in composite parts and, in particular, LCM.

2.2 Impact of Voids on Mechanical Properties

Composites may be used to produce lightweight high strength parts, but they are prone to brittle catastrophic failures when certain defects occur. One primary defect of concern is void content. The effect of void content on mechanical properties is typically measured using three standardized tests: short beam shear (ASTM D2344), three-point flexure (ASTM D790) and tensile testing (ASTM D3039). These three tests are used to measure interlaminar shear strength, flexural strength, flexural modulus, tensile strength and tensile modulus (Liu, 2006). High void contents result in a widespread reduction of mechanical properties regardless of the loading condition with matrix dominated properties being the most affected (Ghiorse, 1993; Liu, 2006; Park, 2011). Matrix dominated properties include: interlaminar shear strength (ILSS), flexural strength, compressive strength and fatigue life (Ghiorse, 1993; Park, 2011).

Ghiorse (1993) and Liu (2006) have performed extensive studies on the effects of void content in carbon epoxy laminates. Ghiorse found that laminates with a void content in the range of zero to five percent would experience a decrease in ILSS and flexural strength of up to ten percent and a decrease in flexural modulus of up to five percent for every one percent of void content. Liu's research on carbon epoxy laminates showed very similar results (see figure 2-1). Their experiments found that ILSS and flexural modulus were typically decreased by six percent and flexural strength was decreased by approximately seven percent for every one percent of void content. Tensile strengths were also found to be decreased by approximately four percent for every one percent of void content, but tensile modulus showed little impact (Liu, 2006).

11
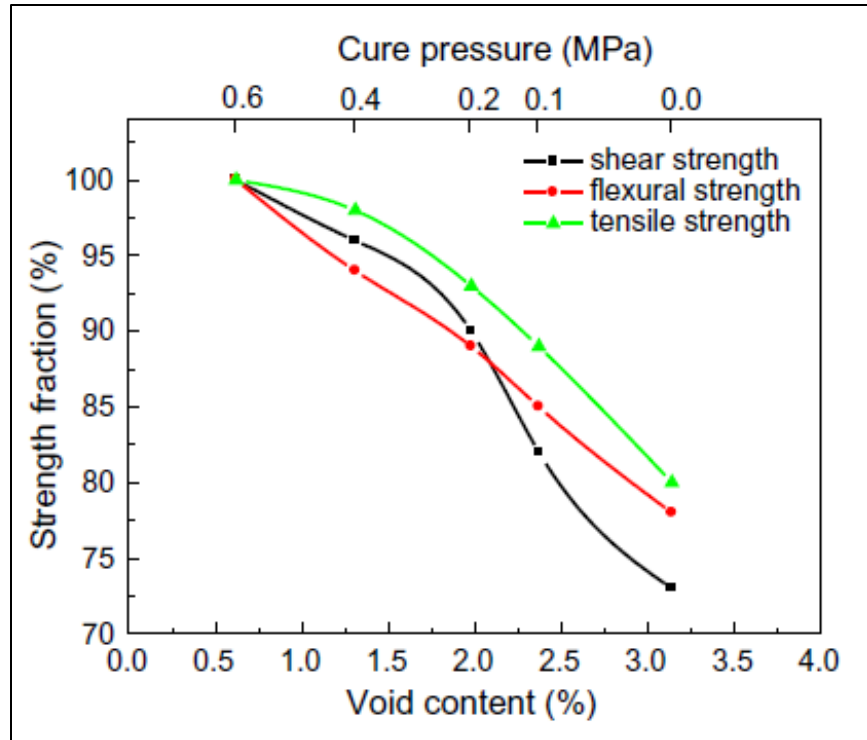
Figure 2-1 - Strength Fraction in Relation to Void Content

While the general effect of voids on composite parts is applicable to all processing

methods, most studies have been conducted using prepreg materials processed with autoclave

curing. It is possible that some variation exists between the effects of voids on the mechanical

properties of parts processed using prepreg versus LCM. In consideration of the unique and

dynamic nature of *in situ* voids, or the wide variety of materials and preform configurations

available, there is considerable difficulty in completing comparable research to what has been

done with prepregs. Varna (1995), Almeida (1994) and Sisodia (2015) have contributed to this

area to some extent, but overall little research exists in relation to LCM. Thus, there is a need for

continued study on the effect of voids in LCM.

Because of the significant impact of voids in general, it is critical that engineers account

for void content in order to optimize production processes and reduce costs. In general, ninety

percent of a composites mechanical performance may be achieved at sixty percent of the cost.
Thus, efforts to obtain the last ten percent of potential performance gains prove to be the costliest
at nearly forty percent of the overall production costs (Liu, 2006). Many applications may not
demand the same performance requirements as with certain industries like aerospace. If the
design criteria permits, processing parameters may be adjusted to achieve significant cost
savings by expanding the void content tolerance.

2.3   Void Formation, Types, Compression and Mobility in LCM

2.3.1 Void Formation

There are several factors that contribute to the formation of voids in LCM processes.
Some of these may include: mechanical air entrapment, nucleation, leakage, cavitation, uneven
resin curing, dissolved air and water within the resin system, cure pressures or other fabrication
mishaps (Park, 2011; Ghiorse, 1993; Liu, 2006). However, when processing conditions are
properly controlled by degassing the resin system, minimizing volatilization during cure and
ensuring that no significant leakage is present in the system, the only cause of voids should be
the mechanical entrapment of air (George, 2014).

The nature of voids caused by mechanical air entrapment is complex and caused by
multiple variables. Fabrics composed of high fiber count tows or complex fiber orientation
patterns will generate bubbles by mechanical entrapment as the resin flow front moves through
the material (Park, 2011). The other critical relationship is due to the competing forces that exist
in the resin flow at the macro and micro scale (George, 2014; Gourichon, 2006; Park, 2011;
Lebel, 2012). This will be discussed in more detail in the following section.

Additionally, there is a relationship between the individual preform layer fiber orientation and the mechanical entrapment of air. Sisodia found that very few voids were found in layers where the fibers were oriented in the 0 degree direction or parallel to the flow direction. Conversely, more voids were generated and trapped within the layers where fibers were oriented off axis to the flow of the resin (Sisodia, 2016).

2.3.2 Void Type

The dual scale nature of resin flow at the macro and micro scale has been well documented by researchers. This nature creates "micro" voids which are located intra-bundle or between the individual fibers in a tow and "macro" voids which are located inter-bundle or between the tows of the preform as seen in figure 2-2 (Gourichon, 2006; Park, 2011; Lebel, 2012; George, 2014). A competition between the forces in the micro and macro scale determine which type of bubble is formed. Forces in the micro scale are driven by capillary flow
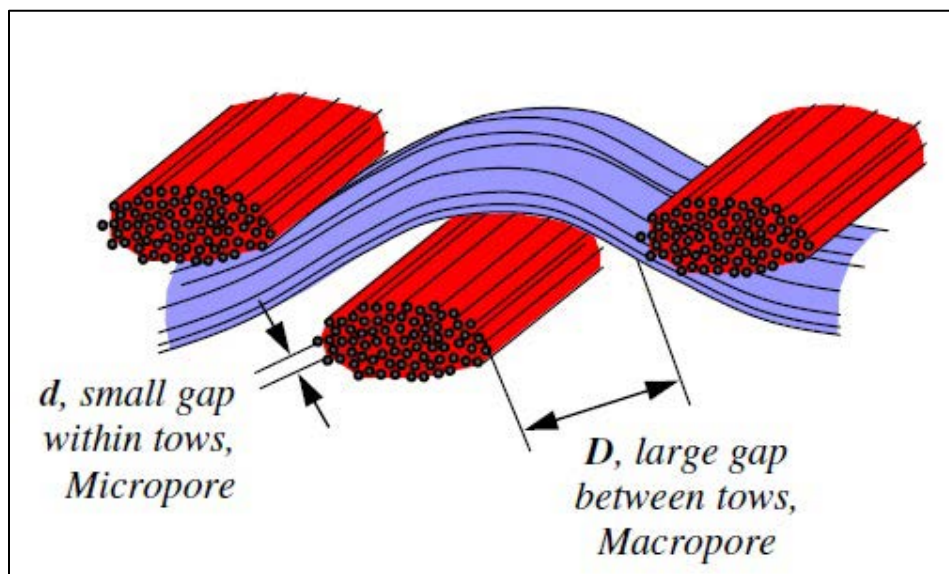
Figure 2-2 - Illustration of Micro and Macropores

while forces in the macro scale are driven by viscous flow. These forces are directly related to the resin flow velocities. When flow velocities are low, macro bubbles will be produced and when they are high, micro bubbles are produced. This imbalance in forces ultimately generates an uneven flow front as the resin moves through and between the fiber tows and traps air pockets accordingly as seen in figure 2-3 (Park, 2011). If the macro pores are filled ahead of the micro pores a needle like or cylindrical bubble will form intra-bundle, but if the micro pores are filled ahead of the macro pores a spherical bubble will form inter-bundle (Park, 2011). To limit this type of void formation, an optimal velocity may be achieved which would cause an even flow front where both the macro and micro flows travel at the same velocity (Patel, 1996 and Leclerc, 2008).
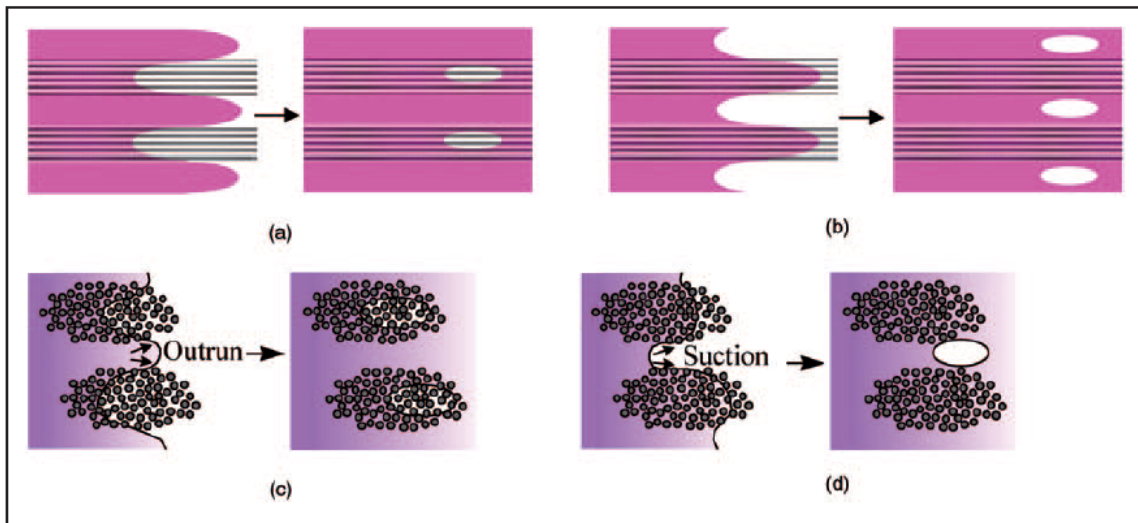
Figure 2-3 - Micro & Macrovoid Formation

Recently Sisodia has identified a third type of void termed "yarn voids." These are the largest type of void and occur in fabrics that use a yarn to keep the tows together. These voids

are generally located close to the yarns and may be curved in shape. They are typically long and may form individually or in clusters as seen in figure 2-4 (Sisodia, 2017).

| Intrabundle | Interbundle | Yarn |
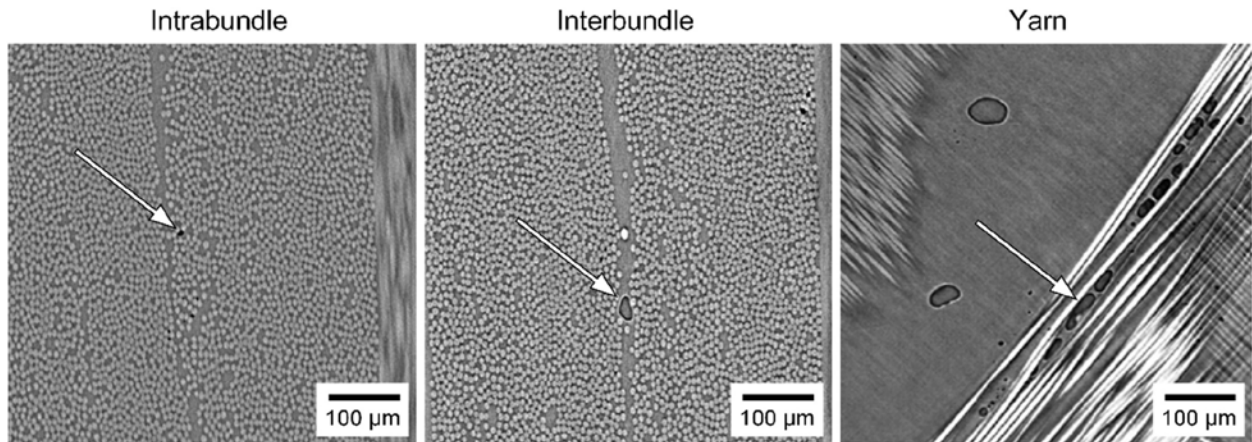
Figure 2-4 - SRCT 2D Slice Images of Voids

2.3.3 Void Compression and Mobility

Once voids have been created at the flow front, the size and form of the void will change over time as it moves with the flow of the resin. These changes are the result of resin pressure as it increases over time and compresses the bubbles (Park, 2011). The ideal gas law is used to describe this compression, but is typically used to describe microvoids rather than macrovoids (Lundström, 1993). As the pressure continues to rise, Henry's Law has been used to describe some dissolution into the resin (Lundström, 1997 and 2010). This compression is critical in the description of microvoids as they will typically remain stuck in the dense fiber bundles until the rising pressure makes them shrink to a critical size for mobilization. At this point, they typically escape the bundle into the channel and move quickly to the flow front (Lundström, 1993 and 1996). Other conditions such as temperature could result in compression, but this is typically controlled in industrial application and not a common point of focus in literature.

In general, some form of void mobility often occurs as the flow front advances. Some voids may remain at their origin while others may move with the resin flow (Park, 2011). Mobile air bubbles will tend to migrate along the micro and macropores towards the air vents in the mold (Park, 2011). Bubbles that may have been stuck in the micropores may become mobile as they are compressed and reach a critical size which facilitates mobility (Lundström, 1993 and 1996). During migration, bubbles may travel out of micropores and into the macropores (Park, 2011). During travel, bubbles may experience resistance or become blocked by mechanical obstructions such as stitching (Lundström, 2010). "Bubble mobility is generally characterized by two non-dimensional parameters: the capillary number and the ratio of the bubble size to the pore size. Bubble mobility has been explained by the force balance between the interfacial adhesion due to surface tension and the drag due to the pressure difference across the bubble. The pressure difference can be interpreted as the resin velocity in the channel flow owing to the resin viscosity and the flow conductance of the channel. Hence, the capillary number, which is the ratio of the resin velocity to the surface tension, is a key parameter for bubble motion as it is for void formation" (Park, 2011). Increases in resin velocity have been found to enhance void mobility (Park, 2011). Some have argued that bubble size will also effect void mobility, but reports are conflicting with some showing smaller bubbles are more mobile while others claim larger bubbles are more mobile (Park, 2011). Void mobility is the reason that manufacturers have found success in reducing void content by "flushing" excess resin through the preform during manufacturing (Lundström, 1994).

2.4 Modeling and Simulating Voids in LCM

The research and development of models that will aid in simulating void formation and movement in LCM has received significant attention by researchers over the last decade. Proper

"void minimization modeling entails determination of optimal process conditions to lessen the amount of bubbles created by mechanical entrapment, and to drive any created bubbles either out of the mold or to non-critical areas of the part" (George, 2014). Creating such models is challenging due to the complex nature of the processes and a multitude of scenarios in part design and preform layup which create variation in permeability (George, 2014). Difficulty in modeling can also be attributed to the complexity of void formation and their influence on the resin flow which takes place at different scales (Park, 2011).

Trochu (2006) has worked on an advanced numerical simulation method for LCM which utilizes "a mesh refinement technique [that] is combined to an extrusion algorithm to generate new non-conforming prismatic finite elements." This technique is used to simulate mold filling scenarios which aid engineers in analyzing and evaluating mold designs by determining the best locations for resin injection ports and air vents to minimize void content (Park, 2011) and has been built upon by other researchers (Gourichon, 2006).

Additional models have since been developed which attempt to predict compression, migration and formation of macrovoids (Park, 2011). However, in LCM intra-bundle air entrapment seems to be more common. Thus, researchers have begun to focus on modeling microvoids (Frishfelds, 2008 and Park, 2011). Wielhorski (2013) created a model aimed at determining the "bubble rate in imbibition through a simple network with two connected capillaries, called "Pore Doublet Model" (PDM)." Lebel, (2014) has put forth work on advanced simulation models that predict optimal capillary numbers. Work on existing and new studies to model and understand voids created in LCM remain in progress, but a common need exists where researchers require empirical data to validate their models.

Ultimately, the goal of simulation is to predict a parts final mechanical properties. In order to do so, the final cured part's void content must be accurately predicted in regards to concentration, size and distribution (George, 2014). Despite the progress made in the many models put forth, no model has yet successfully achieved this goal. Progress in this area is hampered by the difficulty in validating these models through empirical data (George, 2014).

2.5   Experimental Data

2.5.1 Void Content Measurement

2.5.1.1 Post Cure Analysis

The most common type of void measurement is *ex situ* or once the infusion has completed and the resin cured. A common method for post cure void content analysis is through the use of optical microscopy. This is achieved by cutting specific cross sections from the cured laminate and polishing them so that they may be analyzed with an optical microscope. Images are usually collected from the cross section and analyzed with software to determine the void content (George, 2011). This method is limited in its ability to only accurately measure the void content of the actual cross section instead of the entire structure. It is a slow process to collect many samples, polish and analyze them all.

Other destructive methods may be found in detail through ASTM D3171. Two common forms are through acid digestion and combustion (George, 2011). Both methods remove the resin from the fibers using acid (acid digestion) or by burning (combustion) and attempt to calculate resin, fiber and void content by calculating before and after mass and densities of the part. Neither method is ideal as they require special equipment and suffer from accuracy issues.

Acid digestion is prone to inadvertently dissolving materials and combustion can create loss by burning off carbon fibers.

A more recent and widely used method is through ultrasonic c-scan inspection. This method uses ultrasonic waves that penetrate the laminate and detect air pockets created by the voids. While this equipment is costly, it has become a preferred method since it is non-destructive and is capable of establishing a fairly accurate picture of the overall void content in a structure. However, due to the wavelength of ultrasound, very small voids may not be detected at all (George, 2014). Like the *in situ* transmission measurement methods, this test gives no images of the actual voids, and thus no morphology information, only a general degree of porosity.

Other advancements continue be made in this nondestructive testing. Current research surrounding the use of CT-imaging to achieve 3D visualization of voids is gaining popularity (Sisodia, 2016). This method shows promise because of its ability to accurately depict smaller voids that may be lost with ultrasound, but is limited by high equipment costs and time requirements.

Overall, such post-cure characterization only gives information on the final location and distribution of the void content. Process optimization based on minimizing void formation and/or moving the formed bubbles to "safe" locations requires empirical data on what happens before resin cure.

2.5.1.2 *In Situ* Analysis

While post cure void content measuring processes are effective at determining a structures final void content, they lack the ability to describe the dynamic nature of the voids before final cure is achieved. Because of this, researchers have sought methods that would allow

them to observe and measure void formation and evolution *in* situ or during the resin infusion process.

Early efforts yielded the "visualization technique" (Mahale, 1992). This method comprises the use of a liquid solution with a refractive index identical to the fibers used in the preform. This is used to saturate the fibers and "optically" dissolve them, which reveals voids that may be distinguished by dark boundaries. This method is combined with an image analysis system to collect results and is typically used to provide data for designing impregnation and mold filling processes for composite parts (Mahale, 1992). This technique can only be used with glass fibers.

Patel (1995) found success in capturing images of *in* situ voids using a derivation of the visualization technique. They used a clear acrylic mold to perform infusions in fiberglass preforms with UV dye and lighting to enhance visualization of the bubbles during infusion. Images were collected using a magnified video camera and analyzed using software. Their research provided a few images, but no quantitative data. There was also no mention of observing microvoids. Both Lundström (1994) and Gourichon (2006) have also attempted to monitor resin flow and void formation using a mold with a metal base plate and a clear top plate made of PMMA (see figure 2-5). Both experiments used a camera that was suspended over the mold to capture images of the infusion processes. Gourichon used a red dye in the matrix material to enhance bubble visibility (2006). In both instances, fiberglass preforms were used. Little data was provided on the overall success of either setup or in their ability to accurately monitor and capture images of *in situ* void formation and movement.
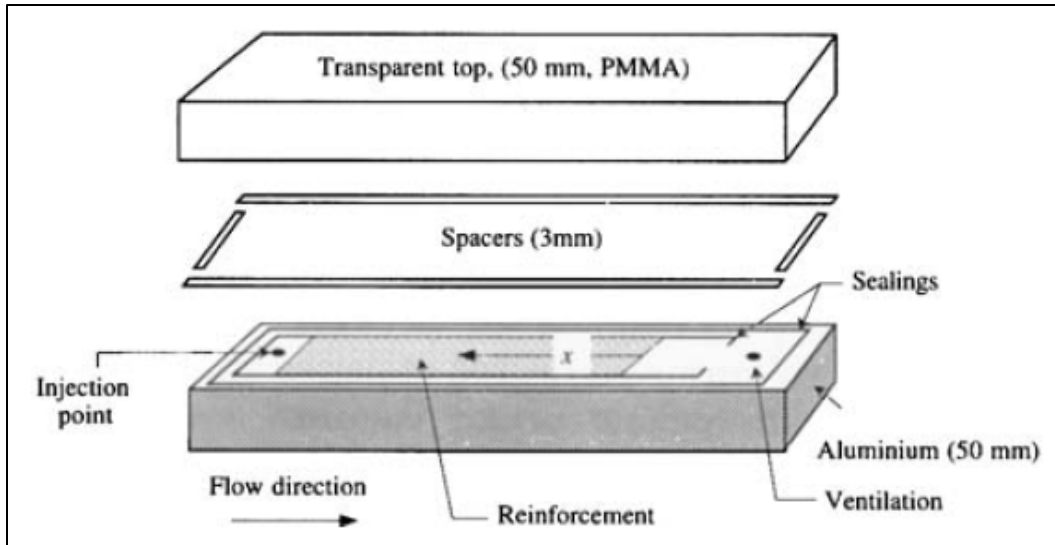
Figure 2-5 - Experimental Setup Using Clear Mold

Another technique was developed in order to study wicking behavior based on capillary rise experiments (Lebel, 2013). The experiment was conducted using fluorescent dye penetration inspection and digital imaging as the monitoring technique to track the capillary flow front. Visual monitoring was "coupled with Wilhelmy's approach based on real-time fluid mass acquisition with a high resolution balance" (Lebel, 2013). Data was collected on the height of the capillary front and the uptake fluid mass absorbed by the fabric which were analyzed using two different imbibition models. The setup comprised a motorized platform, transparent glass mold, data acquisition unit, digital camera and a high resolution balance (see figure 2-6). The experiment was conducted in a dark room to enhance visualization of the capillary rise which was highlighted with the fluorescent dye and UV lighting. An example of the results may be found in figure 2-7.
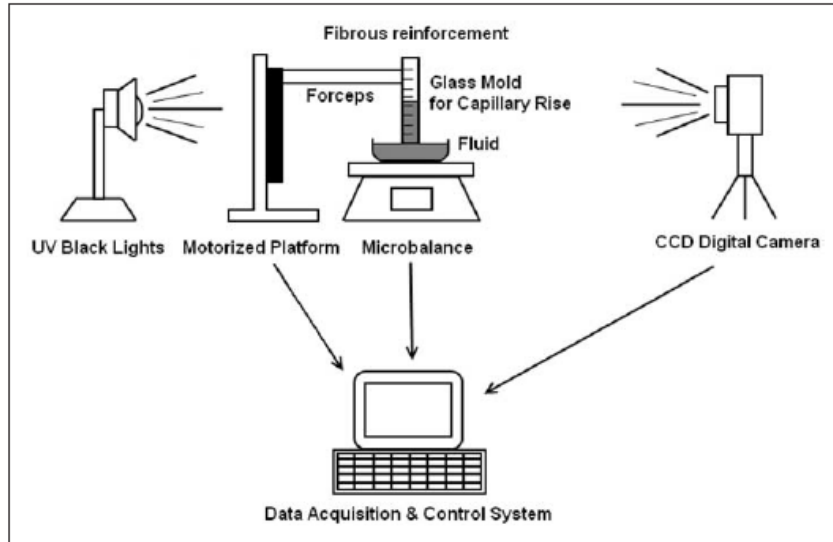
Figure 2-6 - Capillary Rise Experimental Setup
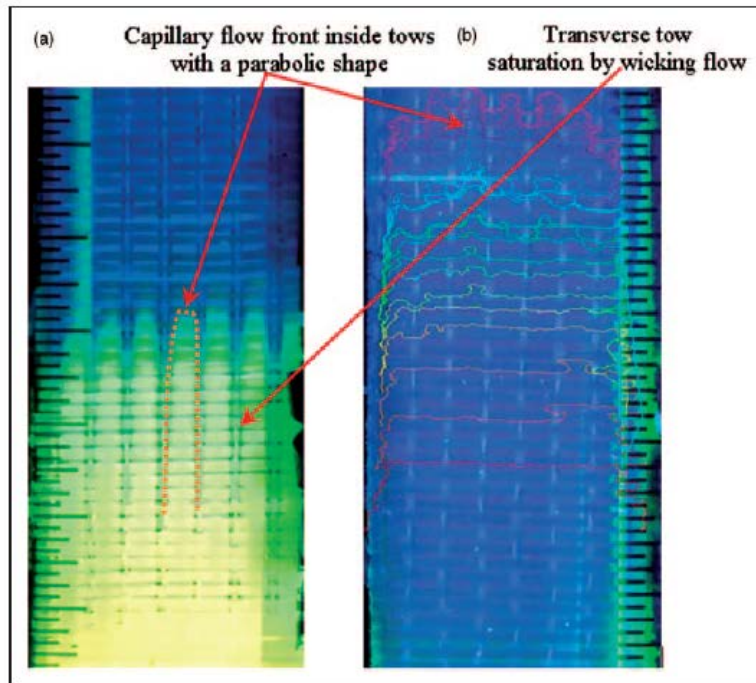
Figure 2-7 - Capillary Rise Experiment Images

Two experimental studies capable of measuring *in situ* voids in carbon fiber were found. Labat (2001) created a sensor that comprises two rectangular brass electrodes on which they would perform infusions. A voltage was periodically passed through the system in order to measure the change in current. In order to achieve conductivity, they used glycerin with a solution of potassium chloride as a test fluid. The voltage readings at various points during the infusion process were used to describe the void content at that given time (see figure 2-8). Saraswat (2007) used ultrasound transducers to monitor void formation and movement during a vacuum assisted RTM process. Both methods were compatible with carbon fibers and showed some success, but overall, neither could acquire images *in situ* voids, nor could they relate any direct information on the void size and shape itself.
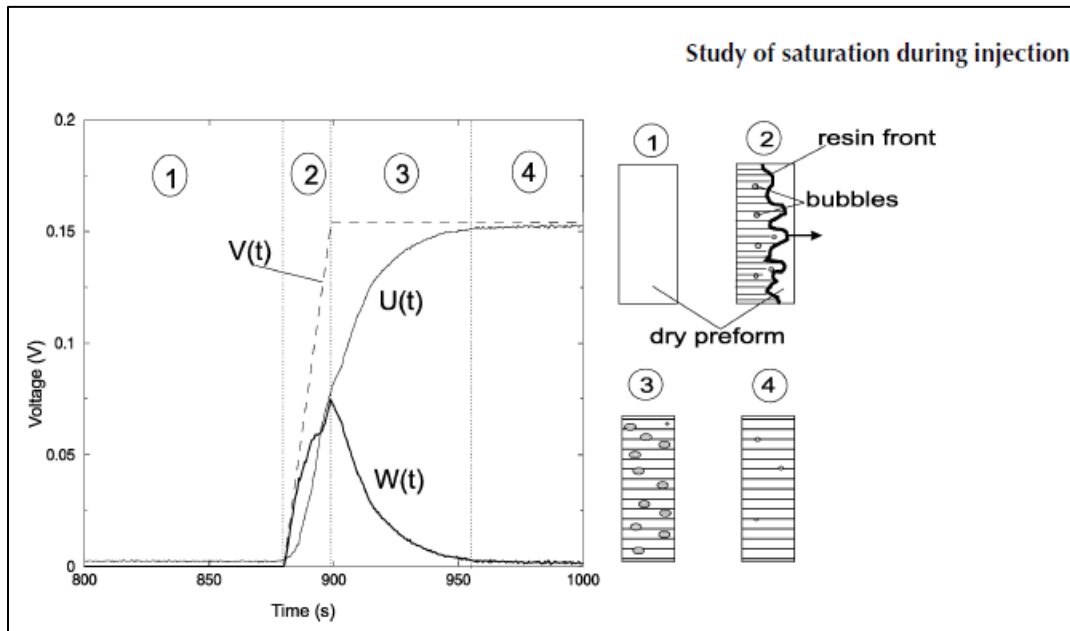
Figure 2-8 - Diagram of Voltage Curve

Overall, *in situ* void measurement has proven difficult in LCM for a number of reasons. One reason is that LCM sometimes uses a matched metal mold that does not permit visualization of the infusion process. Some of these previously mentioned methods have overcome this issue, but have been limited to the use of glass fibers as they have relied on techniques that optically dissolve the fiber to enhance void visibility. Those that have approached carbon fibers have had little success at providing detail on the microscopic level. Another significant obstacle is that even when data is successfully gathered, the amount of time required to manually analyze and evaluate enough data to accurately validate a model is enormous. Before this research, there were no known methods to visually monitor and capture images of *in situ* voids with carbon fibers. Additionally, no standard method for analyzing such pictures has yet been determined. Typically, little to no quantitative data has been provided on the results gained through image analysis nor has then been much documentation on the actual process so that others may adopt and use it.

2.6   Test Fluid Choice

The use of oils in flow tests, instead of the typical thermoset matrices in composites, has been common practice in many infusion flow experiments due to the relative ease of cleanup and low cost of such test fluids. Experimental void measurement studies using non-thermoset test fluids include (Patel, 1995; Gourichon, 2006; Labat, 2001). The general hope is that the similarity in chemical functionality of the test fluid, e.g. canola oil in this study, is similar enough to the typical thermoset such as polyester or epoxy resin, that any differences in surface chemistry would cause little difference in void formation and movement.

No published comparison results between thermosets and non-curing test fluids were found for *in situ* experimental void measurement. But such a comparison has been made in permeability studies, where the relative ease of resin flow is measured for a given reinforcement architecture. These studies have generally agreed that little difference exists for the test fluid (Steenkamer, 1995 and Skartsis, 1992) and any differences shown in earlier studies were attributed to experimental error (Hammond, 1997 and Luo, 2001). As the permeability is dependent on similar fiber-matrix interactions as capillary flow, void formation, and void movement, it is assumed that little difference also exists for fluid choice in void studies.

3 EXPERIMENTAL DESIGN

3.1 RTM and Preform Preparation

3.1.1 Tooling

A two piece mold was created using acrylic plates of one inch thickness. The top plate or side A was machined and prepared from previous experimentations. The bottom plate or side B was machined and prepared to match the bolt pattern from side A along with drilled and tapped holes for the resin inlet and outlet. The bolt patterns consisted of six through holes measuring 0.563" in diameter. The inlet and outlet where drilled and tapped to accept a 3/8" pipe thread. Standard push to connect tube fittings for 8 mm tubing were then threaded on to the exterior side of side B using Teflon tape. See figure 3-1 for a detailed drawing of side B.

The mold cavity was created by placing a silicone seal on side B. This was accomplished by using a ruler and marker to draw the cavity shape, but extending the extremities to include the inlet and outlet within. Using an all-purpose silicone from a hardware store, a thick bead was place around the perimeter of the sketch. Precision steel shim gages were place on both sides of the silicone bead. A perforated vacuum bagging material was then cut and taped to the inside surface of the side A tooling ensuring that no wrinkles were present. Side A was then gently placed on top of side B compressing the silicone bead until it came in contact with the shims. The steel C-channel beams were then placed on top of side A to add weight and ensure that the
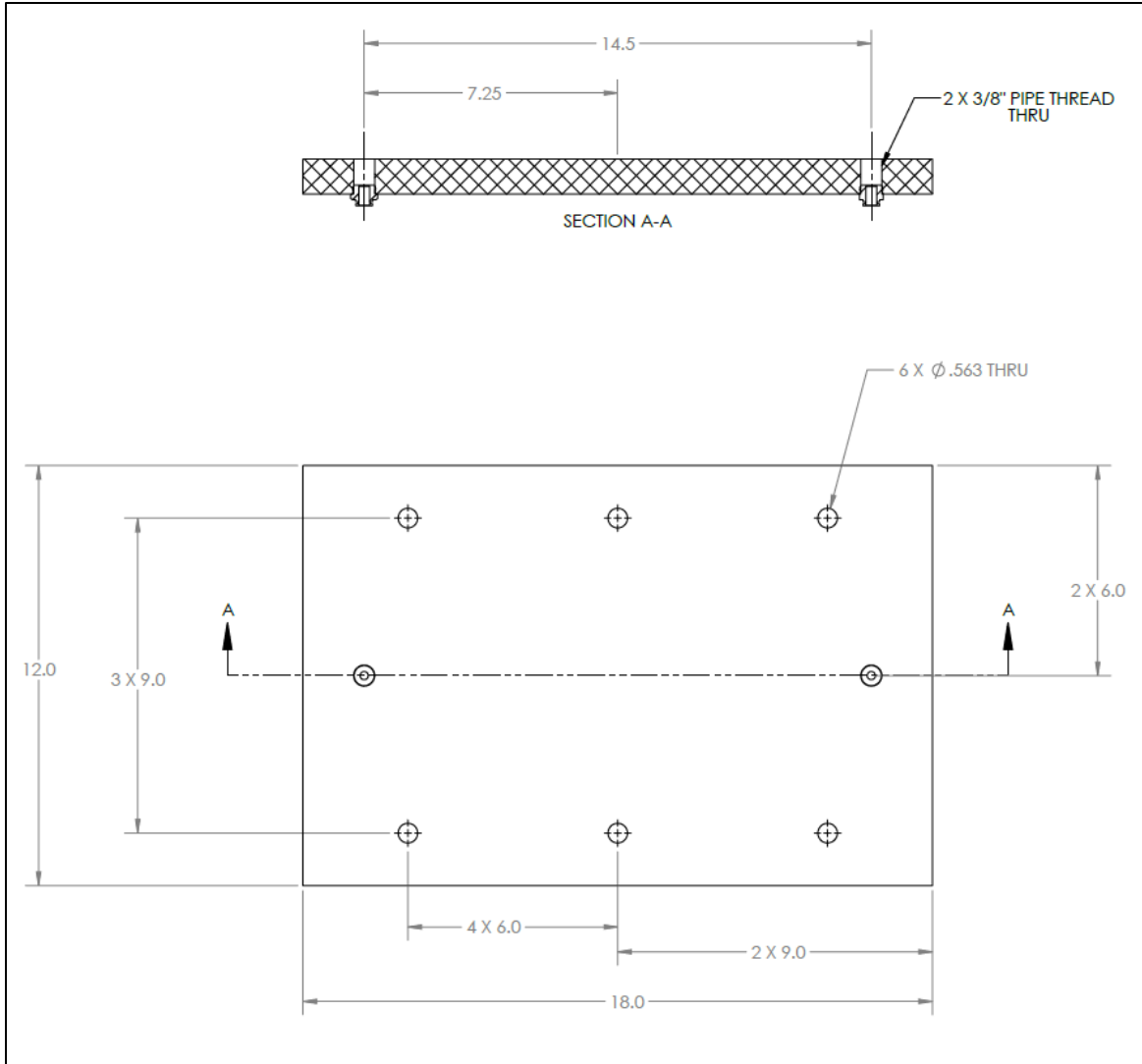
Figure 3-1 - Detail of Tooling Side B

seal did not expand. After 48 hours, side A with the bagging material was removed and the seal was trimmed to a final desired cavity dimensions (see figure 3-2).
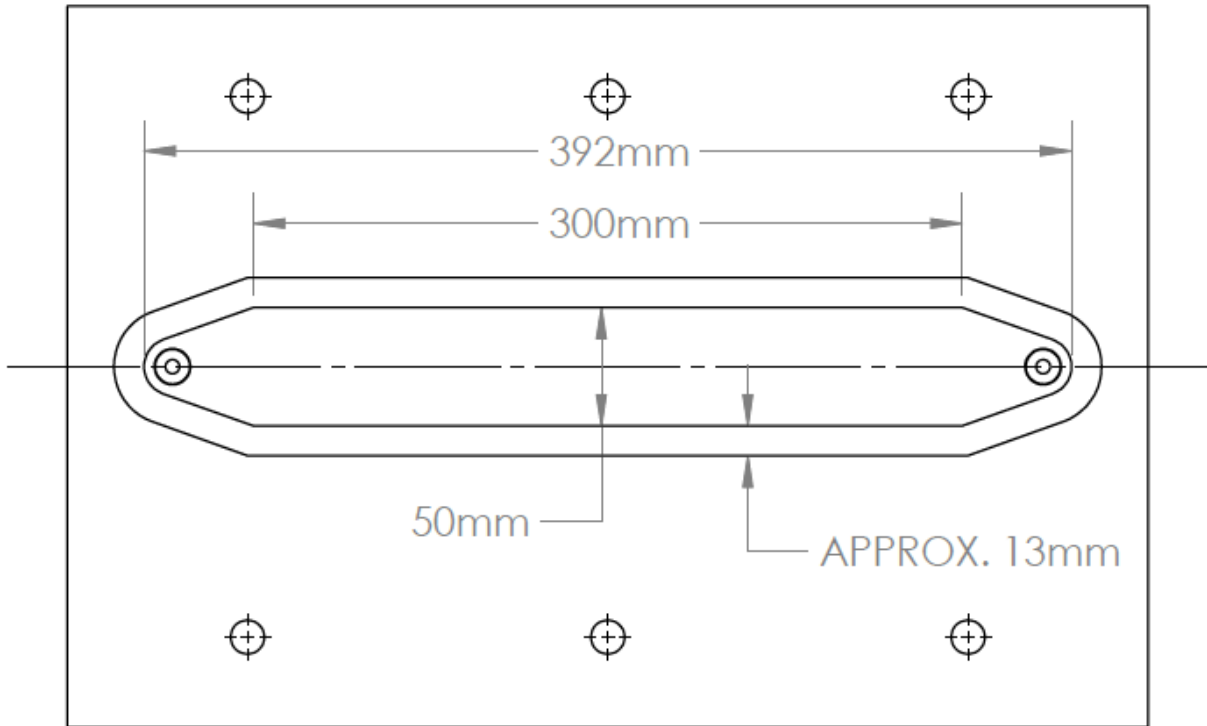
Figure 3-2 - Detail of Silicone Seal and Preform Cavity

Through previous experiments, it was found that the acrylic plates were not sufficiently rigid to withstand the pressure of the infusion process. To address this problem, two steel C-channel beams were added to each side in order to reinforce the mold assembly. Six high-strength grade 8 steel hex head screws and flange nuts were used to fasten the entire assembly together. The bolts were positioned three per side through the C-channel beams. The bolts were tightened using a specific pattern that ensured even pressure across the tooling using a torque wrench set to 20 inch-pounds. Refer to figure 3-3 for more details and see Appendix A for complete detailed drawings of all tooling components.
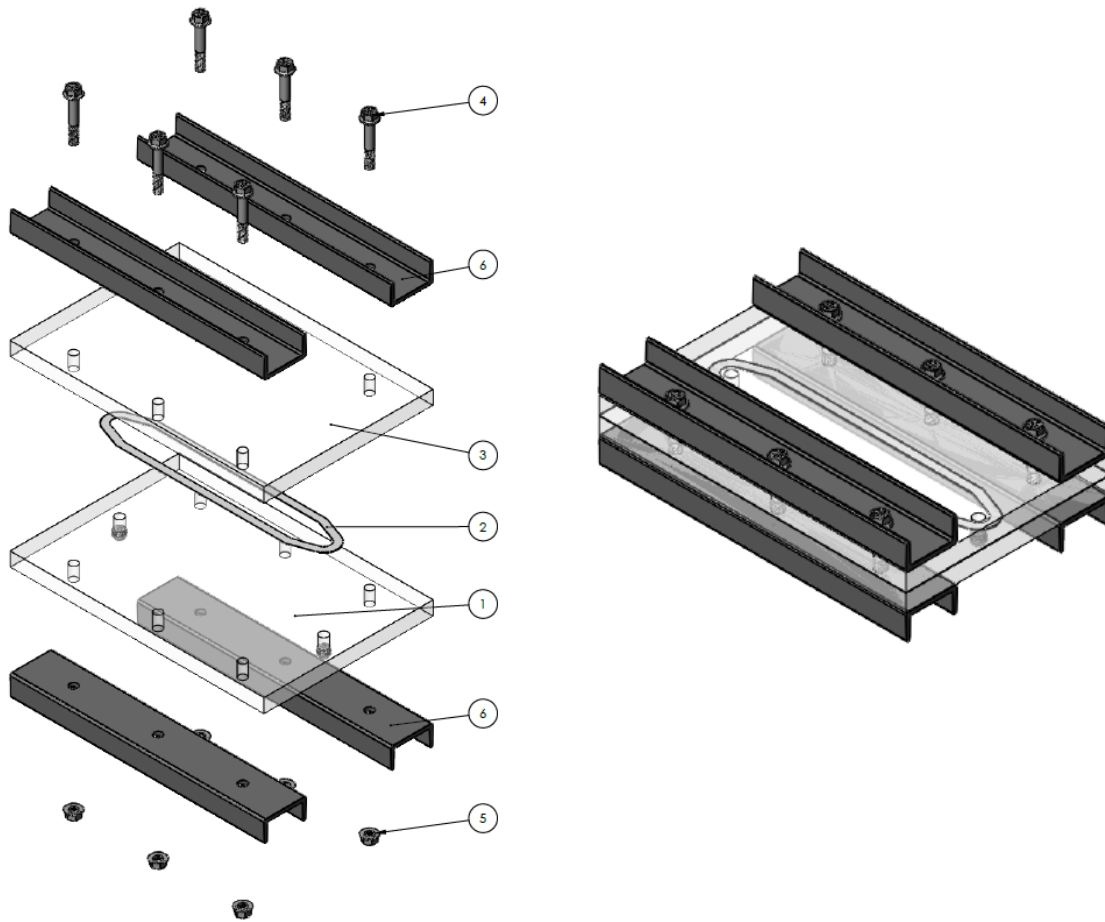
Figure 3-3 - RTM Mold Assembly

3.1.2 Pressurization System

A pressure pot was configured with an adjustable valve and pressure gage for use during the infusion process. A standard push to connect fitting was used for the air inlet and a fitting for 8 mm tubing was used for the resin outlet. An open container of test fluid was placed inside of the pressure pot with 8 mm tubing extending from the pressure pot outlet to the bottom of the container. This same 8 mm tubing extended to the inlet of side B of the tooling. Experiments were conducted at pressures of 0.5 bar, 1.0 bar and 1.5 bar.

3.1.3 Preform Materials and Preparation

Three different materials were used during experimentation. The first material is an E-Glass quadriaxial NCF with z-stitching with a ply thickness of 0.8 mm and fiber areal weight or FAW of 0.858 kg/m². This material was processed using one ply with a width and length of 100 mm x 300 mm and a cavity height of 0.8 mm. Using equation 3-1, the fiber volume was calculated at 42.03%.

$$v_f = \frac{nFAW}{\rho t} \tag{3-1}$$

$n = \#$ of plies

$FAW =$ areal weight of fabric in kg/m^2

$\rho =$ density of the fiber in kg/m^3

$t =$ thickness in meters

Subsequent infusions using a carbon fiber preform were conducted using Hexcel 4H Satin AGP185-CS material with a ply thickness of 0.2 mm and FAW of 0.185 kg/m². This material was processed with one ply using a width and length of 50 mm x 300 mm and a cavity height of 0.2 mm. The fiber volume was calculated at 52.30%.

The majority of infusions took place using Vector Ply C-L 0900 carbon fiber with a ply thickness of 0.6 mm and FAW of 0.584 kg/m². This material was processed with two plies stacked with identical fiber orientation using a width and length of 50 mm x 300 mm and a cavity height of 1.2 mm. The fiber volume was calculated at 54.99%.

All materials were cut and measured by hand using rulers and rotary cutting blades. Care was taken to lose minimal fibers in the cutting and transportation process. Refer to Appendix B for detailed tables on all material information.

3.1.4 Matrix Material and Dyes

In order to facilitate the infusion process and cleanup, a canola oil with a similar viscosity and surface chemistry to typical LCM resin systems was used for the infusion process. In order to maximize the amount of voids observed during infusion, the test fluid was not degassed prior to any infusion processing.

For much of the experimentation, an oil based UV dye was mixed in the test fluid. The dye used was Dye-Lite TP-3400-0601 from Tracer Products. The UV dye was mixed into the test fluid at approximately 5% of the total volume and was stirred thoroughly with a mixing stick. In order to confirm that the UV dye was not significantly altering the viscosity of the test fluid, both virgin and mixed test fluid were measured using a Brookfield DV-E viscometer. The virgin test fluid on average measured 58.8 mPa·s and the test fluid with UV dye measured on average 58.5 mPa·s. This suggests that the dye had no significant effect on the test fluid viscosity. Refer to Appendix B for a table of viscosity measurements.

3.1.5 Lighting Systems

For infusion processes not using UV dye, room lighting was used. Some infusions were performed using LED lighting above or below the tooling, but this generally had a negative effect on contrast. When UV dye was in use, a high powered UV light was placed above the tooling and all other room lighting was extinguished.

3.1.6 Macro Lens Photography and Tripod Setup

Each infusion had many consecutive pictures taken using macro lens photography. The equipment used was a Sony SLTA77V – a77 Digital SLR camera with 24.3 megapixels and a Sigma 50 mm f/2.8 EX DG macro lens with a Sony remote shutter release. The camera was mounted on a tripod and positioned directly over side A of the tooling. Photos were generally taken near the end of the preform closest to the outlet as this provided a higher likelihood of capturing void formation and movement over time.

3.1.7 Infusion Process

For each infusion, the fiber preform was cut and placed inside of the cavity on side B of the tooling. Care was taken to ensure that no loose fiber strands were extending into the seal material potentially causing a weak seal or race tracking. Precision metal shims were placed between side A and side B of the tooling to ensure proper cavity spacing and the tooling was clamped between the steel C-channel beams using the before-mentioned hardware, tightening pattern and torque settings. An empty container was placed below the outlet on side B of the tooling with an 8 mm tube feeding fluid overflow. Test fluid was then placed in a container and situated within the pressure pot ensuring that the outlet tubing extended well into the Test fluid. The pressure pot was sealed and the 8 mm tubing connecting it to the tooling inlet was clamped off. Next, the pressure pot was pressurized to the desired settings (0.5, 1.0, or 1.5 bar).

Once the infusion process was ready, the camera was positioned and focused for photographing void formation and movement. If UV dye was in use, the UV lighting was illuminated and the room lighting was extinguished. When ready, the clamp was released from the inlet tubing and the infusion process was photographed using a rapid photo mode to capture

images at a rate as high as 12 per second for later analysis. See figure 3-4 for Infusion setup and refer to appendix A for more detail.

Figure 3-4 - RTM Experimental Setup

3.2   Image Analysis

For usefulness in validating void theory and models, methodologies should be capable of accurately identifying micro and macrovoids of varying size. Patel and Lee (1995) have

described microvoids as ranging in size from $0.5 \times 10^{-4} - 0.01$ mm ² and macrovoids ranging in size from $0.1 - 10.0$ mm². Some research (Lundström and Gebart 1994) has illustrated voids *in situ* in the approximate range of $0.007 - 0.05$ mm² and *ex situ* or post cure in approximate ranges of $0.7 \times 10^{-4} - 0.05$ mm². No information has been found on critical size ranges required for model validation, but these values provide a good benchmark for what has already been observed.

In general, analytical procedures should be capable of accurately identifying the size, shape and position of the voids as they evolve between images. The methodology developed during this research focused on size in terms of area (mm²) and shape in terms of circularity (see section 3.2.1.3). Positional changes were not measured, but could potentially be derived from the acquired images.

3.2.1 ImageJ Processing

A public domain image analysis software developed by the National Institutes of Health called ImageJ was used for processing and analyzing all images acquired during experimentation. ImageJ has features that allow one to adjust or enhance images for optimal analysis. This may be carried out by using an automated script called a macro function. It also has a particle analysis feature that is used for void measurements and void content analysis. See figure 3-5 for a flow chart on the general process for application of this methodology. Details on how to perform each function may be found in Appendix C.
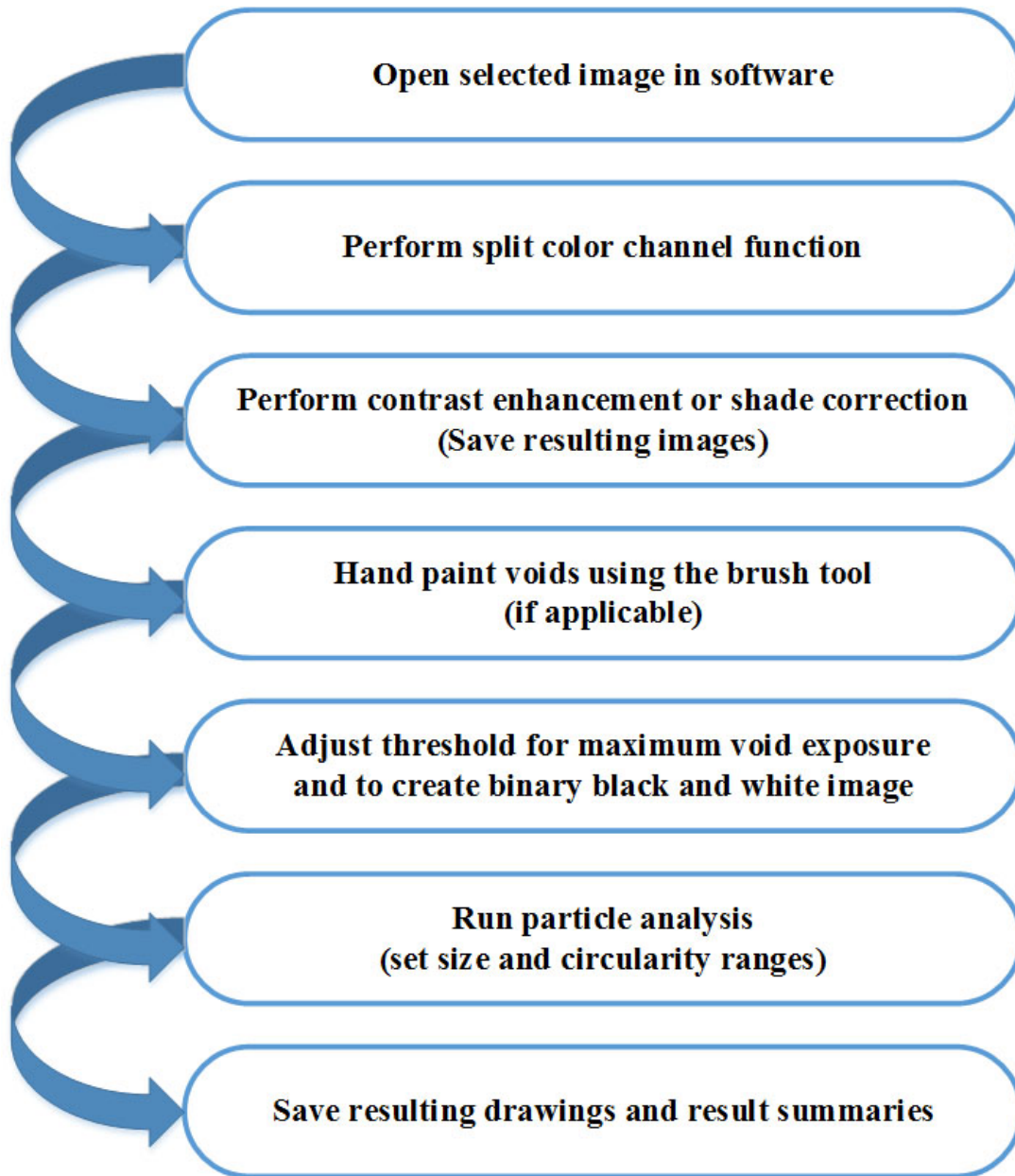
Figure 3-5 - Flow Chart Detail of Image Analysis Process

3.2.1.1 Split Channels and Threshold Adjustment

In order to analyze the void content of each image, the color photos must be converted to a binary black and white image. This was accomplished using two standard features in ImageJ.

The first step was to split the channels of an image. This yields three grey scale images using the blue, green or red components of the photograph (see Figure 3-6, 3-7 & 3-8). After the desired split color channel image was selected, the "adjust threshold" function was used. This would convert the picture to a binary black and white image and allowed the adjustment of the minimum and maximum threshold settings in order to optimize the image for further processing. In all cases during this study, the red image was unusable and appeared solid black. If processing conditions did produce a viable image, it would be recommended to explore the red channel images as well.
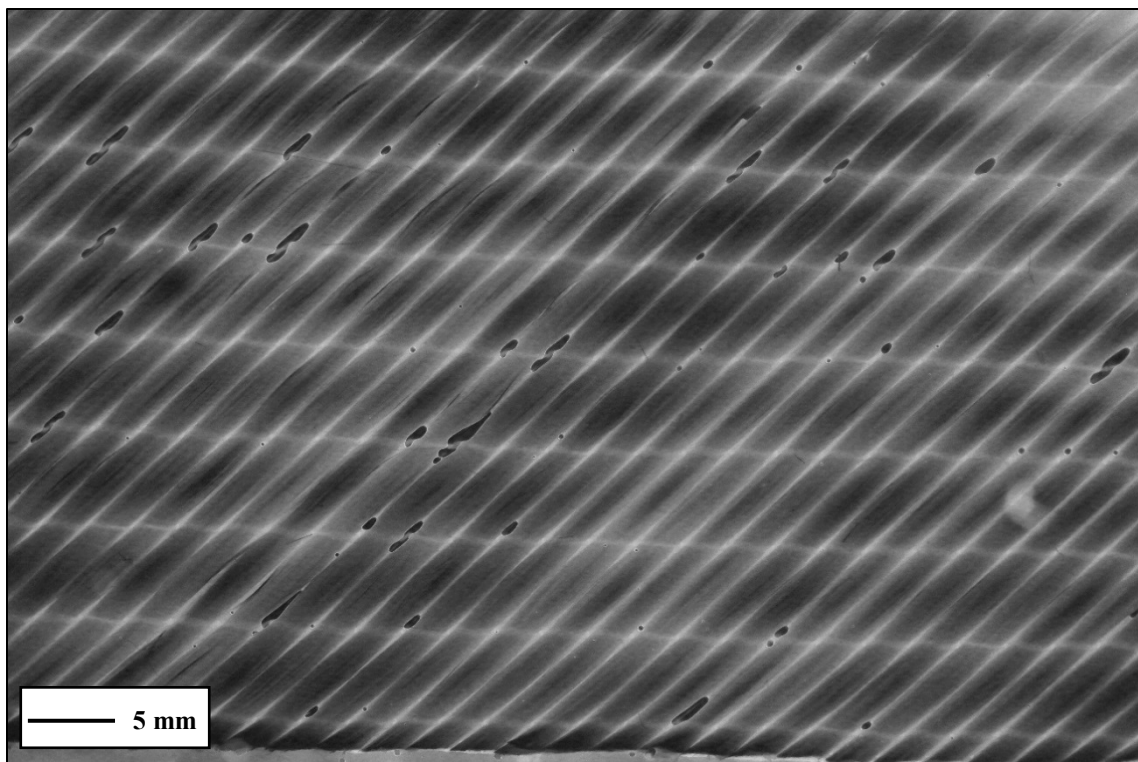
Figure 3-6 - Split Channel Color Image Blue
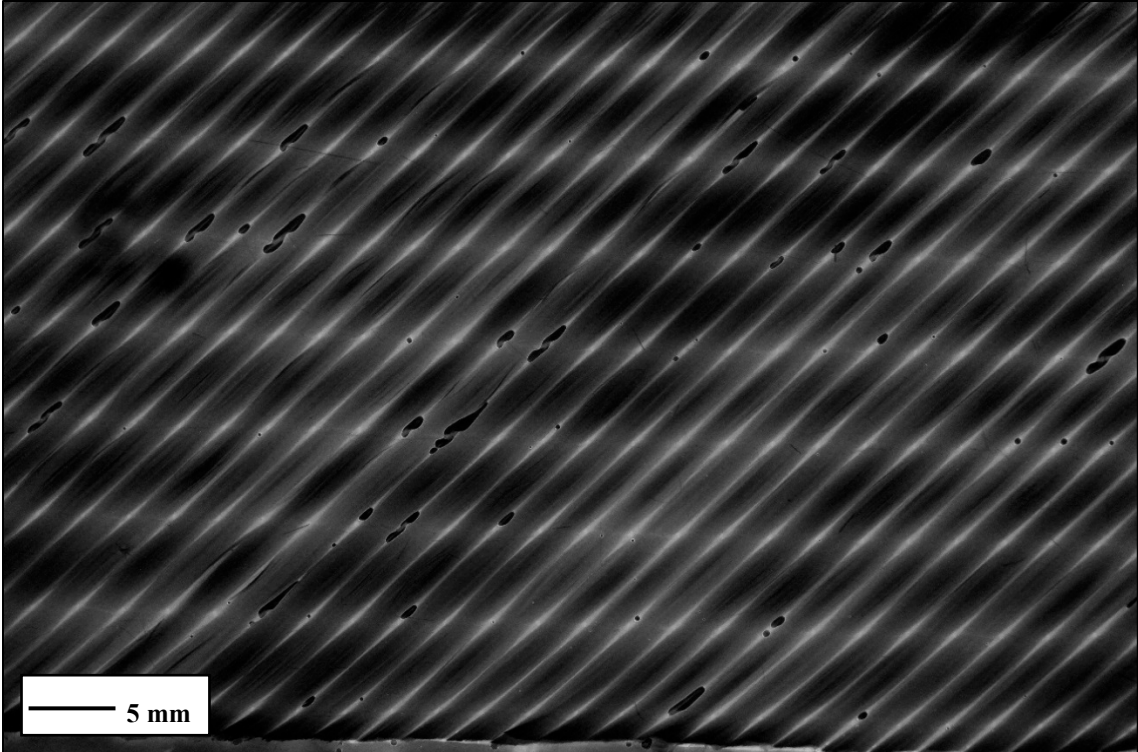
Figure 3-7 - Split Channel Color Image Green

Figure 3-8 - Split Channel Color Image Red

3.2.1.2 Shade Correction and Enhanced Contrast

In order to gain better contrast between voids, fibers and test fluid, two different processing methods were used. The first was an add-in macro called "A Posteriori" shade correction which was created at the University of Reams ("A Posteriori…"). This method attempts to correct and normalize contrast differences in the background of the image. Shade correction was performed using an Automatic background grid with the initial X and Y both set to 0. The number of points on X and Y were both set to 10. The Polynome Degree select for X Degree and Y Degree were both set to 2. This process was typically only performed on split channel images (see Figure 3-9).
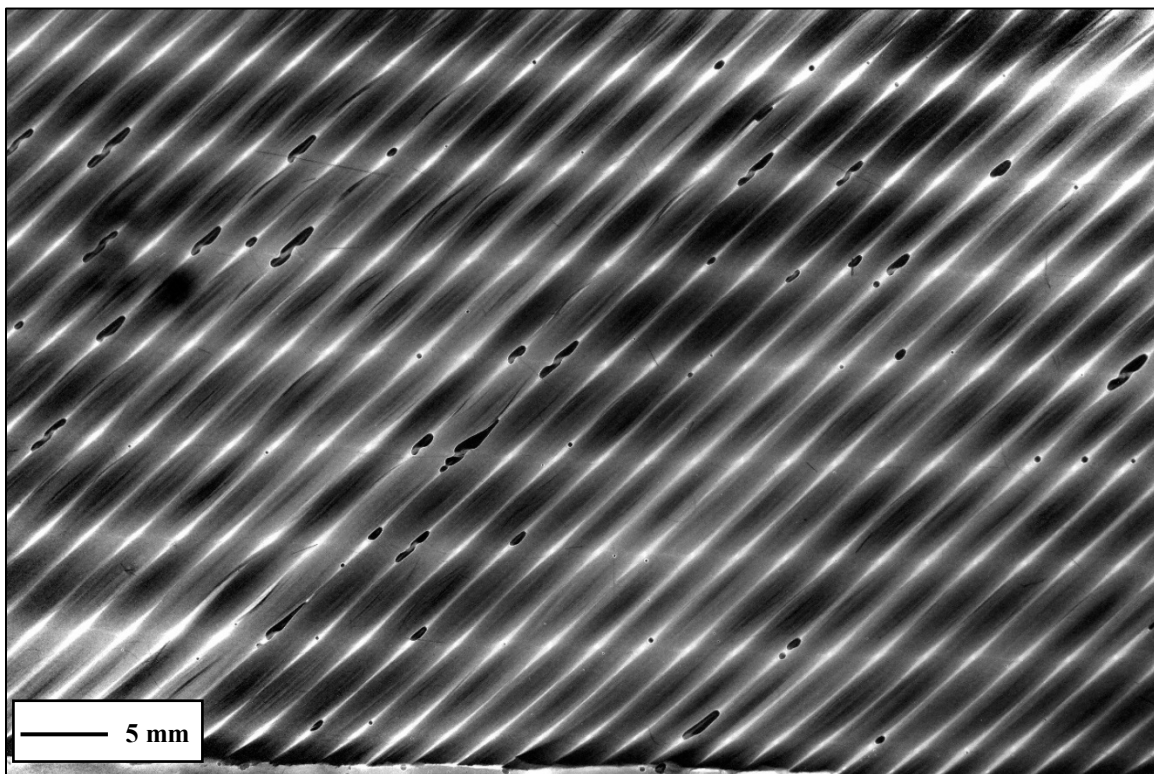
Figure 3-9 - Image from Figure 3-6 After Shade Correction.

An alternative approach to the shade correction procedure was to use the Enhance contrast feature that comes standard in the ImageJ software. This process had positive effects on both colored images and split channel images. For colored pictures, this feature was performed using 0.3% on the Equalized Histogram setting. This method produced a stark improvement in contrast on the original color image for further processing (see Figure 3-10 and 3-11). For split channel images, the feature was performed using 0.3% on the Saturate Pixels setting and the Normalize and Equalize Histogram boxes checked. Similar to the results of this feature on the original color image, this process also yields a very nice contrasting picture from the split color channel images (see Figure 3-12). Both of these tools are used before any threshold adjustment occurs.
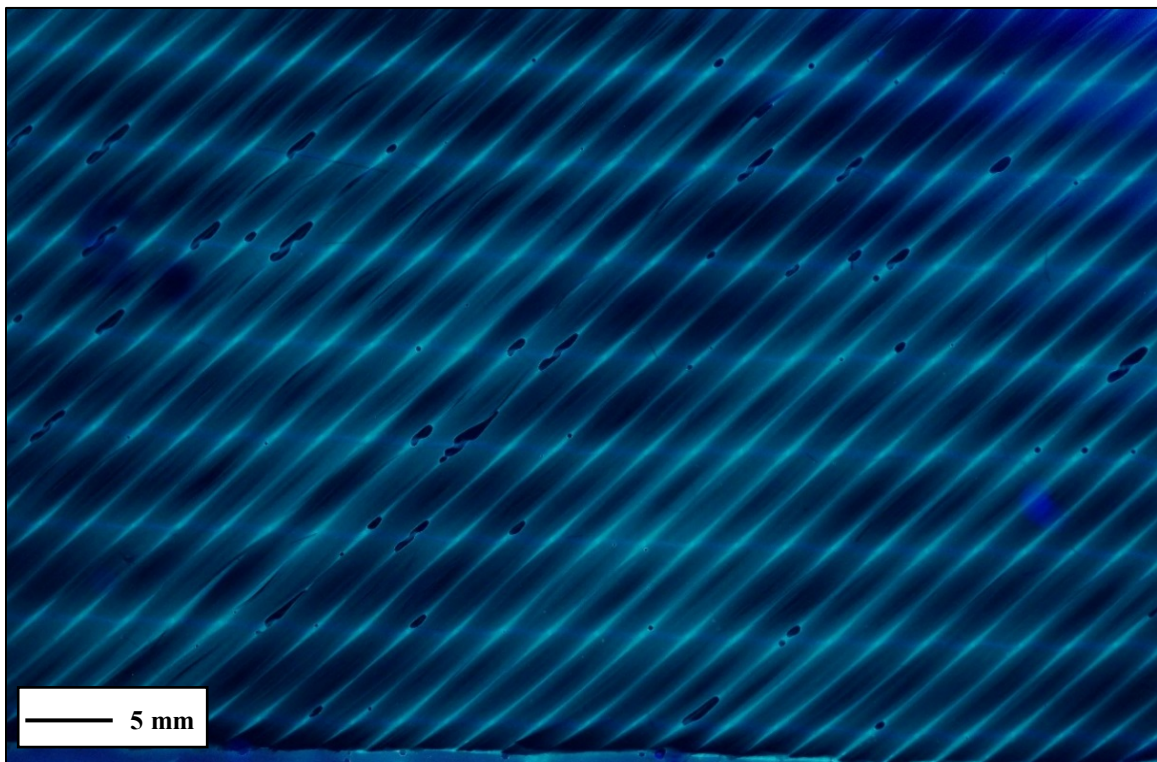
Figure 3-10 - Color Image with *In Situ* Voids
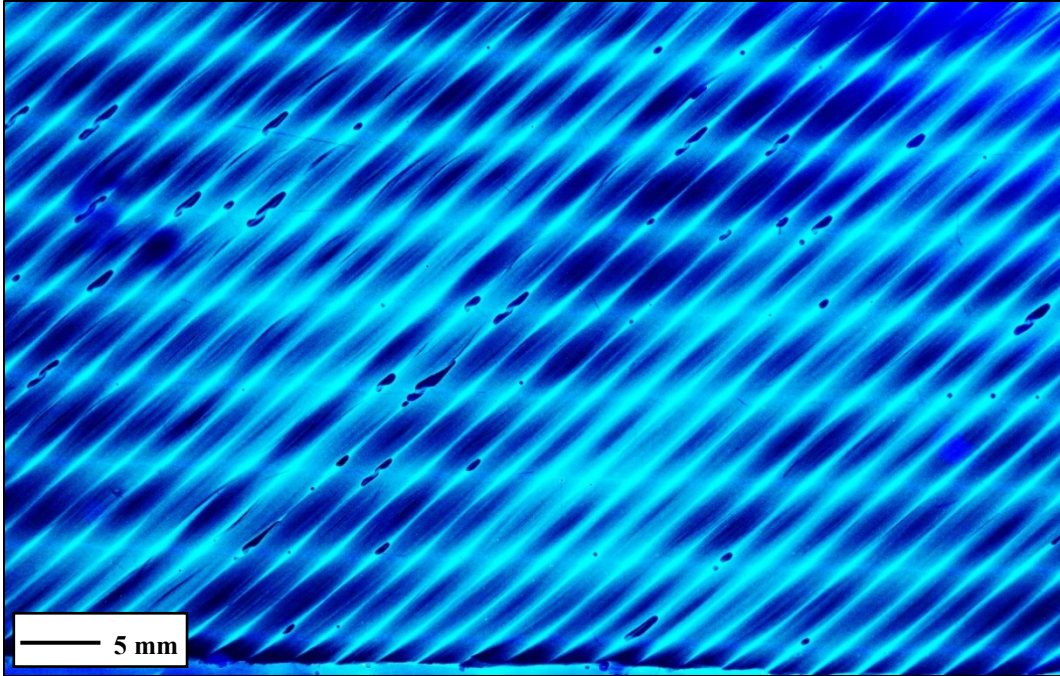
Figure 3-11 - Figure 3-10 After Enhance Contrast Tool.
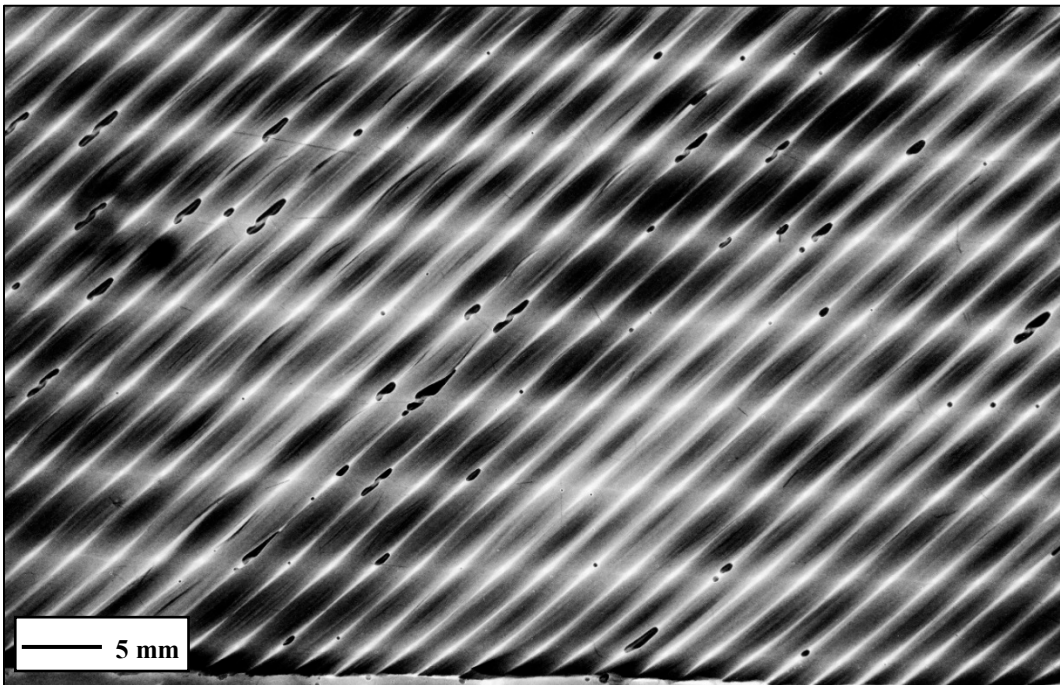
Figure 3-12 - Figure 3-6 After Enhance Contrast Tool.

3.2.1.3 Hand Painting Voids

In order to provide a standard against which the automated methodology is measured against, the bubbles were hand painted in black to ensure their detection during threshold adjustment, using the paint brush tool in the ImageJ tool bar. This tool allows for the bubbles to be filled in with solid black or for the area around the bubble to be painted white so that an accurate estimate of the size and shape of the bubble will appear after threshold adjustment.

3.2.1.4 Particle Analysis Procedure

Once the threshold adjustment had taken place and the black and white binary image was ready, the particle analysis feature was used. This feature can be used to identify and measure the area of circular shapes within the image. This process in controlled by adjusting the size and circularity range. Circularity may be measured using equation (3-2):

$$C = \frac{4\pi A}{P^2}$$ (3-2)

$A = area\ of\ bubble\ in\ mm^2$

$P = perimeter\ of\ bubble\ in\ mm$

In this research, it is used to identify and measure voids. Examples of void morphology identified during this research in relation to a measured range of circularity may be seen in Table 3-1.

Table 3-1 - Chart of Bubble Morphology

Circularity	Example Shape
.400-.600	
.601 - .800	
.801 - .850	
.851 - .900	
.901 - .950	
.951 - 1.0	

This data can be output into an excel spreadsheet along with data on the overall areal percent of particles identified in the image. This information is used to determine the void content captured in the image. In addition to this data, a new image of the particle outlines was generated and saved. The analyze particles function was performed using multiple settings and will be detailed in chapter 4.

3.2.1.5 Macro Script Creation

Once ideal settings were determined, a macro script was created for the image analysis process. This includes the steps of splitting the channels, performing shade correction or enhance contrast features, adjusting the threshold, and particle analysis. Similar to Excel, ImageJ has a macro record feature that facilitates creating a script.

3.2.2 Confirm Results

In order to confirm that the particle analysis performed by ImageJ was accurate and comprehensive, each image of the particle outlines was compared with the original colored image using Adobe Photoshop. The results of many settings were documented in a spreadsheet and tabulated so that the effectivity ratio could be calculated and compared.

3.2.2.1 Photoshop – Image Comparison

Of the images selected for analysis, a master copy in color was printed out and all voids were visually identified and assigned a numerical I.D. Using dual screen monitors, both images were loaded into Adobe Photoshop and a 7 x 7 grid was placed over each image (see figures 3-13 & 3-14). Using the zoom feature both images were compared one grid at a time and data was collected on the accuracy of the particle analysis. The three main features that were recorded
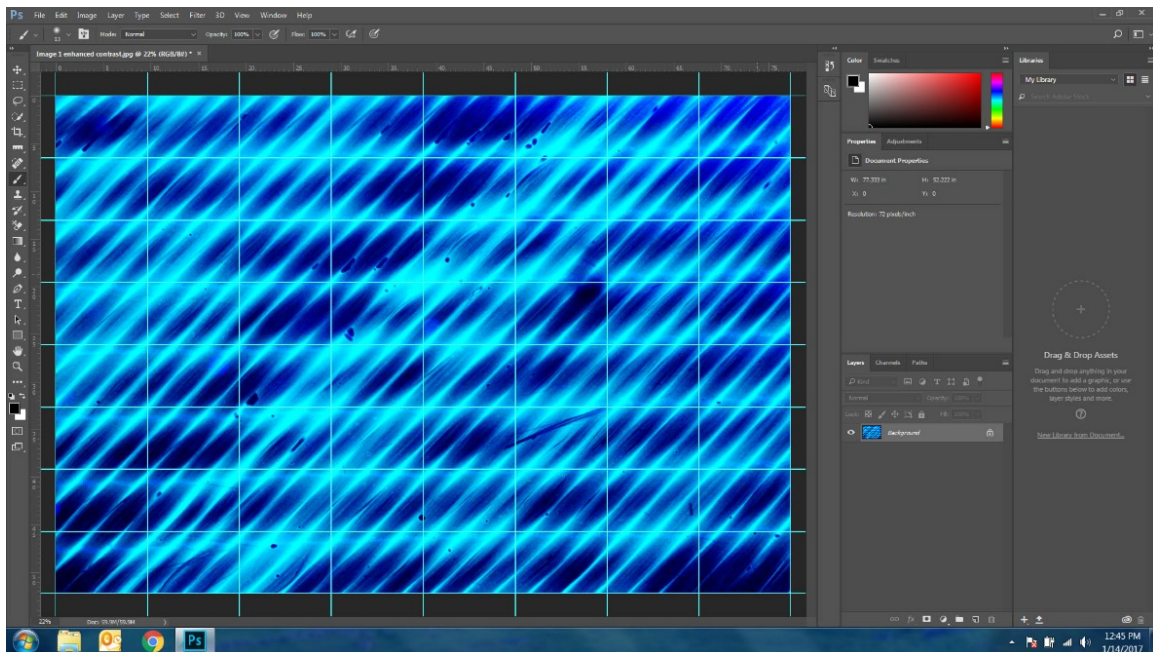
Figure 3-13 - Color Image in Photoshop with Grid
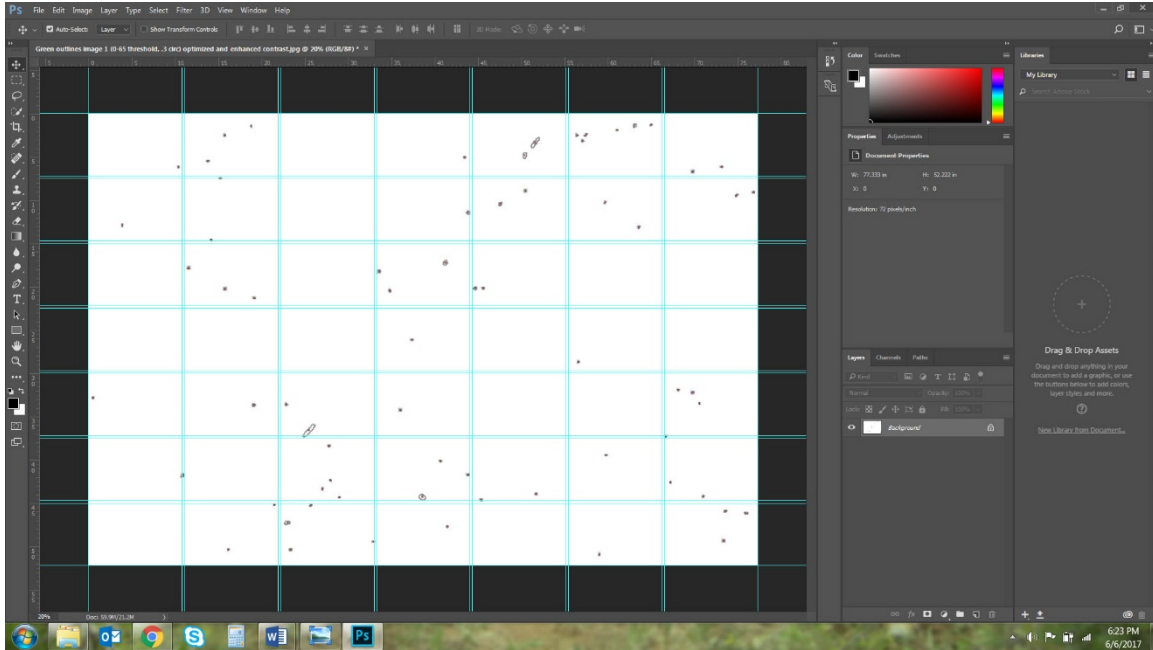
Figure 3-14 - Particle Analysis Image in Photoshop with Grid

were positive void identifications, false void identifications and missing voids. This data was used to compare settings and calculate the effectivity ratio.

3.2.2.2 Effectivity Ratio Calculation

Because there was no current method to rate or compare settings, a rating scale was created, called the Effectivity Ratio. It is calculated using equation 3-3:

$$E = \frac{(R_p/V_t)}{(R_f/R_t)+1} \tag{3-3}$$

R_p = Total number of accurate readings from particle analysis image

R_f = Total number of false readings from the particle analysis image

R_t = Total readings from the particle analysis image

V_t = Total voids identified by eye in the color image

A perfect analysis will result in a score of 1.000 while an image with no accurately identified voids would result in a 0. It is critical to not only account for maximizing accurate readings, but also to minimize the amount of false readings. The effectivity ratio does this by scaling the accuracy of true readings by the amount of false readings, thus, allowing for an accurate portrayal of the overall effectiveness of the image analysis.

4   RESEARCH RESULTS AND ANALYSIS

4.1   RTM and Macro Lens Photography

4.1.1 Fiber Glass with Room Lighting and LED Lighting

Initial expectations were that fiber glass preforms would provide optimal conditions for void observation because of their translucent nature. Therefore, experiments began with using an E-Glass quadriaxial NCF with z-stitching. Using the experimental procedures outlined in chapter 3, baseline testing was first performed on a fiberglass/test fluid combination using room lighting. Images of *in situ* voids were successfully captured (figure 4-1), but the test fluid, fibers and voids all blended together. While the voids were visually distinguishable, there was not enough contrast for accurate image analysis. Next, the same experiment was performed with LED lighting placed below the tooling in hope that this would improve contrast (see Figure 4-2). Results were poor and this method was immediately abandoned.

4.1.2 Fiber Glass with Dye (Red and UV)

Experimentation with a red colorant was brief as it was quickly realized that any easily available dye was water based and would not mix with the test fluid (canola oil). Had the dye been used with an actual epoxy resin system, it may have worked better as epoxies are more polar in their molecular features than oils and are regularly dyed in industry.

Figure 4-1 - Fiberglass with Oil and Room Lighting
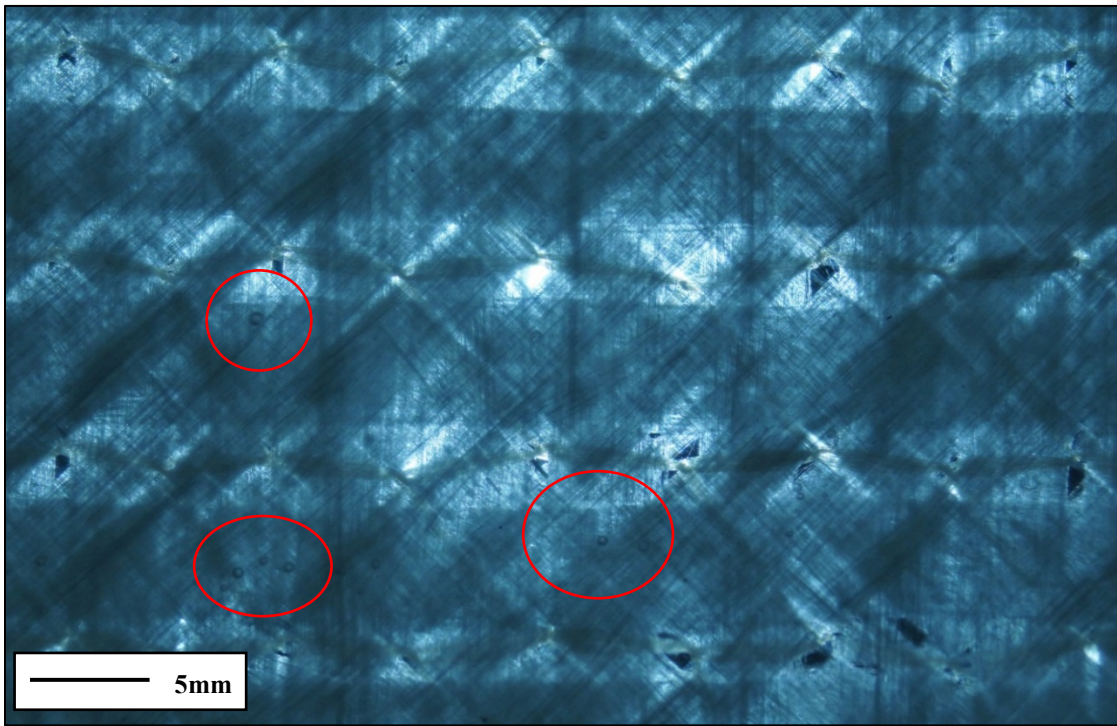
Figure 4-2 - Fiberglass with Oil and LED Under-Lighting

Researching oil based colorants yielded few options. The main option was UV dyes used for leak detection in motors and air conditioning systems. While not as dark as the red colorant that was initially tried, the UV dye would color the test fluid orange when thoroughly mixed. Using this mixture with room lighting yielded similar results to the combination of fiberglass and test fluid with no dye under room lighting (see figure 4-3). Voids were identified by eye, but there was not sufficient contrast for image analysis.

Figure 4-3 - Fiberglass with Oil/UV Dye Mix in Room Lighting

4.1.3 Fiber Glass with UV Dye and UV Lighting

The next progression naturally led to a test fluid mixed with UV dye and UV lighting with all other room lighting extinguished. This combination failed to provide optimal results as well. Like all others combinations previously attempted, images were captured of *in situ* voids, but the overall contrast was poor (see figure 4-4).
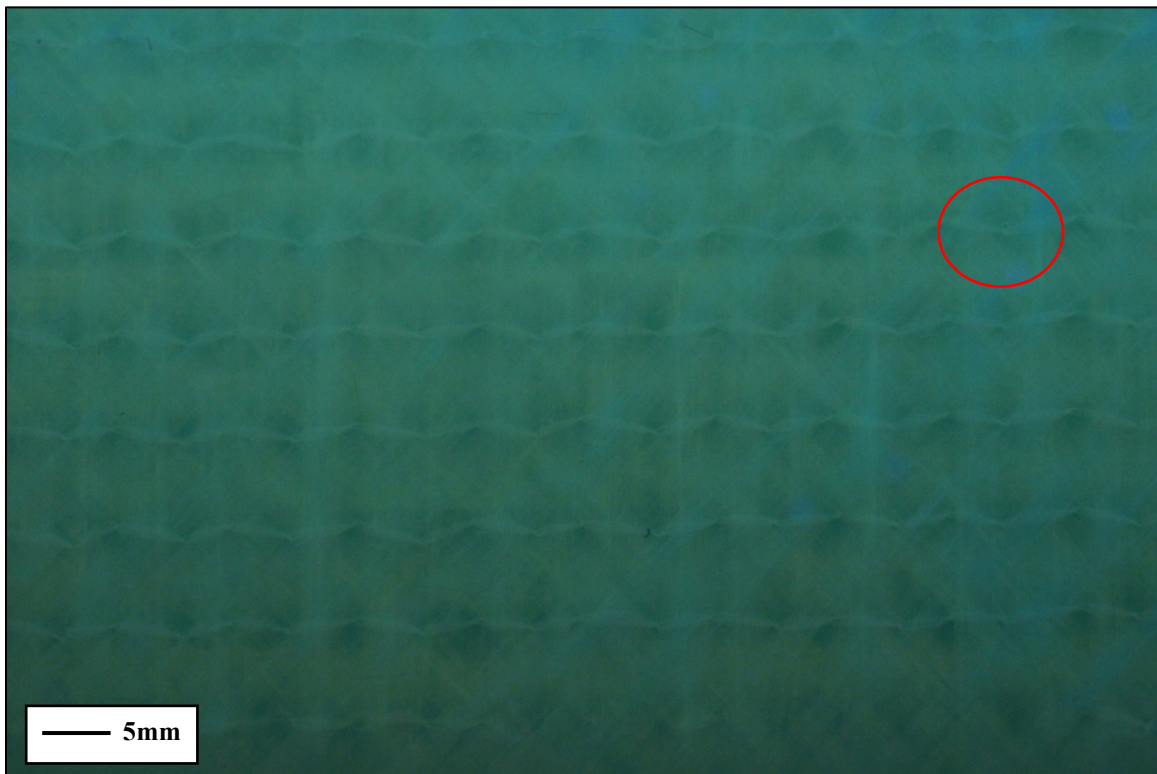
Figure 4-4 - Fiberglass with Oil/UV Dye Mix and UV Lighting

4.1.4 Carbon Fiber with UV Dye and UV Lighting

The first breakthrough came when the fiberglass preform was replaced with one of carbon fiber. Hexcel 4H Satin AGP185-CS was used for the first experiment with a test fluid/UV dye mixture and UV lighting. Not only were several voids captured in process, but

excellent overall contrast was achieved (see figure 4-5). In hindsight, it was easy to see why

carbon fiber provided optimal results. While the translucent fiberglass fibers took on the color of

the test fluid regardless of how it was manipulated, the dark black carbon fibers stood out in stark

contrast to the glowing test fluid/UV dye mixture. The only potential barrier at this point in time

was that some bundles of fiber would press against the tooling. These produced a large dark area

that obscured the image when converted to a binary black and white image and ultimately made

particle analysis more challenging. These are the first known captured images of bubbles *in situ*

during infusion of a carbon reinforcement; all previous such work used glass reinforcements

(refer to Chapter 2 for more information).
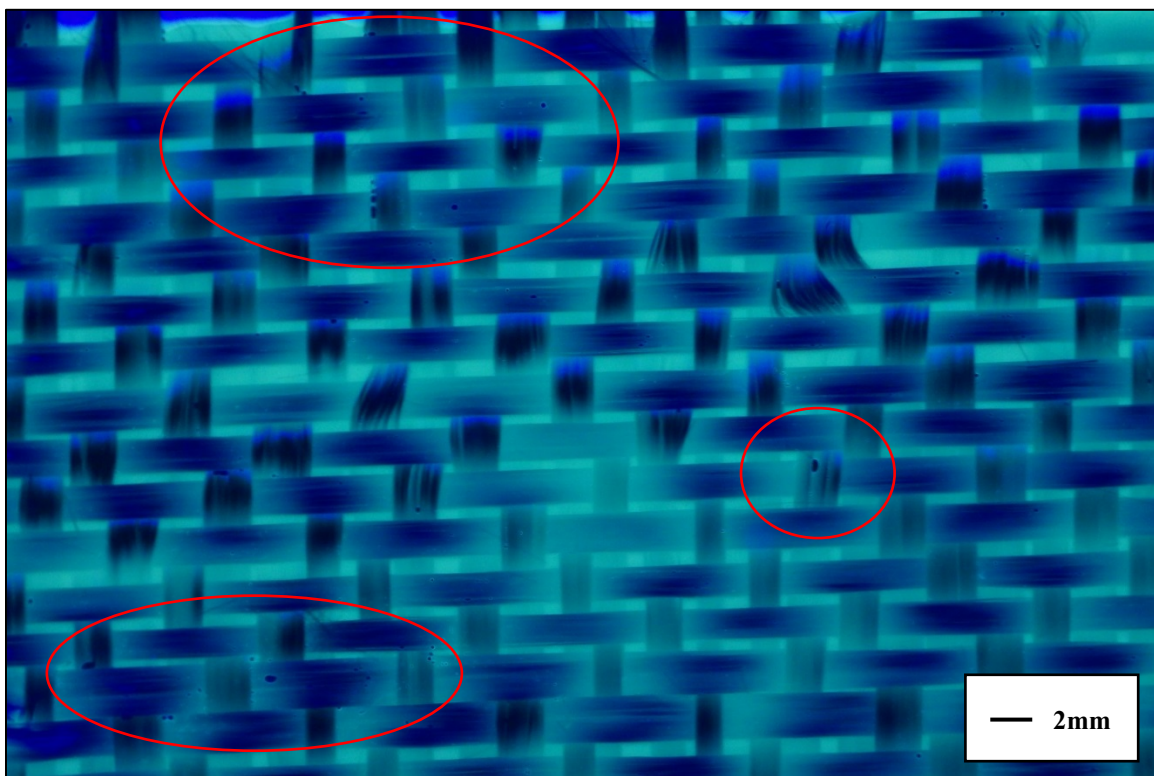
Figure 4-5 - Satin Weave Carbon Fiber with Oil/UV Mixture and UV Lighting

Moving forward, it was decided to perform the bulk of experimentation using Vector Ply C-L 0900 carbon fiber. The Vector Ply material had a much higher FAW than the Hexcel material and a more complex weave pattern that promoted more void formation and movement which was ideal for these experiments. Because two plies and a larger cavity area were used for these experiments the test fluid/fiber contrast was not as great as with the Hexcel material, but sufficient contrast was still present (see figure 4-6). However, the problem of fiber bundles pressing against the tooling and creating noise during image analysis was still a factor.
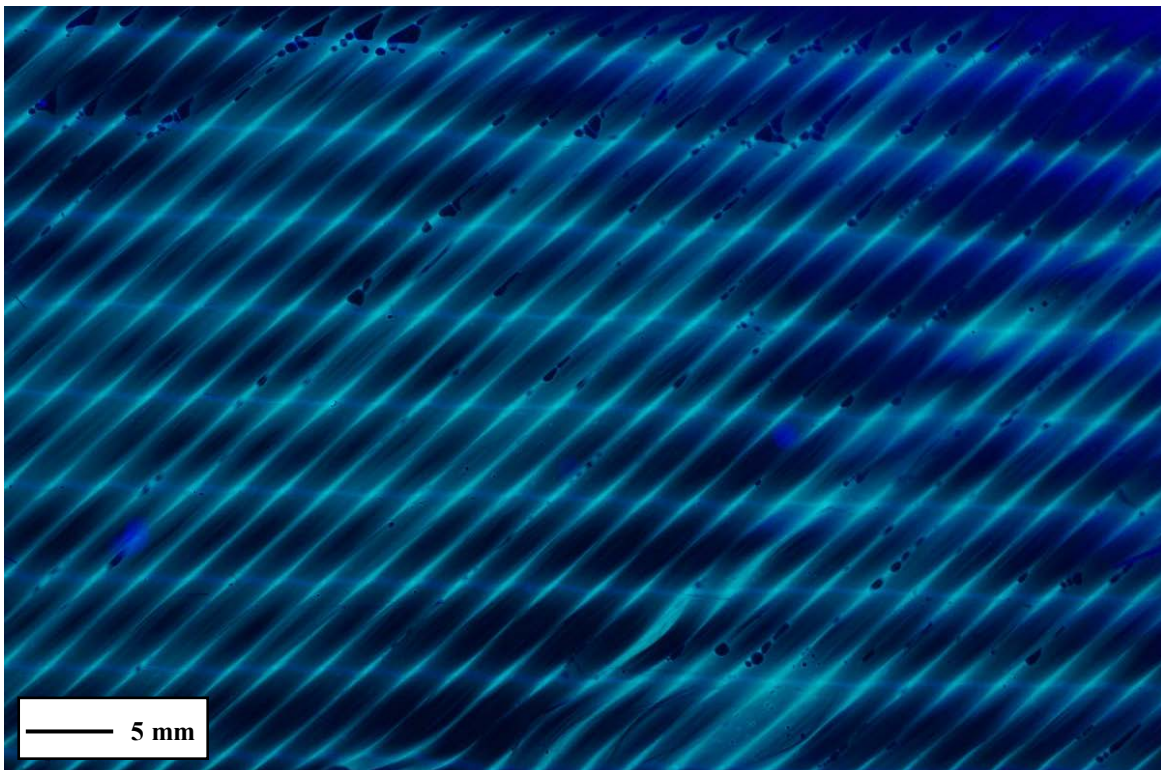
Figure 4-6 - NCF Carbon Fiber with Oil/UV Dye Mix and UV Lighting

To address this problem, precision shim gaging was attempted in order to find an optimal cavity size that would minimize contact between the fiber bundles and the tooling while not allowing race tracking to occur. Steel shims were added to the process in increments of 0.5 mm

to increase the cavity size and see if conditions could truly be optimized. Unfortunately, this process was never produced successful results. As soon as a cavity size was generated in which the fiber bundles made minimal contact with the tooling, race tracking would occur. Void formation and movement could be captured with the present race tracking, but because the test fluid flow was so fast (due to the race tracking) the images were always blurry (see figure 4-7). Fiber bundles would also start to separate from the preform and move with the test fluid flow. Ultimately, this would not have been a viable solution either way as the low fiber contents produced by expanding the mold would not be used in industrial processing. It is likely that the voids would not accurately reflect those in true molding conditions as well.
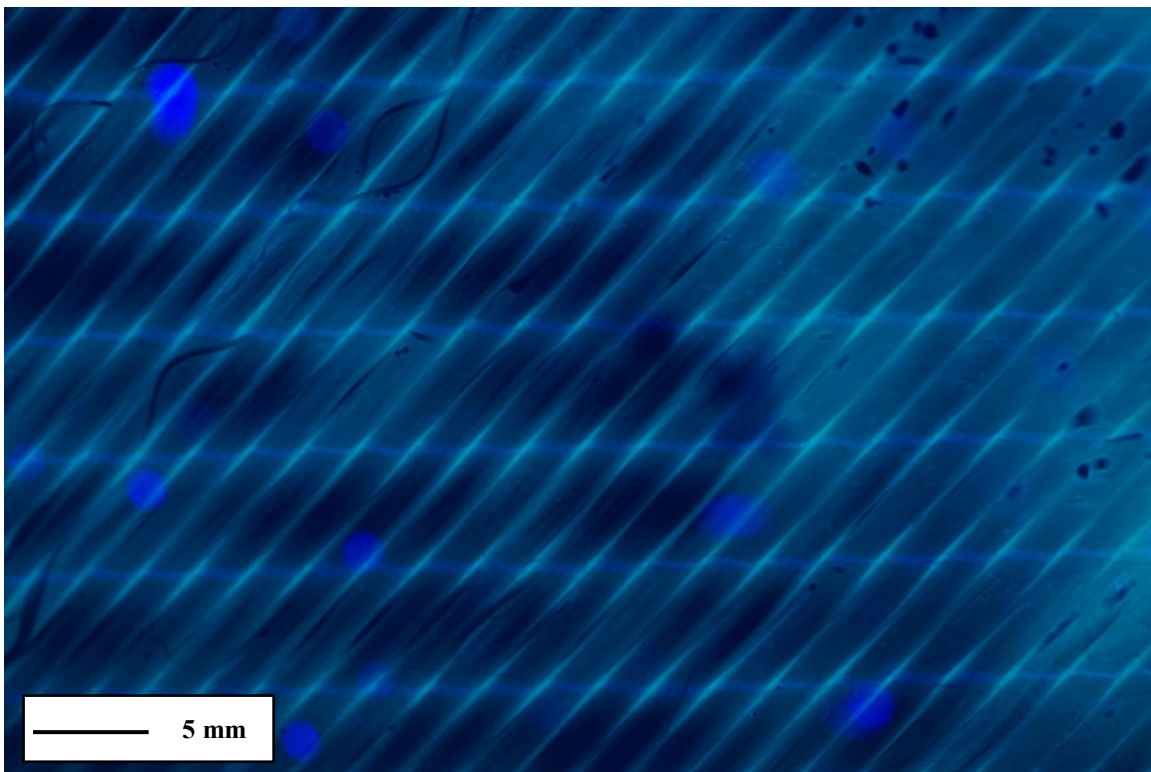
Figure 4-7 - Example of Race Tracking

In the end, it was determined that some contact between fiber bundles and the tooling would have to be acceptable. Moving forward, the method of minimizing contact through adjusting the cavity size with the steel shims was abandoned and shimming was only used to ensure proper cavity spacing. Multiple infusions were carried out yielding many successive images detailing void movement and formation in great contrast and clarity. Of these images, three displaying different void content and formations were selected for extensive testing in order to find optimal image analysis processing parameters. More images can be viewed in Appendix D.

4.2   Image Analysis

4.2.1 Image 1

4.2.1.1 Settings, Results, Effectivity Ratio and Void Content

Image 1 (see figure 4-8) was tested under 13 different parameter settings all with varying success in ImageJ. Each setting had variable conditions in relation to which split channel color was selected and which shading correction or contrast enhancements and threshold adjustments occurred.

On the original color image, 74 different voids were identified and labeled. Between the different settings attempted, 53 of the 74 or 72% of the voids were identified, but no single setting achieved better than 33 of the 74 voids or 45%. Unfortunately, most of these settings also included high numbers of false readings ranging from four up to thirty eight. This data was used to identify the different effects of threshold settings and determine which image enhancements

5 mm

Figure 4-8 - Image 1

5 mm
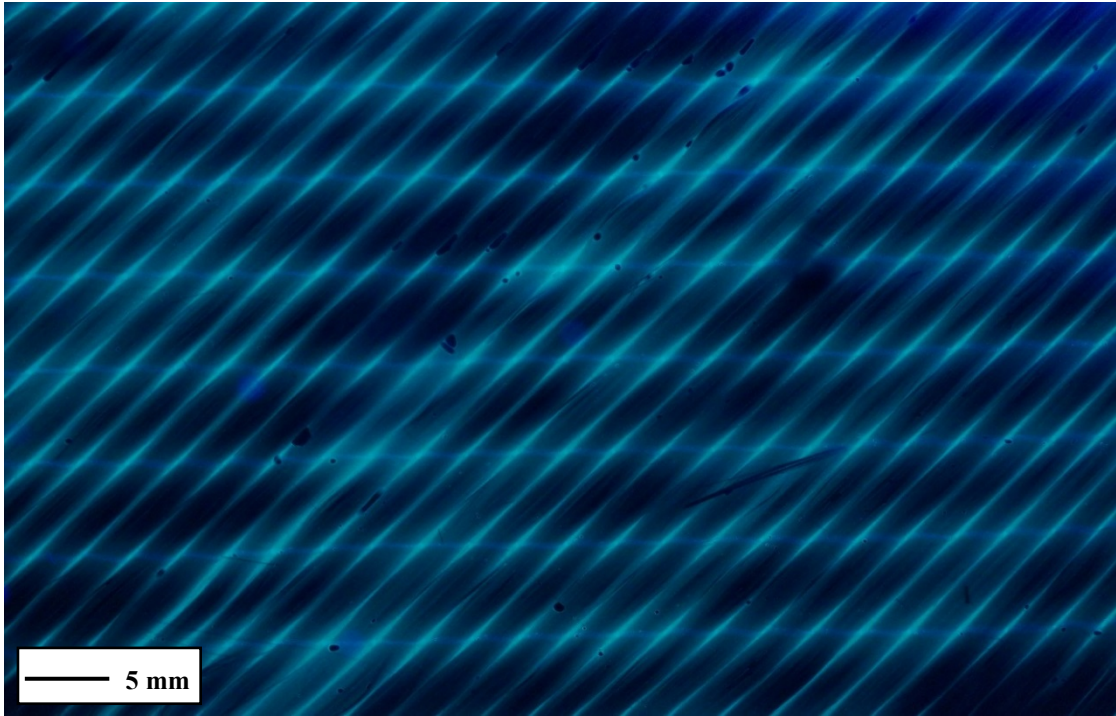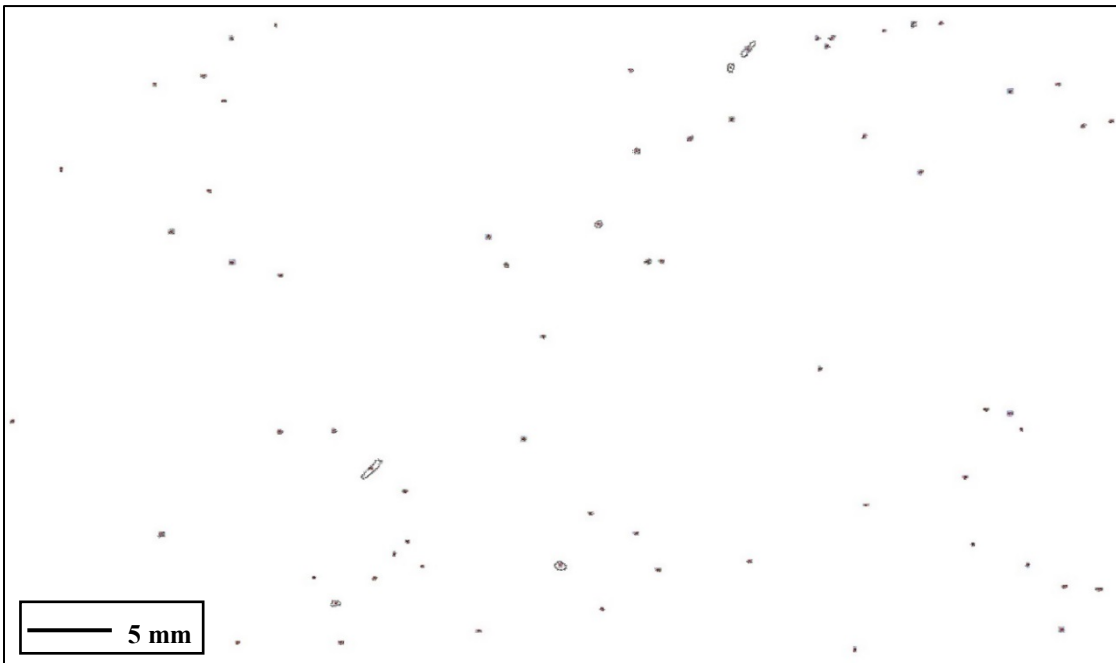
Figure 4-9 - Image 1 Particle Analysis Drawing

were having the greatest success for further testing on the following images. Figure 4-9 is an image outlining the results of the optimal particle analysis of image 1.

See table 4-1 and 4-2 for the effectivity ratios of each parameter and details on the parameters that yielded the best results for image 1.

Table 4-1 - Effectivity Ratio for Each Setting Tested on Image 1

Image 1			
Image Setting #:	**Effectivity Ratio**	**Image Setting #:**	**Effectivity Ratio**
1	0.182	8	0.220
2	0.225	9	0.237
3	0.299	10	0.271
4	0.284	11	0.230
5	0.281	12	0.252
6	0.214	13	0.275
7	0.235		

Table 4-2 - Image 1 Best Parameter and Setting Details

Image 1 - #3 Parameters	
Settings & Parameters:	
Original Image Enhancements	No
Split Channel Color Image	Green
Image Enhancement	Shade Correction
Minimum Threshold Setting	0
Maximum Threshold Setting	65
Analyze Particle Settings:	
Size range (pixel²)	100-10000
Circularity range	0.3 - 1.0
Positive Void I.D.'s	33
False Void I.D.'s	32
Missed Voids	41
Calculated Effectivity Ratio	**0.299**

The measured void content for Image 1 using image settings #3 was 0.106%. More details on results and settings may be found in Appendix E.

4.2.2 Image 2

4.2.2.1 Settings, Results, Effectivity Ratio and Void Content

Much was learned during the analysis of image 1 and ultimately led to improved results with image 2 (see figure 4-10). This was also facilitated by a much lower void content with more circular bubbles. A total of nine image settings were used for initial analysis. Again, each setting had variable conditions in relation to which split channel color, shading correction or contrast enhancements and threshold adjustments were selected.
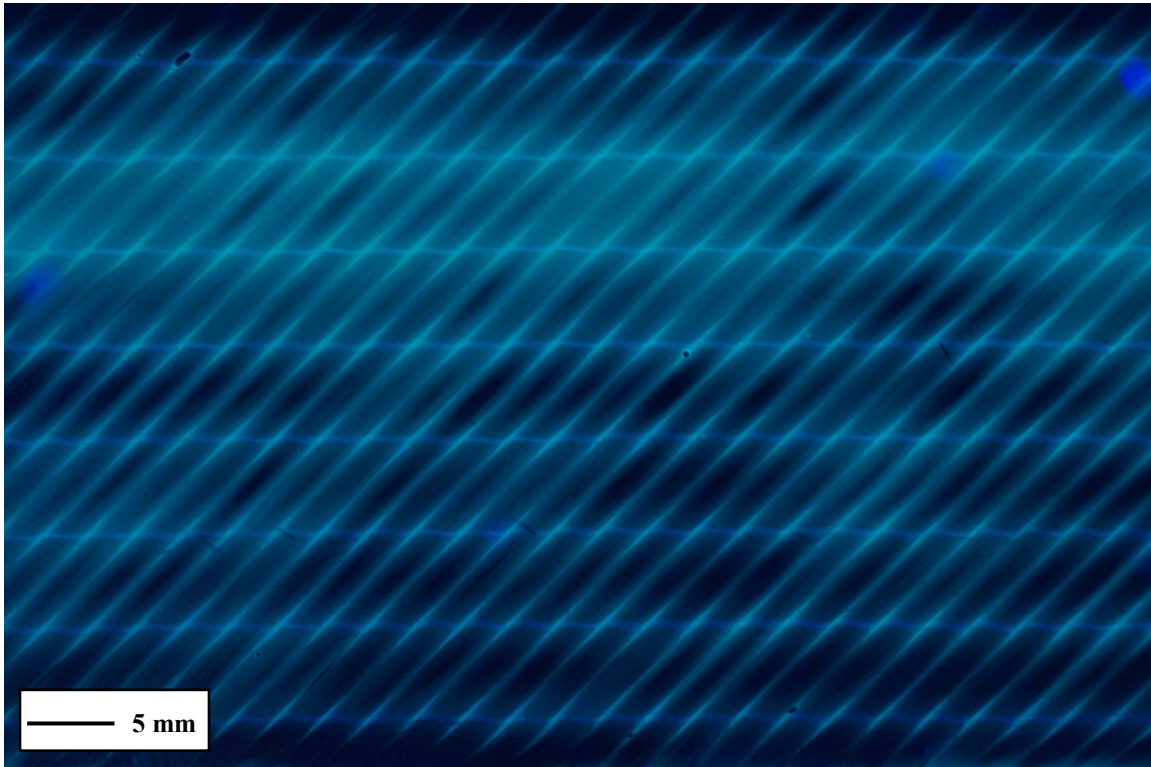
Figure 4-10 - Image 2

On the original color image, seven different voids were identified and labeled. Between the different settings attempted, five of the seven or 71% of the voids were identified. From this data, settings were further optimized and used in two follow-up analyses. Both captured a sixth void and one yielded zero false readings. Overall, 86% accuracy was achieved within one image setting. Figure 4-11 is an image outlining the results of the optimal particle analysis of image 2.

Figure 4-11 - Image 2 Particle Analysis Drawing

See table 4-3 and 4-4 for the effectivity ratios of each parameter and details on the parameters that yielded the best results for image 2.

Table 4-3 - Effectivity Ratio for Each Setting Tested on Image 2

Image Setting #:	Effectivity Ratio	Image Setting #:	Effectivity Ratio
1	0.462	7	0.163
2	0.400	8	0.381
3	0.252	9	0.462
4	0.273	10	0.589
5	0.519	11	0.857
6	0.306		

Table 4-4 - Image 2 Best Parameter and Setting Details

Image 2 - #11 Parameters	
Settings & Parameters:	
Original Image Enhancements	No
Split Channel Color Image	Green
Image Enhancement	Shade Correction
Minimum Threshold Setting	0
Maximum Threshold Setting	103
Analyze Particle Settings:	
Size range (pixel²)	150-8000
Circularity range	0.3 - 1.0
Positive Void I.D.'s	6
False Void I.D.'s	0
Missed Voids	1
Calculated Effectivity Ratio	**0.857**

The measured void content for Image 2 using image settings #11 was 0.023%. More details on results and settings may be found in Appendix E.

4.2.3 Image 3

4.2.3.1 Settings, Results, Effectivity Ratio and Void Content

The analysis of image 3 was more challenging than image 2, but still yielded better results than image 1 (see figure 4-12). These results were exciting as this image has a large void content with complex formations.
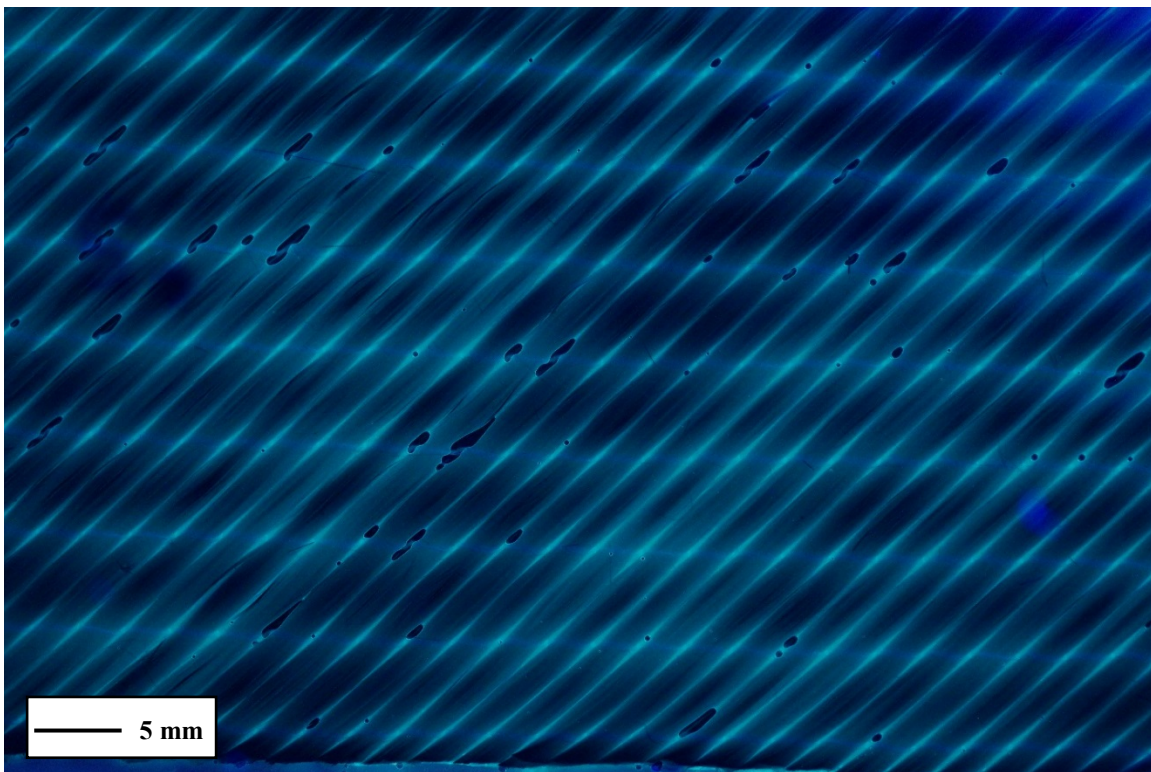
Figure 4-12 - Image 3

A total of eleven image settings were used for initial analysis. Again, each setting had variable conditions in relation to which split channel color, shading correction or contrast enhancements and threshold adjustments were selected.

On the original color image, 77 different voids were identified and labeled. Between the different settings attempted, 61 of the 77 or 79% of the voids were identified. However, the best individual setting was only capable of identifying 47 of 77 voids or 61%. From this data, settings were further optimized and used in six follow-up analyses. Mixed results occurred, but a few yielded more voids and a reduction in false readings. Figure 4-13 is an image outlining the results of the optimal particle analysis of image 3.

Figure 4-13 - Image 3 Particle Analysis Drawing

See table 4-5 and 4-6 for the effectivity ratios of each parameter and details on the parameters that yielded the best results for image 3.

Table 4-5 - Effectivity Ratio for Each Setting Tested on Image 3

Image Setting #:	Effectivity Ratio	Image Setting #:	Effectivity Ratio
Image 3		
1	0.540	10	0.515
2	0.507	11	0.576
3	0.501	12	0.602
4	0.470	13	0.548
5	0.443	14	0.468
6	0.548	15	0.589
7	0.548	16	0.513
8	0.550	17	0.502
9	0.447		

Table 4-6 - Image 3 Best Parameters and Settings

Image 3 - #12 Parameters	
Settings & Parameters:	
Original Image Enhancements	No
Split Channel Color Image	Blue
Image Enhancement	Shade Correction
Minimum Threshold Setting	0
Maximum Threshold Setting	140
Analyze Particle Settings:	
Size range (pixel²)	100-15000
Circularity range	0.3 - 1.0
Positive Void I.D.'s	49
False Void I.D.'s	3
Missed Voids	28
Calculated Effectivity Ratio	**0.602**

The measured void content for Image 3 using image settings #12 was 0.499%. More details on results and settings may be found in Appendix E.

4.3   Threshold Settings

Determining the optimal threshold settings is the most challenging component in identifying and measuring voids using ImageJ. In an effort to better understand the effect of threshold settings, data was compared between the various image setting results between images 1-3 to see if any relationships exist.

4.3.1 Individual Settings Results

Five different image enhancements were used before the threshold was adjusted and the image was converted to binary black and white: green channel image with enhanced contrast performed on the original color, blue channel image with enhanced contrast, green channel image with enhanced contrast, blue channel image with shade correction and green channel image with shade correction. Adjusting the threshold settings is one of the most subjective and time consuming tasks when establishing analysis parameters and it would be ideal if a trend in optimal threshold settings could be identified. In an effort to identify a relationship, the data from all settings were plotted in line graphs with a trend line. Figures 4-14 through 4-18 represent the relationship between effectivity ratio and the maximum threshold from all experimental settings across the three images.
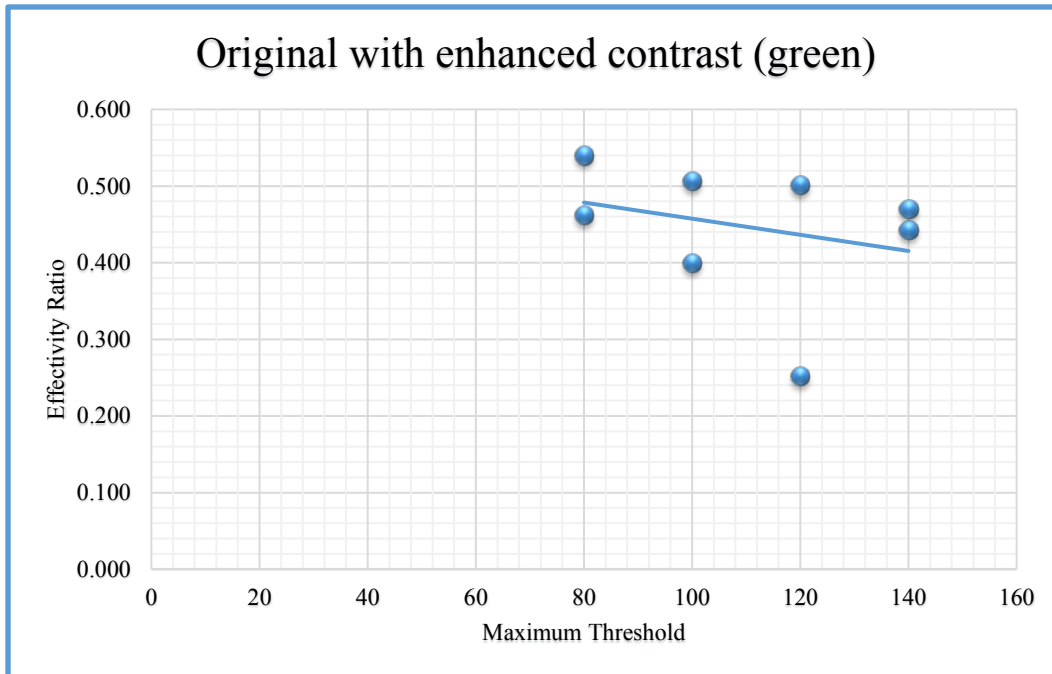
Figure 4-14 - Threshold Levels for Original with Enhanced Contrast.
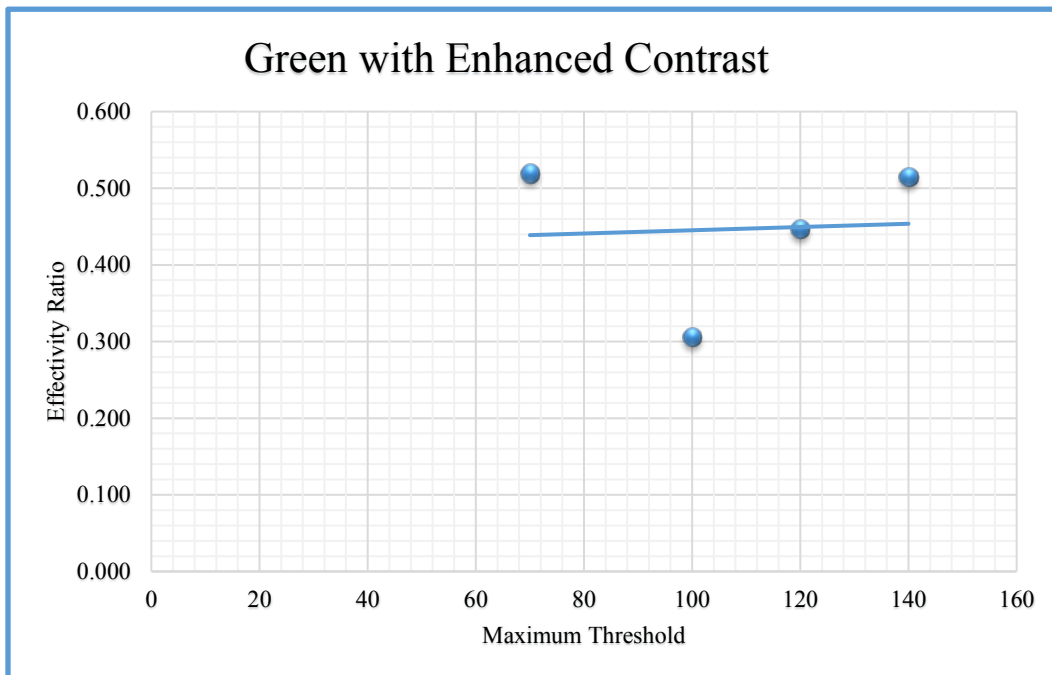
Figure 4-15 - Threshold Levels for Green with Enhanced Contrast
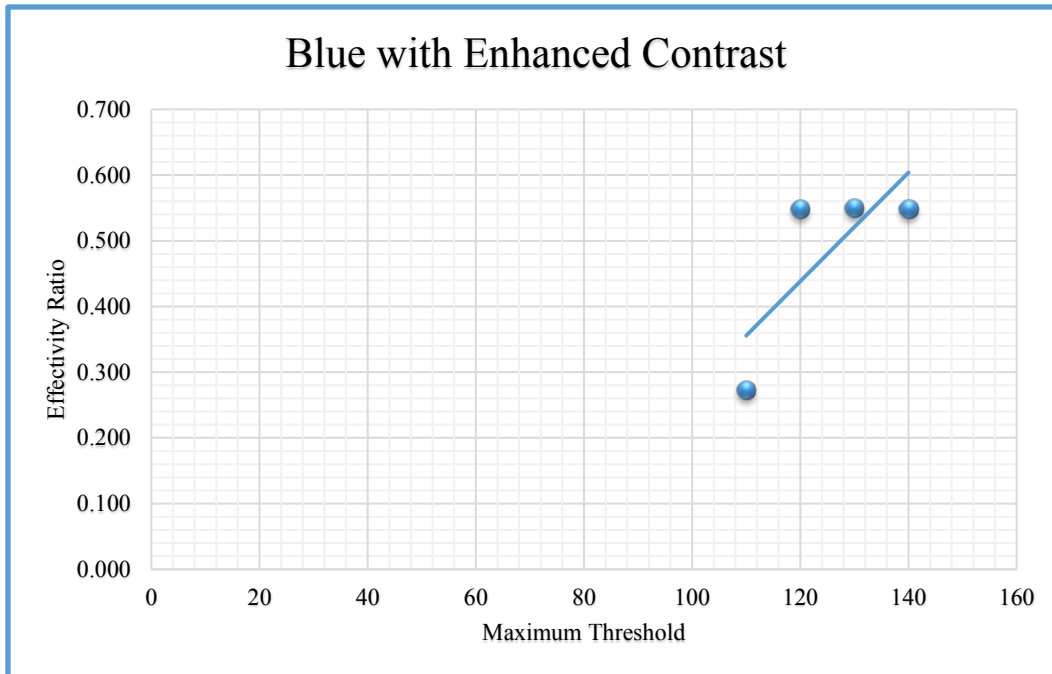
Figure 4-16 - Threshold Levels for Blue with Enhanced Contrast
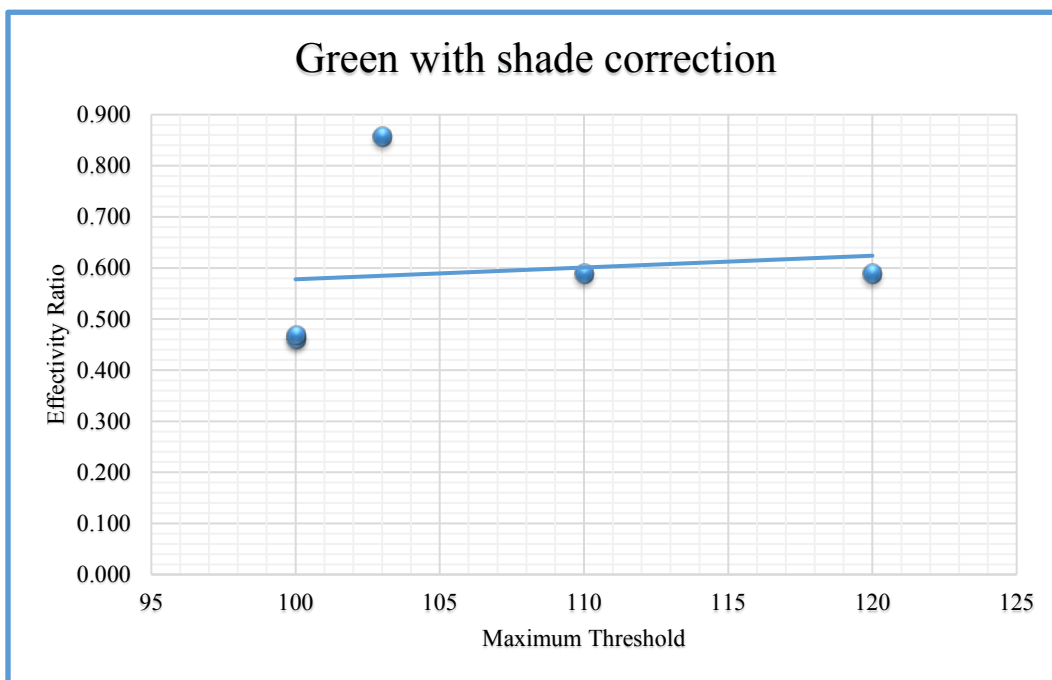
Figure 4-17 - Threshold Levels for Green with Shade Correction
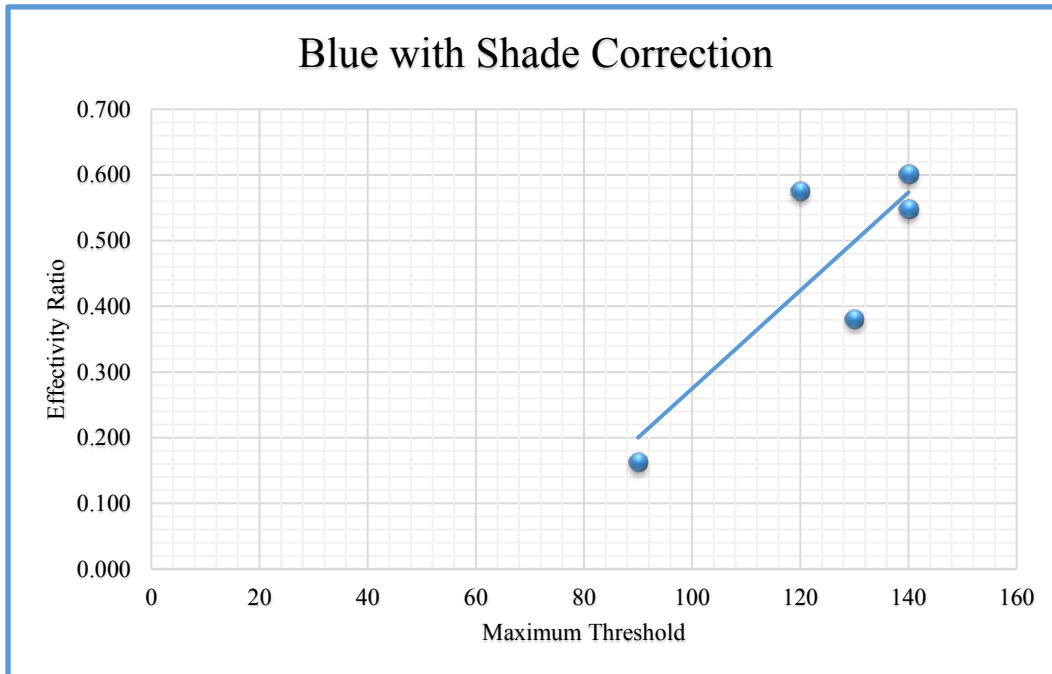
Figure 4-18 - Threshold Levels for Blue with Shade Correction
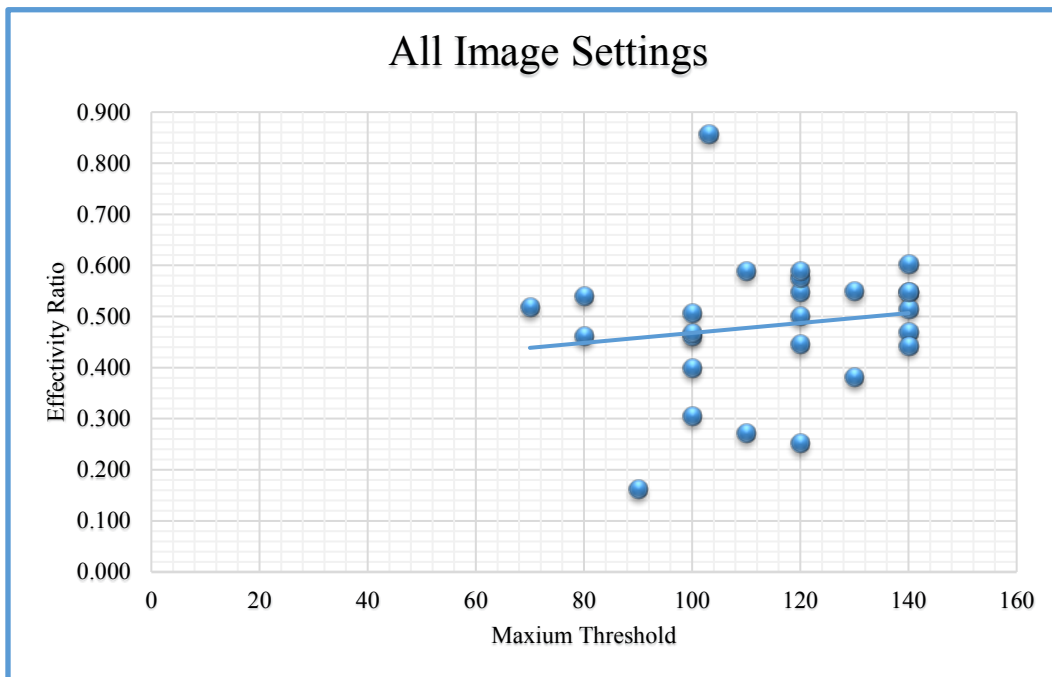
Figure 4-19 - Threshold Levels Across All Image Settings

4.3.2 Overall Settings Results

Data was also plotted ignoring image enhancement settings and only viewing the relationship between effective ratio and maximum threshold across all images and settings (Figure 4-19). In general, it appears that higher threshold settings yield better results.

4.4 Validation of Theoretical Models

In order to successfully validate theoretical void models and simulations, a tool must be capable of characterizing both micro and macro voids of varying morphology *in situ* during the infusion process. This characterization must take place over time in order to observe what type of formation, compression and movement the bubble undergoes as it flows through the material.

In an effort to evaluate the methodology developed during this research for such characterization, a set of five successive images captured during infusion was analyzed from both the Hexcel 4H satin weave and then from the Vector Ply C-L 09000 NCF preforms.

4.4.1 Hexcel 4H Satin Weave

The five consecutive images (Figures 4-20) used for analysis were found to show bubble evolution and mobility in good detail. These images were captured at an approximate rate of 12 per second after formation had occurred and the flow front had passed. An example obtained from those images may be seen in Figure 4-21, where a magnified view is presented of a bubble shrinking in size and moving through the reinforcement.
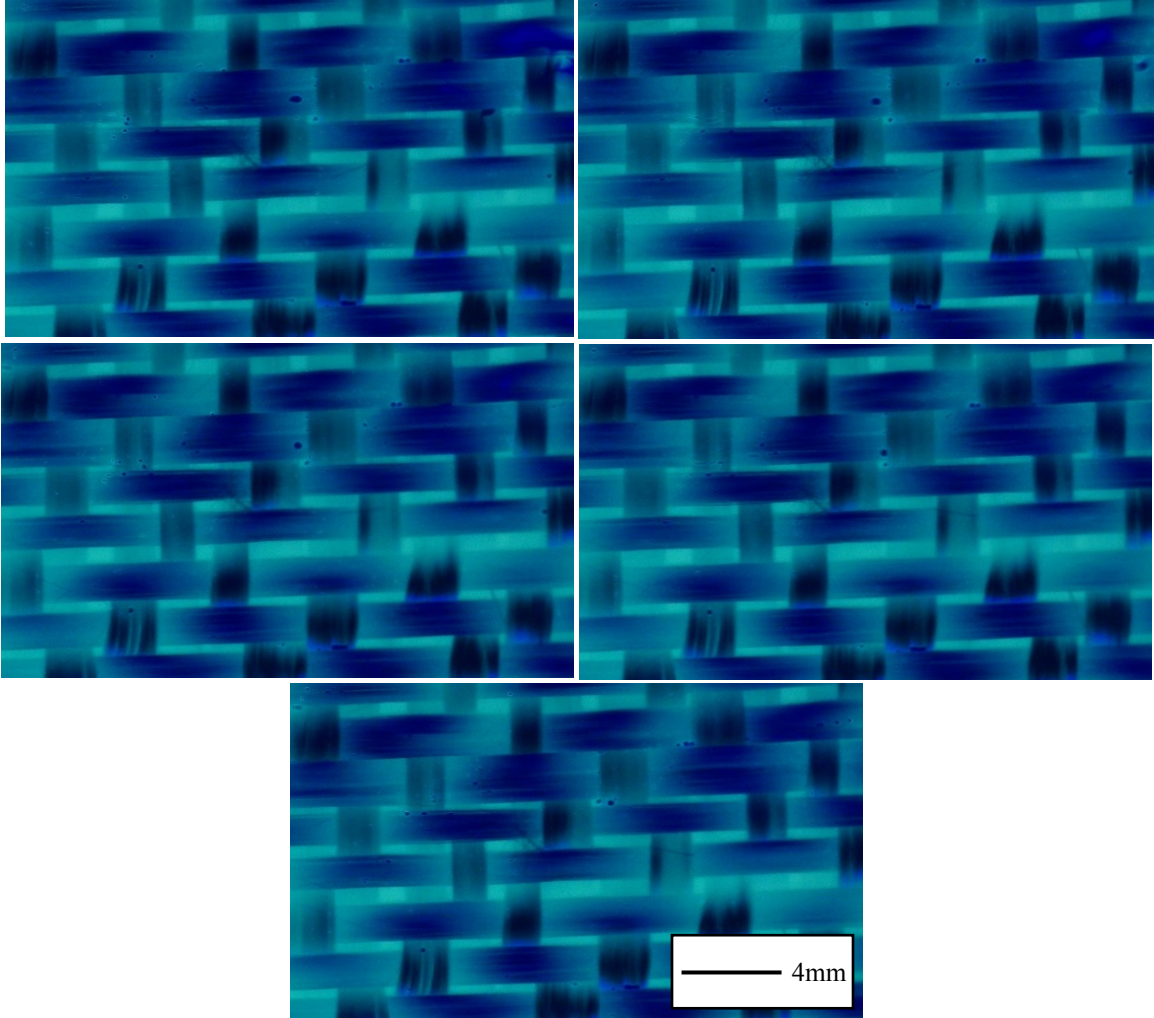
Figure 4-20 - Satin Weave - Flow & Time Are Left to Right & Top to Bottom
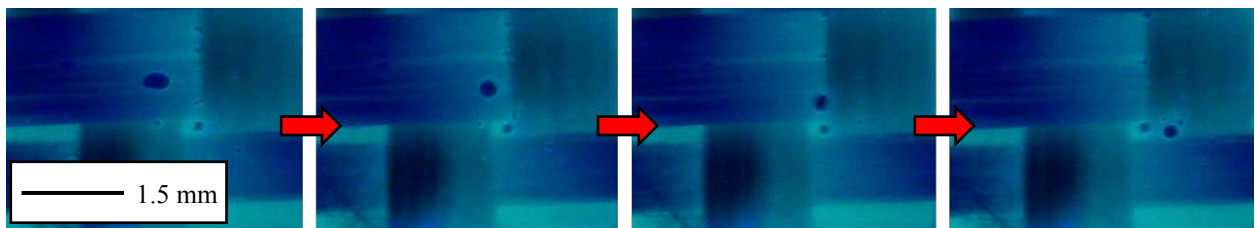
Figure 4-21 - Bubble Evolution in Satin Weave - Time & Flow Left to Right

The five images from Figure 4-20 were first analyzed in ImageJ using a modified approach to what has been previously detailed. In order to establish an accurate baseline for comparison, the voids in each image were hand painted using the brush tool in ImageJ after contrast adjustment. The threshold was then adjusted so that only the painted voids appeared in the binary image. Figure 4-22 shows the binary image for the first of the five sequential images. Next, the particle analysis process was performed in order to identify the area, perimeter, and circularity of each void along with the void content of each image. This analysis was repeated using the automated process developed during this research, where several permutations of the image analysis parameters were iterated for the first of the five images until the best effectivity ratio was achieved, and that same analysis script was run on the other four images. The data was
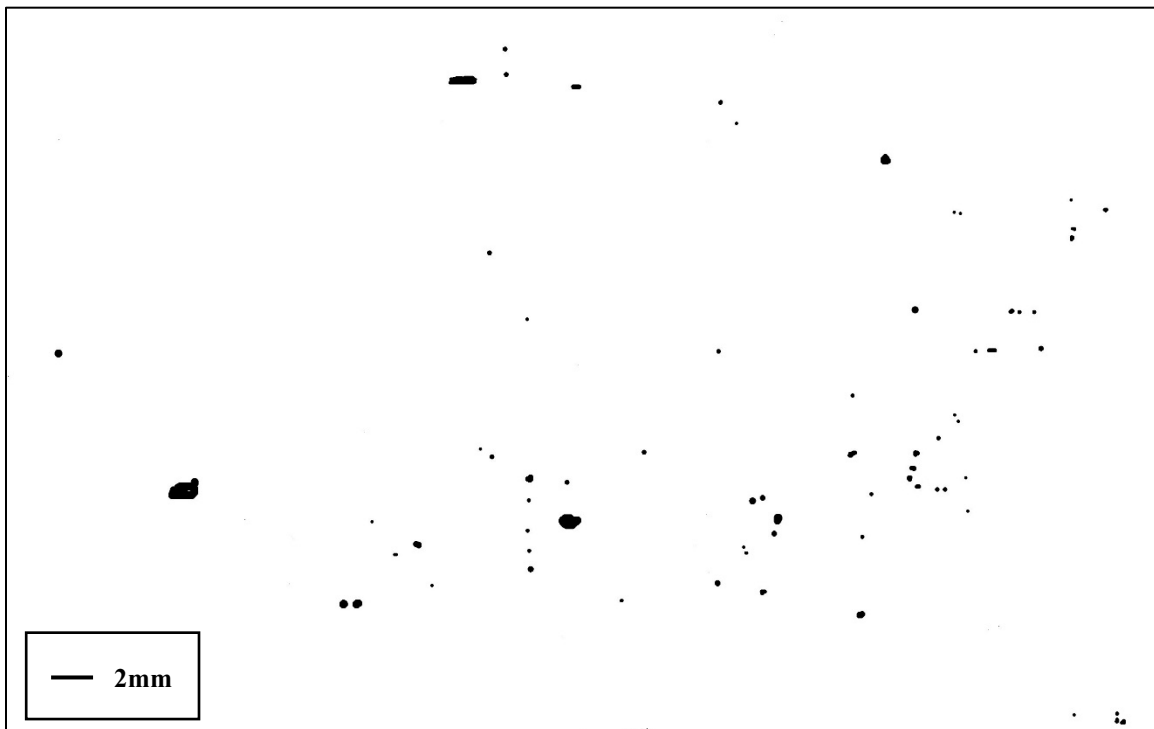
Figure 4-22 - Hand Painted Satin Weave Image

then tabulated for comparison (see Table 4-7). Complete data sets from this analysis may be found in Appendix F.

Table 4-7 - Comparison of Hand Painted VS Automated Processing - Satin Weave

		Hand Painted			Automated Analysis		
		Size (mm²)	Perimeter (mm)	Circularity	Size (mm²)	Perimeter (mm)	Circularity
Average Size	Image 1	0.0180	0.4297	0.96	0.0228	0.5215	0.81
	Image 2	0.0148	0.3783	0.97	0.0329	0.6780	0.74
	Image 3	0.0157	0.4171	0.97	0.0204	0.5125	0.81
	Image 4	0.0243	0.5550	0.90	0.0354	0.8653	0.55
	Image 5	0.0161	0.4324	0.95	0.0187	0.5426	0.70
Max Size	Image 1	0.2316	2.0276	1.05	0.1613	1.7821	0.98
	Image 2	0.1709	1.9370	1.13	0.1190	1.7098	0.94
	Image 3	0.1323	1.6141	1.03	0.0886	1.1448	1.20
	Image 4	0.1595	1.7324	0.98	0.0637	1.3981	0.68
	Image 5	0.1430	1.7902	1.13	0.0718	1.4637	0.94
Min Size	Image 1	0.0044	0.2289	0.57	0.0045	0.2472	0.64
	Image 2	0.0018	0.1406	0.54	0.0060	0.3072	0.46
	Image 3	0.0058	0.2647	0.64	0.0055	0.2927	0.65
	Image 4	0.0094	0.3493	0.58	0.0054	0.3158	0.41
	Image 5	0.0018	0.1404	0.56	0.0045	0.2991	0.42
Void Content		% Area			% Area		
	Image 1	0.302%			0.093%		
	Image 2	0.249%			0.095%		
	Image 3	0.231%			0.054%		
	Image 4	0.215%			0.042%		
	Image 5	0.236%			0.058%		

Best efforts to process the images using the automated analysis produced little success. Twenty permutations were attempted which identified 43 of the 70 voids or 61% (see Appendix F for complete details). The single best setting yielded an effectivity ratio of 0.433. In this case, 17 of 40 voids or 24% were identified with 4 false readings. There was no clear trend in voids that were more difficult to identify. Both micro and macro voids of sizes ranging from 0.0045 mm² to 0.1613 mm² and circularity ranging from 0.64 – 0.98 were identified. The limiting factor continues to be the dark areas of noise created where the fiber bundles compress against the

tooling. Typically, larger macro voids will require a reduction in the grey level threshold setting to separate themselves from the bundle and this will often eliminate other smaller micro and macro voids. Additionally, larger scale threshold adjustments will often alter the true size of many of the voids that are identified. From these results, it was determined that in this case the automated settings are not an adequate solution as too many voids are missed and the true size and morphology is significantly altered.

Despite the lack of success using the automated process, there was significant success when using the hand painted method. While more time consuming, the hand painting method produces highly accurate results for any size and shape of bubble that can be clearly captured in an image. Using the images and data acquired during this process allowed for the clear characterization of bubble evolution and movement during the infusion process with a high degree of accuracy. Precise measurements were recorded on the change in area and circularity of any void captured in the image. Varying behavior was found throughout the five images of bubbles moving in and out of channels, becoming temporarily stuck against a bundle, splitting or compressing. The data found in table 4-7 provides a general summary on how the bubbles evolved across the five images, but greater detail on each individual void may be found in Appendix F. Figure 4-23 illustrates the effectiveness of this method by examining a specific void from figure 4-20. The motion and compression of the bubble are clearly illustrated visually and empirically by the area and circularity measurements obtained during analysis.

Across the five images (figure 4-20), the bubbles range from highly circular to a circularity of about 0.5. While macro and micro voids were observed, the long needle-like voids
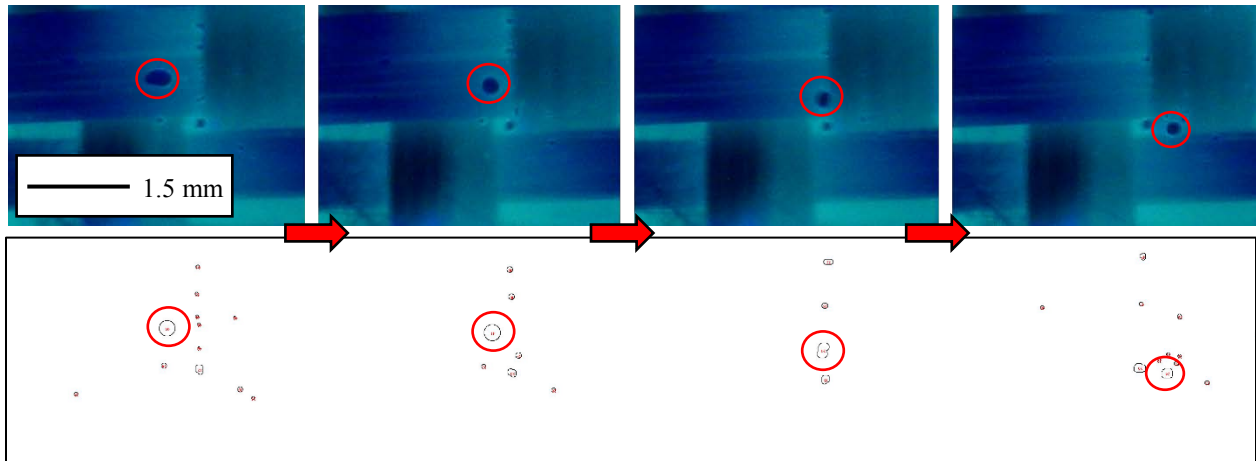
Figure 4-23 - Particle Analysis VS Figure 4-21 - Time & Flow from Left to Right

or yarn voids seen elsewhere are absent here (Hernandez 2011 and Sisodia 2016). Those long voids were observed in the resin-rich interface areas between laminate layers and were detected by either 2-D micrographs of the through-thickness cross-section of the laminate or 3-D volumes generated by CT imaging. In this case, a 2-D view is seen of the entire in-plane surface of a laminate layer as it interfaces with the tooling. While there may be some difference caused by the flat tool surface compared to two fabric layers in contact with each other, it is thought that the biaxial weave structure in this study also minimizes the propensity for formation of long voids compared to a uni-directional weave or prepreg in the above-cited studies, or similarly in an NCF; in all of these cases the inter-tow gaps are more continuous than in a biaxial weave.

The rising pressure gradient at any given location during infusion is suspected to move bubbles towards the flow front and cause the size of all bubbles to decrease with time. The overall void content does seem to generally decrease across the five images. Compression may be seen on individual voids, but no clear decreasing trend is seen in average bubble size across the images. This is most likely due to the small time scale involved of approximately 0.5 seconds. But the images clearly show another mechanism at play, where the merging and

splitting of bubbles seems to be much more significant of a size determinant than bubble compression over this time duration. The size of the bubbles seen changes significantly due to periodic splitting into smaller bubbles, and from small bubbles moving between channels until colliding and merging with a large bubble stuck in the inter-tow channels (see figure 4-21).

The hand painted images were also sufficient for analysis using a Matlab program (Fullwood 2013, George 2014) that is capable of determining the average void size in both the X and Y directions, nearest neighbor distance, Betti Numbers and the maximum cluster size (see table 4-8). This information can be of significant importance for further characterization of the bubbles during infusion, but also for predicting the potential of mechanical failure in the final part. If measurements are taken close to or at final cure, the information provided by the Matlab program on average nearest neighbor distance, betti numbers and cluster size may be used to help predict how the part will fail under load as the cracks are most likely to propagate between voids. It is hoped that such a methodology may also allow for development of void movement simulation tools, based on tracking void mobility as seen in the above examples, so that the final void distribution may be predicted based on process parameters such as applied pressure, and the metrics shown in Table 4-8 might similarly be predicted. More details on the results from the Matlab program may be found in Appendix F.

Table 4-8 - Satin Weave Images Results Summary from Matlab

	Image 1	Image 2	Image 3	Image 4	Image 5
Average void size in x-direction (mm)	0.1229	0.1465	0.1173	0.1736	0.1274
Average void size in y-direction (mm)	0.1049	0.11147	0.1062	0.1313	0.1045
Nearest Neighbor Distance (mm)	0.7744	1.02	0.7918	0.7427	0.7879
Betti Numbers	70/0/0	46/1/0	61/0/0	37/0/0	60/0/0
Max cluster size (mm²)	0.4726	0.4409	0.2453	0.3455	0.3899

No clear trends are seen across these images, again most likely due to the short time duration. The max cluster size does seem to generally decrease, signifying an increasingly broad dispersion of the voids, or possibly continual merging of small voids into larger ones. This would agree with void mobility theory that small microvoids formed within the tows continually work their way out of the tows and then move rapidly in the inter-tow gaps (Park et al 2011 and Lundström et al 2010). Many such small bubbles were observed in this image set to quickly move in the inter-tow gaps until colliding with other trapped larger bubbles.

Data produced using the Matlab program may also be represented through histograms (see figure 4-24) and images that depict the average shape and orientation of voids (see figure 4-25). The histogram of void sizes shows that the vast majority of the detected bubbles are small micro-voids of an approximate area of 0.01 mm^2, with a small number of macrovoids at much larger sizes. The average orientation of the bubbles, as depicted in Figure 4-25, shows an
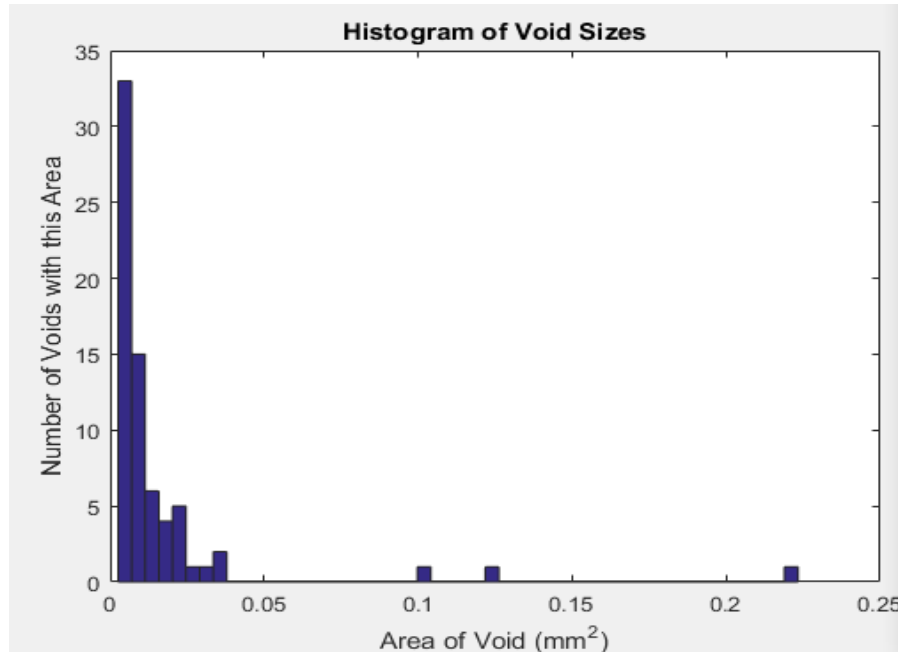
Figure 4-24 - Histogram of Void Sizes for Satin Weave Image 1

elliptical shape aligned with the flow direction. Overall, it is important to note that this methodology may be used to obtain important statistics in the same manner that is currently used for post-cure analysis.
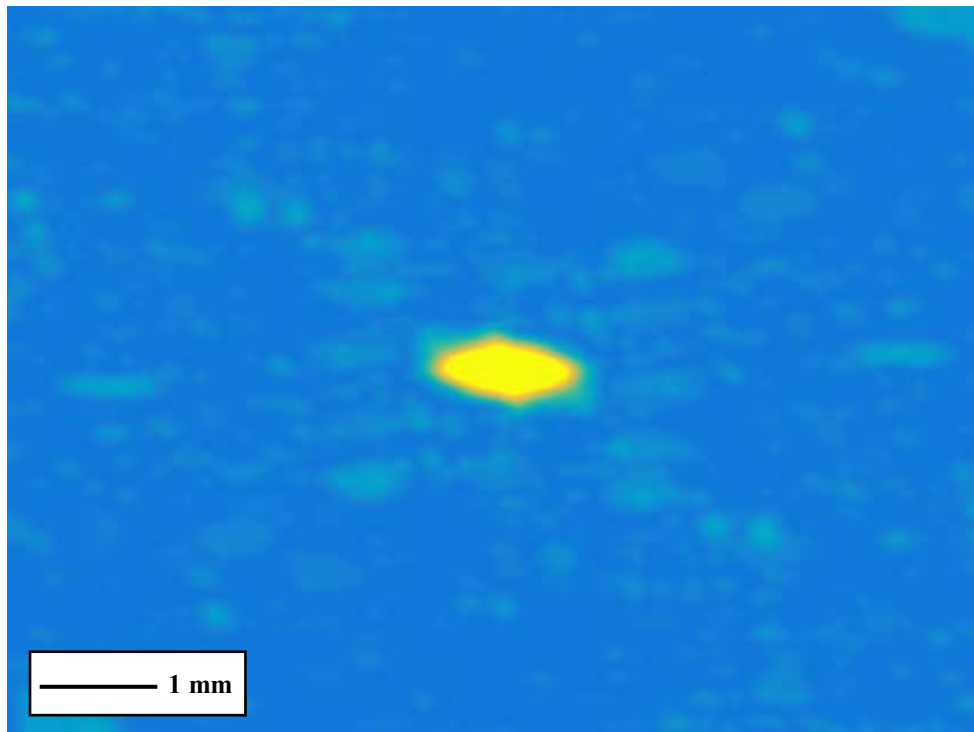
Figure 4-25 - Average Shape of Voids for Satin Weave Image 1

4.4.2 Vector Ply C-L 09000 NCF

Using the same process as with the Hexcel satin weave material, five consecutive images (see figure 4-26) captured during the infusion of the Vector Ply C-L 09000 NCF were analyzed in order to characterize bubble evolution and mobility. Again, these images were produced after the flow front had passed at an approximate rate of 12 per second. They provided excellent samples with more variation than with the Hexcel satin weave. The bubbles depicted in these

images tended to be longer macrovoids that had a much wider range of circularity. This is well illustrated in figure 4-27, a magnified view derived from the pictures seen in figure 4-26.
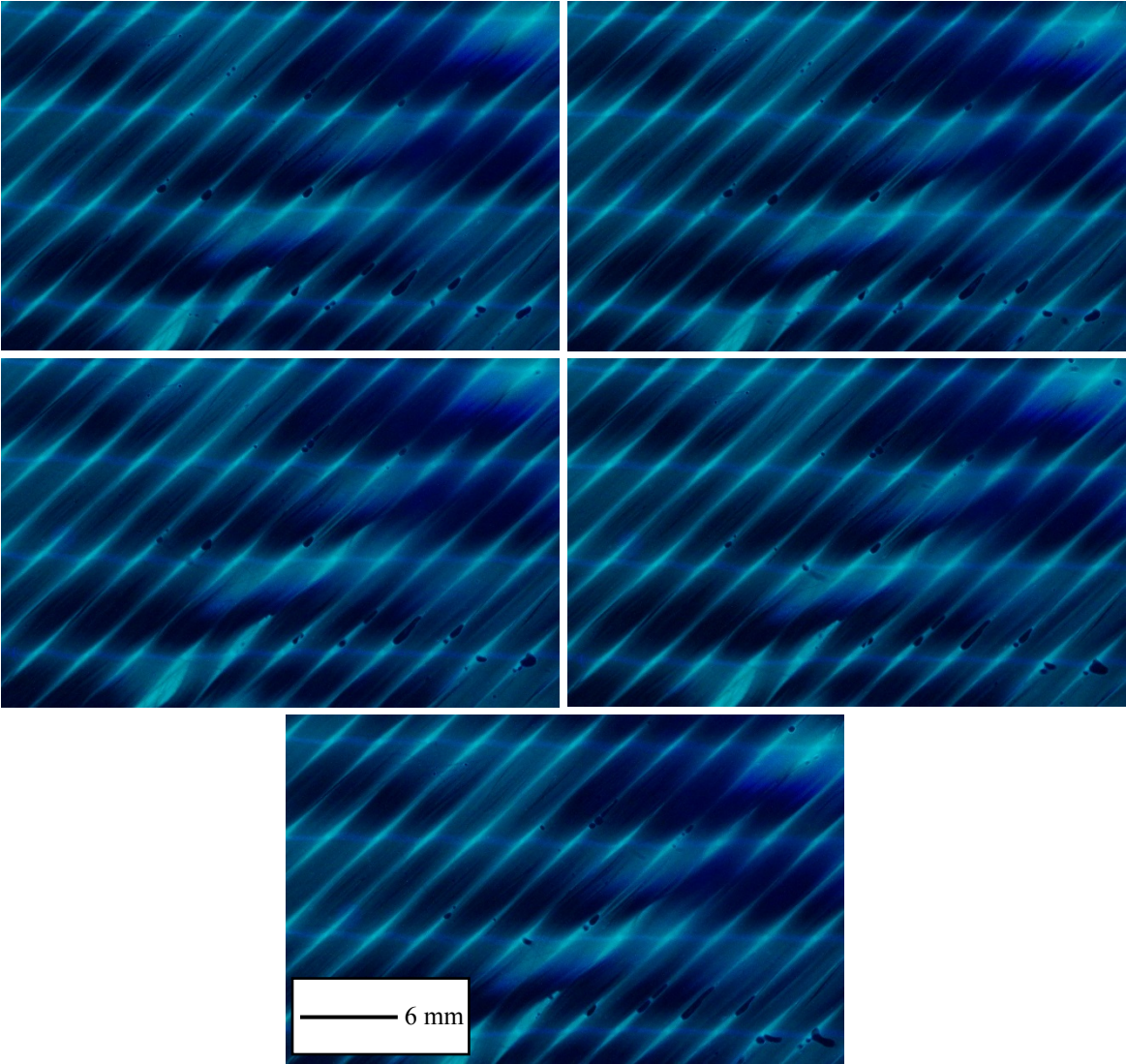
Figure 4-26 - Vector Ply NCF - Flow & Time from Left to Right & Top to Bottom
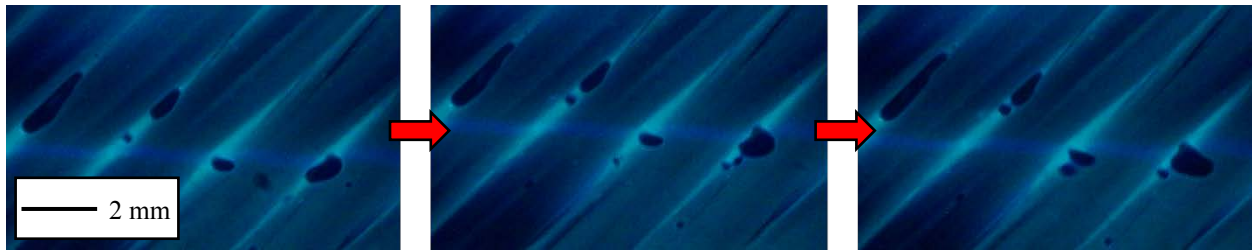
Figure 4-27 - Bubble Evolution in Vector Ply NCF - Flow & Time from Left to Right

The data collected in processing both the hand painted and automatically processed images may be found in table 4-9. Improved results were achieved in attempting the automated process, but the method was still not sufficient. 27 permutations were attempted in order to achieve the highest effectivity ratio. Across all settings, 29 of the 33 voids or 88% were identified. The single best setting captured 15 of 33 or 45% with six false readings for an effectivity ratio of 0.354. Similar to with the Hexcel material, there was no obvious trend in which type of void was easily identified. The success rate continued to be directly related to grey level threshold setting adjustments. The results of running these optimized settings across the remaining images was more successful in consistency and effectiveness than with the Hexcel material, but as mentioned, it was still not sufficient for accurate analysis. Full details may be found in Appendix F.

In analyzing the data derived from the hand painted images, it was observed that this set of images displayed varying behavior where large macro bubbles would regularly travel between fiber bundles and then become stuck, split, compress or join other bubbles (see figure 4-27). Bubbles both inter and intra-tow were identified ranging is sizes of 0.028 mm² to 0.107 mm² with a range of circularity from 0.28 to 1.0.

Table 4-9 - Comparison of Hand Painted VS Automated - Vector Ply NCF

		Hand Painted			Automated Analysis		
		Size (mm²)	Perimeter (mm)	Circularity	Size (mm²)	Perimeter (mm)	Circularity
Average Size	Image 1	0.0861	1.0115	0.85	0.1183	1.3527	0.65
	Image 2	0.1065	1.1723	0.83	0.1560	1.6435	0.63
	Image 3	0.1070	1.2333	0.81	0.1429	1.5037	0.64
	Image 4	0.0966	1.1076	0.83	0.0914	1.1377	0.69
	Image 5	0.1038	1.2065	0.82	0.0902	1.2443	0.67
Max Size	Image 1	0.6436	4.0163	1.02	0.5908	4.1242	0.85
	Image 2	0.6532	4.3633	1.02	0.6167	4.3688	0.92
	Image 3	0.6216	4.5924	1.02	0.6173	4.6652	0.88
	Image 4	0.6752	4.9112	1.06	0.4818	3.2166	0.89
	Image 5	0.5660	4.9579	1.09	0.2982	3.2383	0.89
Min Size	Image 1	0.0086	0.3352	0.48	0.0093	0.4266	0.39
	Image 2	0.0088	0.3395	0.43	0.0123	0.4110	0.41
	Image 3	0.0087	0.3380	0.36	0.0107	0.3910	0.36
	Image 4	0.0040	0.2194	0.34	0.0101	0.3770	0.48
	Image 5	0.0028	0.1796	0.28	0.0089	0.3592	0.33
		% Area			% Area		
Void Content	Image 1	0.539%			0.337%		
	Image 2	0.590%			0.317%		
	Image 3	0.521%			0.294%		
	Image 4	0.612%			0.273%		
	Image 5	0.667%			0.221%		

As with the Hexcel 4H satin weave, no yarn voids were observed. While some microvoids are present, the majority tended to be macrovoids traveling between the bundles. It was also observed that the bubbles traveling between bundles would sometimes change direction and move along the stitching (see figure 4-28). Overall, the data showed an increase in void content over time and little change in the average void size. Again, this is likely attributed to the small time scale as these images were obtained in approximately 0.5 seconds. A general increase in the max bubbles size can be seen however in Table 4-9, as well as a decrease in size of the smallest bubble. This is suspected to be due to the merging of small microvoids with the large, stuck macrovoids.
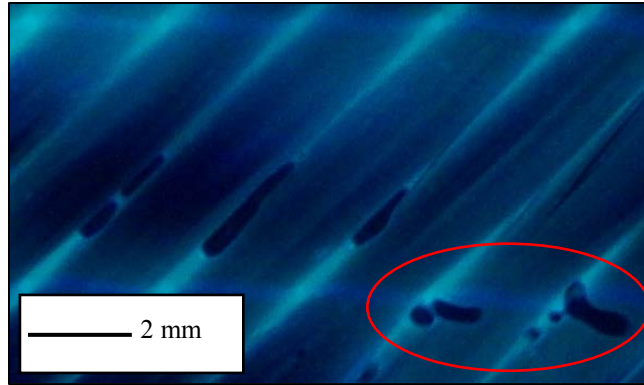
Figure 4-28 - Bubble Migration - Vector Ply NCF

This set of images were also processed using the Matlab program (see table 4-10). Similar to the Hexcel material, no obvious trends were identified. The nearest neighbor distance grew and then shrunk and the maximum cluster size steadily increased. It is believed that this is also caused by the small time scale in combination with the fact that these images were acquired very early on in the infusion process. Figures 4-29 and 4-30 illustrate examples of one of the histograms generated along with an image of the average shape of voids from the first of the five image sequence. Complete results may be found in Appendix F. The void size histogram details similar results to that from the satin weave. The average shape, orientation and distance between neighbors shown in Figure 4-30 shows some significant differences however from the satin weave. The voids are now aligned with the bias direction inter-tow channels instead of with the

Table 4-10 - Vector Ply NCF Images Results Summary from Matlab

	Image 1	Image 2	Image 3	Image 4	Image 5
Average void size in x-direction (mm)	0.3174	0.3595	0.3808	0.3586	0.4025
Average void size in y-direction (mm)	0.3110	0.3613	0.3095	0.3432	0.3804
Nearest Neighbor Distance (mm)	1.3273	1.7673	1.7150	1.2012	1.1537
Betti Numbers	33/3/0	30/6/0	26/3/0	33/3/0	33/2/0
Max cluster size (mm²)	1.5994	1.5120	1.7197	2.0711	2.2381
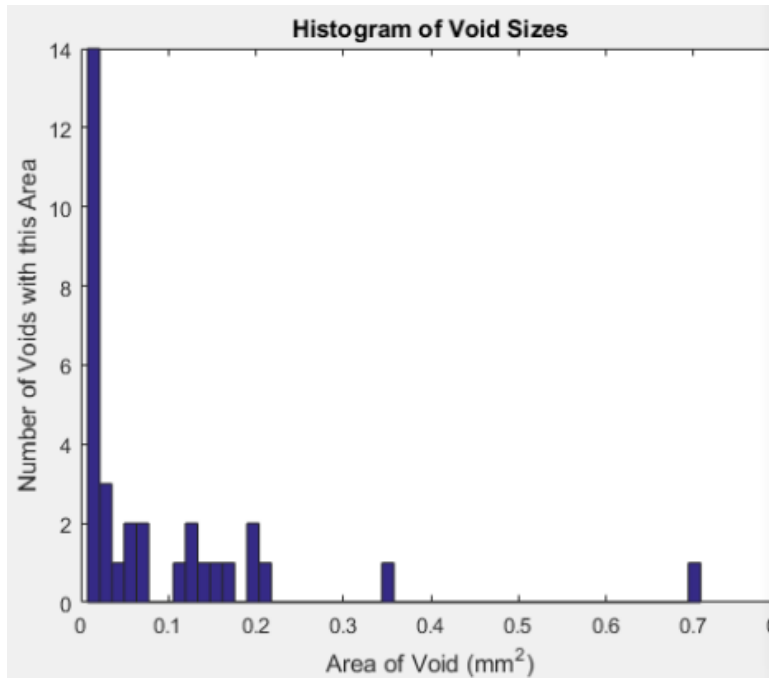
Figure 4-29 - Histogram of Void Sizes for NCF Image 1

2 mm
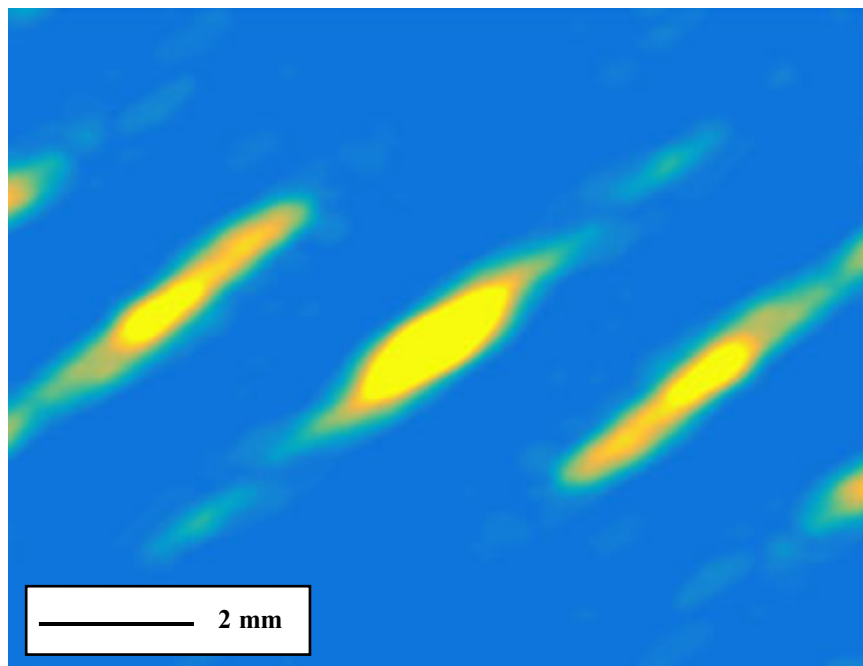
Figure 4-30 - Average Shape & Distance Between Voids for NCF Image 1

flow direction. The voids are more elongated than in the satin weave, which confirms the suspicion that the longer straighter inter-tow channels of an NCF create longer voids than the satin weave. The voids were also observed to not be as clustered or near to their closest neighbor as observed in the satin weave material where they were highly clustered.

In general, there appeared to be significant movement by bubbles of an area of 0.08 mm² or less. The larger bubbles appeared to be stuck or moving very slowly between the bundles and as these smaller bubbles would collide with them, they would grow in size and begin to move. This suggests that the most prevalent changes in void content observed during this limited time scale were the continual escape of microvoids from inside of the tows into the inter-tow gaps and their quick movements until they collided with the larger macrovoids. This provides an explanation for why the macrovoids are growing in size while the overall void content remains the same or is slowly decreasing with the rising pressure gradient.

4.5   Discussion

4.5.1 *In Situ* Void Monitoring Methodology

The developed methodology for capturing images of *in situ* voids appears to be the first known method that accomplishes this task when using carbon fibers. This is a critical step forward in the progress towards the generation and validation of models and simulation techniques for LCM. In general, the established setup was effective in yielding the proper results but could be further optimized for improved results.

4.5.1.1 RTM Setup and Photography

The general methodology of using clear tooling with a macro lens camera positioned directly over the mold using a tripod has proven to be capable of acquiring images of *in situ* void formation and evolution. Because lighting and photography were all directed from above, it may not be necessary to use clear tooling for side B or the bottom plate. Because of the reflective nature, it is possible that a metal bottom plate would improve the effectiveness of the UV dye and lighting.

Another significant improvement could come from performing the infusions in an actual dark room environment. While all lights were extinguished, the lab in which these infusions were performed did not provide a true dark room atmosphere. It is possible that this could add difficulty to focusing the camera, but should promote even more contrast from the UV dye and lighting.

Perhaps the greatest advancement that could be made to this methodology would be to identify a manner in which the noise created by the fiber bundles contacting the tooling may be reduced or eliminated. While this did not have a major impact on image acquisition itself, it did add significant difficulty to image analysis and drastically reduced the overall effectiveness and accuracy of the procedure. This will be difficult to accomplish as adjustment to the cavity spacing will likely result in race tracking and un-realistic processing conditions.

4.5.1.2 Materials and Preform Preparation

Carbon fiber preforms seem to be the optimal material for this methodology. It was possible to acquire images of *in situ* void formation using fiberglass preforms, but they could not be accurately measured using the established image analysis methodology in ImageJ. Optimal contrast was never achieved with glass fibers because they would absorb any colorants and

lighting introduced to enhance contrast. Regardless, clear images of *in situ* voids were obtained and it is possible that other image analysis systems may be capable of successfully mapping the voids captured.

When using the methodology developed in this study, high void contents were desirable during the infusion processes. Using complex fiber weaves and fiber orientations promotes void formation and movement and are recommended for optimal results. Additionally, increasing the ply count will also generate more voids. It should be noted however, that as the ply count is increased the brightness achieved using UV dye and lighting was reduced. This resulted in degraded image contrast.

4.5.1.3 Test Fluid/Dye Mixtures

UV dye appears to be the prime solution for work with carbon fiber preforms in this context. It was originally hypothesized, however, that some dye could provide adequate contrast between fiber, test fluid and voids when using glass fibers, but this has thus far proven to not be true. Through experimentation, it was found that regardless of lighting and fluid/dye mixture that everything would blend together in color and contrast when using glass fibers. There were conditions where voids where quite visible in the images, but they could not be processed through this methodology due to a lack of contrast. Continued efforts to find a dye color that may validate this hypothesis may be worthwhile. As previously mentioned, dye options that would be compatible with the test fluid used in this research were very limited. If a viable black or dark blue/purple dye were found, it would be interesting to test.

4.5.1.4 Photography Equipment and Lenses

Perhaps the most challenging aspect of photographing the macro images obtained during research was properly focusing the camera in low light conditions. It was previously mentioned that increasing the ply count would decrease the brightness of the UV dye. This brightness reduction would further exacerbate the difficulty of focusing the camera. An improved understand of low light photography and the use of improved equipment would greatly facilitate further study in this area.

Another area for opportunity could reside in the use of polarized lenses. Some reflection occurred on the surface of the acrylic tooling and on the carbon fibers themselves. Brief experimentation had shown that a polarized lens could reduce this reflection and improve the overall image quality. Unfortunately, the use of the polarized lens required more lighting to properly focus the camera than what was available in these testing conditions. This added difficulty in focusing was never surmounted during this study, but it is likely that further research on low light photography would aid in finding a solution that could yield acceptable results.

4.5.2 Image Analysis

The methodology created using ImageJ attempted an approach in automated image analysis of pictures containing *in situ* voids. Currently, this methodology is very limited by the quality of image being analyzed and has not produced the required accuracy needed for proper validation. It requires a high level of contrast between the voids and test fluid, which is not always easily obtained. As the quality and contrast of the images to be analyzed improves, this method will likewise increase in effectiveness, accuracy and ease of use and may be potentially used for automated image processing in the future.

4.5.2.1 Best Methodology

In order to achieve full automation of the image analysis process, it is critical to find a single image analysis methodology that would be capable of processing any image of *in situ* void formation and movement. Unfortunately, this was never achieved. The image analysis of the three primary images previously discussed has shown that different settings are required depending on the materials, processing conditions and image contrast quality. This study has, however, yielded a methodology to optimize the image analysis settings for specific conditions. Once optimal settings have been found for a specific group of images, then a macro function may be used to process the images in mass, but these conditions were never found to be accurate enough for application in validating models. Instead, a modified approach where the voids were hand painted before threshold adjustment was used for optimal accuracy.

4.5.2.1.1   Setting Optimization

Once a group of images containing *in situ* void formation and movement have been produced, one or two images should be selected for optimizing image analysis parameters. To do so, the chosen image is uploaded into ImageJ and the enhance contrast feature is performed on the original color image. Once this is complete, the split color channels function should be performed on both the original color image and the enhanced contrast image. This will yield a total of six split color channel images. During this study, the red channel never yielded a usable image, but this may not always be the case under different conditions. All images should be saved at this point. Using the split color channel images from the un-altered original, the enhance contrast feature should be performed on each image and then saved. This step is repeated on the original split color channel images of the un-altered original, except this time the "A Posterioiri" shade correction function is performed and the yielded images are saved. Once

these steps have been completed, a total of nine images should have been created: three split channel color images from the un-altered original with enhanced contrast, three split channel color images from the un-altered original with shade correction and three split channel color images from the original image that had enhanced contrast.

Using these nine images, the threshold adjustment must now be completed. This is the most challenging step in determining the optimal processing parameters. The approach taken during this study was to have the original color image open during threshold adjustment and to try and visually adjust the maximum threshold so that the majority of the voids where still visible and depicted as unique circular objects in the black and white binary image (see figure 4-31). If the voids are connected to the areas of noise created by the fiber bundles in any manner then they
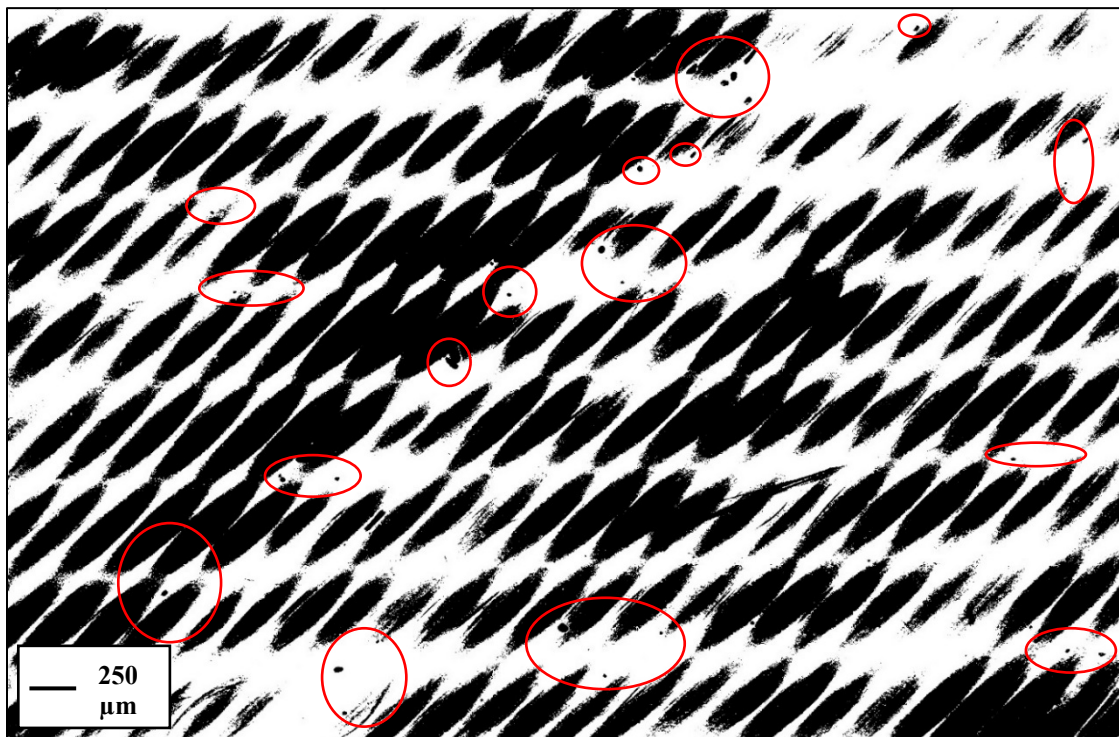
Figure 4-31 - Example of Threshold Adjustment

86

will not be identified during particle analysis. Once a setting that appeared visually acceptable was established, the parameters were recorded and applied and the image was saved. Multiple additional images were generated and saved by repeating the previous step and adjusting the maximum threshold in both directions in increments of ten. Note that the threshold cannot be re-adjusted once applied. All new settings must be derived from the original split color channel image. Again, this must be completed visually and is limited according to the researcher's discretion. The threshold setting graphs previously shown may provide positive starting points depending on the image conditions being adjusted.

Once all binary images have been obtained, the analyze particles function is performed for each one. This function will yield outline images that must then be compared against the original images to identify positive and false void identifications as detailed in Chapter 3. Once the effectivity ratios have been calculated and compared using equation 3-3, further optimization may be completed repeating the same process. Care must be taken at all steps to record parameters and settings used along with saving images using a name that will link it to the proper settings.

4.5.2.1.2   Macro Script Creation

Once the optimal settings have been established, a macro script may be created using the record function in ImageJ (see figure 4-32). The record function operates similar to that used in Microsoft Excel by simply recording each step used according to the previously optimized procedure. This will generate a script that may be re-run. The concept would be to have a folder of images taken under similar conditions to those used to optimize the parameters and use the generated script to process all of them in mass for further analysis of the completed data.
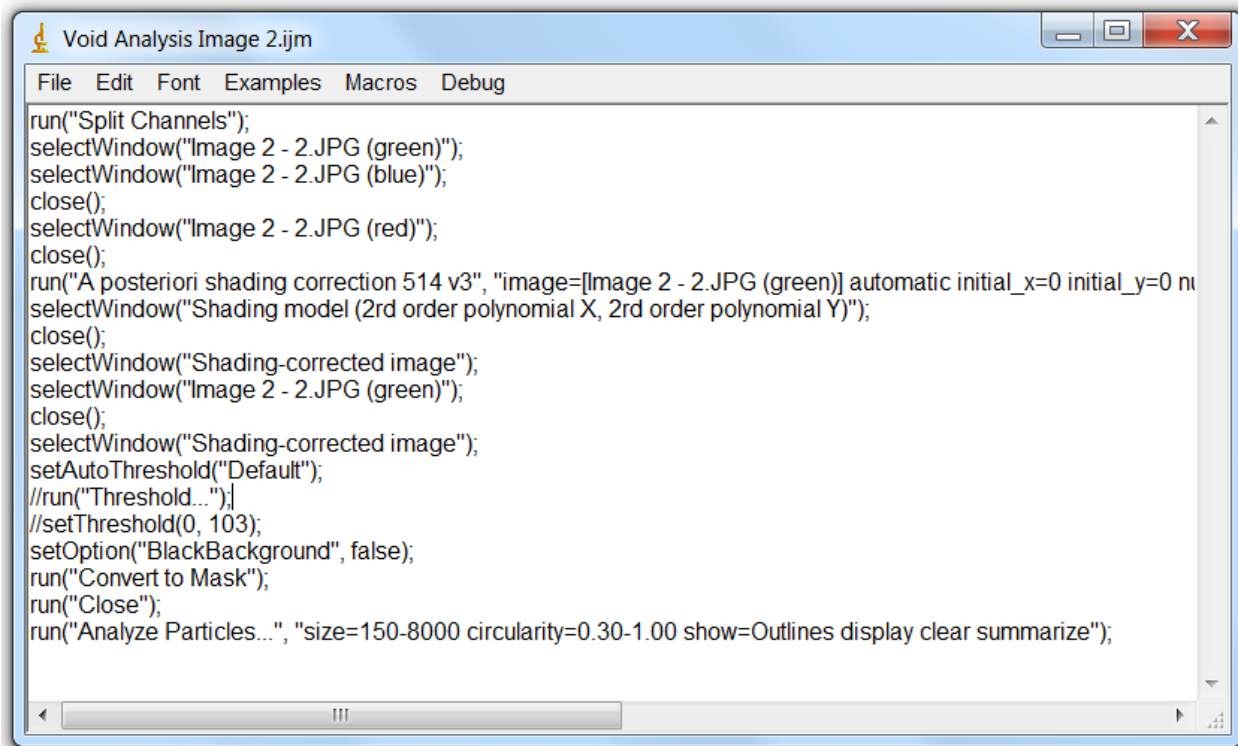
Figure 4-32 - Example of ImageJ Macro Script

4.5.2.1.3 Void Characterization Accuracy with Optimized Settings

As previously mentioned, the inaccuracy obtained using the automated approach for both the Hexcel satin weave and the Vector Ply NCF materials was deemed too great for the use in validation of void theory and models. No obvious trend was found between overall accuracy in relation void location or size, so instead we focused on the relationship between accuracy and circularity. Figures 4-33 through 4-36 represent the relationship between circularity and size accuracy and positive void identification within the automated process for both the satin weave and NCF materials. Size accuracy was determined by comparing the area values from the hand painted images against the values from the automated images. Identification accuracy was simply determined by the presence of the voids when compared between the hand painted and automated analyses.
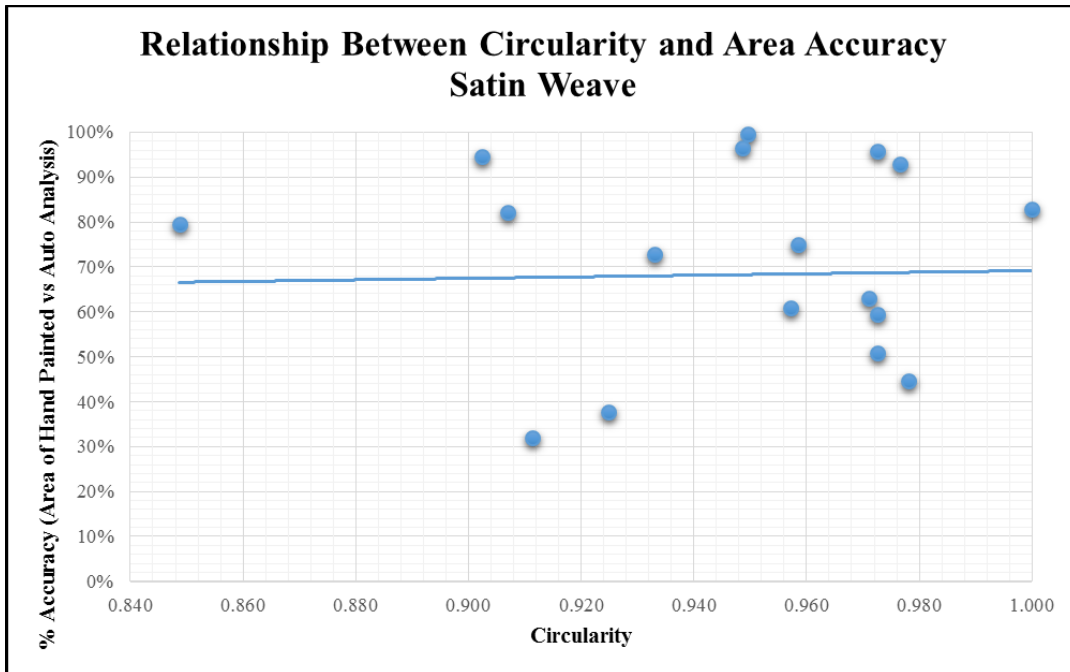
Figure 4-33 - Circularity VS Area Accuracy - Satin Weave
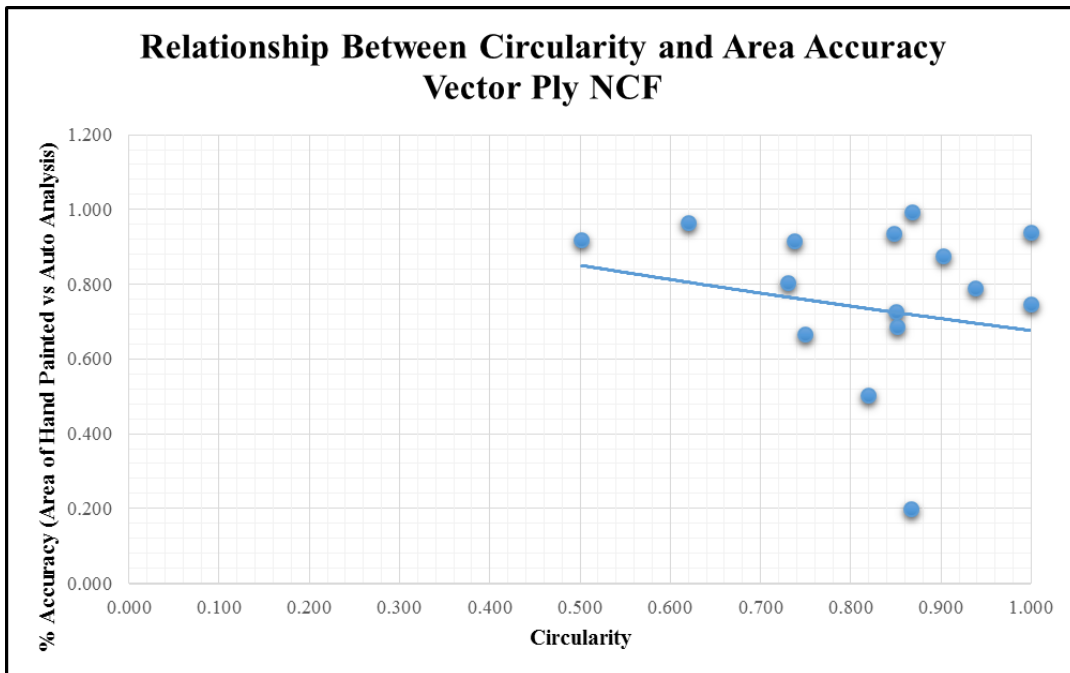
Figure 4-34 - Circularity VS Area Accuracy - Vector Ply NCF
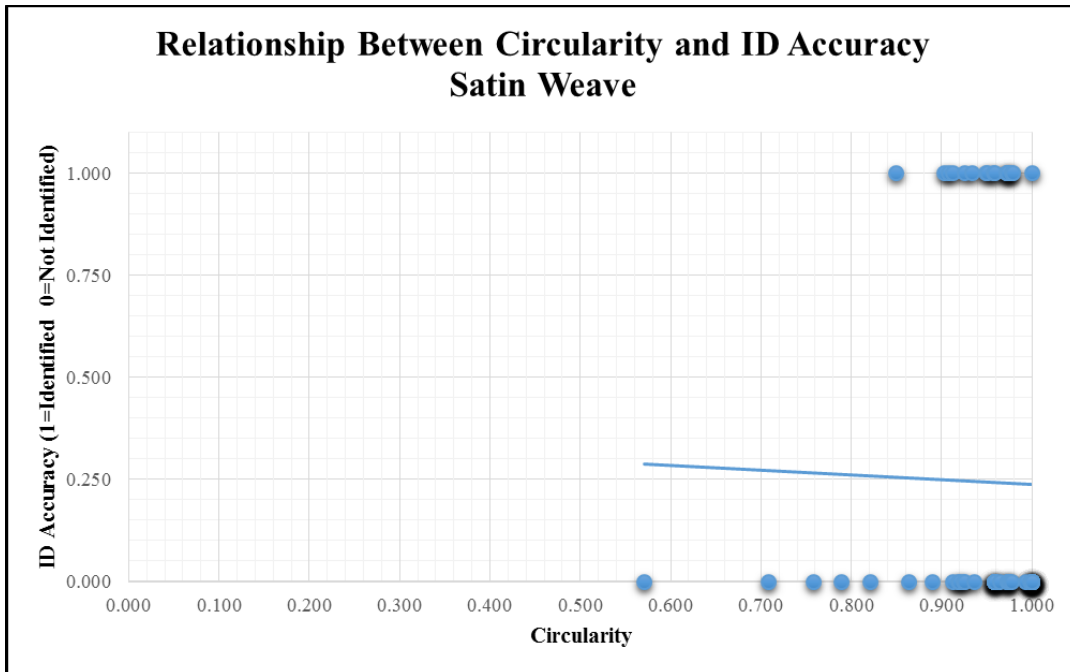
Figure 4-35 - Circularity VS ID Accuracy - Satin Weave
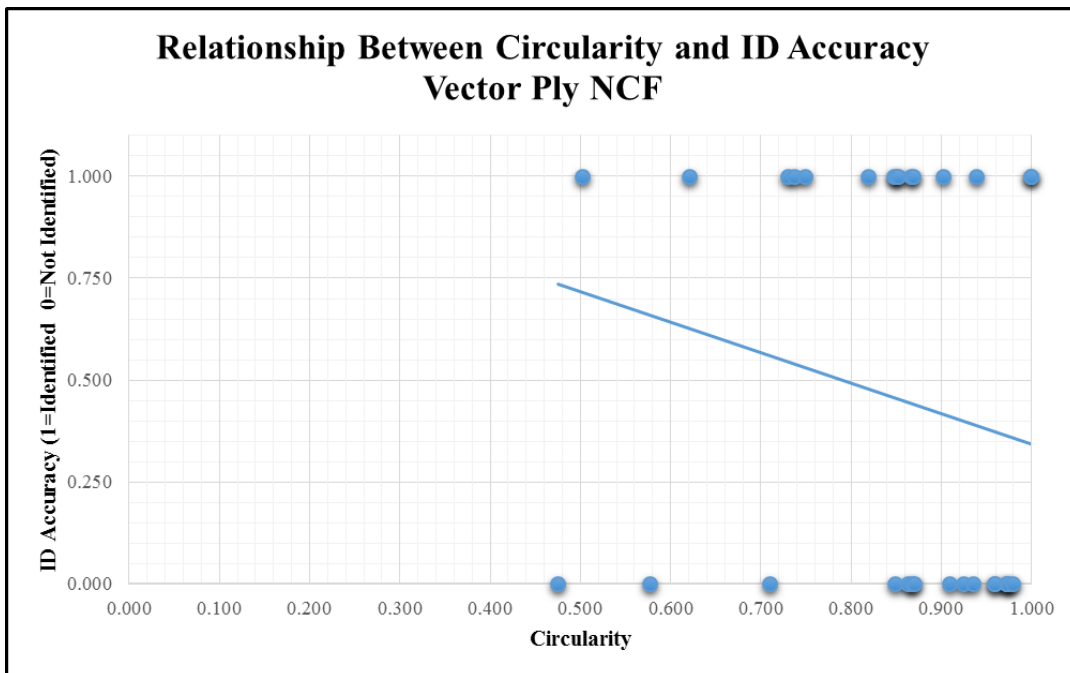
Figure 4-36 - Circularity VS ID Accuracy - Vector Ply NCF

The results are interesting with opposite trends occurring when relating circularity to size accuracy between the two image types analyzed. It appears that circularity had little effect on the accuracy when using the satin weave materials, but did exhibit some trend towards inaccuracy with more circular bubbles in the NCF material. This could be explained by the high volume of macrovoids with low circularity found in the NCF and was definitely complicated by the high level of threshold adjustment required to separate them from the fiber tows for particle analysis. Both data sets relating circularity to void identification accuracy trend towards higher circularity reducing accuracy. This trend may, however, be skewed as the optimization process was biased more towards threshold adjustments that identified macrovoids that were deemed more important for comparative analysis. This was done because they were more obviously seen and tracked across the consecutive images. It is likely that the same could be done in targeting microvoids.

5   CONCLUSIONS

Composites have proven their place as an advanced material that provides maximum strength to weight ratio, but high costs and slow processing times will continue to inhibit its adoption in certain industries. Liquid composite molding (LCM) shows great promise in reducing processing times and costs.

While not a new process within the composites industry, LCM processes such as RTM and VI have seen little research when compared to traditional prepreg and autoclave processes commonly used within the aerospace industry. Void formation is often the primary defect of concern in LCM processing and researchers are working to gain the same understanding of void prediction and minimization as exists with prepregs. Significant research is under way on theoretically understanding void formation and movement in LCM processing, but this research needs empirical data for validation. Such empirical data has been historically challenging to acquire. Existing methods for *in situ* void measurement based on light transmission have only been successful with the use of glass fibers as carbon fibers are opaque. Additionally, any empirical data analysis used to validate a model requires significant amounts of data and this is complicated by the manual and time consuming nature of current processes.

The purpose of this research has been to identify a methodology that would facilitate the collection of such empirical data and provide an improved means of analysis in order to compare the results with theoretical data. This was achieved by capturing images of *in situ* void evolution

during RTM using a clear mold with UV dye and lighting to enhance contrast between the test fluid, preform material and voids. The captured images were then processed and analyzed by a methodology developed using ImageJ software to identify and characterize the voids.

5.1   RTM and Macro Lens Photography

The methodology developed in this research is believed to be the first used to successfully capture images of *in situ* void formation and movement in LCM using carbon fibers. It is also capable of capturing *in situ* voids when using glass fibers, but using carbon fibers is required in order to obtain enough contrast to successfully use the accompanying image analysis method.

Improvements to this process could come from enhancing the contrast gained by using UV dye and lighting by: using a metal bottom plate in the mold, performing infusions in an actual dark room environment and somehow mitigating the image noise caused by contact between the fiber bundles and the clear top plate of the tooling. This last point is especially critical as this contact significantly complicates the image analysis process established in this research.

Increased ply counts and more fibers oriented off axis in relation to the test fluid flow are suspected to facilitate more void formation during the infusion process as was observed in this study. These variables may be adjusted in order to control void formation according to research needs. It should be noted that increased ply counts will reduce the effects of the UV dye and lighting, thus diminishing the image resolution.

While UV dye appears to be the optimal solution for the methodologies developed in this research, other dyes may provide potential solutions for obtaining the proper contrast when using

glass fibers. It may be worth testing black, dark blue or dark purple dyes, but research will be

required to find solutions that are compatible with the test fluids used in this study.

Other improvements could come from advanced photography equipment. Polarized

lenses and other equipment may be used to enhance the effectiveness of using macro lens

photography in low light conditions. Focusing the camera was often problematic and improved

photography skills would be beneficial.

5.2   Image Analysis

As a result of this research, a new method of image analysis was developed that uses

ImageJ software to identify and characterize voids in the images captured using the *in situ* void

monitoring method previously detailed. This methodology is capable of analyzing large batches

of images when properly setup. A potential for automation exists, but is dependent on process

conditions and image quality. This methodology details a process for the optimization of

settings in order to achieve the highest level of accuracy. Then a macro script can be generated

to analyze all like images for void size and circularity along with overall void content.

In its current state, this process requires further improvements to enhance its accuracy in

identifying voids and accurately measuring size and circularity. It is most likely that this will be

accomplished by improving the process in which images are obtained because when optimal

image quality and contrast are provided, this method has a higher level of accuracy.

Additionally, this method is not capable of processing images acquired when processing

glass fibers. This is due to the poor overall contrast of the images. Again, if this is to be

overcome it is more likely to come from process improvements that enhance the contrast

between the test fluid, fibers and voids. If proper contrast is obtained, this method should be capable of identifying voids using any matrix or fiber reinforcement.

5.3   Usefulness as a Tool for Theory and Model Validation

In order to validate models and simulations in void theory, empirical data must be collected on the *in situ* formation and evolution of voids during the infusion process. The methodology and tool used to acquire this data should be capable of identifying and characterizing both micro and macrovoids of various sizes. Patel and Lee (1995) have described microvoids as ranging is size from $0.5 \times 10^{-4} – 0.01$ mm² and macrovoids ranging in size from $0.1 – 10.0$ mm². Similar values have been seen in *ex situ* or post cure void content analysis. In addition to size, the shape and location of the void must be accurately identified as well. These metrics will allow researchers to study void evolution and compare with theoretical results.

The methodologies created during this research proved capable of capturing detailed images of a variety of void types, sizes and shapes. Many consecutive images where captured which clearly illustrated change in void position, size and shape. The process is limited to observing bubbles between the preform material and tooling and certain interactions between plies may be missed, but this has generally been deemed acceptable and is a standard method that has been regularly used. Overall, the dynamic nature of voids observed between the material and tooling is believed to be generally representative of bubble size, shape, movement, compression and collapse within and between other plies of the part.

The two selected preform materials, a four harness satin weave and double bias NCF, were chosen because they provide a general representation of most typical fiber weaves that would be commonly used in industry. As detailed in chapter 4, both materials generated a variety of micro and macrovoids of varying size and morphology for analysis. Void sizes

ranging from .0018 – 0.675 mm² were accurately analyzed. Even smaller voids were sometimes observed, but a lack of clarity and resolution in the images prevented accurate analysis and these were generally ignored during this research. A variety in morphology was also observed and characterized through circularity. Both materials generated bubbles that ranged from highly circular to as low as 0.28, which were generally long oblong macrovoids.

The methodology for image analysis had varying degrees of success. When using the more manual method that required voids to be hand painted, voids of any type, size and morphology could be accurately identified and characterized. This was more time consuming and somewhat limited by the skill of accurately painting the voids, but still highly effective. Significant time was devoted to a fully automated solution but the accuracy is currently insufficient to serve as an effective tool for validation of models. The automated approach could easily identify both micro and macrovoids of varying size and circularity, but often struggled to distinguish all voids in the binary black and white images. This was due to the noise created by areas of fiber bundles compressed against the tooling. Additionally, the threshold adjustments would often alter the true area of the void reducing overall accuracy sometimes as high as 40% on specific voids. The use of macro scripts to process multiple images showed some level of consistency and repeatability, but was ultimately rendered ineffective by the inability to achieve a single image setting that was accurate enough for validation.

As previously mentioned, it is hoped that further work in both process improvement and image acquisition will improve the overall accuracy of the fully automated approach. Until such improvements are made, the hybrid approach of hand painting the voids will be the most accurate method for using this as a tool in model validation. This process will still allow for the

use of macro scripts as the image contrast adjustments and particle analysis process could both be scripted and provide some level of automation.

5.4   Potential Applications and Further Research

Ideally, this research will be built upon and the overall methodology for both acquisition of *in situ* void images and image analysis will be strengthened and improved by further work. Once both processes are capable of producing highly accurate results, then this methodology may be used to collect and analyze empirical data that would be used to validate void theory models. This validation process will hopefully lead to full scale simulations that are capable of predicting the final void content of composite parts used in LCM. This ability would allow engineers to design parts and processes with LCM more quickly and cost effectively. LCM processes have the potential to meet the demands of mass manufacturing industries like automotive and these tools would facilitate their adoption and use moving forward.

Potential commercial applications exist for using this methodology as an empirical tool that could assist in detecting vacuum leaks, identifying areas of high void formation or optimization of processing times to reduce resin flushing periods.

REFERENCES

Almeida, S. F. M., and Z. dos Santos Nogueira Neto. "Effect of void content on the strength of composite laminates." *Composite structures* 28, no. 2 (1994): 139-148.

Frishfelds, V., T. S. Lundström, and A. Jakovics. "Bubble motion through non-crimp fabrics during composites manufacturing." Composites Part A: Applied Science and Manufacturing 39, no. 2 (2008): 243-251.

Fullwood, D., D. Gerrard, A. George, and D. Halverson. "Dispersion metrics for composites–a machine learning based analysis." SAMPE 2013, Long Beach, USA (2013).

George, A. R., "Optimization of Resin Infusion Processing for Composite Materials: Simulation and Characterization Strategies" PhD thesis, Institute of Aircraft Design, University of Stuttgart, 2011.

George, A., M. Brandley, R. Dart, and D. Fullwood. "Void modeling in resin infusion." *Proceedings of CAMX, Orlando, USA* (2014): 14-16.

Ghiorse, S. R. "Effect of void content on the mechanical properties of carbon/epoxy laminates." *SAMPE quarterly* 24, no. 2 (1993): 54-59.

Gourichon, B. C. Binetruy, and P. Krawczak. "A new numerical procedure to predict dynamic void content in liquid composite molding." *Composites Part A: applied science and manufacturing* 37, no. 11 (2006): 1961-1969.

Hammond, V. H., and A. C. Loos. "The effects of fluid type and viscosity on the steady-state and advancing front permeability behavior of textile preforms." *Journal of reinforced plastics and composites* 16, no. 1 (1997): 50-72.

Hernández, S., F. Sket, J. M. Molina-Aldareguı, C. González, and J. LLorca. "Effect of curing cycle on void distribution and interlaminar shear strength in polymer-matrix composites." Composites science and technology 71, no. 10 (2011): 1331-1341.

Labat, L., M. Grisel, J. Breard, and G. Bouquet. "Original use of electrical conductivity for void detection due to injection conditions of composite materials." *Comptes Rendus de l'Académie des Sciences-Series IIB-Mechanics* 329, no. 7 (2001): 529-534.

Lebel-Lavacry, A., C. H. Park, A. Saouab, S. Guéroult, L. Bizet, and J. Bréard. "Modeling and Simulation of Void Formation During the Resin Transfer Molding Process." In *ASME 2012 11th Biennial Conference on Engineering Systems Design and Analysis*, pp. 83-91. American Society of Mechanical Engineers, 2012.

LeBel, F., A. E. Fanaei, E. Ruiz, and F. Trochu. "Experimental characterization by fluorescence of capillary flows in dual-scale engineering fabrics." *Textile Research Journal* 83, no. 15 (2013): 1634-1659.

LeBel, F., A. E. Fanaei, É. Ruiz, and F. Trochu. "Prediction of optimal flow front velocity to minimize void formation in dual scale fibrous reinforcements." *International journal of material forming* 7, no. 1 (2014): 93-116.

Leclerc, J. S., and E. Ruiz. "Porosity reduction using optimized flow velocity in Resin Transfer Molding." *Composites Part A: Applied Science and Manufacturing* 39, no. 12 (2008): 1859-1868.

Liu, L., B. M. Zhang, D. F. Wang, and Z. J. Wu. "Effects of cure cycles on void content and mechanical properties of composite laminates." *Composite Structures* 73, no. 3 (2006): 303-309.

Lundström, T. S., B. R. Gebart, and C. Y. Lundemo. "Void formation in RTM." *Journal of Reinforced Plastics and Composites* 12, no. 12 (1993): 1339-1349.

Lundström, T. S., and B. R. Gebart. "Influence from process parameters on void formation in resin transfer molding." *Polymer Composites* 15, no. 1 (1994): 25-33.

Lundström, T. S.. "Bubble transport through constricted capillary tubes with application to resin transfer molding." *Polymer Composites* 17, no. 6 (1996): 770-779.

Lundström, T. S.. "Measurement of void collapse during resin transfer moulding." *Composites Part A: Applied Science and Manufacturing* 28, no. 3 (1997): 201-214.

Lundström, T. S., and A. Holmgren. "Dissolution of voids during compression molding of SMC*." Journal of Reinforced Plastics and Composites* 29, no. 12 (2010): 1826-1837.

Lundström, T. S., V. Frishfelds, and A. Jakovics. "Bubble formation and motion in non-crimp fabrics with perturbed bundle geometry." *Composites Part A: Applied Science and Manufacturing* 41, no. 1 (2010): 83-92.

Luo, Y., I. Verpoest, K. Hoes, M. Vanheule, H. Sol, and A. Cardon. "Permeability measurement of textile reinforcements with several test fluids." *Composites Part A: Applied Science and Manufacturing* 32, no. 10 (2001): 1497-1504.

Mahale, A. D., R. K. Prud'Homme, and L. Rebenfeld. "Quantitative measurement of voids formed during liquid impregnation of nonwoven multifilament glass networks using an optical visualization technique." *Polymer Engineering & Science* 32, no. 5 (1992): 319-326.

Park, C. H., A. Lebel, A. Saouab, J. Bréard, and W. L. Lee. "Modeling and simulation of voids and saturation in liquid composite molding processes." *Composites Part A: Applied science and manufacturing* 42, no. 6 (2011): 658-668.

Park, C. H., and L. Woo. "Modeling void formation and unsaturated flow in liquid composite molding processes: a survey and review." *Journal of reinforced plastics and composites* 30, no. 11 (2011): 957-977.

Patel, N., and L. J. Lee. "Effects of fiber mat architecture on void formation and removal in liquid composite molding." Polymer Composites 16, no. 5 (1995): 386-399.

Patel, N., and L. J. Lee. "Modeling of void formation and removal in liquid composite molding. Part II: Model development and implementation." *Polymer Composites* 17, no. 1 (1996): 104-114.

Saraswat, M. K., D. Heider, and Y. S. Song. "A qualitative study of the void formation using ultrasounds during the vartm process." In SAMPE 2007 Technical Conference. 2007.

Sisodia, S., E. K. Gamstedt, F. Edgren, and J. Varna. "Effects of voids on quasi-static and tension fatigue behaviour of carbon-fibre composite laminates." *Journal of composite materials* 49, no. 17 (2015): 2137-2148.

Sisodia, S. M., S. C. Garcea, A. R. George, D. T. Fullwood, S. M. Spearing, and E. K. Gamstedt. "High-resolution computed tomography in resin infused woven carbon fibre composites with voids." *Composites Science and Technology* 131 (2016): 12-21.

Skartsis, L., J. L. Kardos, and B. Khomami. "Resin flow through fiber beds during composite manufacturing processes. Part I: Review of Newtonian flow through fiber beds." *Polymer Engineering & Science* 32, no. 4 (1992): 221-230.

Steenkamer, D., S. H. McKnight, D. J. Wilkins, and V. M. Karbhari. "Experimental characterization of permeability and fibre wetting for liquid moulding." *Journal of materials science* 30, no. 12 (1995): 3207-3215.

Trochu, F., E. Ruiz, V. Achim, and S. Soukane. "Advanced numerical simulation of liquid composite molding for process analysis and optimization." Composites Part A: applied science and manufacturing 37, no. 6 (2006): 890-902.

Varna, J., Roberts J., L. A. Berglund, and T. S. Lundström. "Effect of voids on failure mechanisms in RTM laminates." *Composites Science and technology* 53, no. 2 (1995): 241-249.

Wielhorski, Y., A. B. Abdelwahed, and J. Bréard. "Theoretical approach of bubble entrapment through interconnected pores: supplying principle." Transport in porous media 96, no. 1 (2013): 105-116.

"A Posteriori Shade Correction." http://helios.univ-reims.fr/Labos/INSERM514/ImageJ/#List (Accessed August 2016).

APPENDICES

APPENDIX A. CAD DRAWINGS AND SETUP DETAILS

Base Plate Drawing
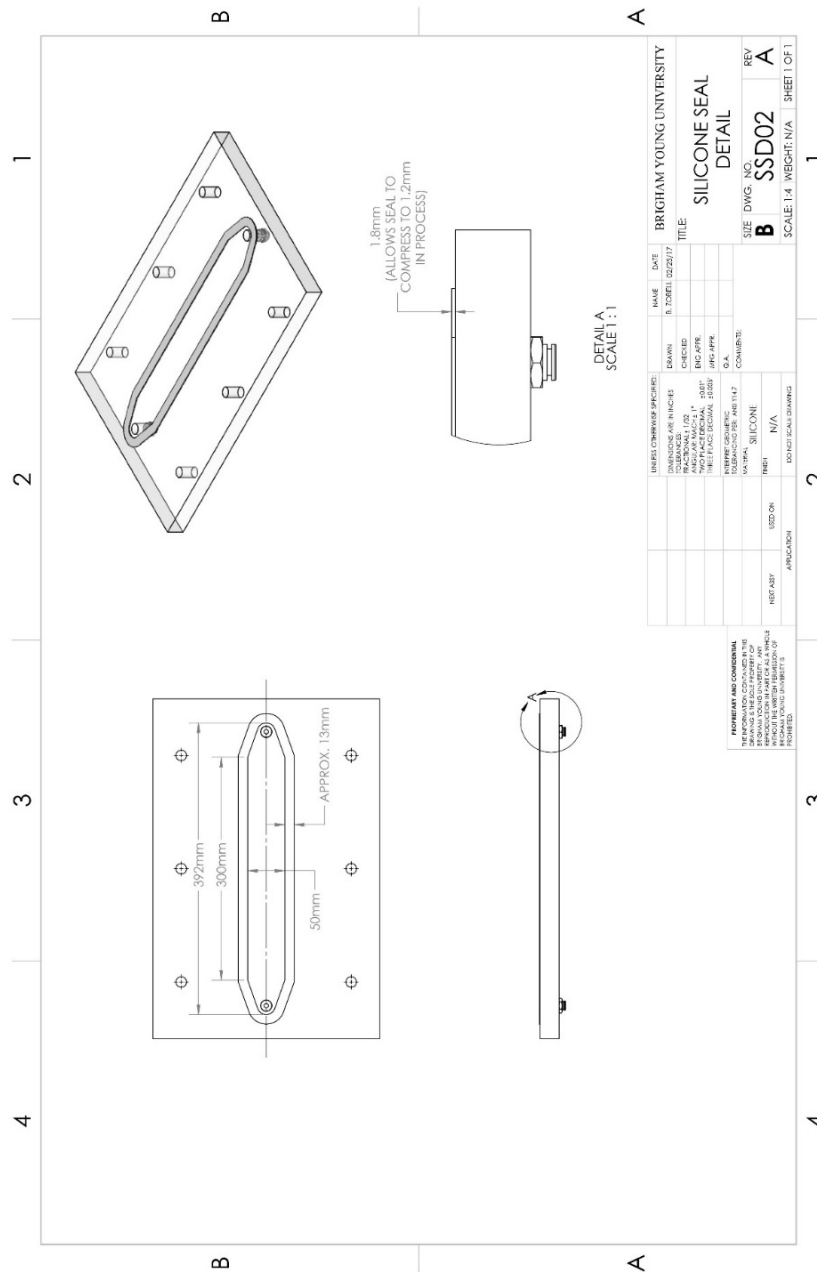
Base Plate With Seal Drawing
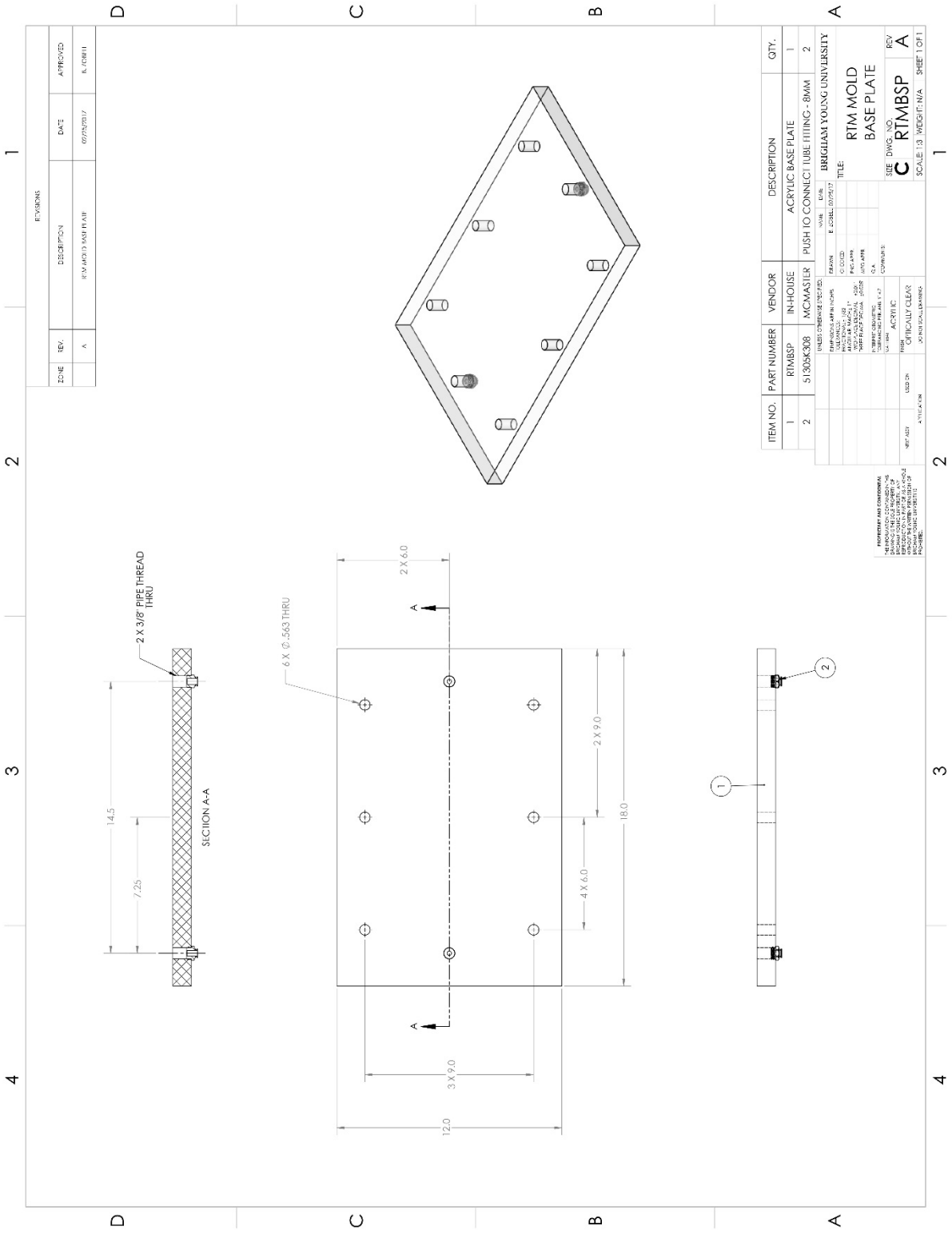
RTM Mold Assembly Drawing

ITEM NO.	PART NUMBER	VENDOR	DESCRIPTION	QTY.
1	Base Plate	IN-HOUSE	BASE PLATE WITH CONNECTORS	1
2	Silicone seal	HARDWARE STORE	SILICONE SEAL – CLEAR OR WHITE	1
3	Top Plate	IN-HOUSE	TOP PLATE	1
4	92316A774	MCMASTER	1/2"-20 X 3" HEX HEAD SCREW	6
5	94902A105	MCMASTER	1/2"-20 FLANGE NUT	6
6	C Channel	METAL MART	STEEL C-CHANNEL SUPPORT BEAMS	4

RTM MOLD

TITLE: BRIGHAM YOUNG UNIVERSITY

DWG. NO. RTMMOLD REV A

SIZE C   SCALE: 1:4   WEIGHT: N/A   SHEET 1 OF 1

REVISIONS

ZONE	REV.	DESCRIPTION	DATE	APPROVED
	A	RTM MOLD ASSEMBLY	02/25/2017	B. ZOBELL

McMaster Flange Nut Drawing

1/2"-20 Thread

29/64"
0.05"

1 1/32"
3/4"

McMaster Bolt Drawing

0.5"

Thread length may vary from
1 1/4" to 1 3/4" in length.

3"

1/2"-20 Thread

33/64"

1 5/64"

3/4"
Hex

McMASTER-CARR®

http://www.mcmaster.com
© 2014 McMaster-Carr Supply Company
Information in this drawing is provided for reference only

PART
NUMBER **92316A774**

Flange Head
Cap Screw
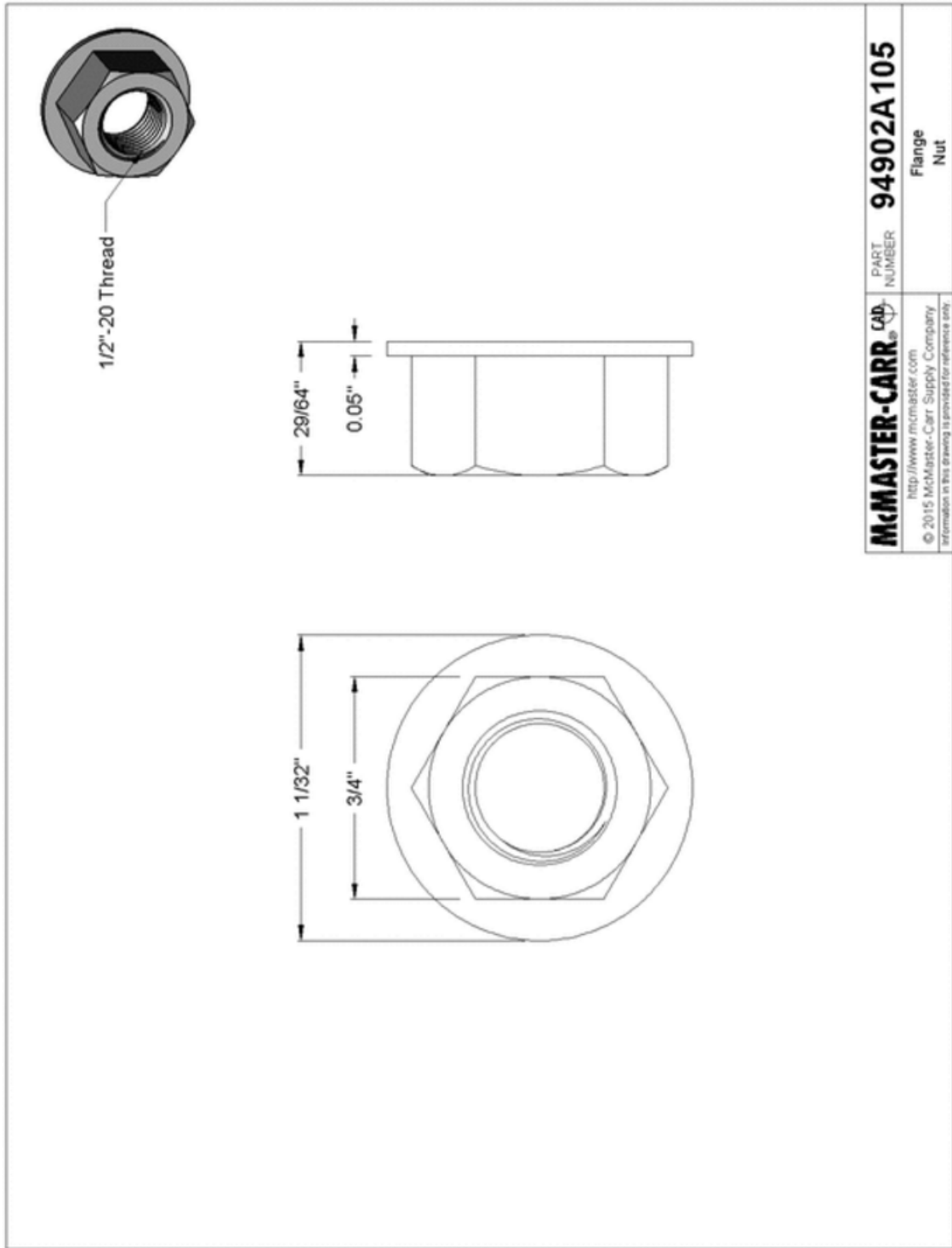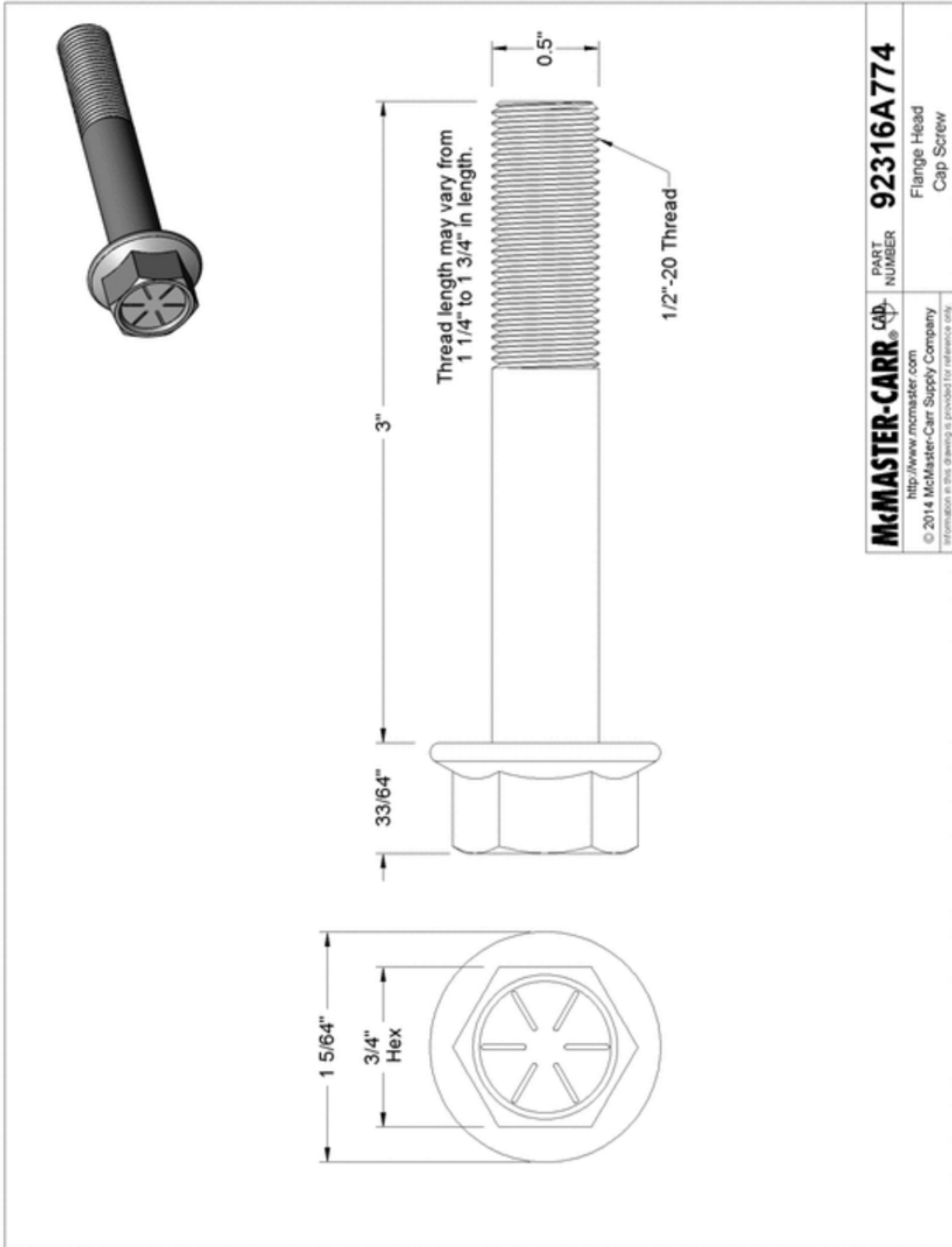
Inlet and Outlet Tube

Crack-Resistant Polyethylene Semi-Clear Tube

I.D.: 6mm

O.D.: 8mm

Vendor: McMaster

Part#: 5958K14

RTM Setup Diagrams

Front View
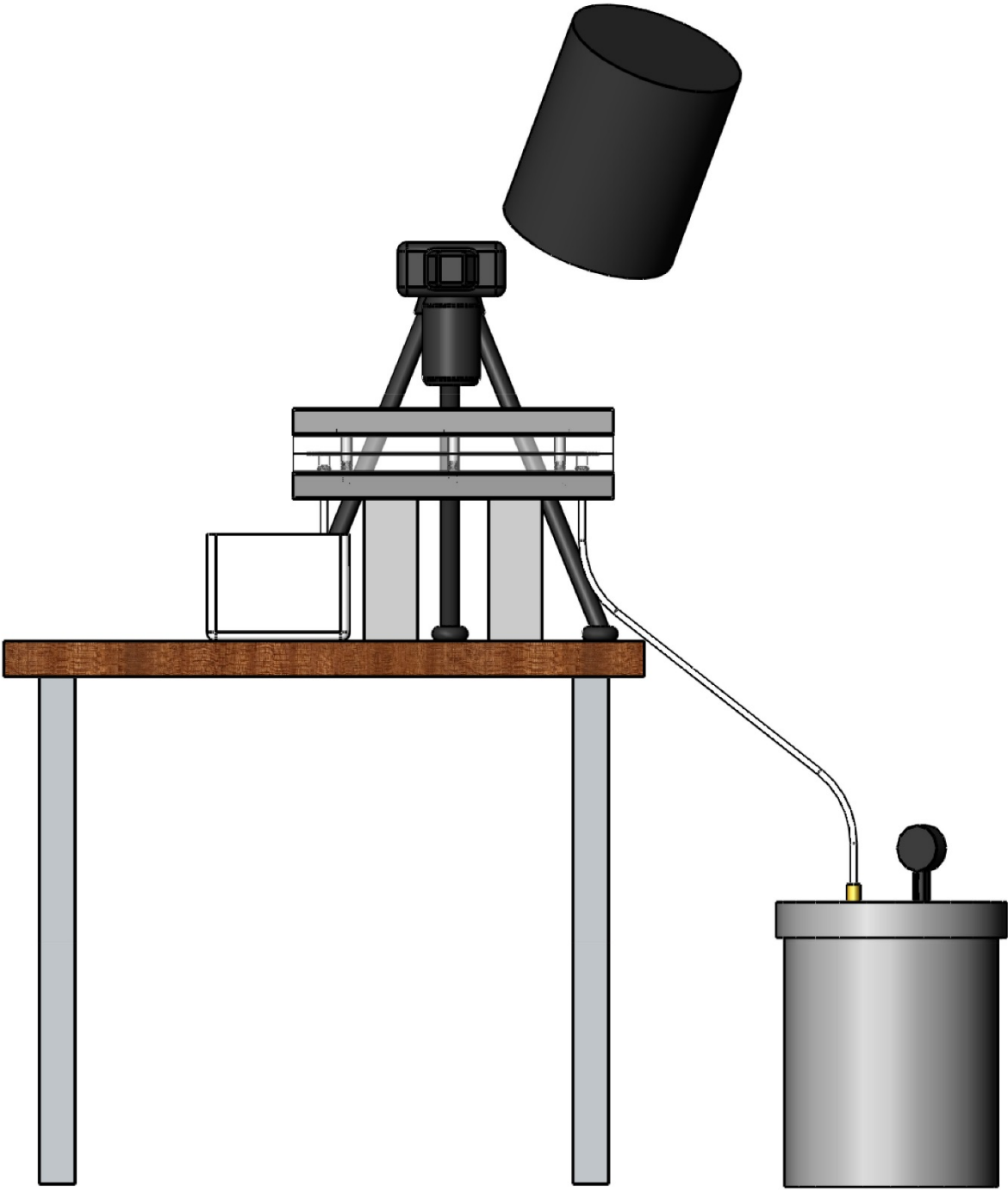
Side View
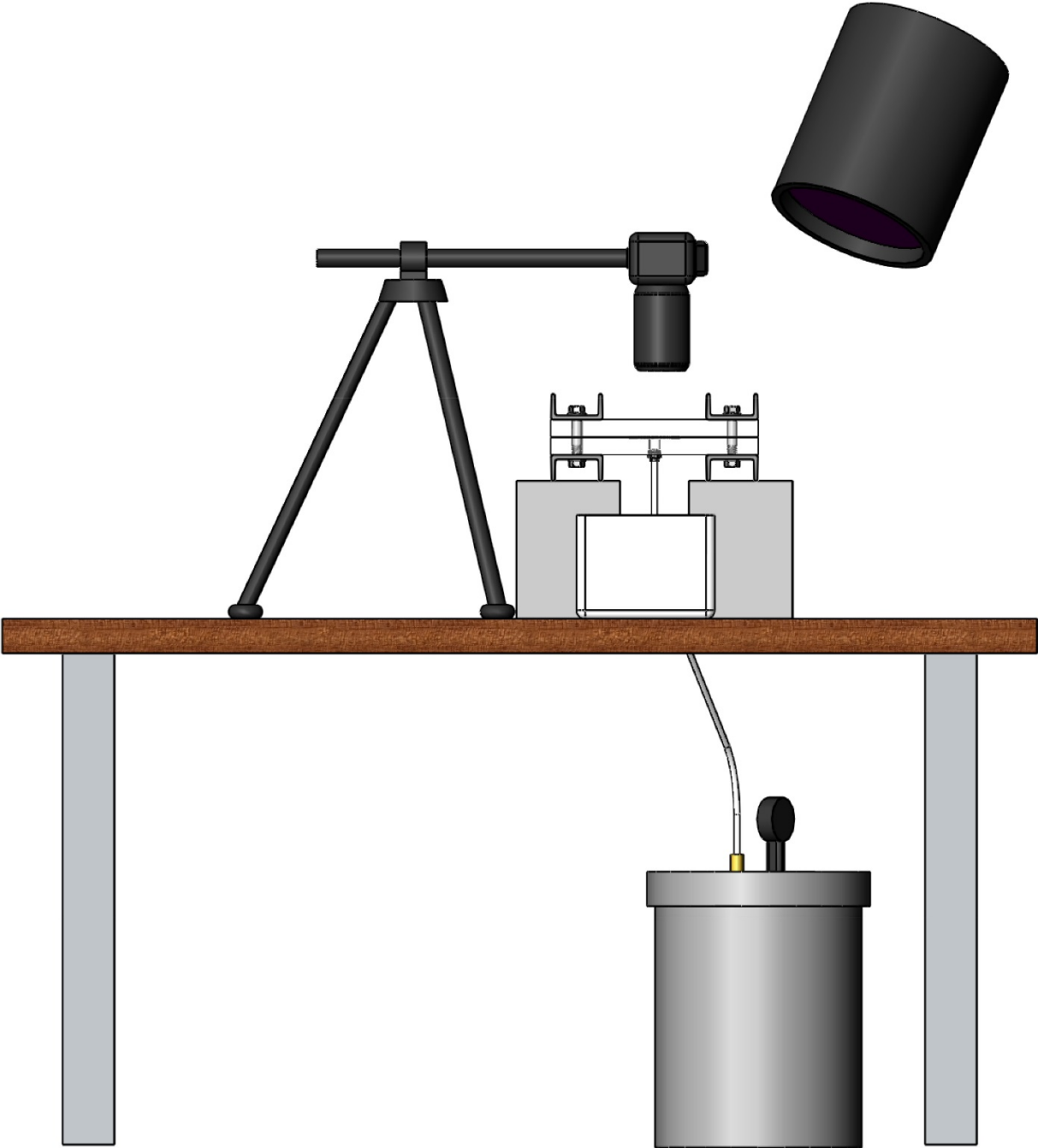
ISO View
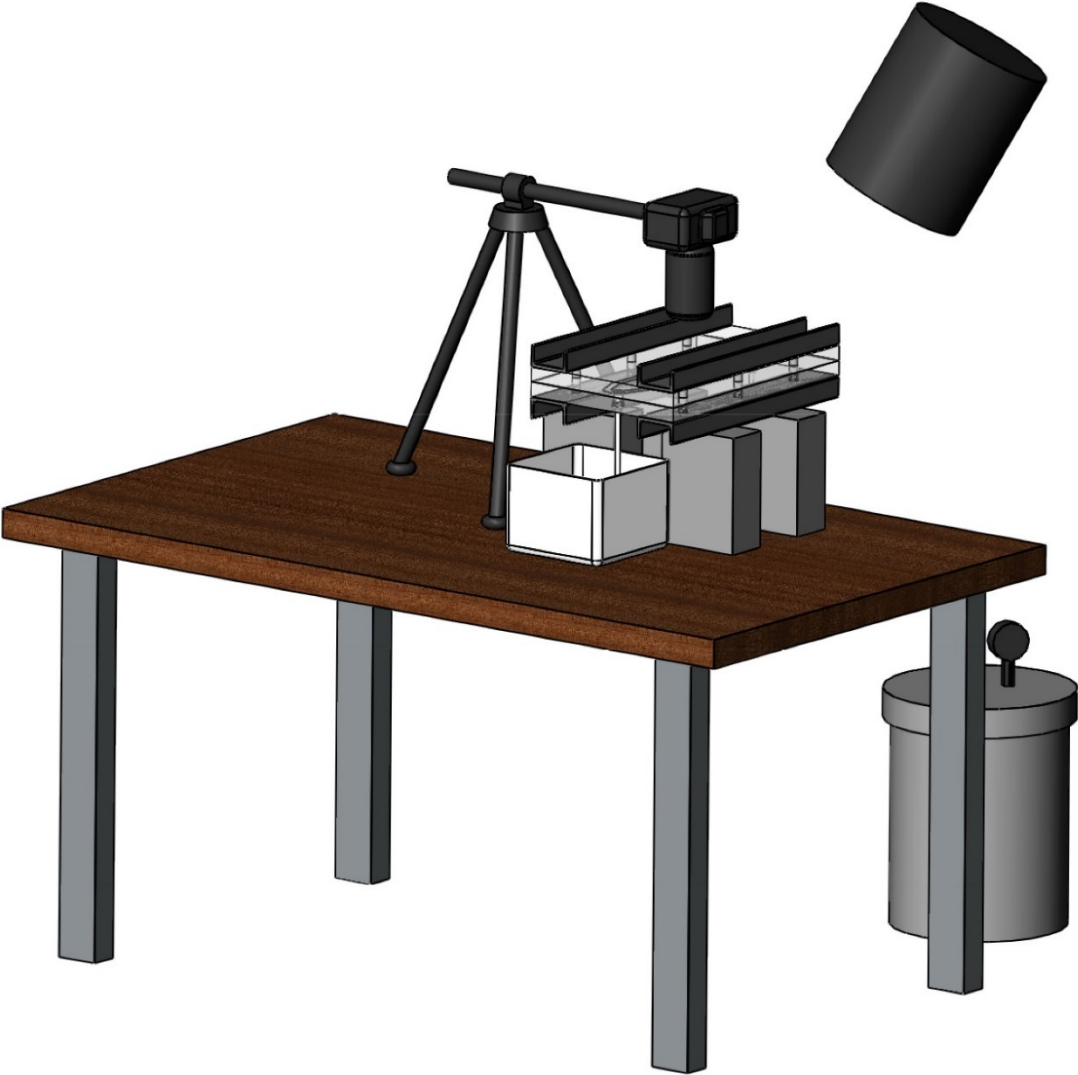
APPENDIX B.   MATERIALS, PROPERTIES AND SPECIFICATIONS

Materials and Specifications

E-Glass quadriaxial NCF with z-stitching

- 1 ply = 0.8mm thickness
- FAW = 25.30 oz./yd^2 or 857.5 g/m^2 or .8575 kg/m^2
- 100mm X 300mm preform sizes, 1 ply of material
- Cavity = approx. 0.8mm
- vf% = 42.03%

Vector Ply C-L 0900 Carbon Fiber

- 1 ply = 0.6mm thickness
- FAW = 8.61 oz./yd^2 or 292 g/m^2 or (.584 kg/m^2 at correct thickness)
- 50mm X 300mm preform sizes, 2 plies of material
- Cavity = 1.2mm
- vf% = 54.99 %

Hexcel 4H Satin AGP185-CS

- 1 ply = 0.2mm thickness
- FAW = 5.46 oz./yd^2 or 185.13 g/m^2 or .18513 kg/m^2
- 50mm X 300mm preform sizes, 1 ply of material
- Cavity = 0.2mm
- vf% = 52.30 %

Typical Densities of Fibers:

Carbon = 1770 kg/m^3

Fiberglass = 2550 kg/m^3

UV Dye Information

TP-3400-0601

Dye-Lite All in One – Leak Detection Tracer Dye

Tracer Products

www.tracerline.com

Viscosity Measurements

Resin (oil) viscosity:

RPM	%	Spindle	mPas
10	9.6	s61	57.6
12	11.5	s61	57.5
20	19.6	s61	58.8
30	29.6	s61	58.6
50	49.2	s61	59.0
		Average	**58.3**

Resin (oil & UV die) viscosity:

RPM	%	Spindle	mPas
10	9.7	s61	58.2
12	11.5	s61	57.5
20	19.5	s61	58.5
30	29.5	s61	59.0
50	49.3	s61	59.1
		Average	**58.5**

APPENDIX C. IMAGEJ OPERATIONS

Split Color Channels
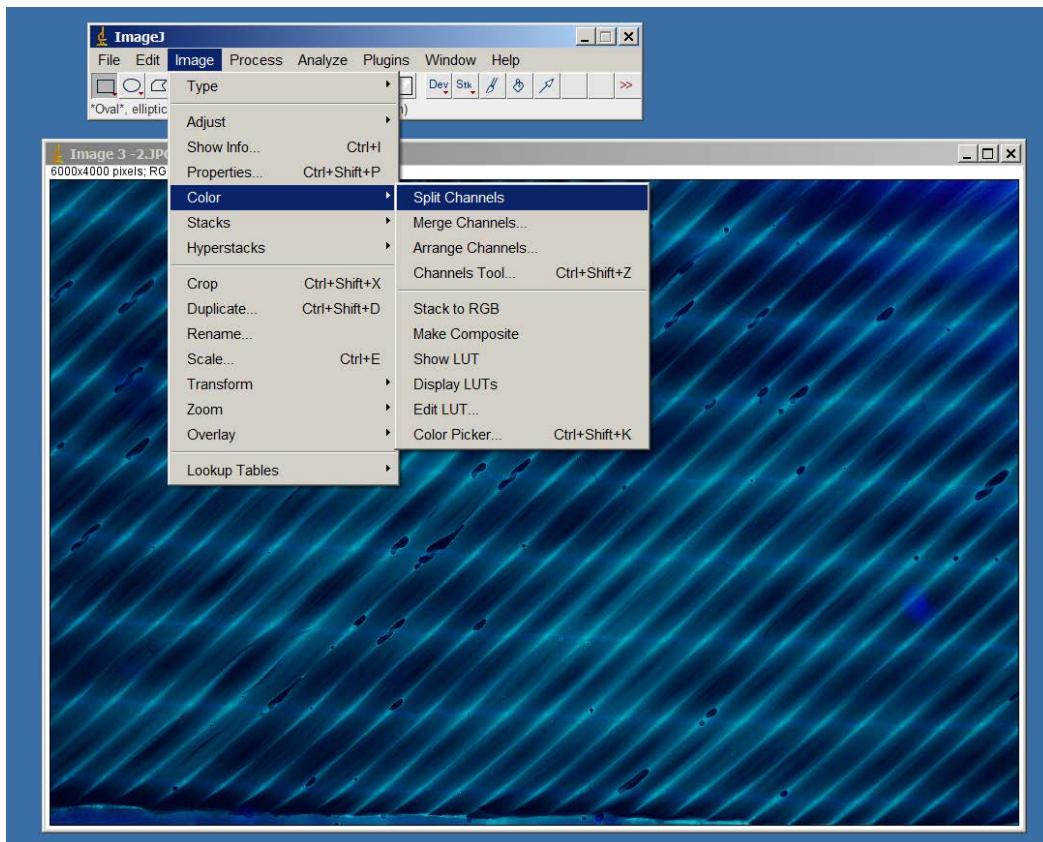
1. Open the image to be analyzed.

2. Select the Image menu.

3. Click on the Color option.

4. Select Split Channels.
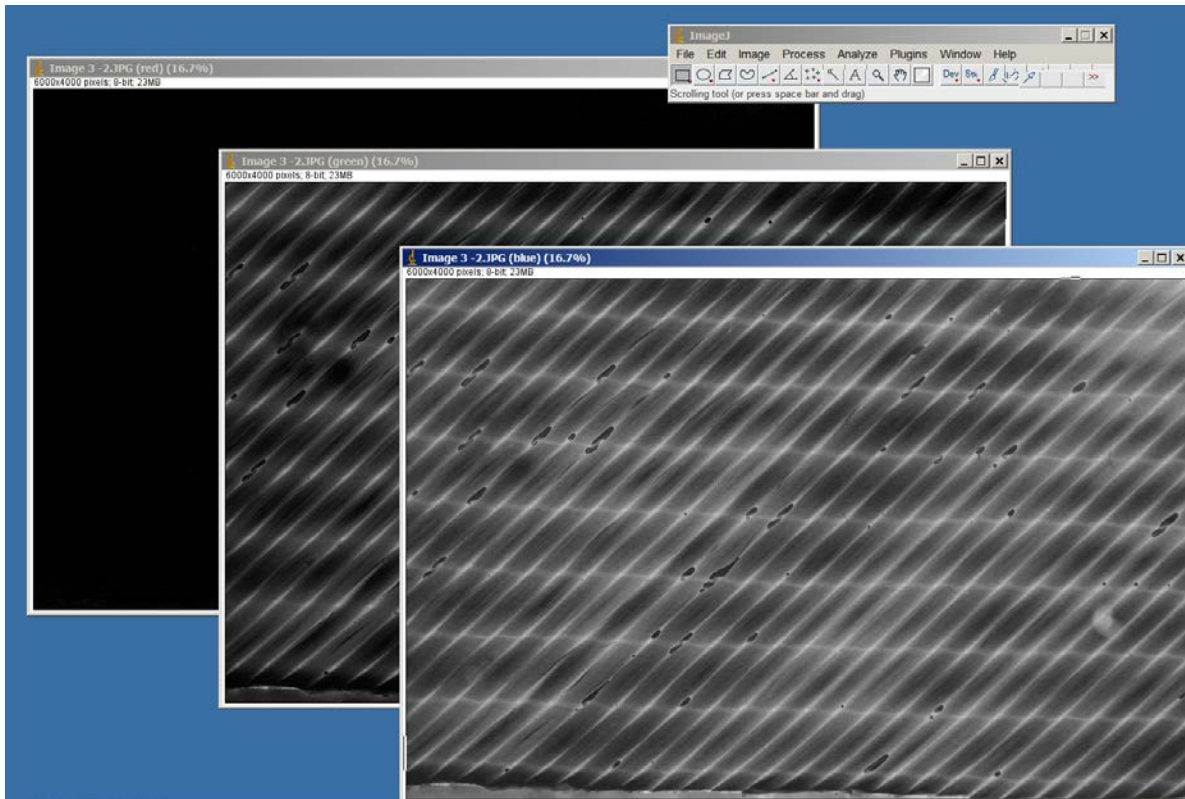
5. Review the images and save those selected for further processing.

Shade Correction
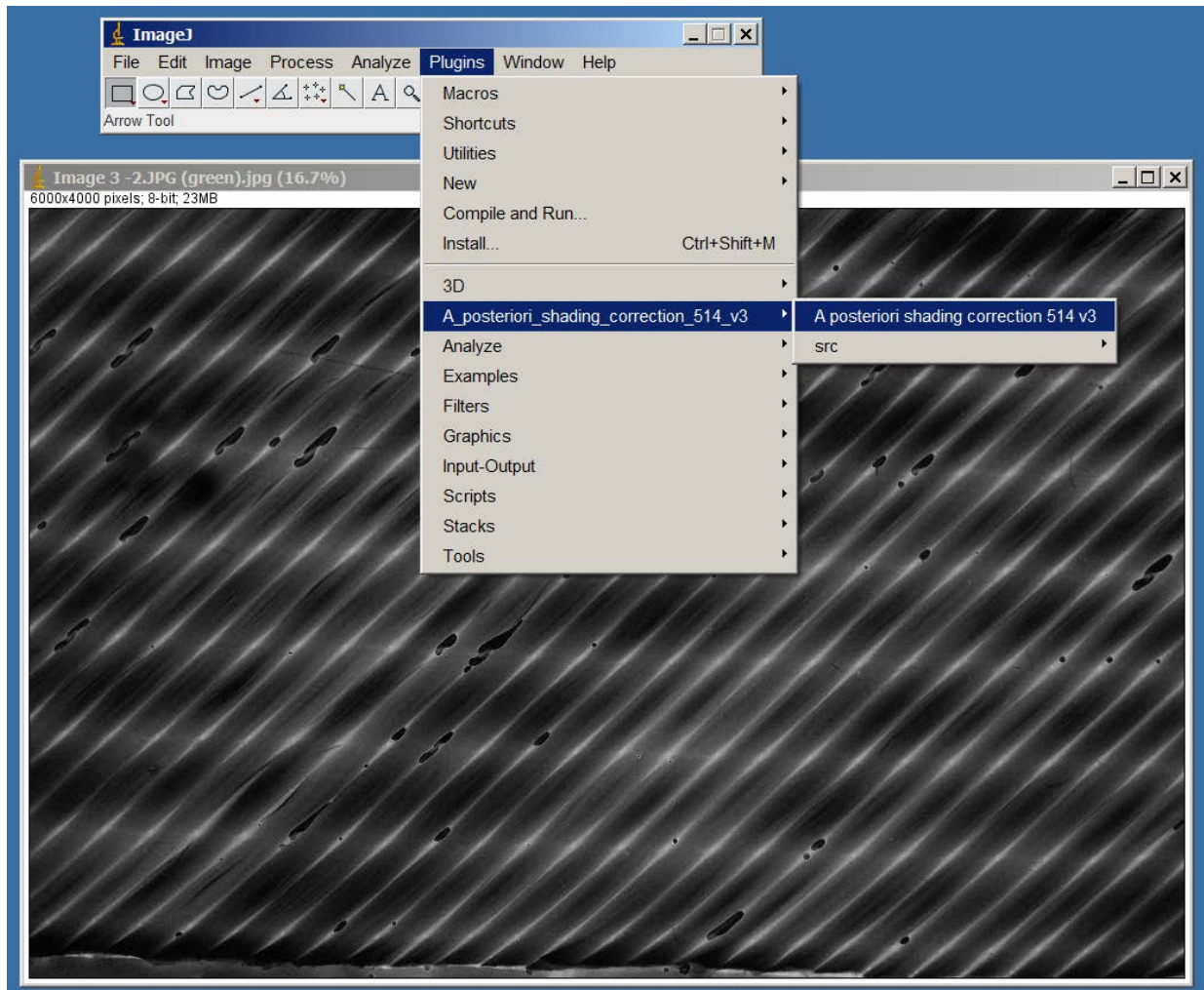
1. The "A_posteriori_shading_correction_514_v3" macro will need to be downloaded and installed (a newer version may exist). This can be found at https://imagej.nih.gov/ij/plugins/inserm514/

2. Open a previously derived image from the split channel process.

3. Select the Plugins menu.

4. Click on A_posteriori_shading_correction_514_v3.
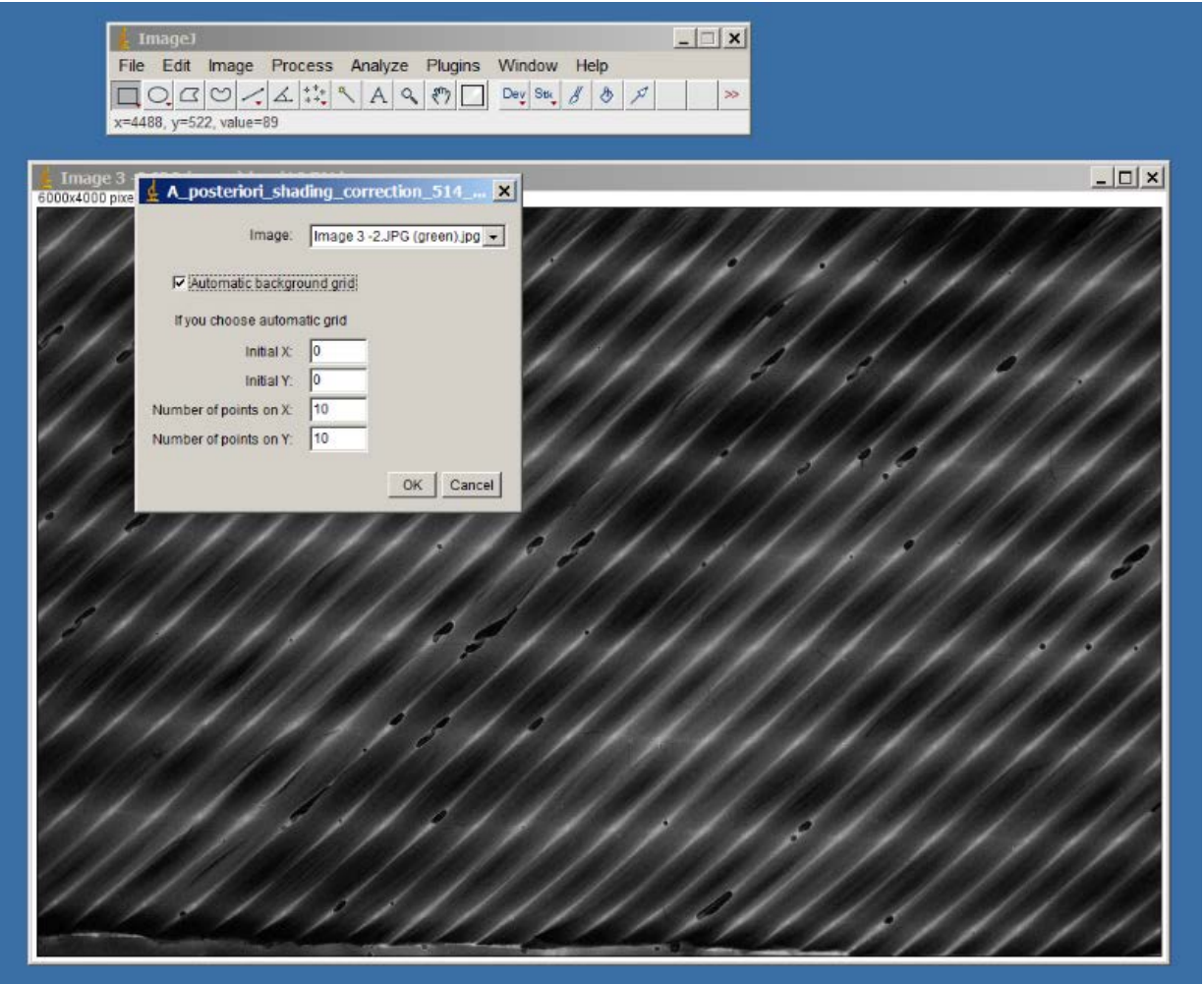
5. Select A posteriori shading correction 514 v3.

6. Check the Automatic background grid box.

7. Click on OK.
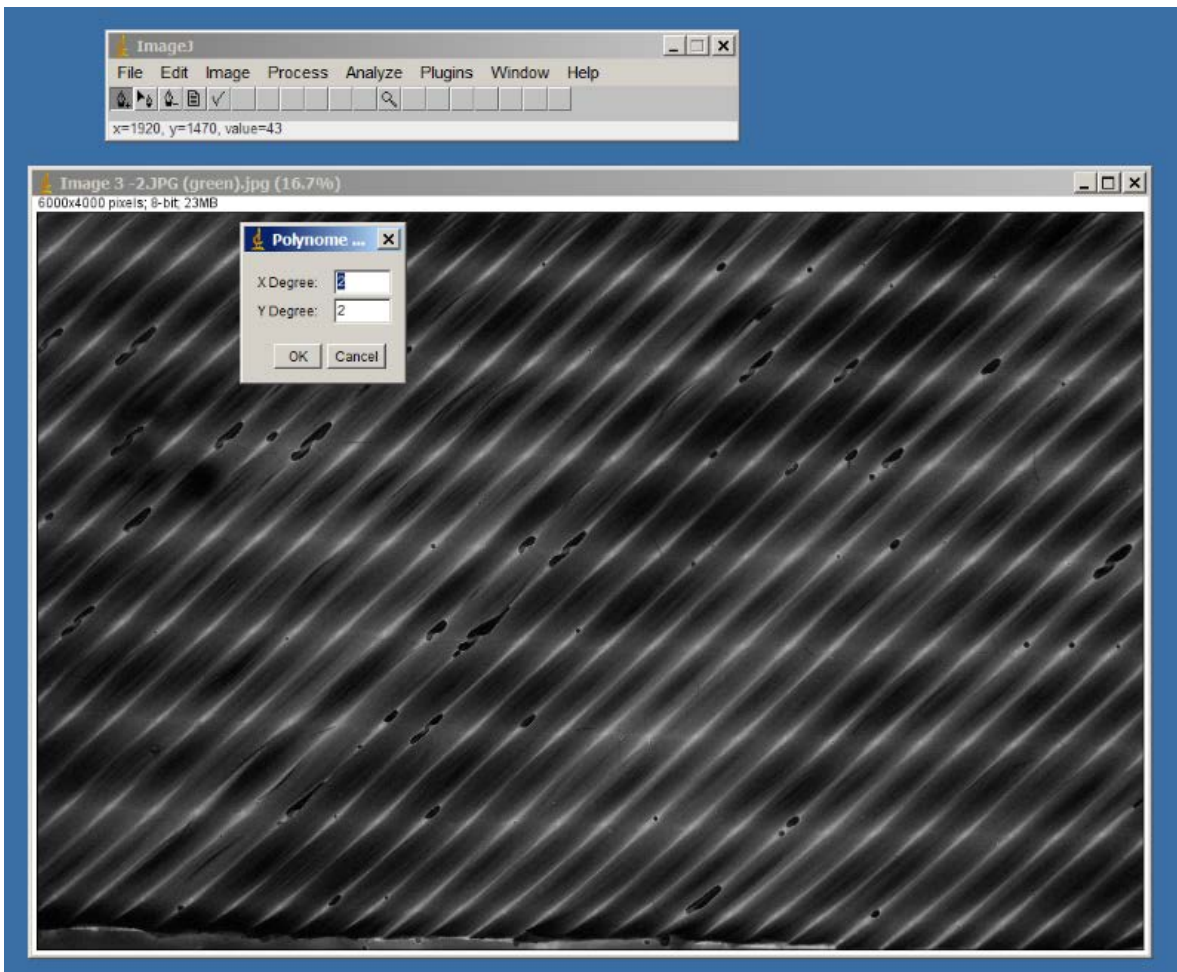
8. The default X and Y degree settings should be 2. If not, set them so they are.

9. Click OK.
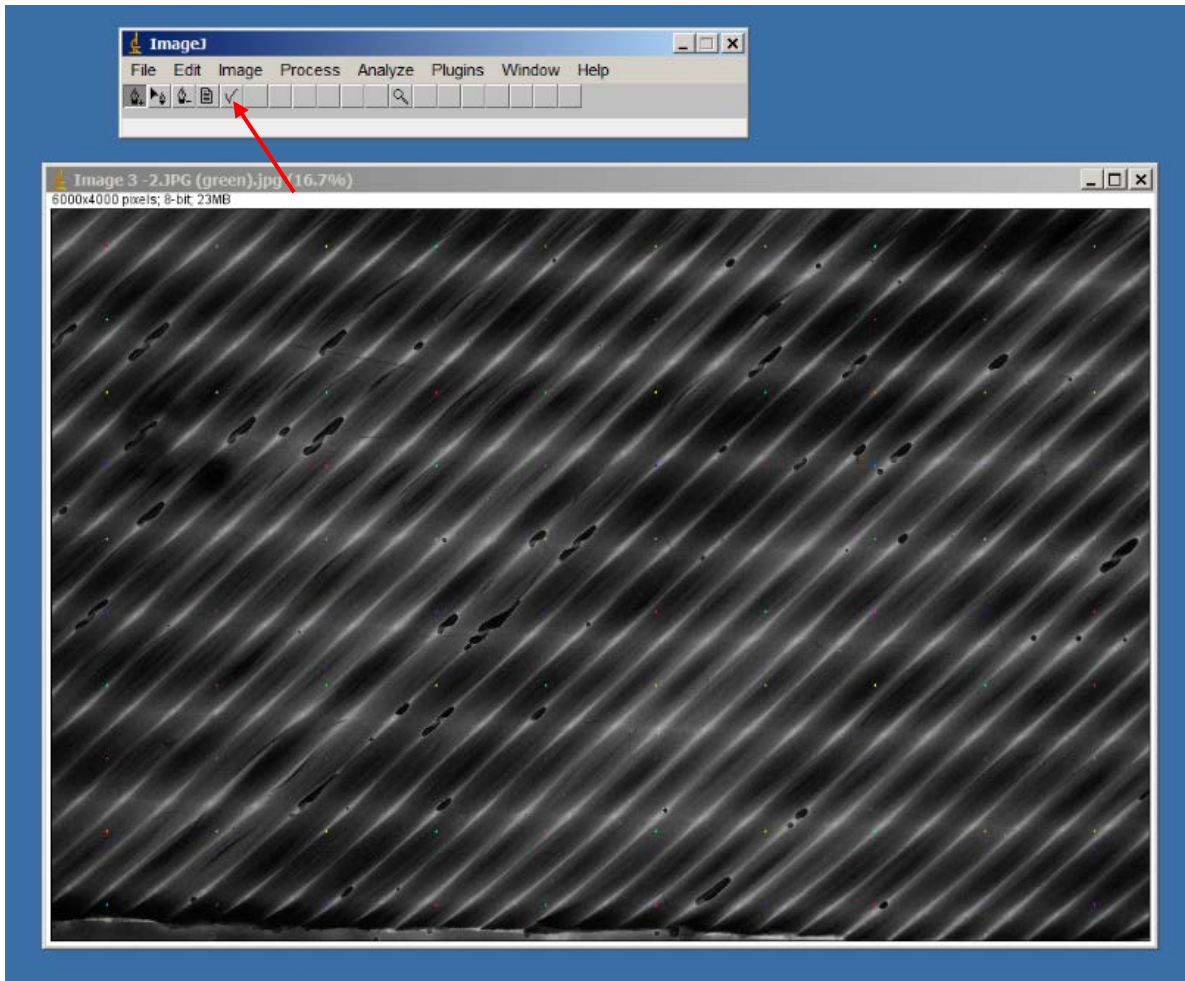
10. The grid back ground should appear on the image.

11. Click on the check mark button located below the menus (see red arrow).

12. If the polynome degree settings box reappears (from step 8), click OK.
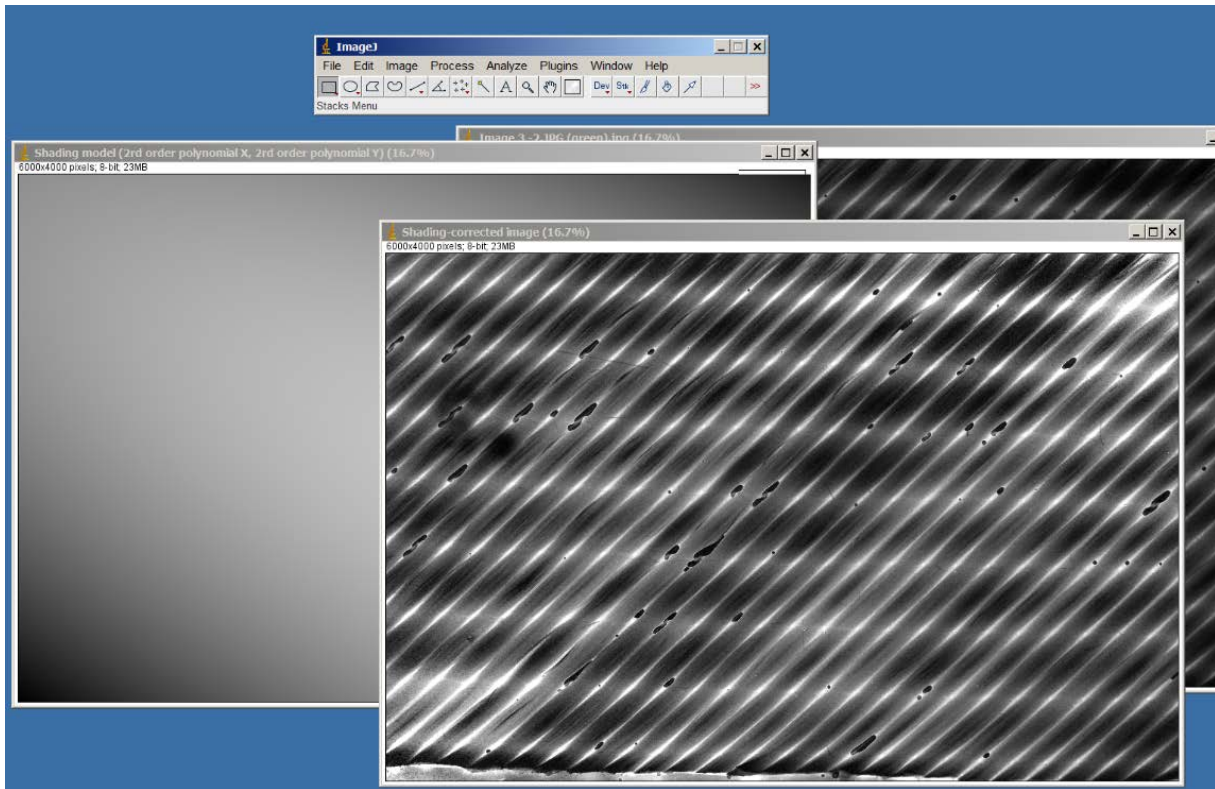
13. After a moment, the shading corrected image will appear along with a model of the background adjustments.

14. Save the image for further processing.

Enhance Contrast

Split Channel images
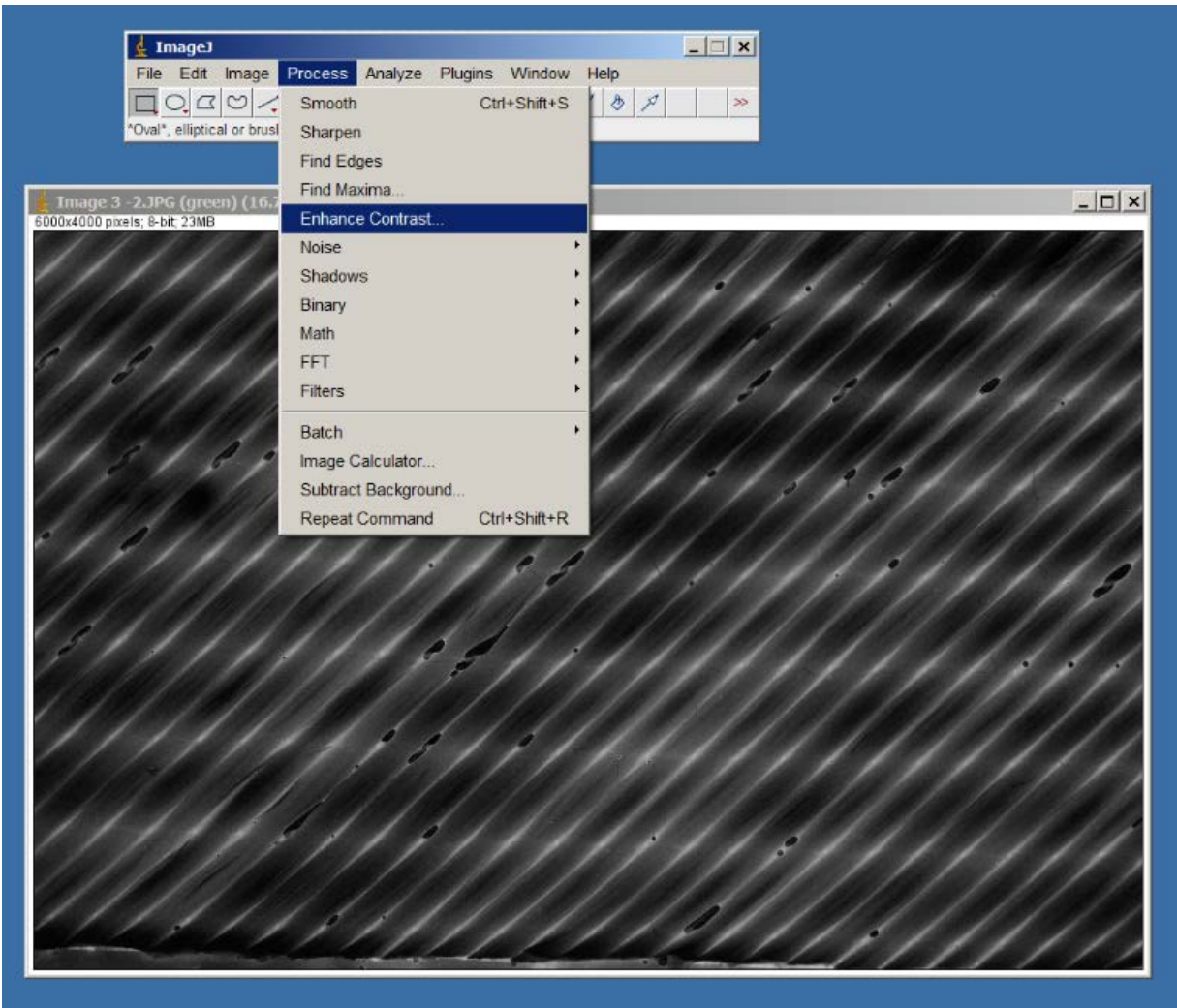
1. Open a previously derived image from the split channel process.

2. Select the Process menu.

3. Select Enhance Contrast.
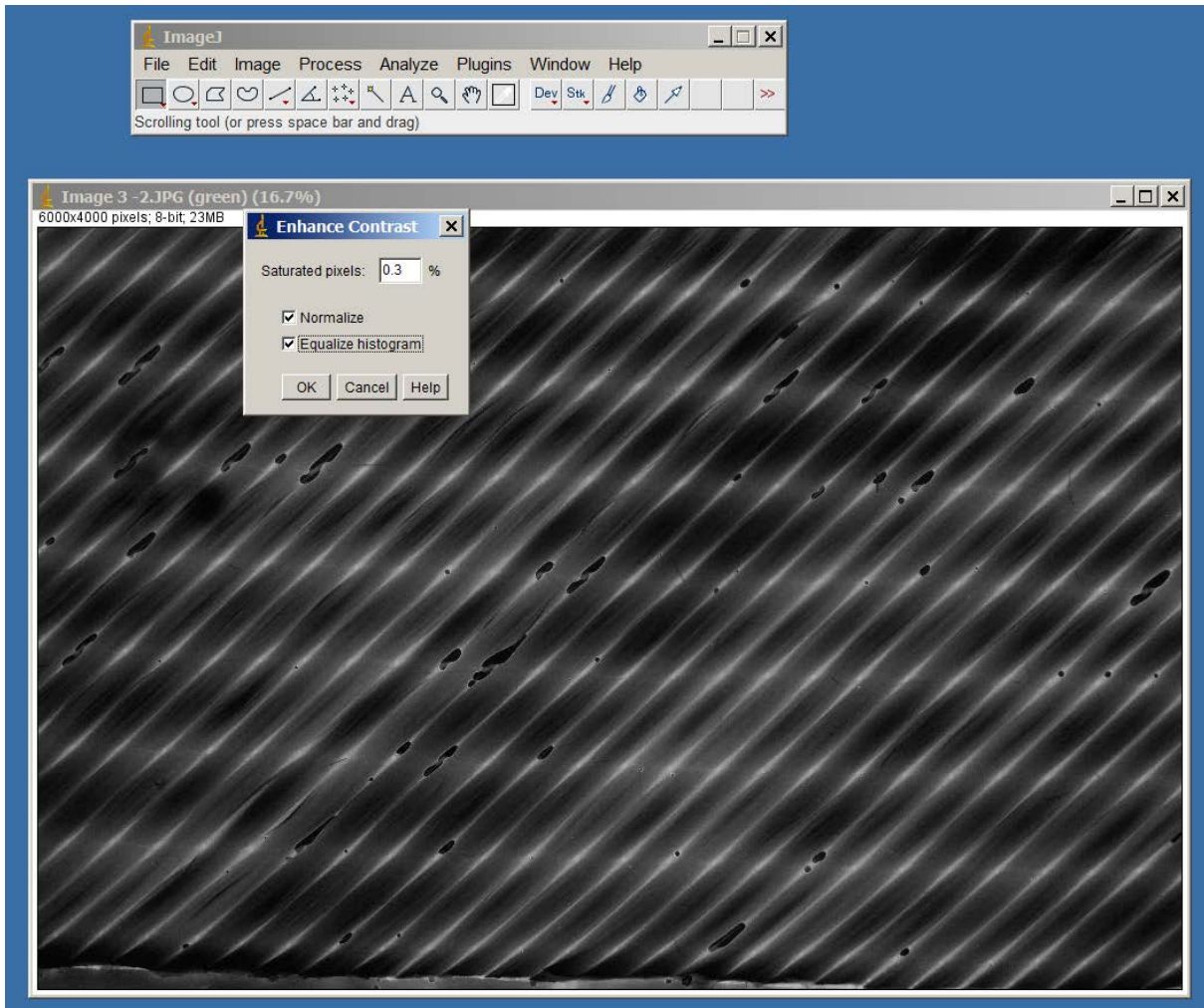
4. Saturated pixels setting should be preset to 0.3%. If not, change it to this setting.

5. Check the Normalize box.

6. Check the Equalize histogram box.

7. Click OK.
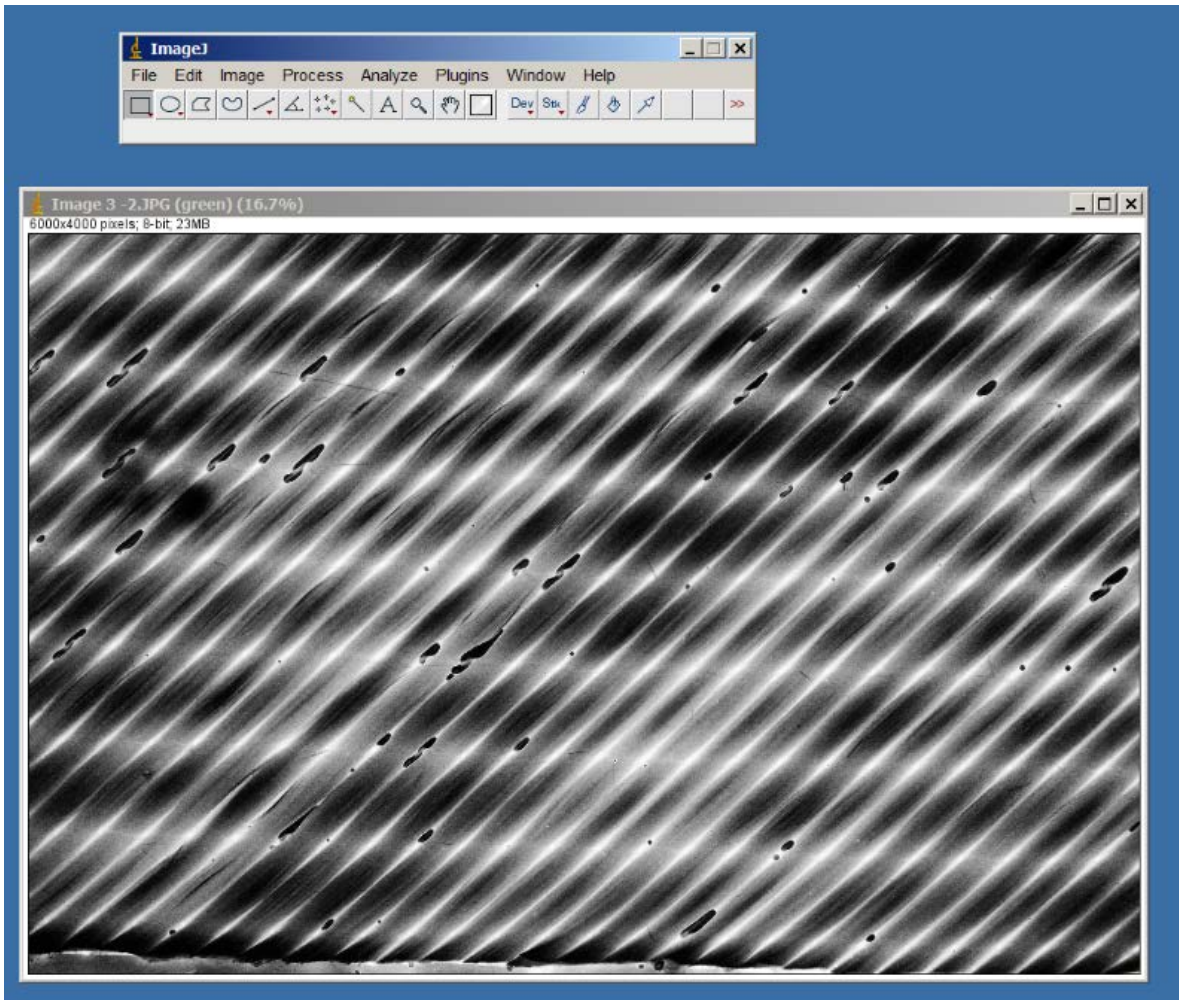
8. Original image will be adjusted for enhanced contrast.

9. Save for further analysis.

Color Images
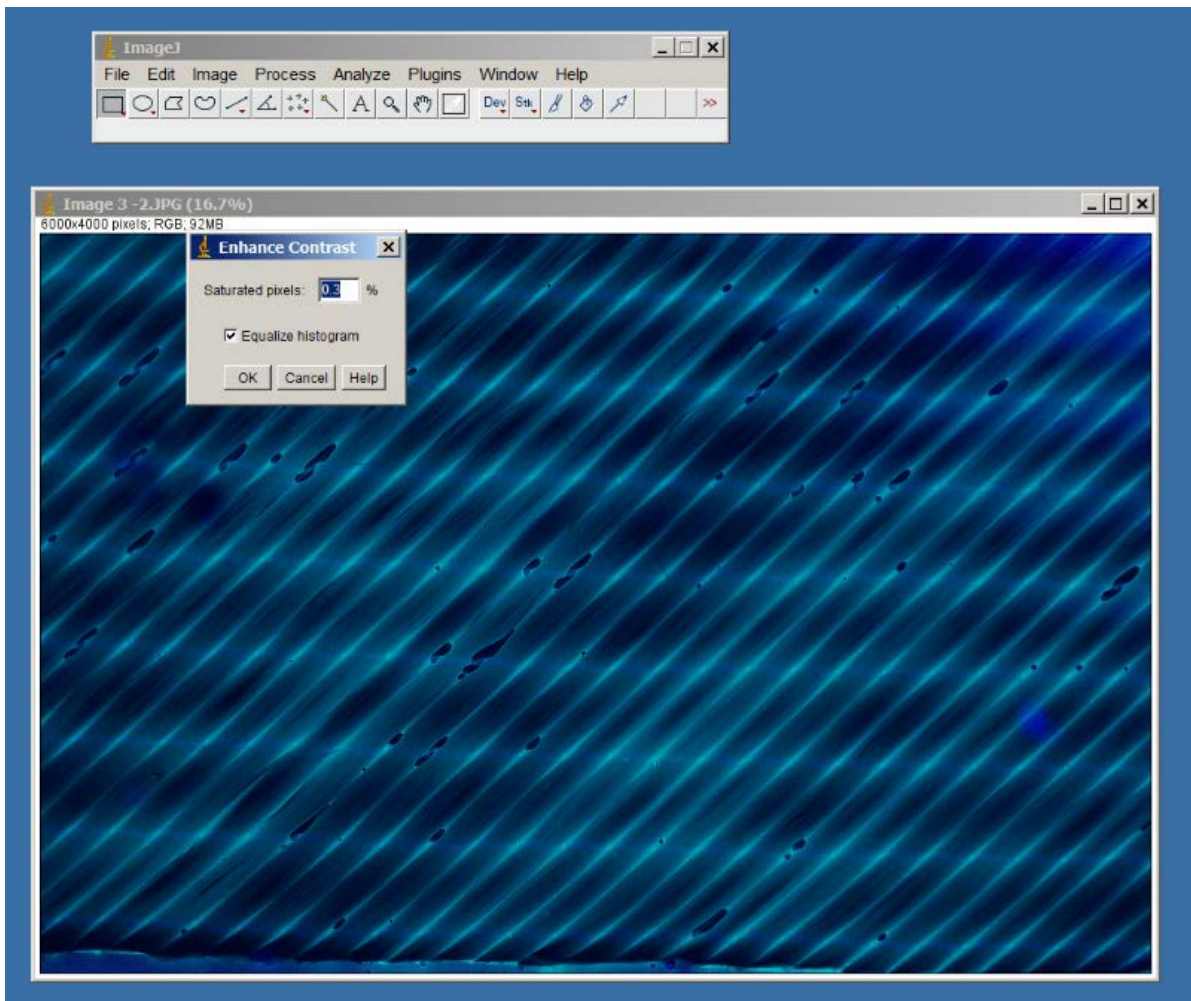
1. Open image.

2. Select the Process menu.

3. Click on Enhance contrast.

4. Saturated pixels setting should be preset to 0.3%. If not, change it to this setting.

5. Check Equalize histogram box.

6. Click OK.
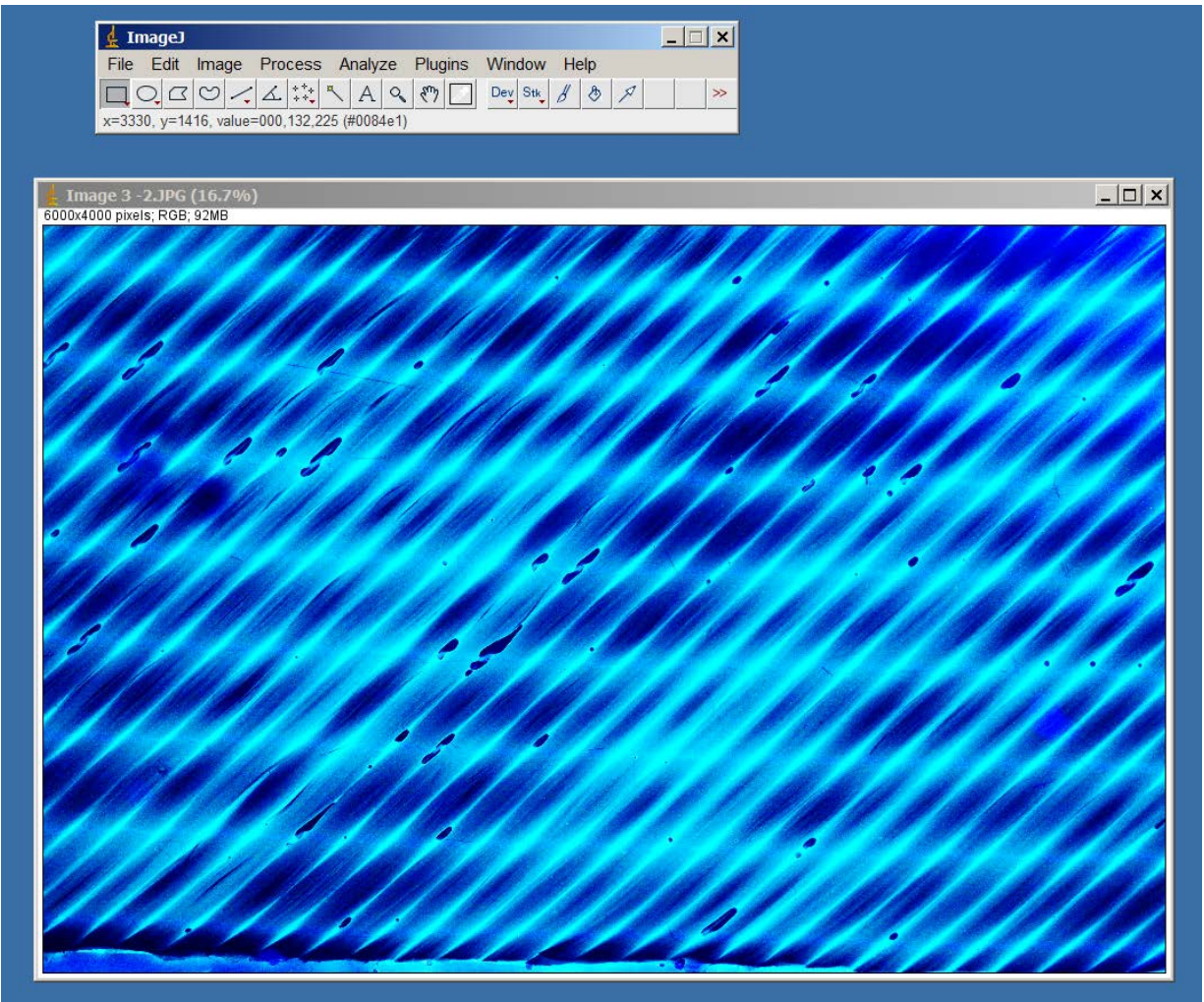
7. Original image will be adjusted for enhanced contrast.

8. Save for further analysis.

Adjust Threshold
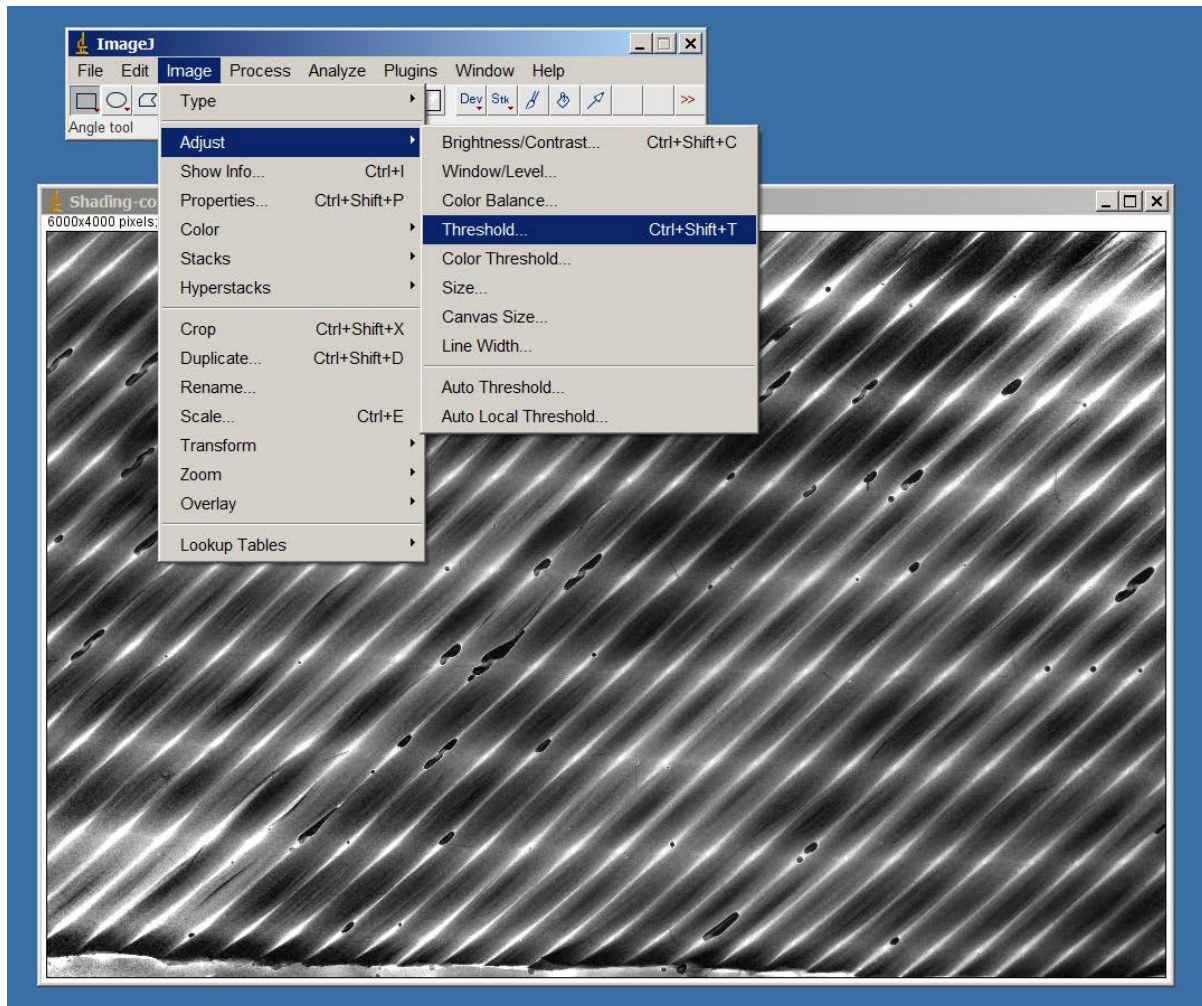
1. Open image that has had the color channels split and has been otherwise enhanced (if desired).

2. Select the Image menu.

3. Click on Adjust.

4. Click on Threshold.
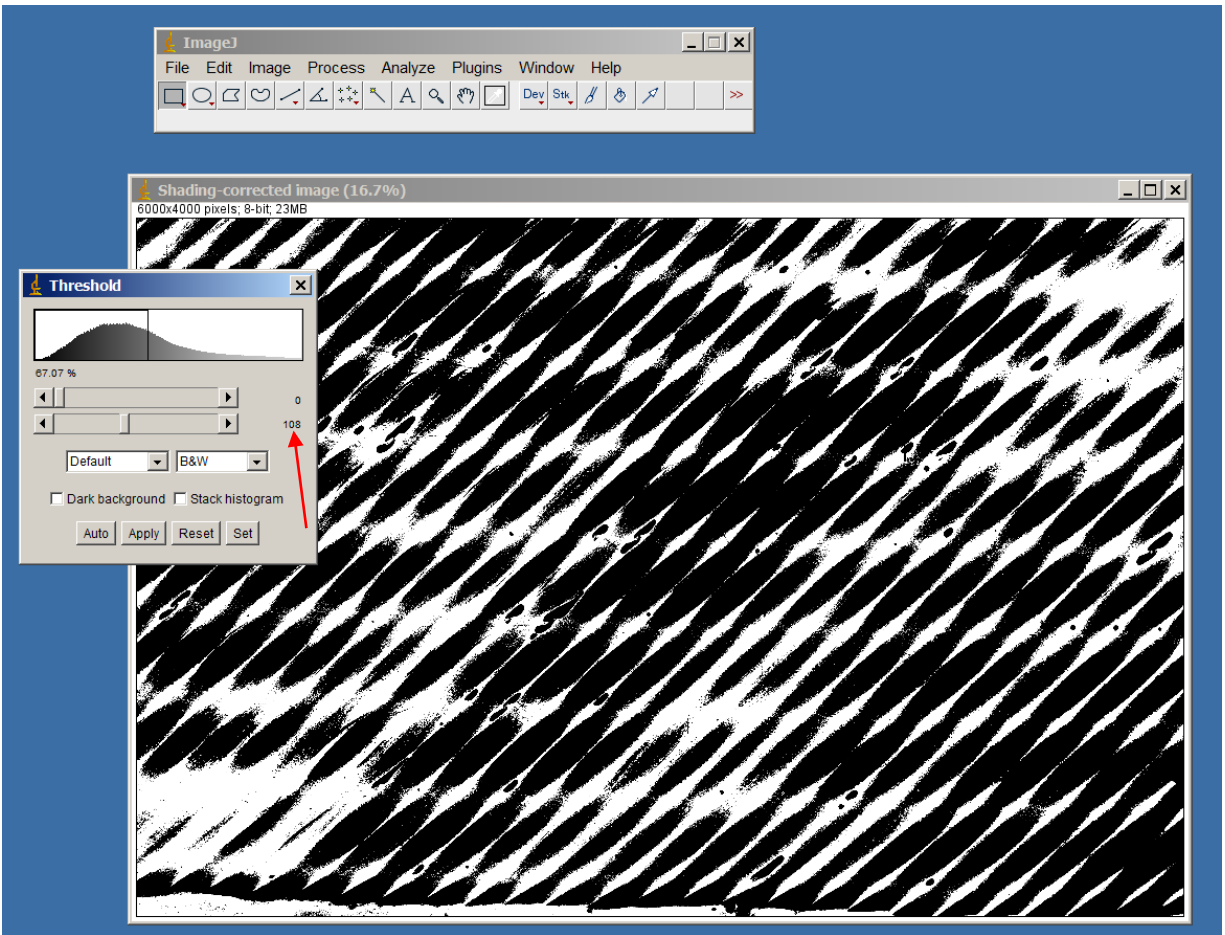
5. Image will be converted to a binary black and white image.

6. Adjust maximum threshold setting (see red arrow) as desired.

7. Click Apply and close the Threshold window.

8. Save image for further processing.

Analyze Particles
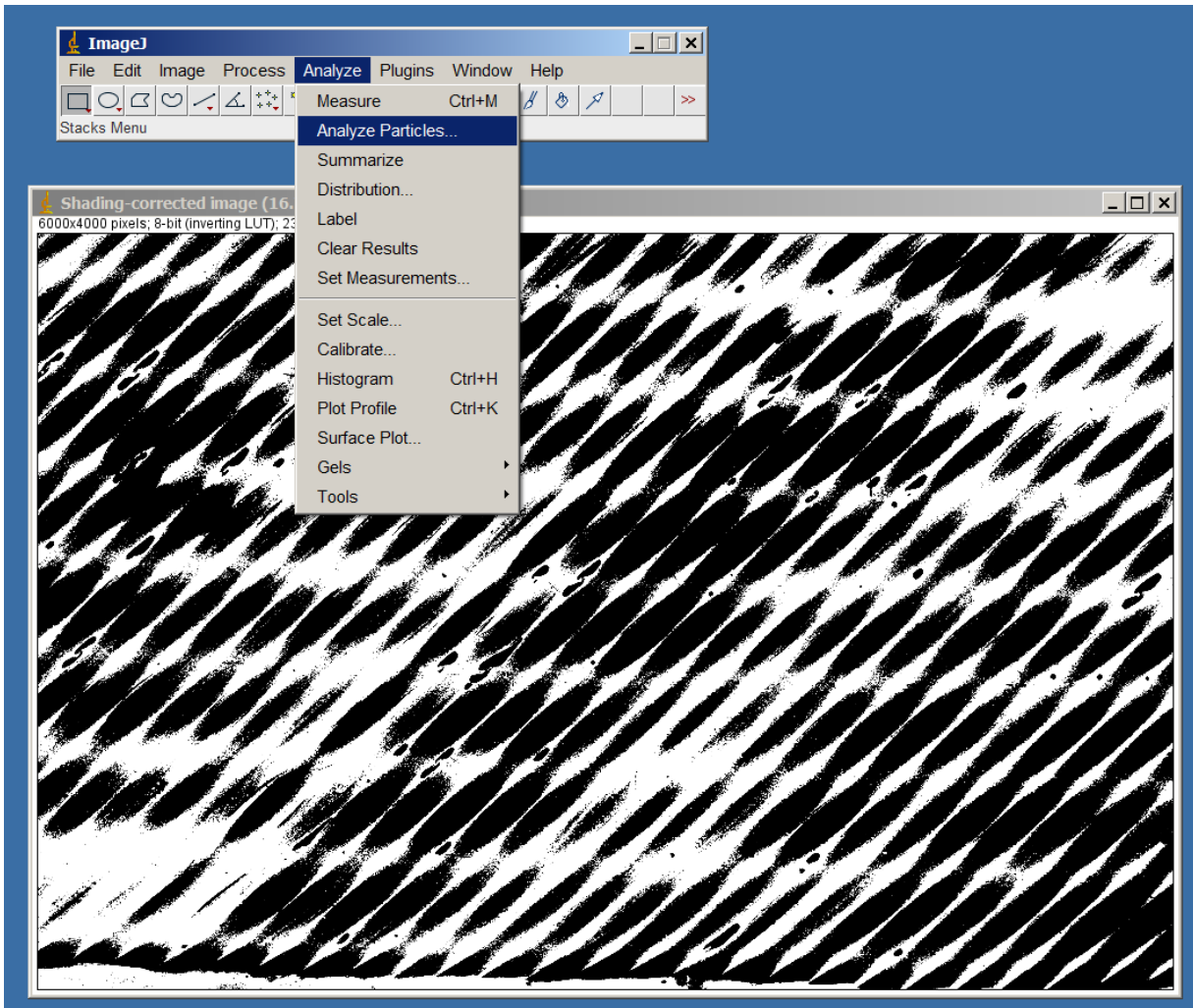
1. Open binary black and white image that has undergone threshold adjustment.

2. Select the Analyze menu.

3. Click on Analyze Particles.
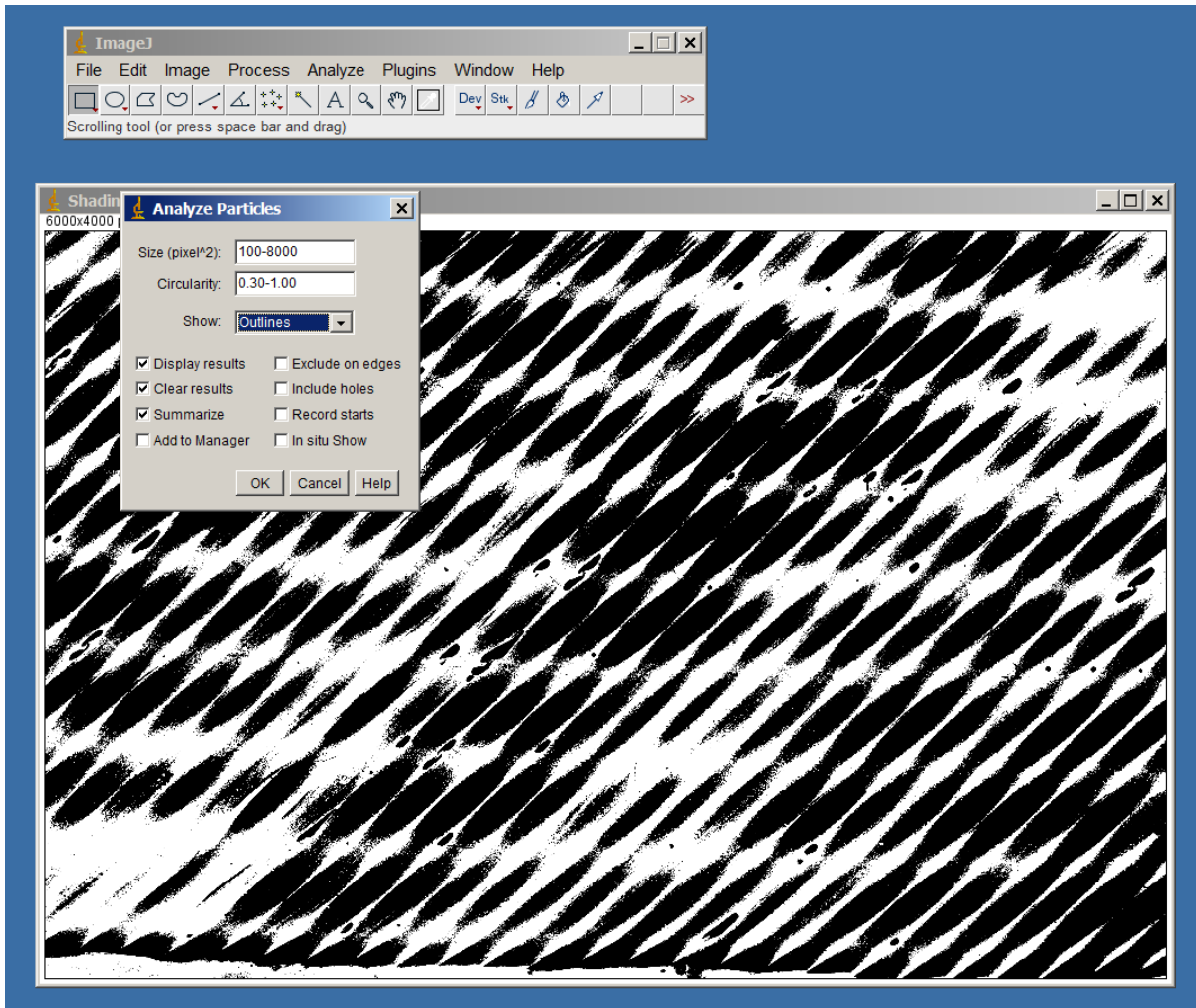
4. Set Size as desired.

5. Set Circularity as desired.

6. For Show, select Outlines in the drop down menu.

7. Check the Display results box

8. Check the Clear results box.

9. Check the Summarize box.

10. Click OK.
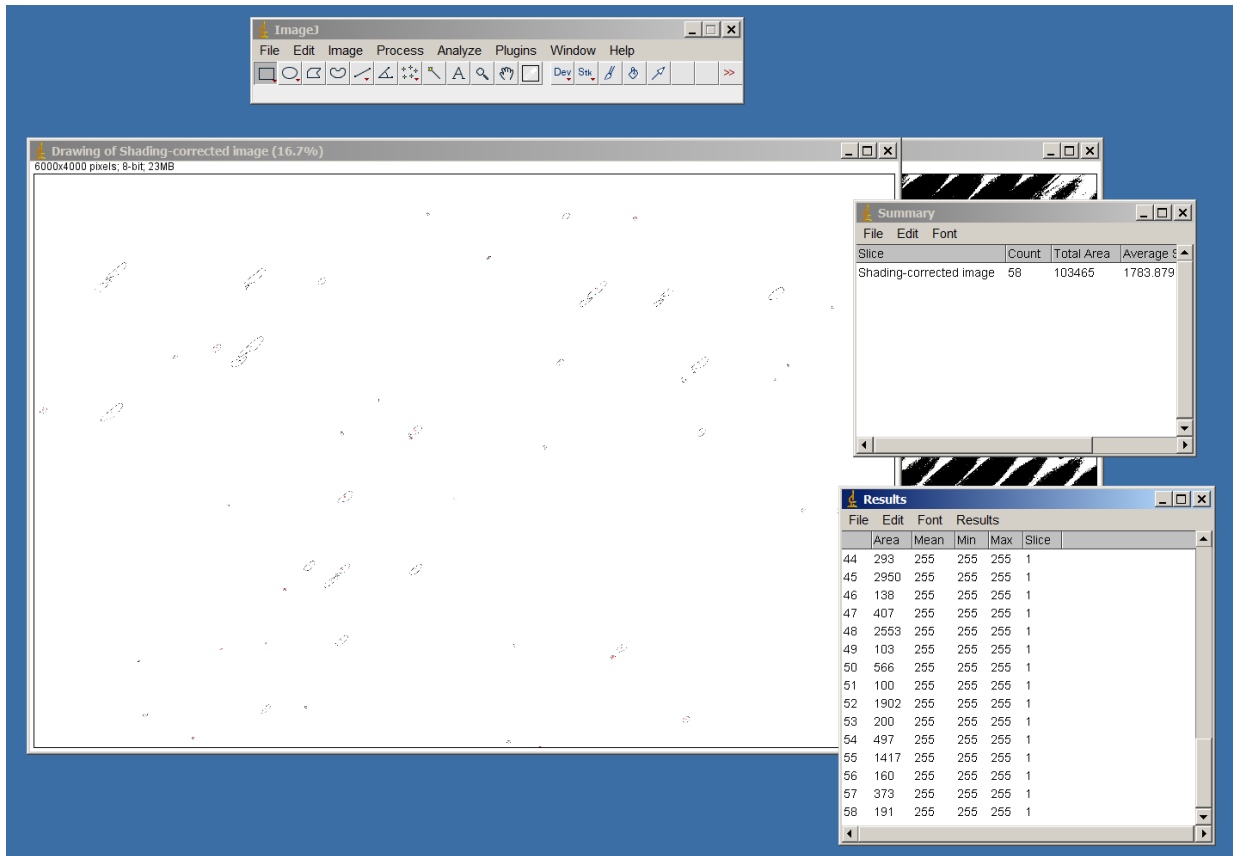
11. Save Summary.

12. Save Results.

13. Save Outline Image for further analysis.

Create Macro
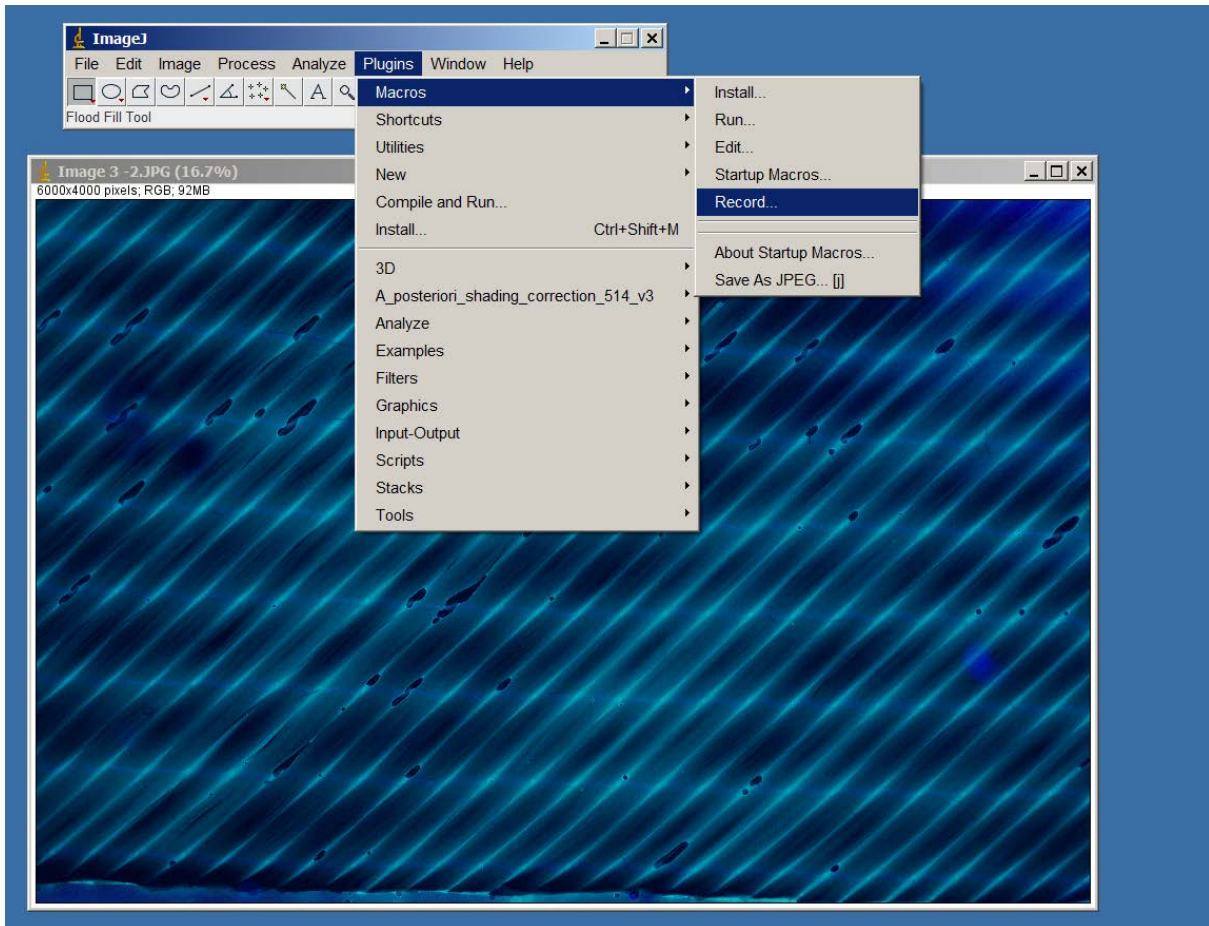
1. Select Plugins Menu.

2. Click on Macros.

3. Select Record.
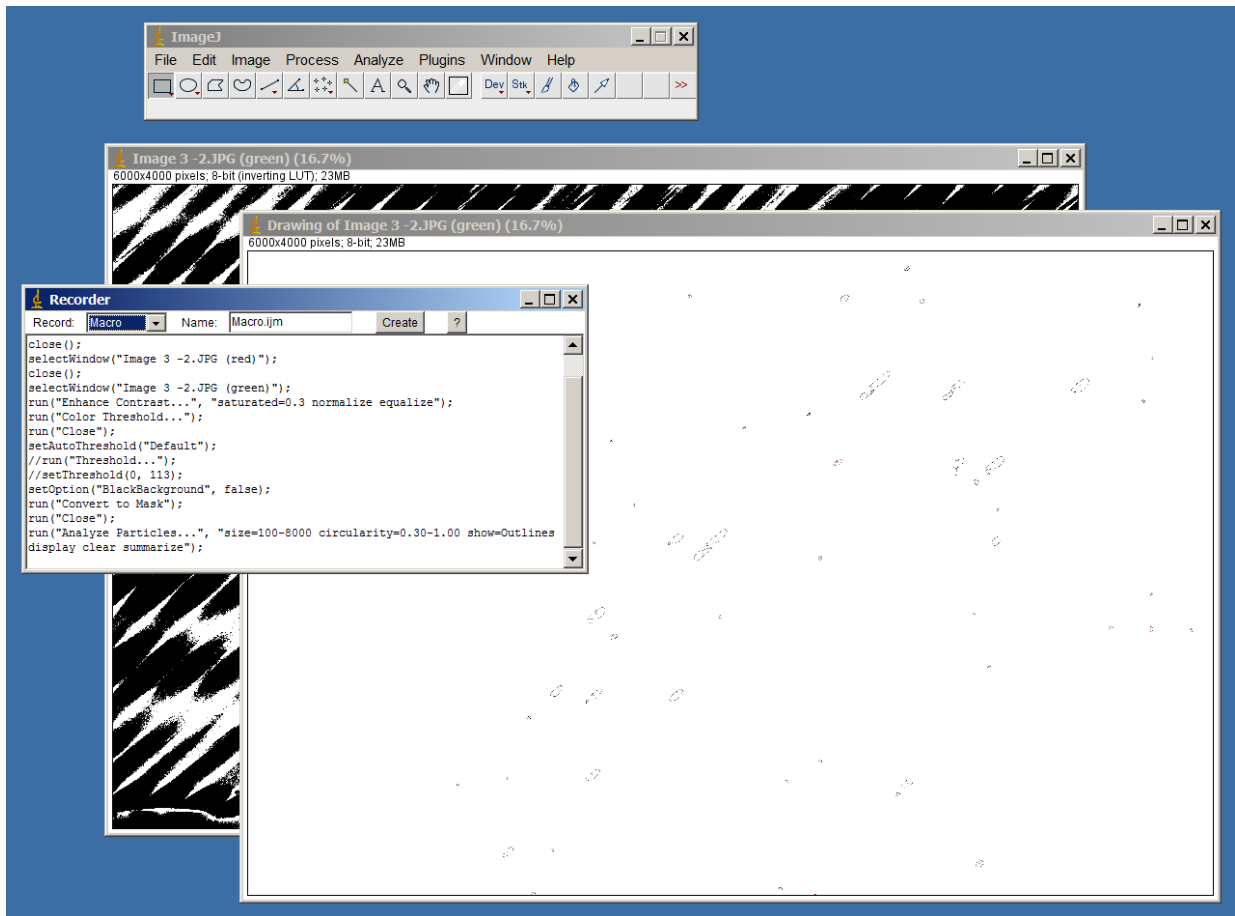
4. Proceed to process image step by step.

5. Recorder window will show the script for each step.
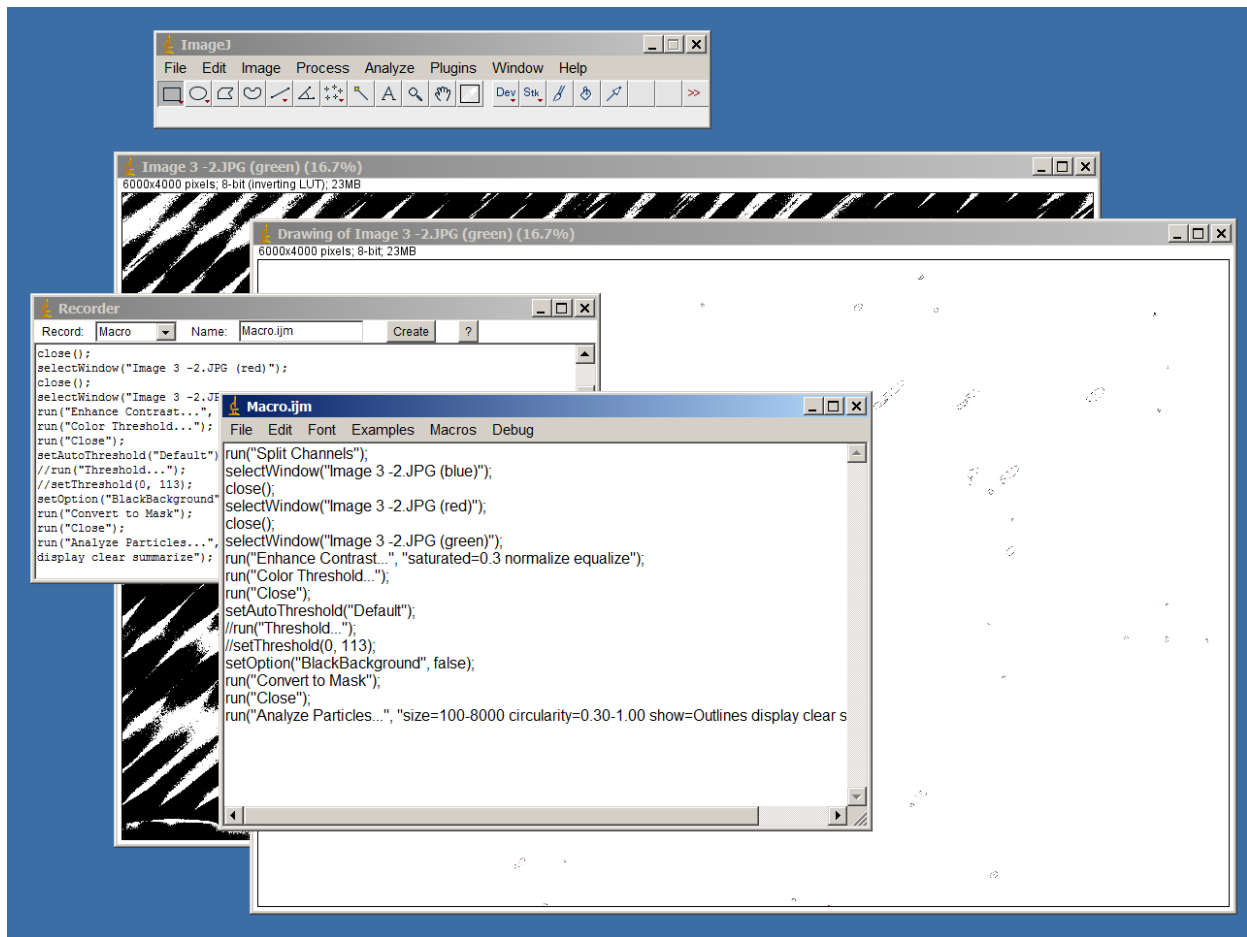
6. When all steps have been completed, click on the Create button in the Recorder window.

7. The final macro script will appear in a new window.
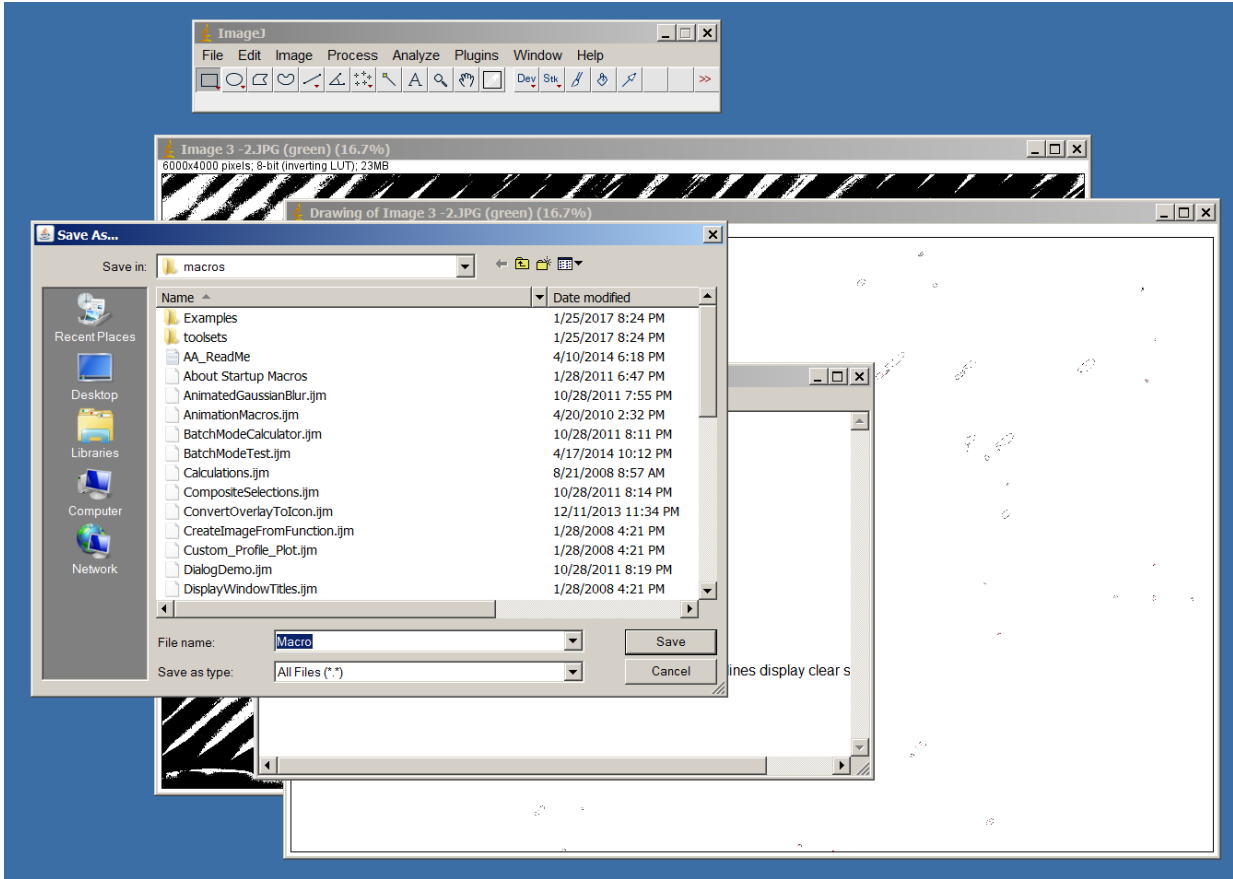
8. Using the final script window generated in Step 7, save the macro.

APPENDIX D. IMAGES OF *IN SITU* VOIDS FROM RTM EXPERIMENTS

Fiberglass with Virgin Test Fluid and Room Lighting
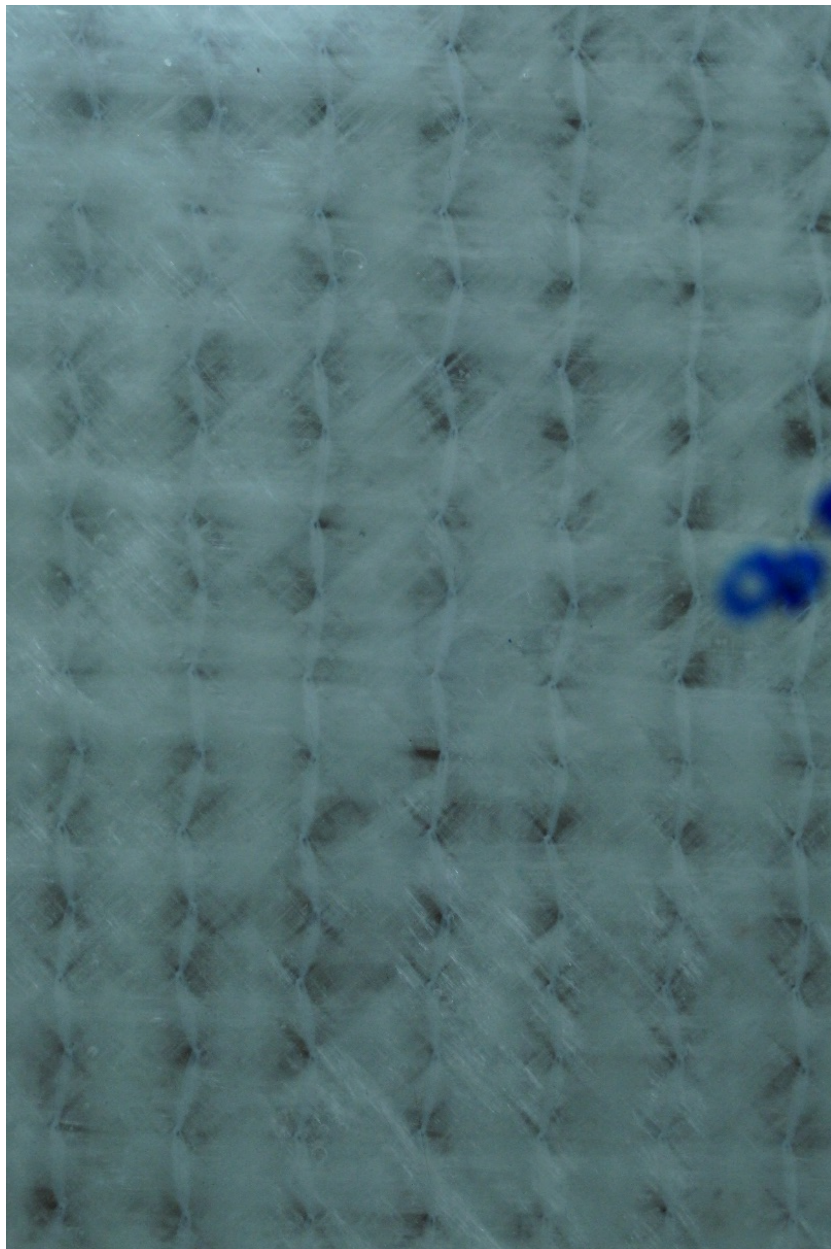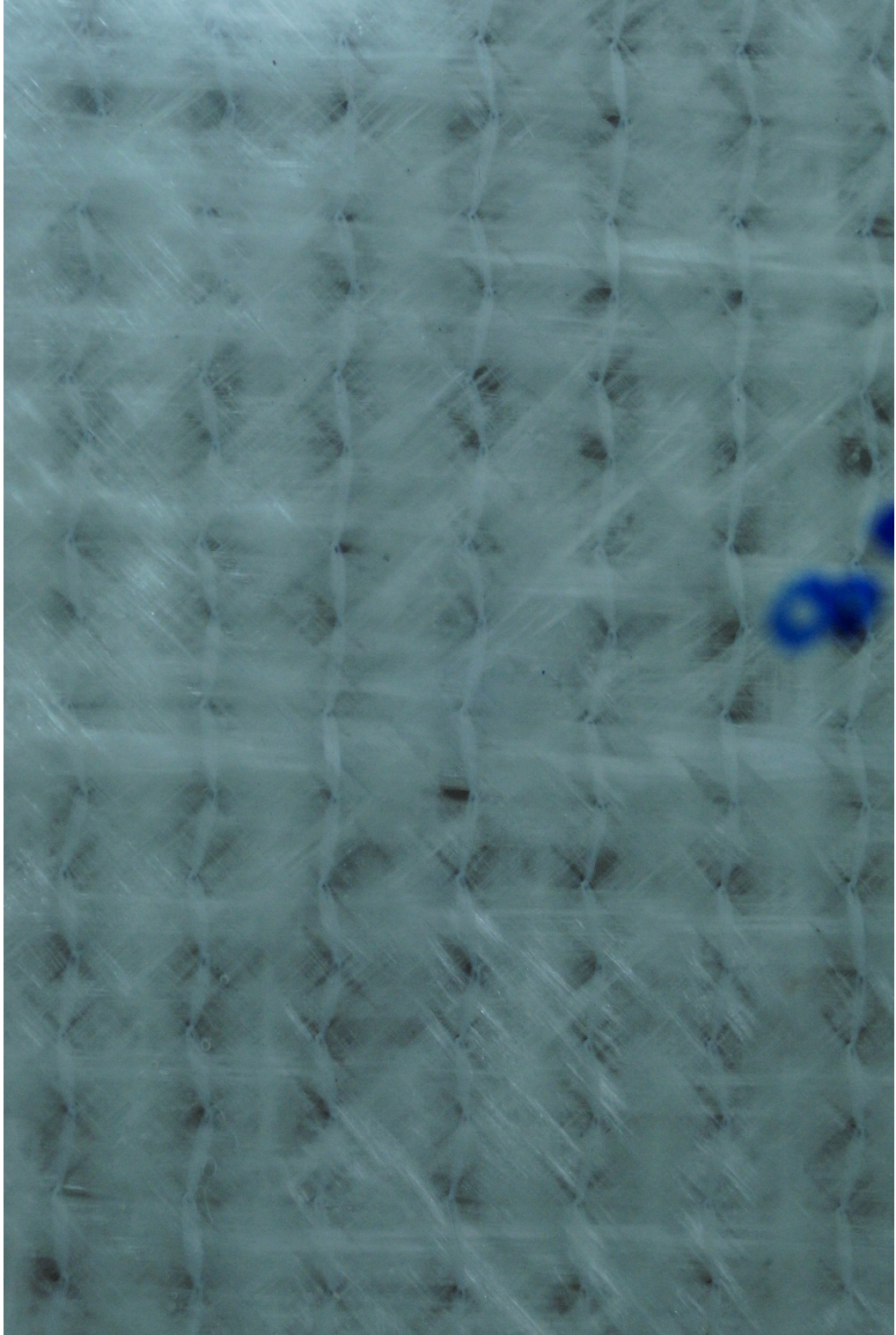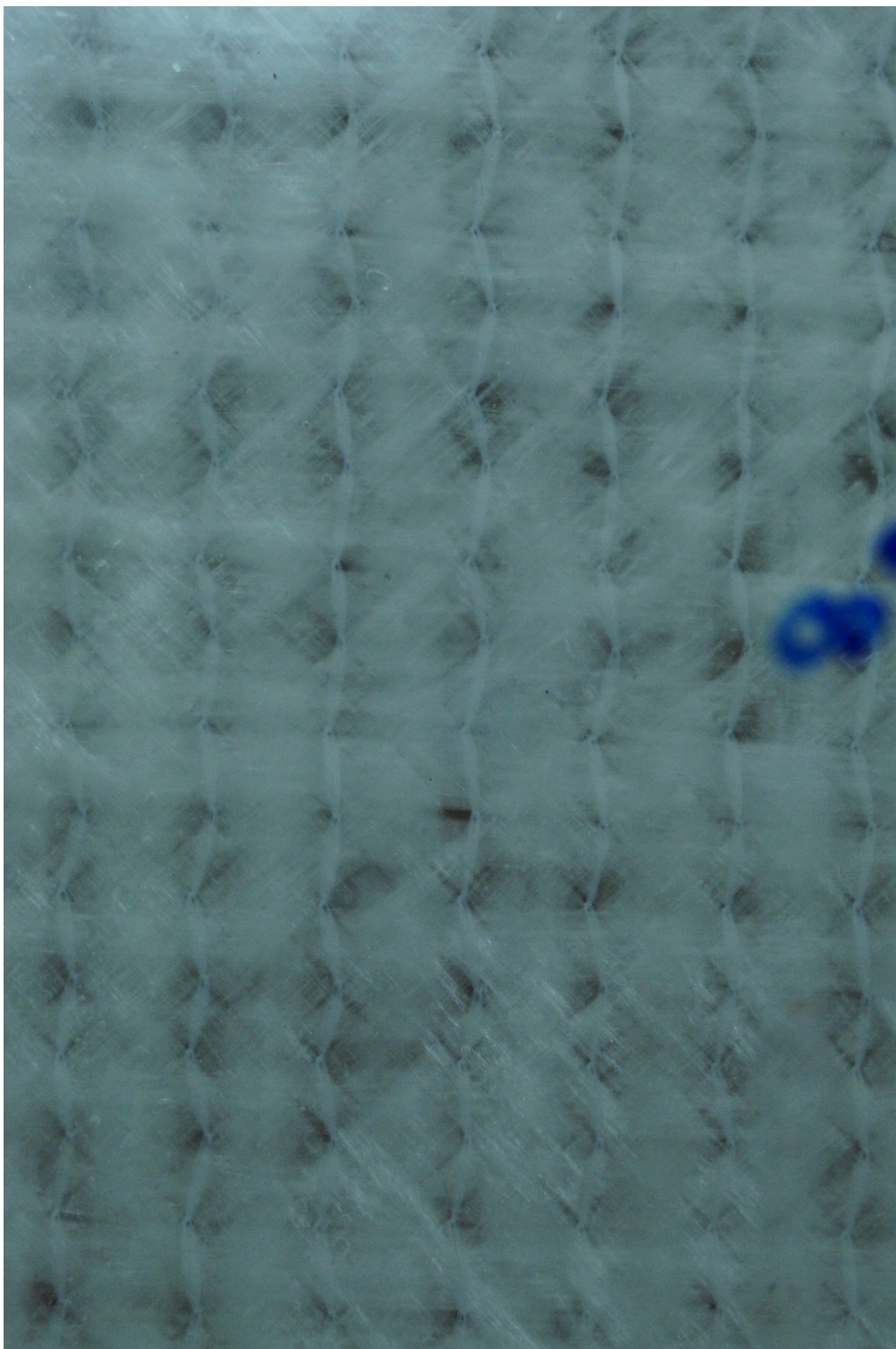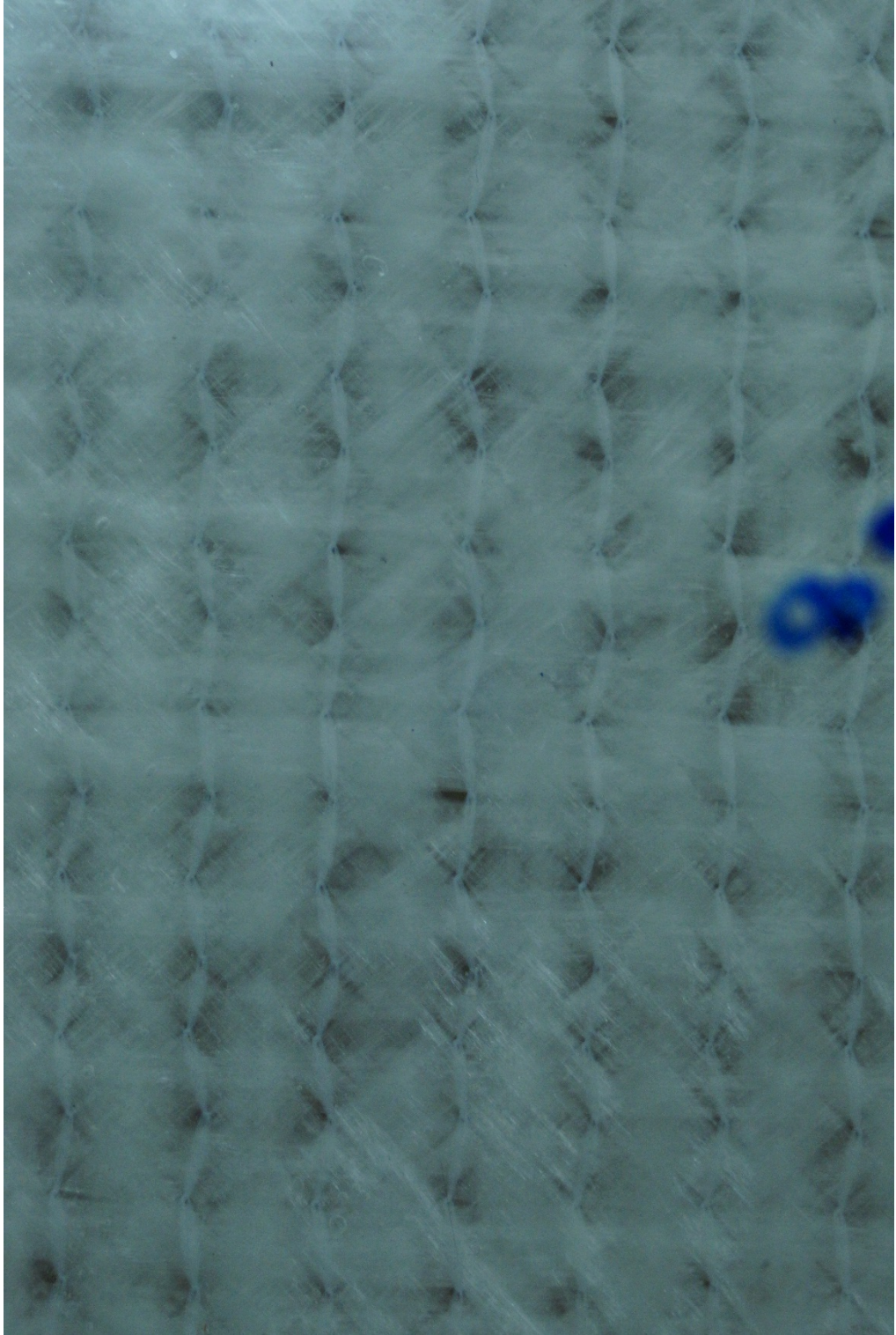
Fiberglass with Virgin Test Fluid and LED Lighting Beneath Tooling
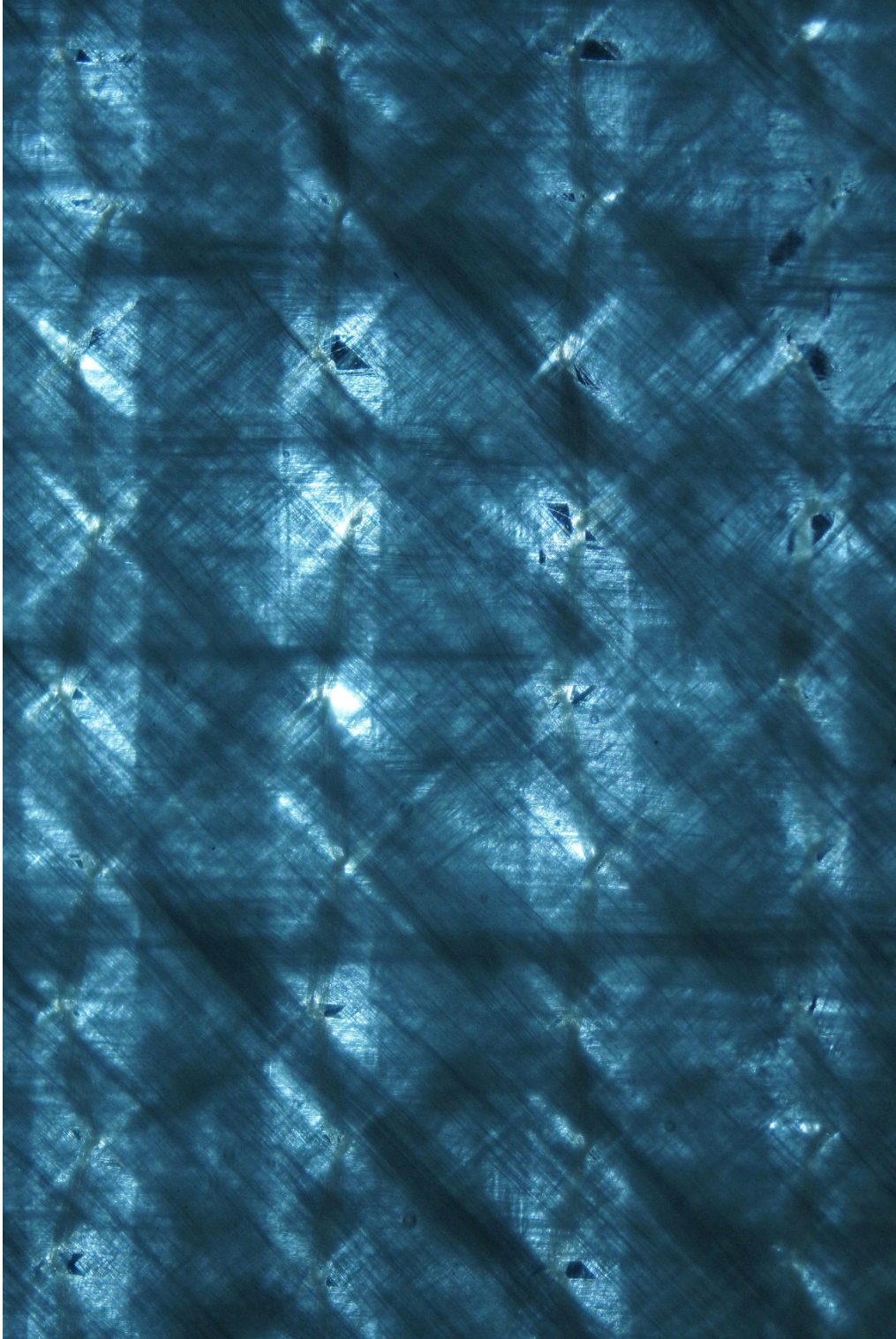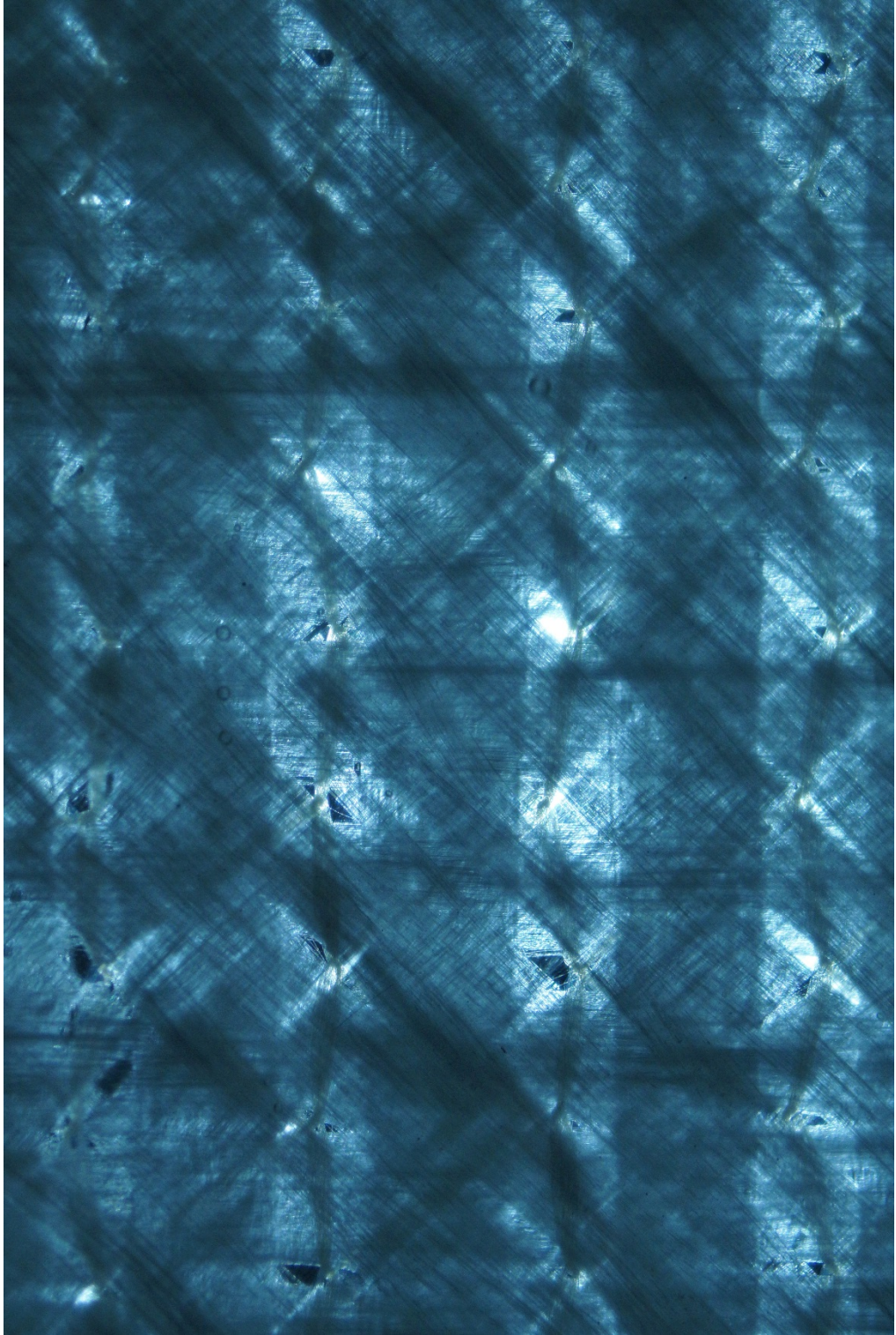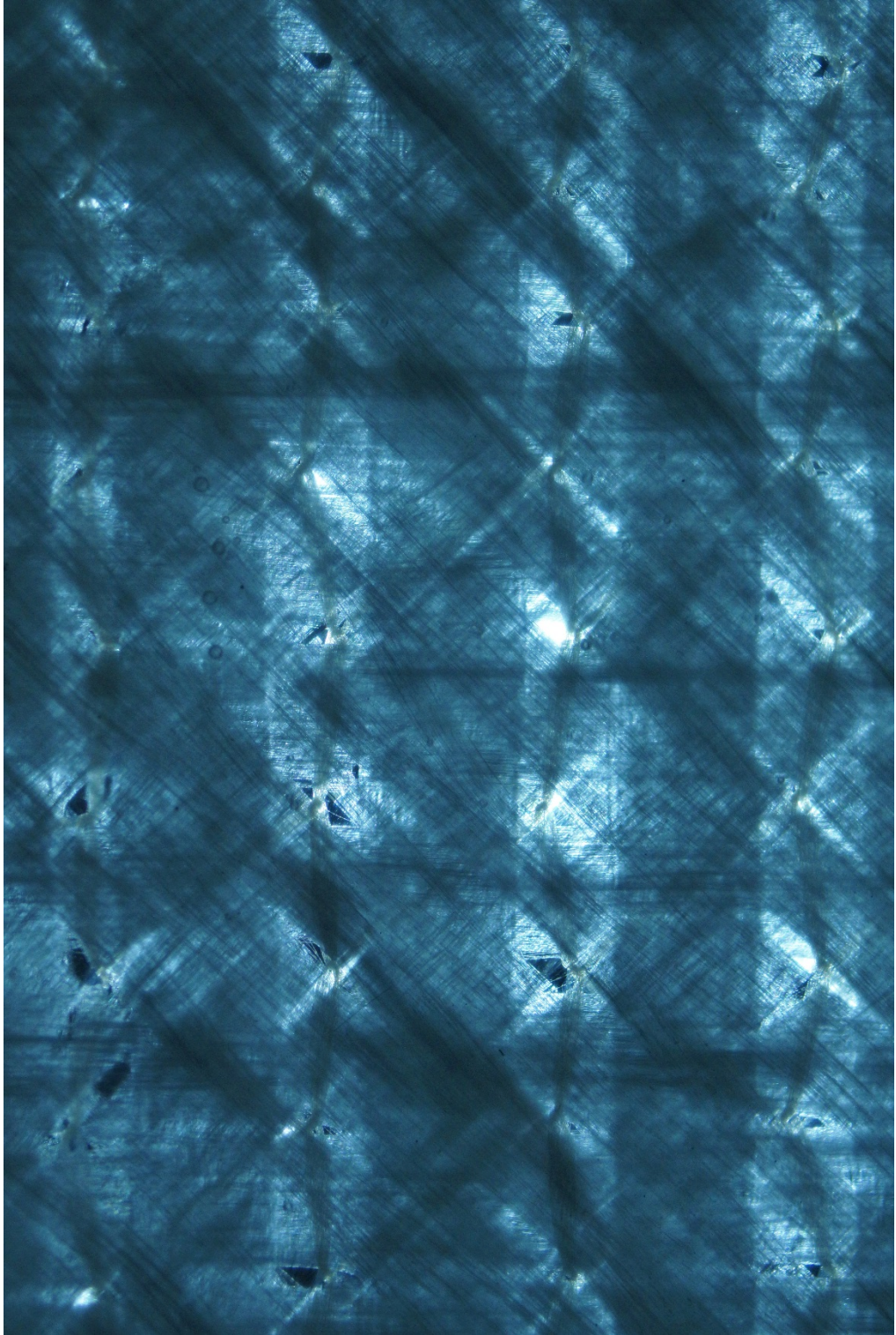
Fiberglass with Test Fluid/UV Dye Mix and Room Lighting

Fiberglass with Test Fluid/UV Dye Mix and UV Lighting
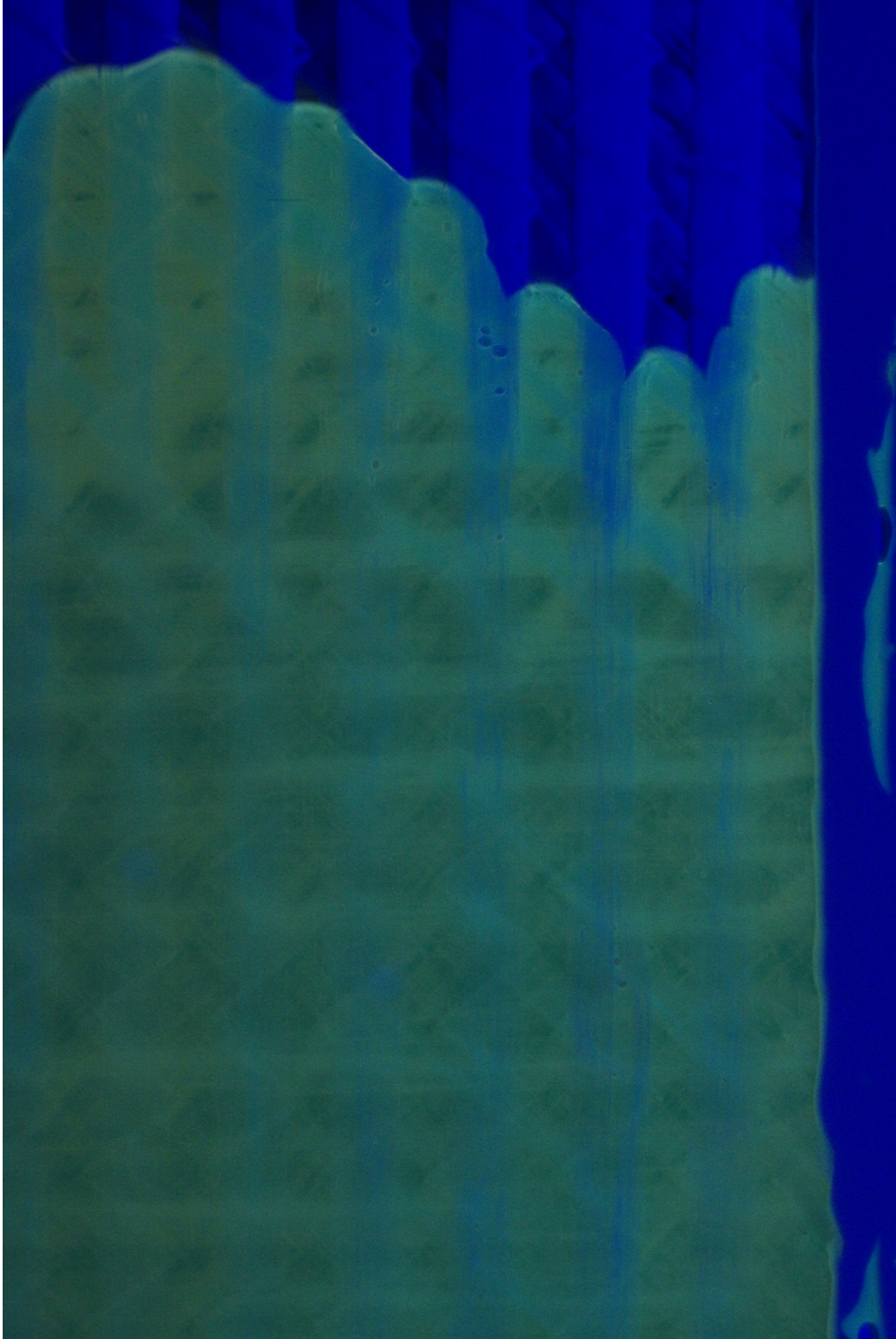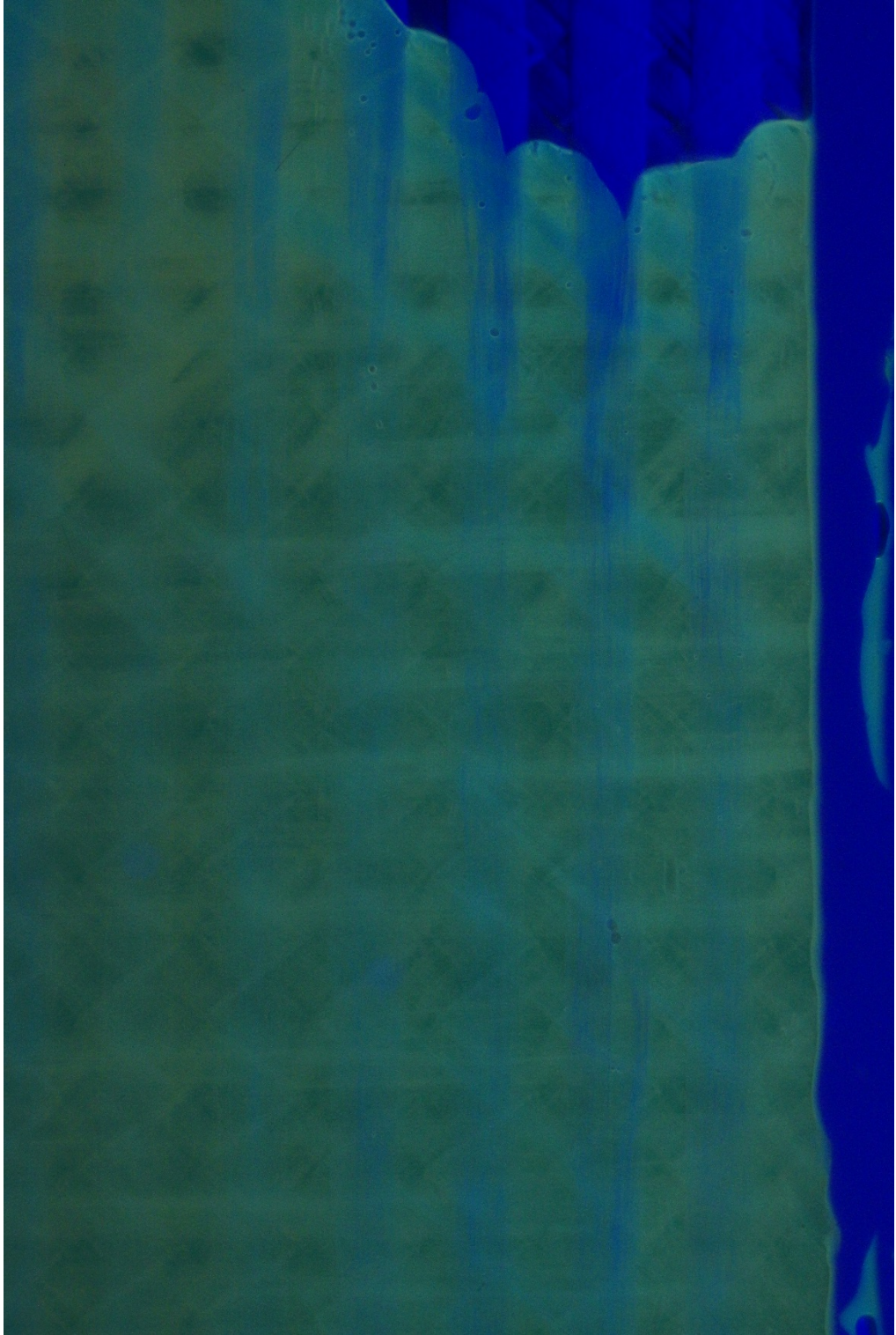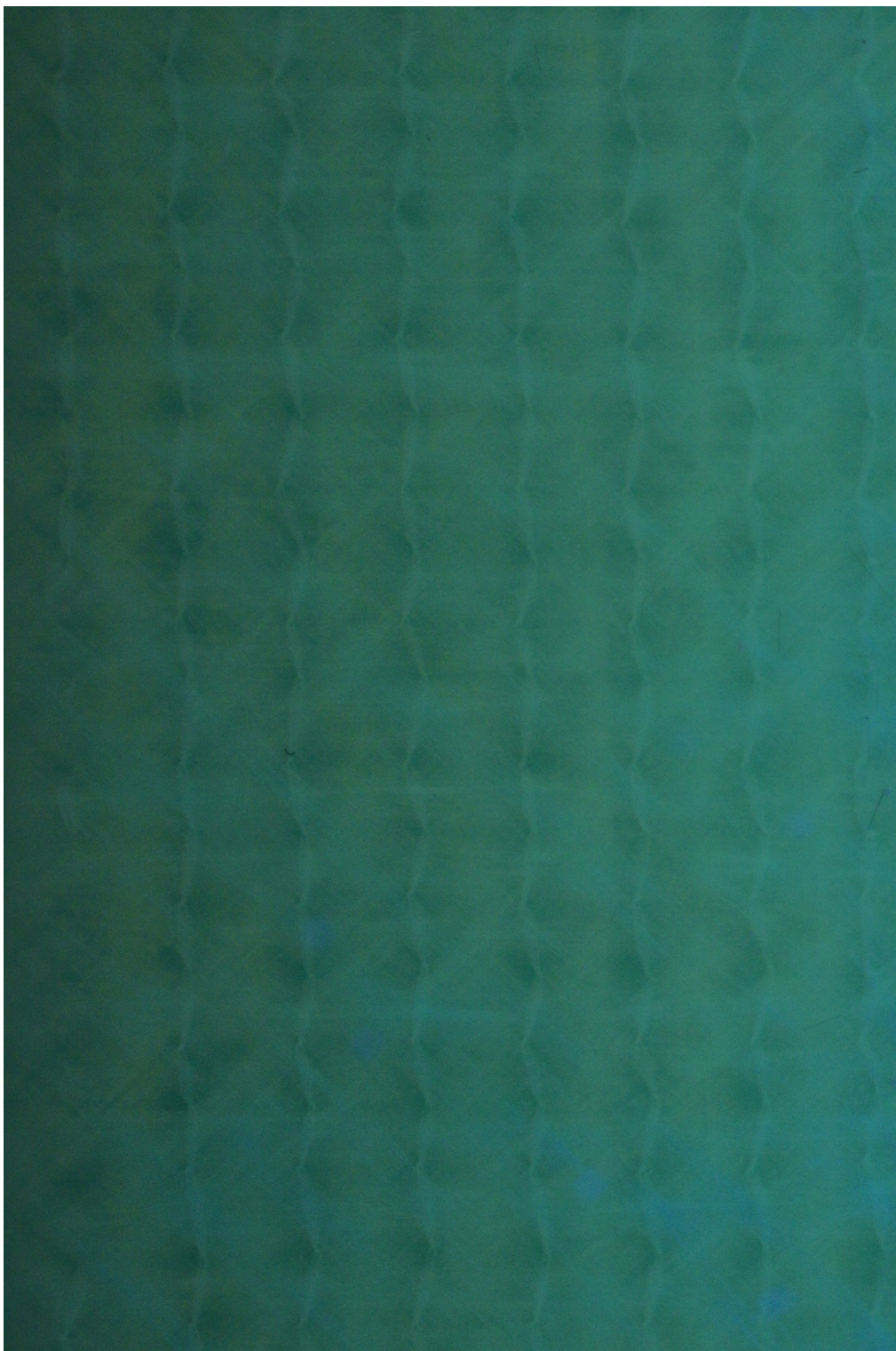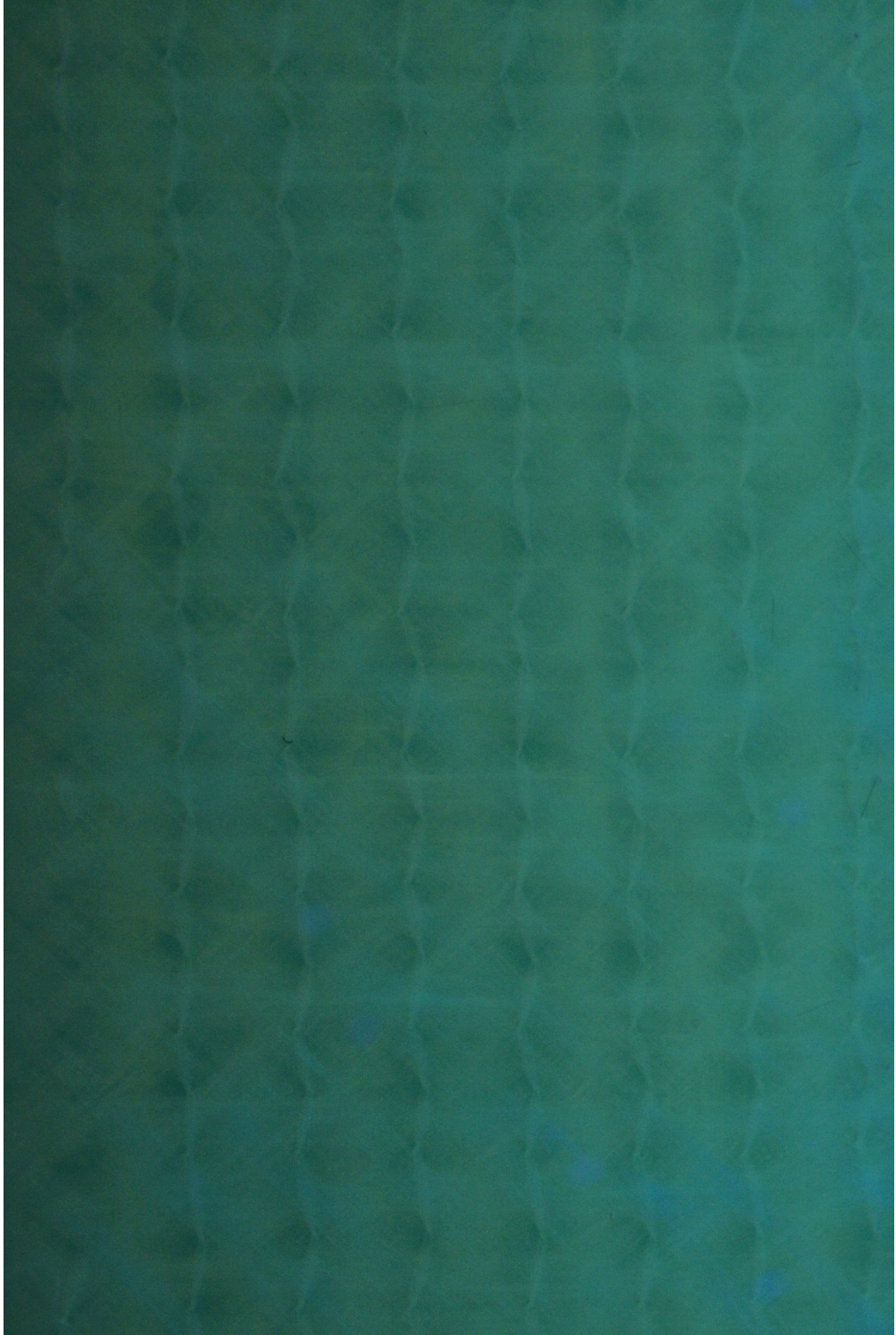
Carbon Fiber with Test Fluid/UV Dye Mix and UV Lighting

Hexcel Carbon Fiber
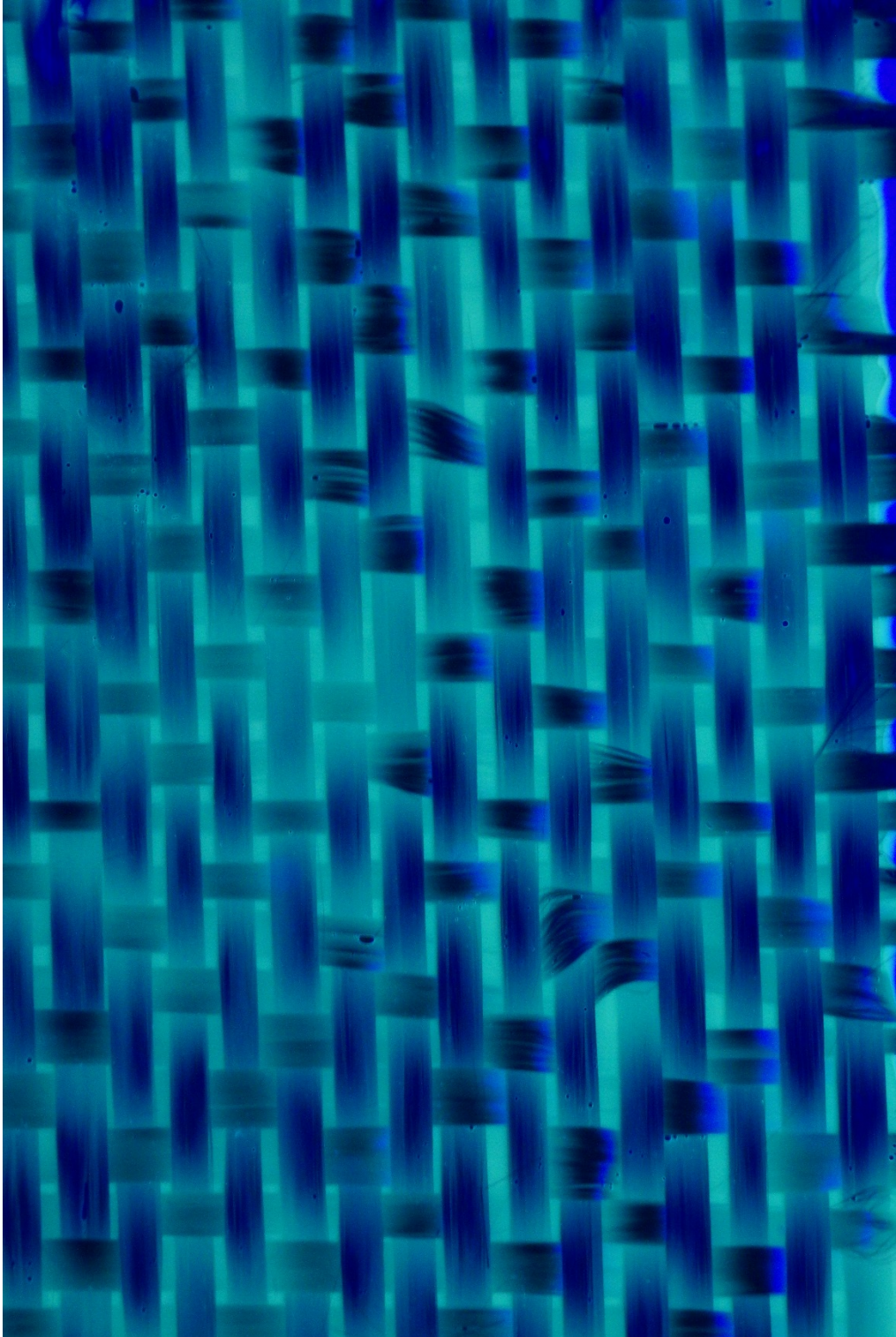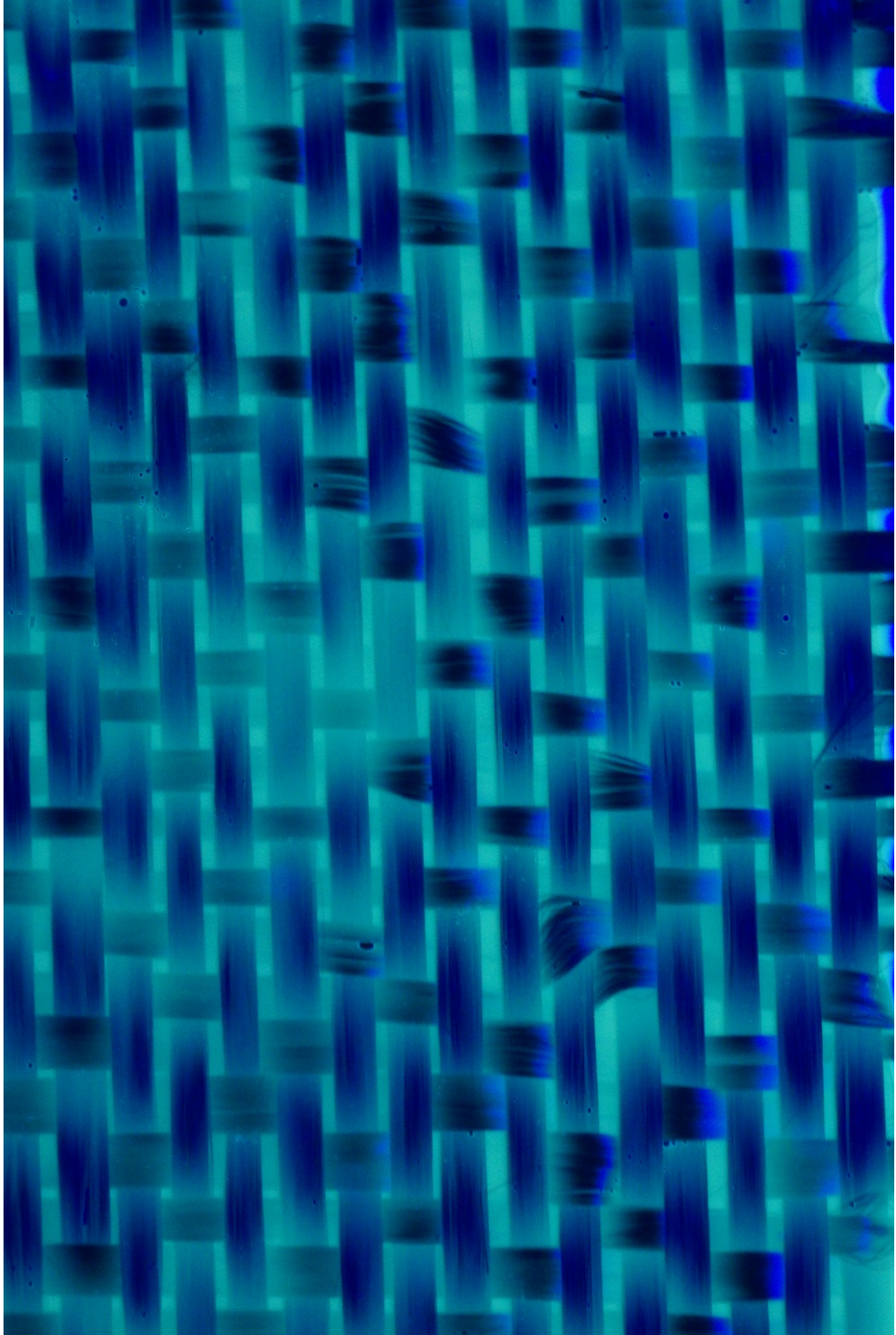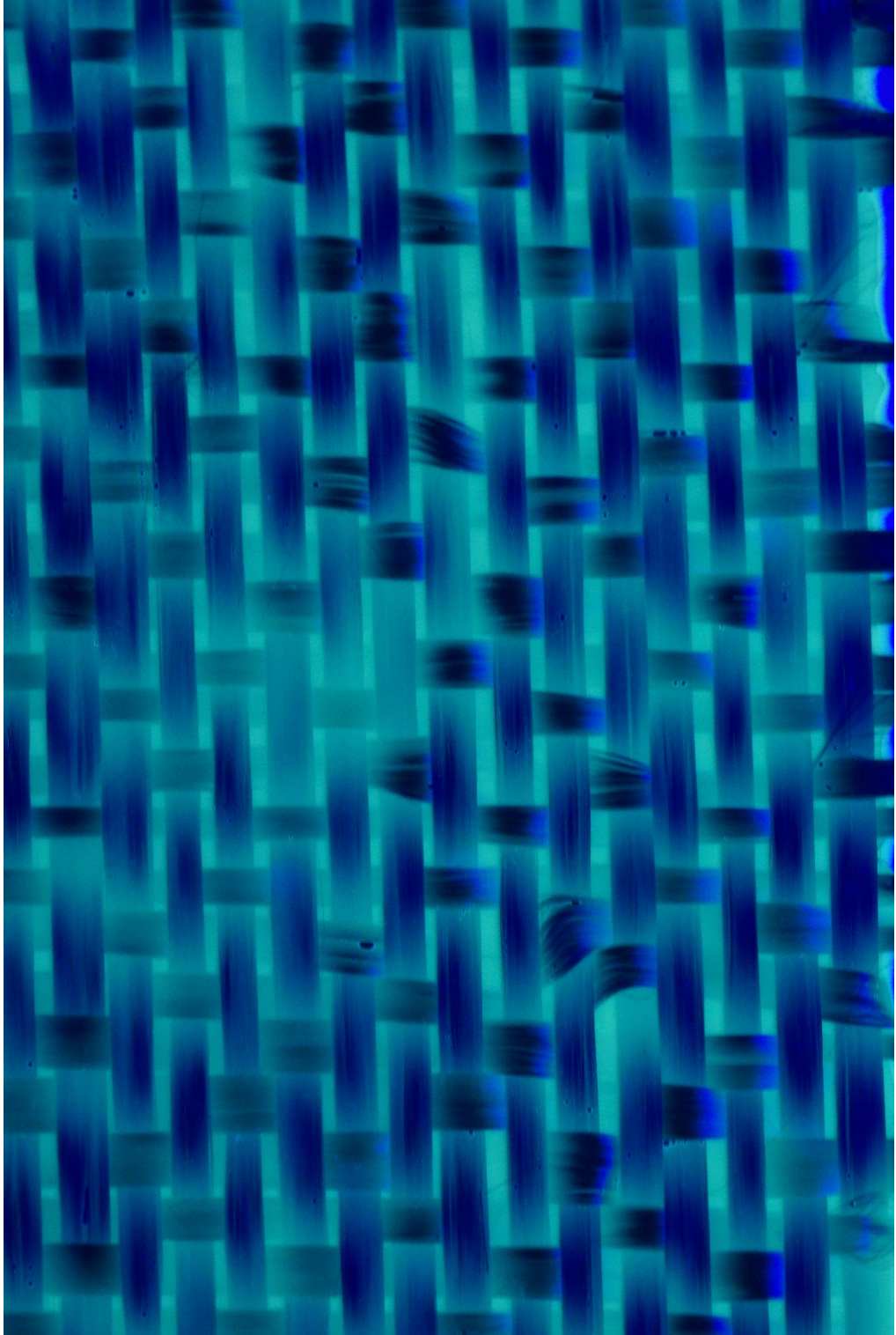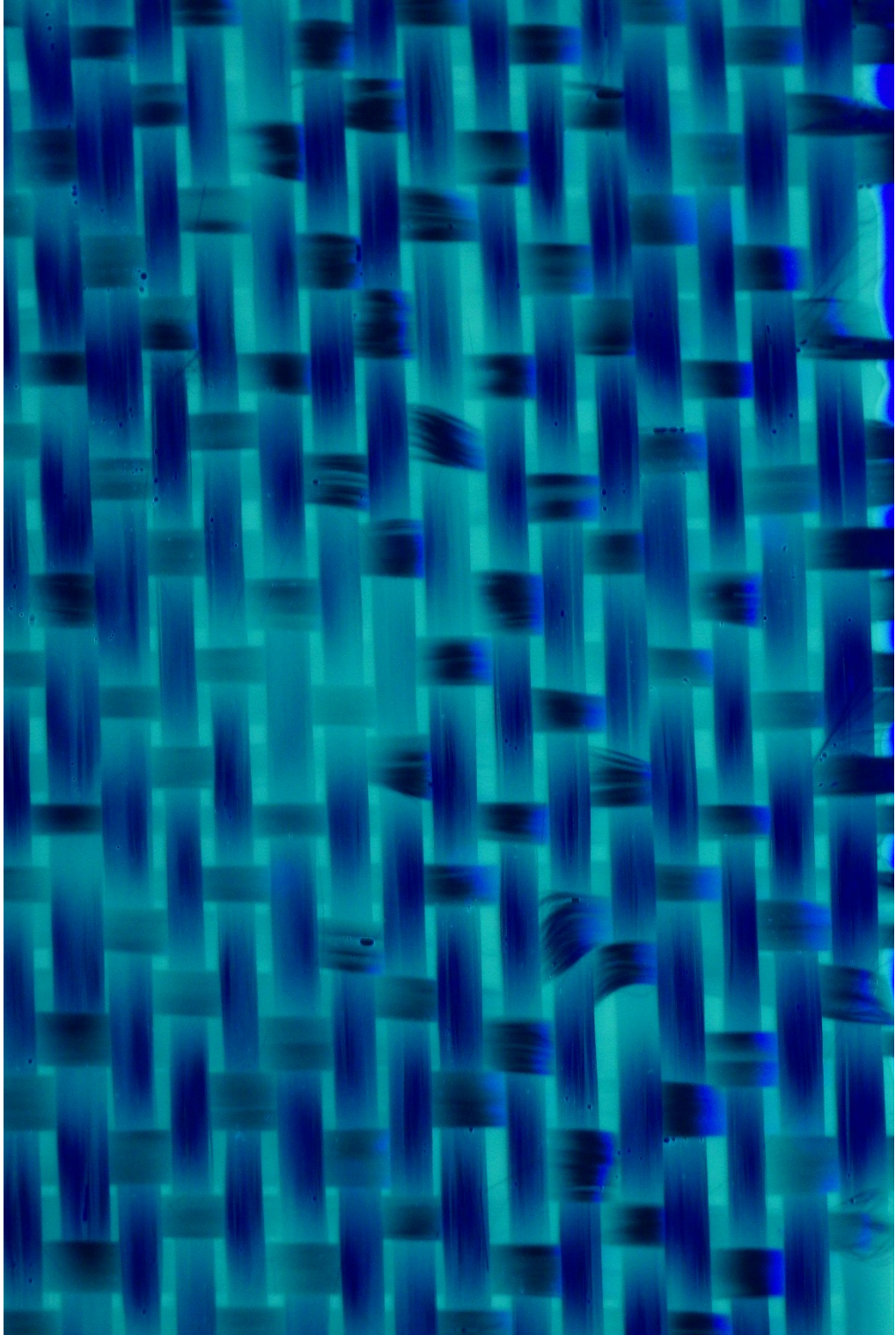
Vector Ply Carbon Fiber
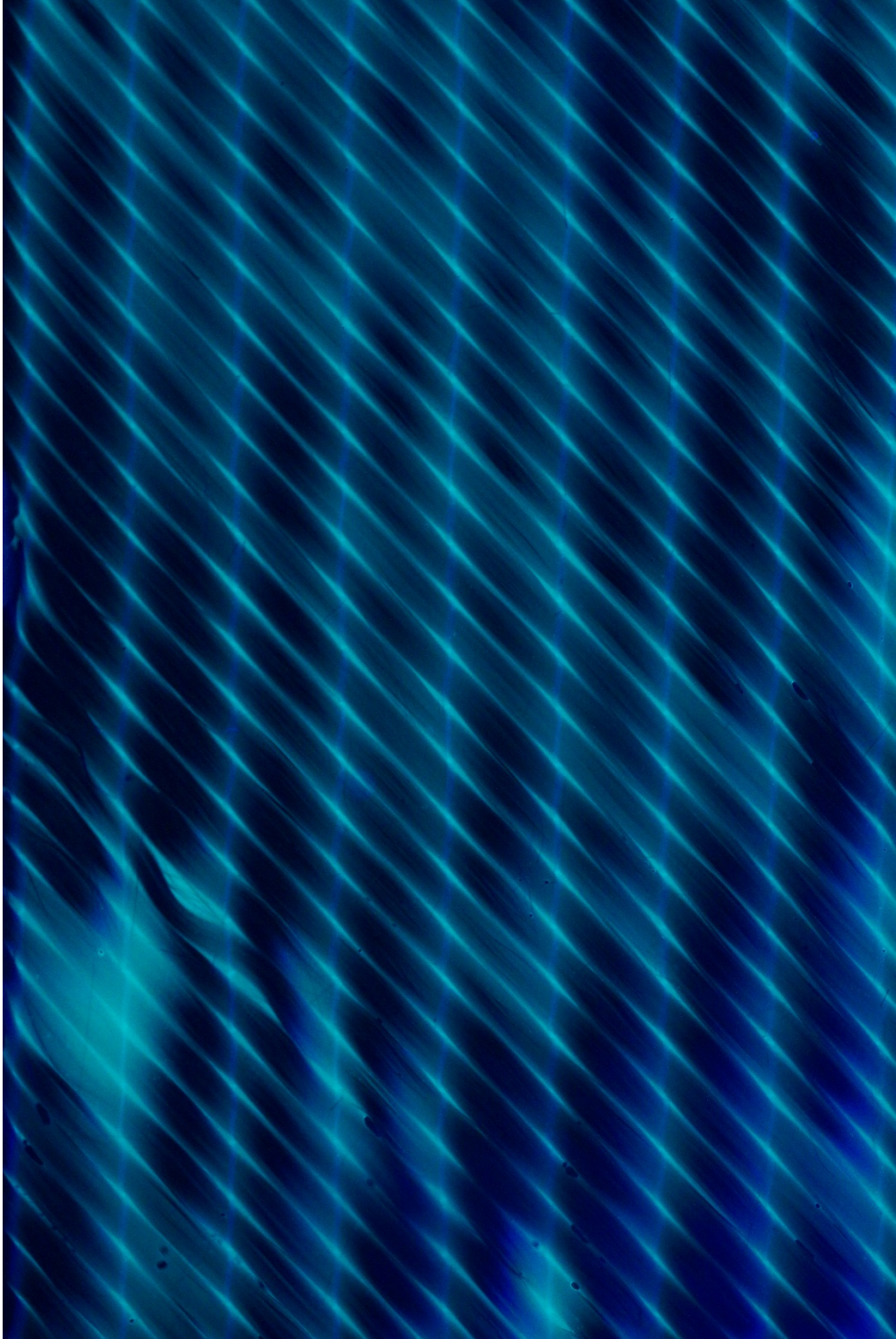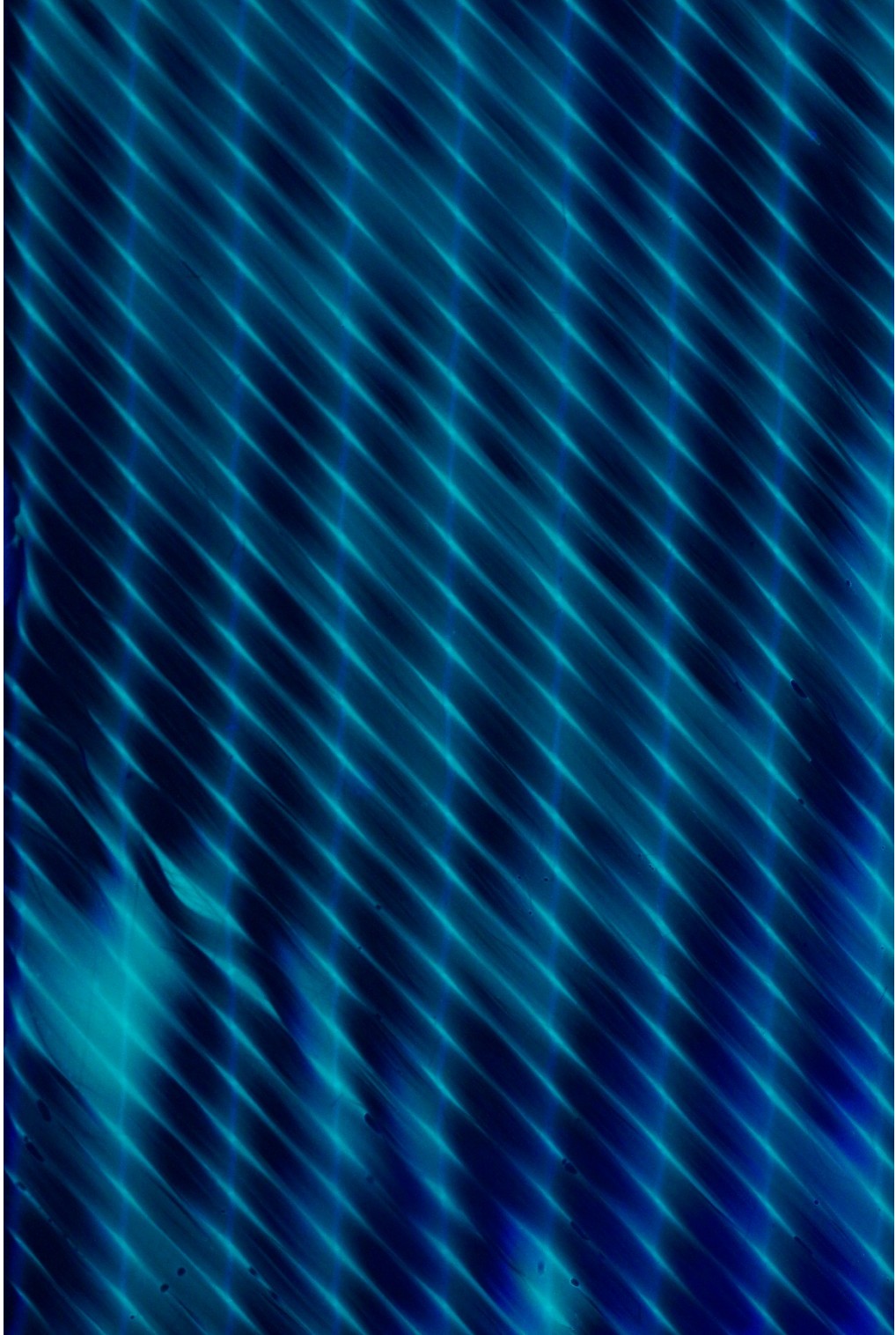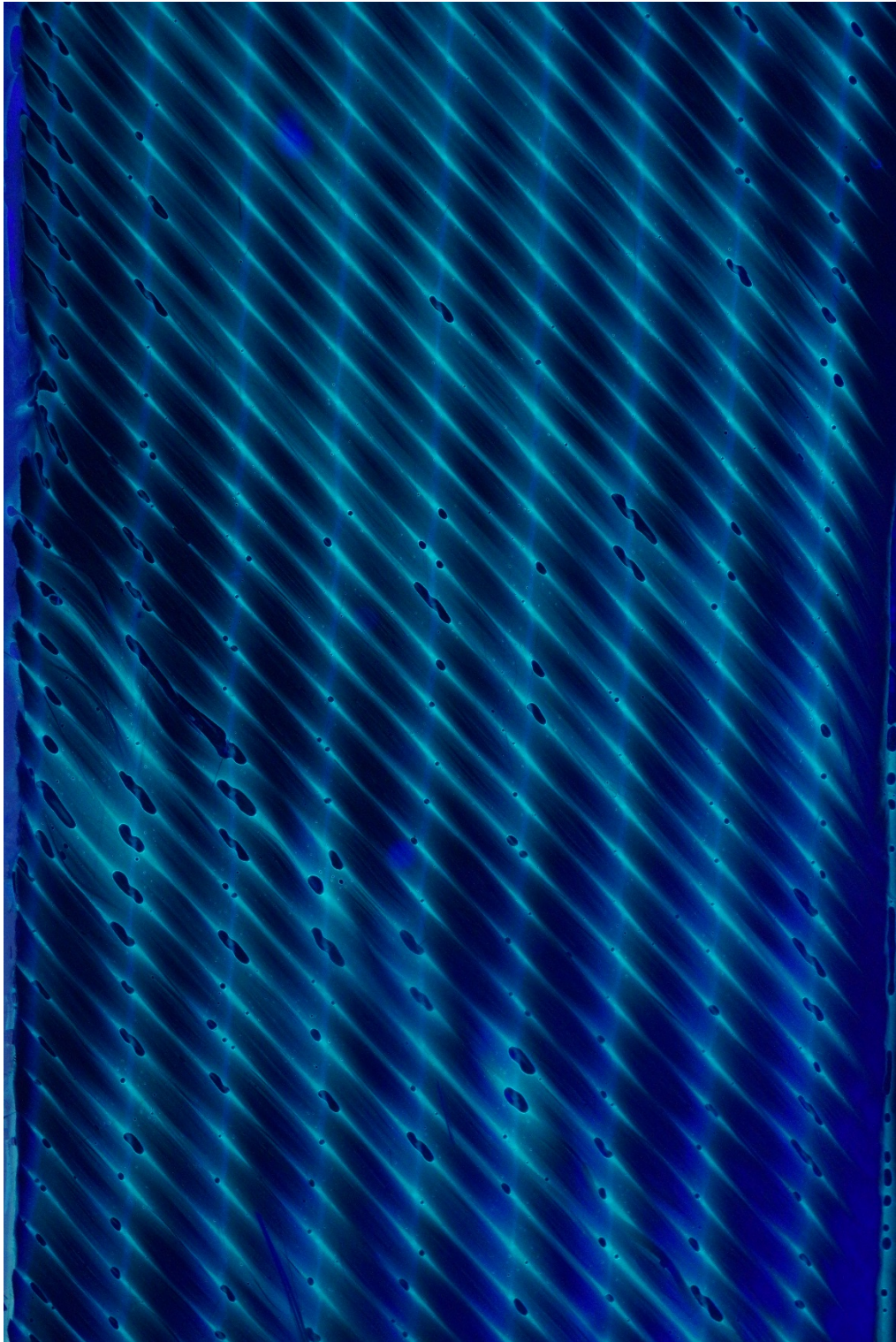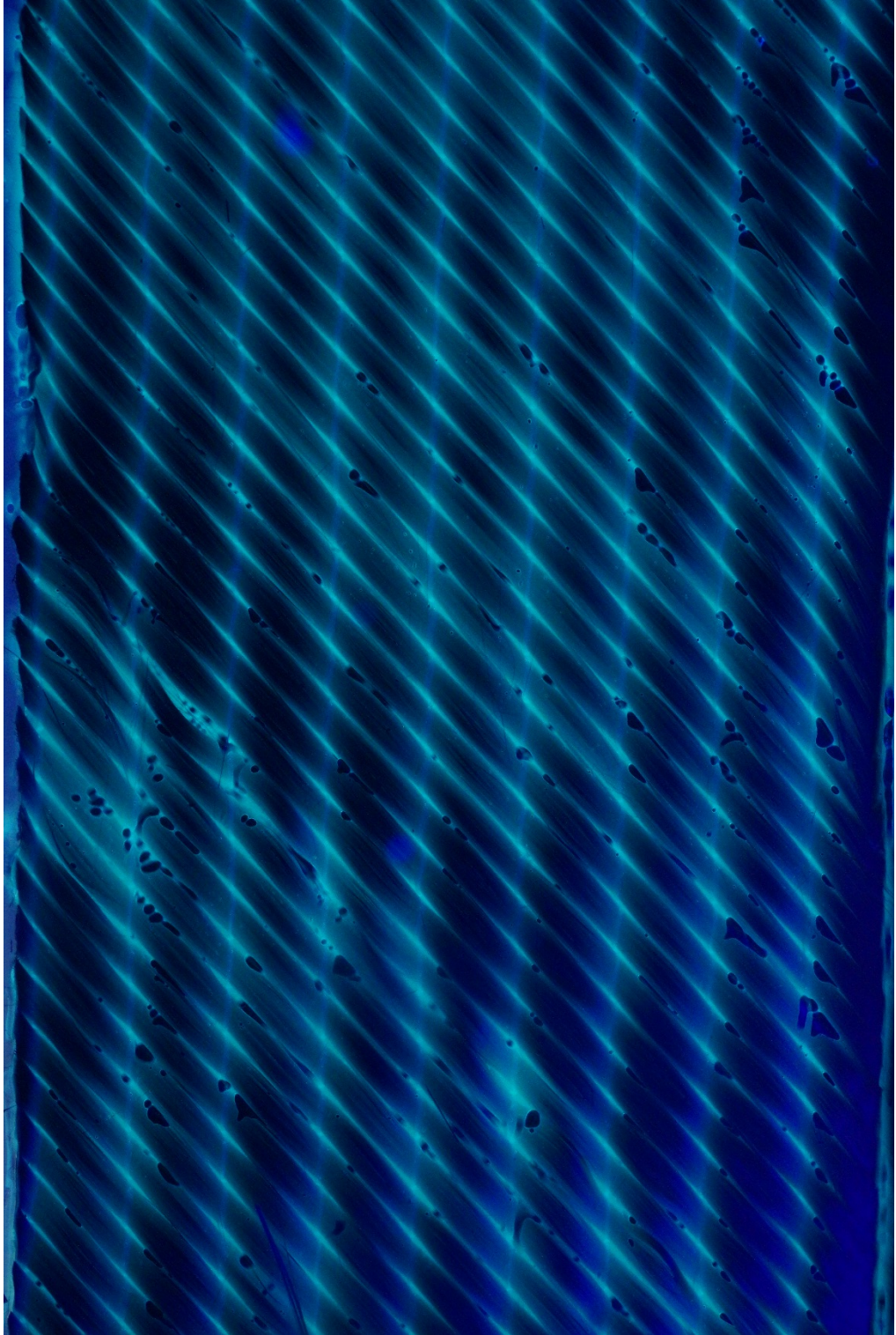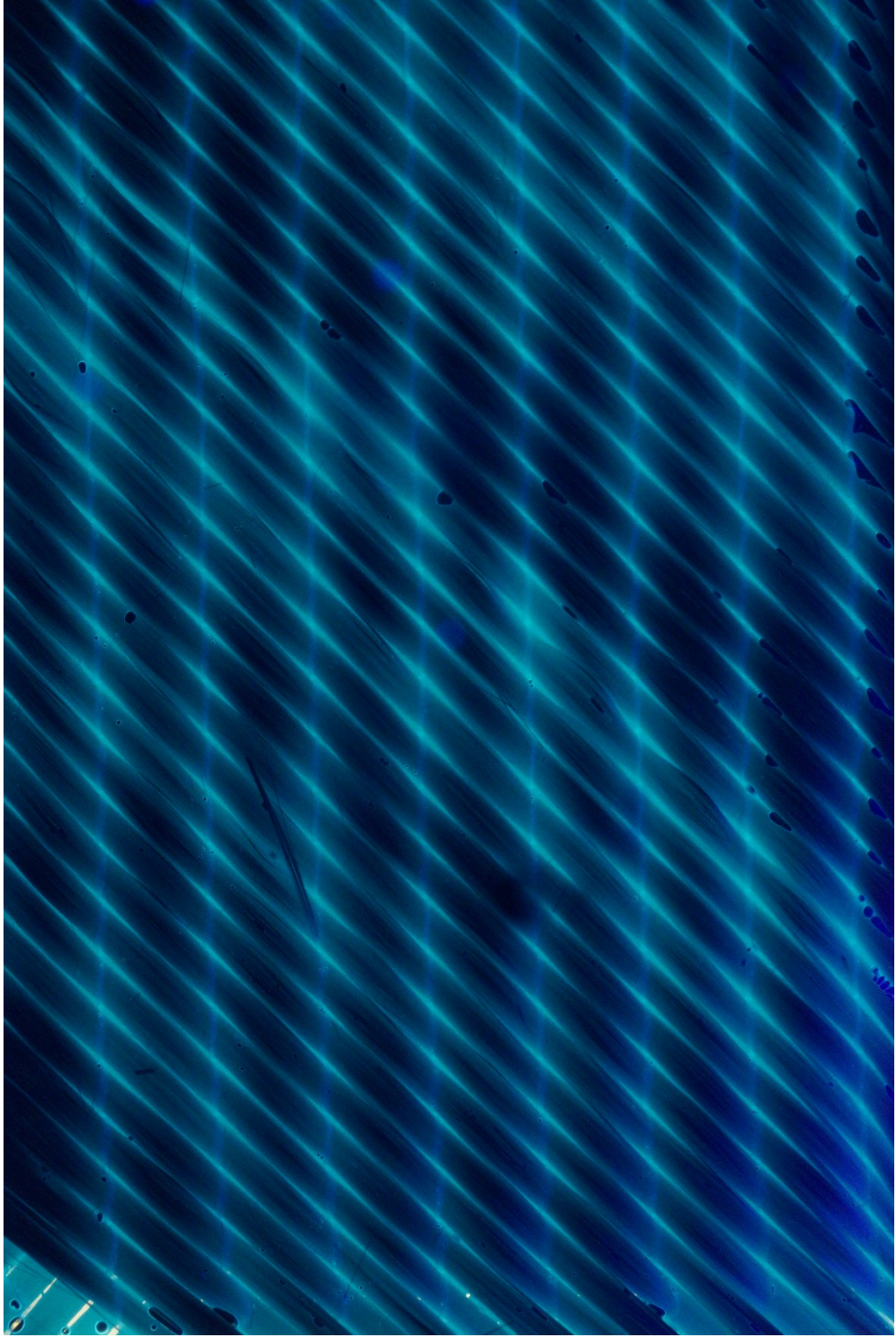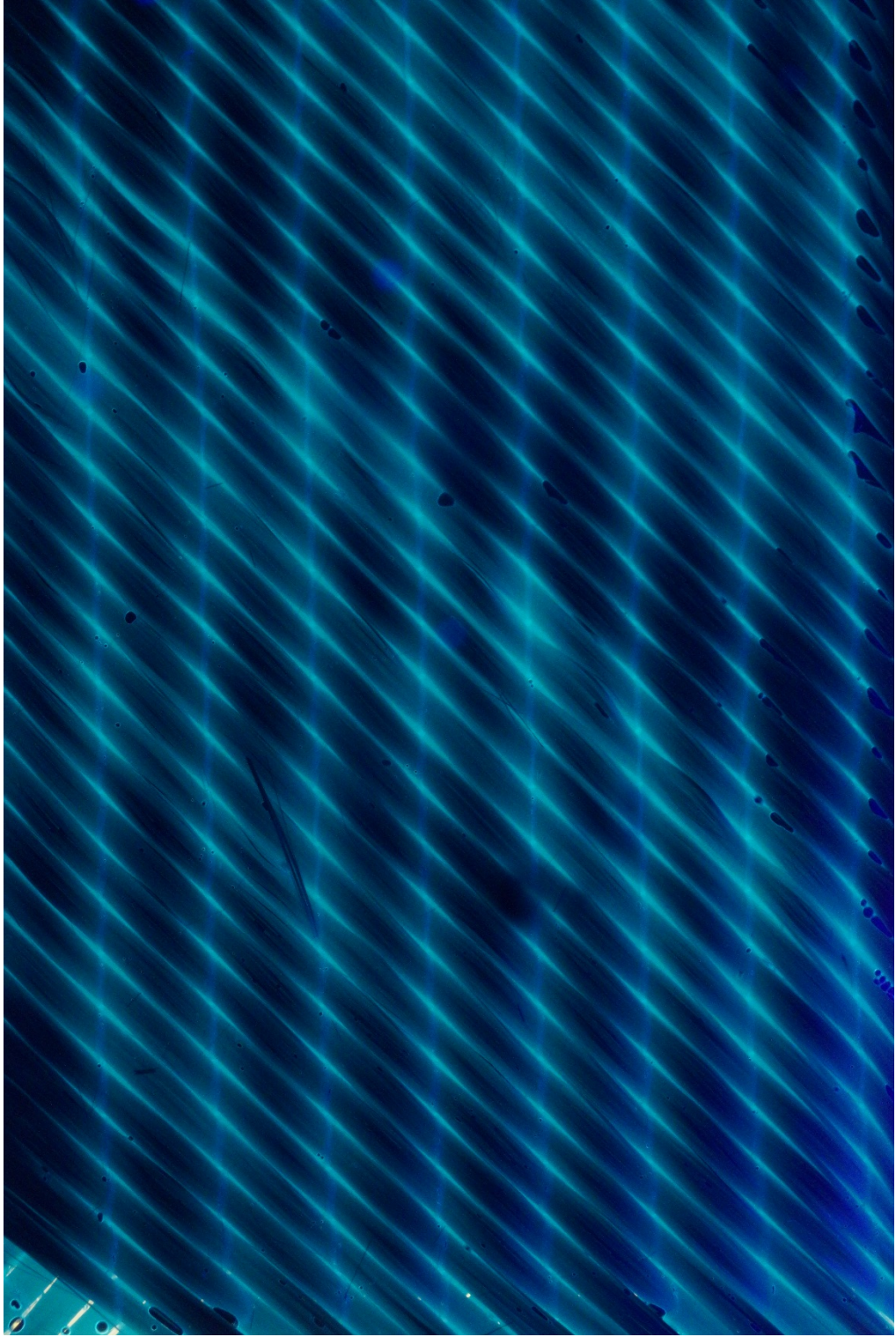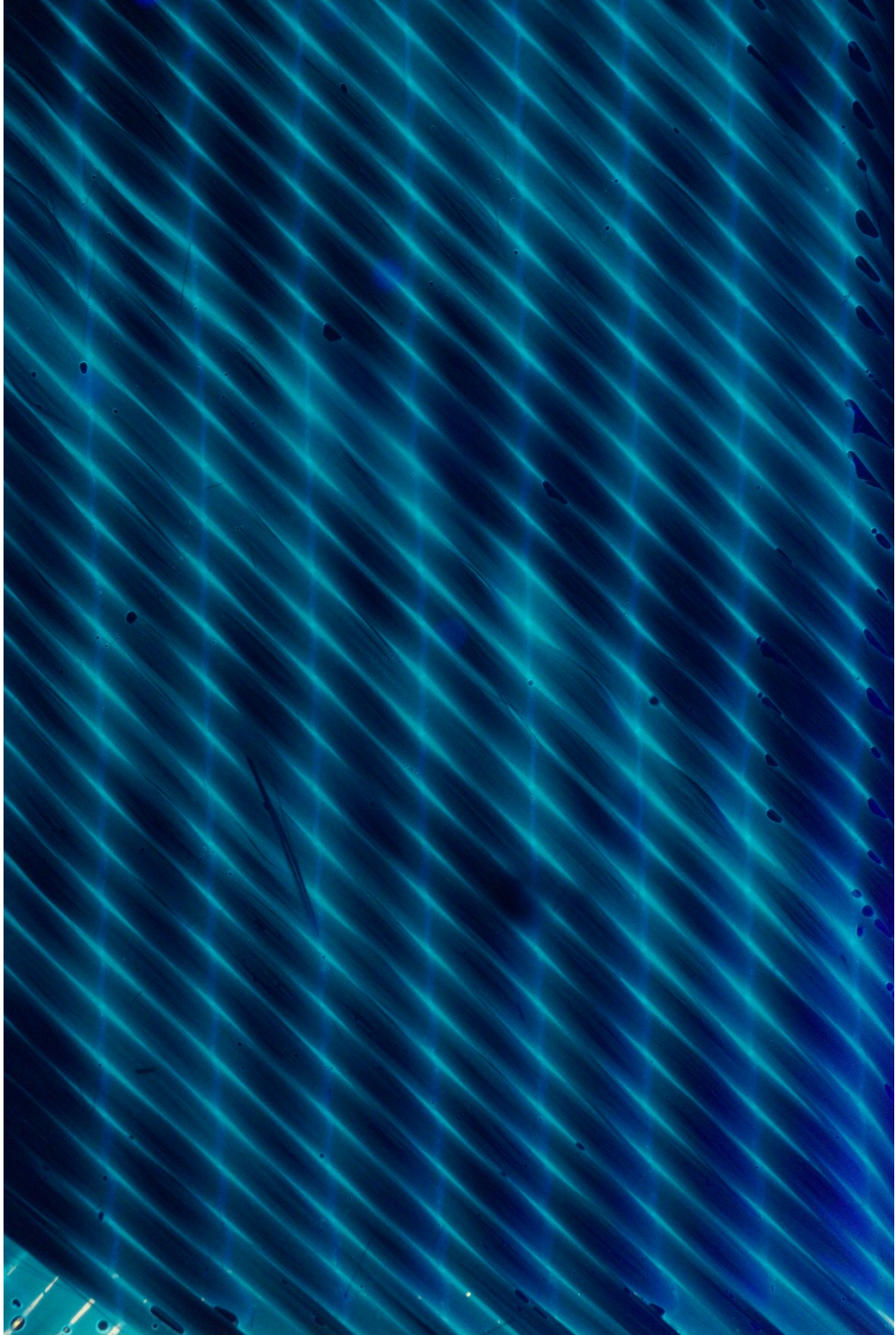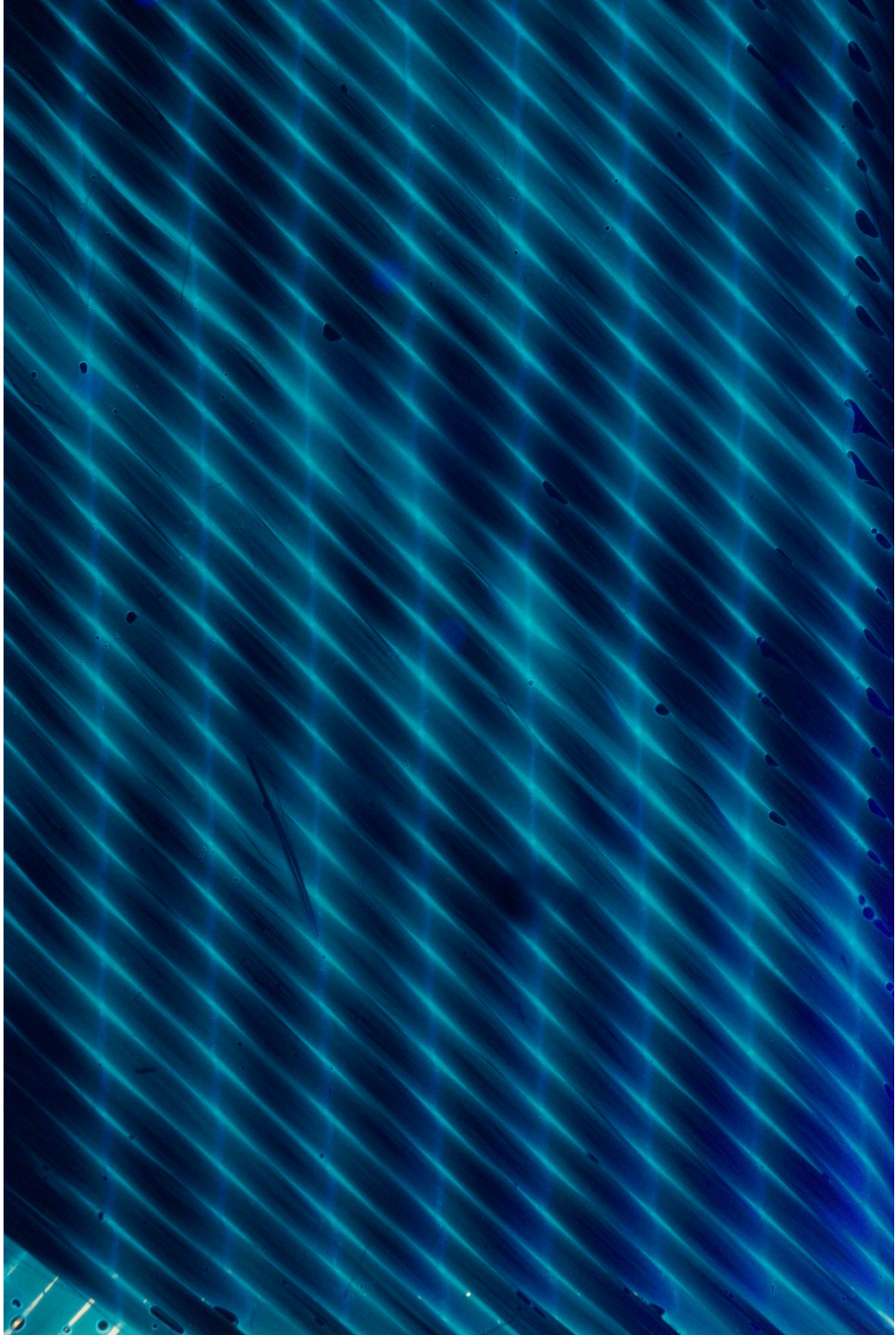
APPENDIX E.　　IMAGEJ SETTINGS AND DATA FROM RESEARCH

Image 1

Comparative Data from Different Analysis Settings

Image 1 Analysis Settings:													
Void	**1**	**2**	**3**	**4**	**5**	**6**	**7**	**8**	**9**	**10**	**11**	**12**	**13**
1	X	X				X	X	X	X	X	X	X	
2													
3		X	X		X								X
4													
5													
6	X					X	X		X	X			
7	X					X			X	X			
8	X					X	X		X	X			
9			X	X									X
10													
11		X	X	X	X		X	X			X	X	X
12													
13	X	X				X	X	X	X	X	X		
14	X	X		X	X	X	X		X	X	X	X	X
15	X	X	X	X	X		X	X	X	X	X	X	X
16		X	X	X	X	X	X	X	X	X	X	X	
17		X		X	X				X	X	X	X	X
19	X	X	X	X	X	X	X	X	X	X	X	X	X
20		X	X	X	X		X	X			X	X	X
21													
22	X	X	X	X	X	X			X				
23													
24			X	X	X	X		X			X	X	X
25	X	X	X	X	X	X	X	X	X	X	X	X	X
26					X								
27			X	X									X
28		X	X	X								X	X
29													
30			X	X	X								
31			X		X								
32													
33	X	X				X	X	X	X	X	X	X	X
34		X						X	X	X	X	X	X
35	X					X	X		X	X			
36	X	X	X	X	X		X	X			X	X	X
37			X	X	X								
38	X					X			X	X			
39		X	X	X	X		X	X		X	X	X	X
40		X	X	X	X		X	X	X		X	X	X
41					X								
42													
43	X	X	X	X	X	X	X	X	X	X	X	X	X
44			X	X	X	X	X	X	X	X	X	X	
45	X	X	X		X		X	X			X	X	X
46			X										
47		X											
48													
49	X	X	X	X	X	X	X	X	X	X	X	X	X
50													X

	1	2	3	4	5	6	7	8	9	10	11	12	13
51													
52													
53													
54			X	X	X							X	X
55		X	X		X			X			X	X	X
56		X	X	X			X	X	X		X	X	X
57													
58			X		X								
59													
60			X		X								X
61		X	X	X	X	X	X	X	X	X	X	X	X
62			X	X	X	X	X	X	X	X	X	X	X
63			X	X	X							X	X
64	X					X			X	X			
65	X					X			X	X			
66													
67													
68													
69													
70			X										
71													
72	X	X	X										
73													
74													
75													
76													
77													
78													
79													
80													
81	X	X											
82	X					X							
83					X								
84			X	X								X	X
85									X				
86	X					X							
87													
88	X	X									X	X	
89						X			X				
90													
91		X											
92					X								
93	X					X							
94	X												
95	X												
96	X												
97		X							X		X		
98		X											
99			X										
100			X		X							X	X
101									X				
Positive Readings	22	26	33	26	30	22	23	23	26	23	25	27	27
False Readings	38	33	32	8	24	14	11	16	24	4	22	22	13
Missed Voids	52	48	41	48	44	52	51	51	48	51	49	47	47

Effectivity Ratios and Void Data

Image 1			
Image Setting #:	**Effectivity Ratio**	**Image Setting #:**	**Effectivity Ratio**
1	0.182	8	0.220
2	0.225	9	0.237
3	0.299	10	0.271
4	0.284	11	0.230
5	0.281	12	0.252
6	0.214	13	0.275
7	0.235		

Image 1					
Void	**Area (Pixels)**	**Void**	**Area (Pixels)**	**Void**	**Area (Pixels)**
1	435	24	134	47	105
2	131	25	203	48	605
3	106	26	1013	49	117
4	114	27	101	50	107
5	205	28	209	51	122
6	114	29	362	52	113
7	104	30	244	53	275
8	2031	31	121	54	1919
9	169	32	235	55	115
10	1115	33	121	56	102
11	267	34	103	57	192
12	141	35	133	58	126
13	122	36	193	59	202
14	108	37	247	60	278
15	122	38	134	61	385
16	120	39	118	62	996
17	110	40	443	63	195
18	139	41	248	64	122
19	296	42	133	65	108
20	126	43	3234	66	348
21	496	44	155	67	100
22	578	45	161	68	110
23	150	46	107		

Image 2

Comparative Data from Different Analysis Settings

Image 2 Analysis Settings:											
Void	**1**	**2**	**3**	**4**	**5**	**6**	**7**	**8**	**9**	**10**	**11**
1									X	X	X
2	X	X	X	X	X	X	X	X	X	X	X
3	X	X	X	X	X	X	X	X	X	X	X
4	X	X	X	X	X	X		X	X	X	X
5	X				X				X	X	X
6	X	X			X			X		X	X
7											
Positive Readings	5	4	3	3	5	3	2	4	5	6	6
False Readings	6	3	7	4	3	2	6	4	6	5	0
Missed Voids	2	3	4	4	2	4	5	3	2	1	1

Effectivity Ratios and Void Data

Image 2			
Image Setting #:	**Effectivity Ratio**	**Image Setting #:**	**Effectivity Ratio**
1	0.462	7	0.163
2	0.400	8	0.381
3	0.252	9	0.462
4	0.273	10	0.589
5	0.519	11	0.857
6	0.306		

Image 2	
Void	**Area (Pixels)**
1	3411
2	169
3	820
4	340
5	545
6	253

Image 3

Comparative Data from Different Analysis Settings

Void	1	2	3	4	5	6	7	8	9	10	11	12	13	14	15	16	17
1	X	X			X					X					X		
2	X	X	X	X	X	X	X	X		X	X	X	X		X	X	X
3																	
4	X	X	X	X	X	X	X	X	X	X	X	X	X	X	X	X	X
5	X	X	X	X	X	X		X	X	X	X	X	X	X	X	X	X
6	X				X												
7									X								
8																	
9	X									X			X	X		X	X
10							X	X	X						X		
11																	
12		X	X	X	X	X	X	X		X	X	X	X	X	X	X	
13							X	X	X		X	X	X	X		X	
14	X	X	X	X	X	X	X	X		X	X	X	X		X	X	X
15	X	X	X	X	X	X	X	X	X	X	X	X	X	X	X	X	X
16	X	X	X	X	X	X	X	X	X	X	X	X	X		X	X	X
17	X	X	X	X	X	X	X	X		X	X	X	X	X	X	X	X
18																	
19	X	X	X	X	X	X	X	X	X	X	X	X	X	X	X	X	X
20																	
21			X	X	X		X	X	X	X	X	X	X	X	X	X	X
22	X	X	X	X		X	X	X	X	X	X	X	X	X	X	X	X
23	X	X	X	X	X	X	X	X	X	X	X	X	X	X	X	X	X
24	X	X	X			X	X			X	X	X			X		
25	X	X	X	X	X	X	X	X	X	X	X	X			X		
26	X	X	X	X	X	X	X	X	X	X	X	X	X	X	X	X	X
27	X	X	X	X	X	X	X	X	X	X	X	X	X	X	X	X	X
28	X	X	X	X	X	X	X	X		X	X	X	X		X	X	X
29	X	X	X	X	X	X		X	X	X			X		X	X	X
30	X	X	X	X	X	X	X	X	X	X		X	X		X	X	X
31	X	X	X	X	X	X	X	X	X	X	X	X	X	X	X	X	X
32	X	X	X	X	X	X	X	X	X	X	X	X	X	X	X	X	X
33	X	X	X	X	X	X	X	X	X	X	X	X	X	X	X	X	X
34																	
35	X	X	X	X	X	X	X	X	X	X					X		
36	X	X	X	X	X	X	X	X	X	X	X	X	X	X	X	X	X
37																	
38											X	X		X			
39	X	X	X	X	X	X	X	X	X	X	X	X	X	X	X	X	X
40	X	X	X	X	X	X	X	X	X	X	X	X	X	X	X	X	X
41	X	X	X	X	X	X	X	X	X	X	X	X	X	X	X	X	X
42																	
43	X	X	X	X	X	X	X	X		X		X	X		X	X	
44	X	X	X	X	X	X	X	X							X		
45	X				X				X		X	X	X	X	X	X	X
46											X	X		X			
47	X	X	X	X	X	X	X	X	X	X	X	X	X	X	X	X	X
48											X	X	X	X		X	
49																	
50														X			

	1	2	3	4	5	6	7	8	9	10	11	12	13	14	15	16	17
51	X	X	X	X	X	X	X	X	X	X	X	X	X	X	X	X	X
52	X											X		X	X	X	X
53	X	X	X	X	X	X	X	X	X	X	X	X	X		X	X	X
54		X	X	X	X	X	X	X		X	X	X	X	X	X	X	X
55	X	X	X	X	X	X	X	X	X	X	X	X	X	X	X	X	X
56																	
57																	
58	X	X															
59																	
60																	
61	X	X	X	X	X	X	X	X	X	X	X	X	X	X	X	X	X
62	X	X	X	X	X	X	X	X	X	X	X	X	X	X	X	X	X
63	X	X	X	X	X	X	X	X	X	X	X	X	X	X	X	X	X
64	X	X	X			X	X					X			X	X	X
65		X		X					X	X	X	X		X		X	
66	X	X	X	X	X	X	X	X	X	X	X	X	X	X	X	X	
67		X	X	X	X			X	X		X	X	X	X		X	
68	X		X			X	X	X			X	X	X	X	X		X
69	X	X	X	X	X	X	X	X	X	X	X	X	X	X	X	X	X
70	X	X	X	X	X	X	X	X	X	X	X	X	X	X	X	X	X
71	X																
72	X	X	X	X	X	X	X	X		X				X		X	X
73									X		X	X					
74																	
75																	
76																	
77		X	X	X	X	X	X	X	X		X	X	X	X	X	X	X
Positive Readings	47	46	45	43	45	44	44	45	37	43	47	49	44	40	48	46	42
False Readings	7	10	9	10	21	2	2	3	3	4	3	3	2	5	3	9	4
Missed Voids	30	31	32	34	32	33	33	32	40	34	30	28	33	37	29	31	35

Effectivity Ratios and Void Data

Image 3			
Image Setting #:	**Effectivity Ratio**	**Image Setting #:**	**Effectivity Ratio**
1	0.540	10	0.515
2	0.507	11	0.576
3	0.501	12	0.602
4	0.470	13	0.548
5	0.443	14	0.468
6	0.548	15	0.589
7	0.548	16	0.513
8	0.550	17	0.502
9	0.447		

Image 3					
Void	**Area (Pixels)**	**Void**	**Area (Pixels)**	**Void**	**Area (Pixels)**
1	865	21	163	41	1008
2	265	22	7324	42	2752
3	1630	23	1400	43	3178
4	552	24	3384	44	3112
5	111	25	2262	45	101
6	5726	26	102	46	307
7	1640	27	12973	47	3006
8	4293	28	120	48	138
9	101	29	246	49	386
10	4965	30	179	50	2584
11	5301	31	154	51	142
12	2191	32	554	52	564
13	213	33	4365	53	9452
14	7986	34	445	54	2014
15	1963	35	112	55	217
16	565	36	248	56	1467
17	3655	37	3155	57	131
18	4850	38	706	58	288
19	2208	39	800		
20	837	40	349		

Top Three Effectivity Ratios from all Settings and Images

		Threshold Top	Threshold Bottom	Circularity Min.	Circularity Max	Size Min.	Size Max.	Effectivity Ratio	Origin Picture
Image 1	1	0	65	0.3	1.0	100	5000	0.299	Green with shading correction
	2	0	70	0.3	1.0	100	5000	0.284	Green with shading correction
	3	0	75	0.3	1.0	100	5000	0.281	Green with shading correction
Image 2	1	0	103	0.3	1.0	150	8000	0.857	Green with shading correction
	2	0	110	0.3	1.0	100	8000	0.589	Green with shading correction
	3	0	70	0.3	1.0	100	8000	0.519	Green with enhanced contrast
Image 3	1	0	140	0.3	1.0	100	15000	0.602	Blue with shade correction
	2	0	130	0.3	1.0	100	12000	0.589	Blue with enhanced contrast
	3	0	120	0.3	1.0	100	8000	0.550	Green with enhanced contrast

Threshold Data

Individual Settings

Original with enhanced contrast (green)		Blue with enhanced contrast		Green with enhanced contrast		Blue with shade correction		Green with shade correction	
Threshold	Effectivity Ratio	Threshold	Effectivity Ratio	Threshold	Effectivity Ratio	Threshold	Effectivity Ratio	Threshold	Effectivity Ratio
80	0.462	110	0.273	70	0.519	90	0.163	100	0.462
80	0.540	120	0.548	100	0.306	120	0.576	100	0.468
100	0.400	130	0.550	120	0.447	130	0.381	103	0.857
100	0.507	140	0.548	140	0.515	140	0.602	110	0.589
120	0.252					140	0.548	120	0.589
120	0.501								
140	0.470								
140	0.443								

Overall Data

All Image Settings			
Threshold	Effectivity Ratio	Threshold	Effectivity Ratio
70	0.519	120	0.501
80	0.462	120	0.548
80	0.540	120	0.447
90	0.163	120	0.576
100	0.400	120	0.589
100	0.507	130	0.550
100	0.306	130	0.381
100	0.462	140	0.470
100	0.468	140	0.443
103	0.857	140	0.548
110	0.273	140	0.515
110	0.589	140	0.602
120	0.252	140	0.548

APPENDIX F.   DATA FROM EVALUATION OF AUTOMATED PROCESS

Individual Image Results

Hexcel Satin Weave

Hexcel Satin Weave - Image 1					
	Hand Painted			**Auto Analysis**	
Void #	**Size (mm^2)**	**Perimeter (mm)**	**Circularity**	**Size (mm^2)**	**Perimeter (mm)**	**Circularity**
1	0.009	0.349	0.973	0.010	0.406	0.750
2	0.009	0.349	0.973	0.016	0.542	0.676
3	0.108	1.541	0.571			
4	0.023	0.587	0.821			
5	0.009	0.336	0.993			
6	0.004	0.229	1.0			
7	0.040	0.750	0.902	0.043	0.831	0.777
8	0.004	0.229	1.0			
9	0.009	0.349	0.964			
10	0.004	0.229	1.0			
11	0.004	0.229	1.0			
12	0.009	0.346	0.924			
13	0.012	0.385	0.974			
14	0.009	0.349	0.973			
15	0.019	0.511	0.911	0.006	0.286	0.929
16	0.012	0.404	0.907	0.010	0.396	0.774
17	0.007	0.297	0.959	0.005	0.279	0.816
18	0.007	0.297	0.959			
19	0.005	0.247	1.0			
20	0.012	0.385	0.974			
21	0.018	0.554	0.758			
22	0.008	0.317	1.0			
23	0.007	0.297	0.959			
24	0.025	0.562	0.978	0.011	0.456	0.666
25	0.007	0.297	0.959			

26	0.004	0.229	1.0			
27	0.004	0.229	1.0			
28	0.008	0.317	1.0			
29	0.004	0.229	1.0			
30	0.009	0.349	0.973			
31	0.017	0.469	0.957	0.010	0.385	0.860
32	0.023	0.604	0.789			
33	0.009	0.349	0.973	0.005	0.247	0.985
34	0.015	0.453	0.925	0.006	0.292	0.845
35	0.025	0.581	0.936			
36	0.015	0.443	0.949	0.014	0.463	0.837
37	0.004	0.229	1.0			
38	0.232	2.028	0.708			
39	0.009	0.349	0.973			
40	0.012	0.391	0.975			
41	0.008	0.317	1.0			
42	0.008	0.317	1.0			
43	0.007	0.297	0.959			
44	0.013	0.406	1.0			
45	0.019	0.511	0.911			
46	0.007	0.297	0.959			
47	0.004	0.229	1.0			
48	0.038	0.733	0.889			
49	0.128	1.378	0.849	0.161	1.782	0.638
50	0.004	0.229	1.0			
51	0.007	0.297	0.959			
52	0.013	0.406	1.0			
53	0.007	0.297	0.959			
54	0.024	0.575	0.925			
55	0.004	0.229	1.0			
56	0.007	0.297	0.959			
57	0.006	0.266	1.0			
58	0.007	0.302	0.971	0.004	0.253	0.877
59	0.015	0.437	0.978			
60	0.014	0.424	0.997			
61	0.004	0.229	1.0			
62	0.015	0.472	0.864			
63	0.006	0.266	1.0	0.007	0.323	0.831
64	0.035	0.677	0.950	0.035	0.737	0.804
65	0.029	0.614	0.977	0.027	0.689	0.721
66	0.025	0.581	0.933	0.018	0.500	0.917
67	0.007	0.297	0.959			
68	0.004	0.229	1.0			
69	0.010	0.378	0.917			
70	0.013	0.422	0.919			
Average Size	0.018	0.430	0.960	0.023	0.522	0.806
Max Size	0.232	2.028	1.0	0.161	1.782	0.985
Min Size	0.004	0.229	0.571	0.004	0.247	0.638

Hexcel Satin Weave - Image 2					
	Hand Painted			Auto Analysis		
Void #	Size (mm^2)	Perimeter (mm)	Circularity	Size (mm^2)	Perimeter (mm)	Circularity
1	0.008	0.318	1.0	0.011	0.407	0.852
2	0.008	0.318	1.0			
3	0.171	1.937	0.572			
4	0.012	0.386	0.974	0.006	0.307	0.797
5	0.004	0.229	1.0			
6	0.009	0.349	0.973			
7	0.009	0.349	0.973			
8	0.003	0.193	1.0			
9	0.025	0.563	0.978	0.037	0.746	0.828
10	0.003	0.193	1.0			
11	0.008	0.339	0.855			
12	0.006	0.274	0.976			
13	0.003	0.193	1.0			
14	0.008	0.331	0.880			
15	0.004	0.229	1.0	0.006	0.412	0.462
16	0.003	0.193	1.0			
17	0.003	0.193	1.0			
18	0.009	0.349	0.973			
19	0.010	0.413	0.752			
20	0.030	0.642	0.925			
21	0.010	0.403	0.781			
22	0.005	0.242	1.0			
23	0.003	0.193	1.0			
24	0.008	0.333	0.878			
25	0.003	0.193	1.0			
26	0.020	0.546	0.835	0.010	0.375	0.903
27	0.003	0.193	1.0			
28	0.005	0.242	1.0			
29	0.014	0.441	0.926			
30	0.009	0.349	0.973	0.008	0.381	0.709
31	0.046	1.036	0.539			
32	0.026	0.603	0.914			
33	0.049	1.022	0.587			
34	0.009	0.349	0.973			
35	0.007	0.310	0.968			

36	0.003	0.193	1.0			
37	0.003	0.193	1.0			
38	0.003	0.193	1.0			
39	0.009	0.359	0.854			
40	0.002	0.141	1.0			
41	0.003	0.193	1.057			
42	0.013	0.472	0.759			
43	0.002	0.141	1.0			
44	0.085	1.062	0.947	0.119	1.570	0.607
45	0.024	0.687	0.638			
46	0.003	0.193	1.0			
47	0.006	0.266	1.0			
48	0.002	0.141	1.0			
49	0.003	0.193	1.0			
50	0.002	0.141	1.0			
51	0.007	0.305	0.923			
52	0.003	0.193	1.0			
53	0.003	0.193	1.0			
54	0.013	0.407	1.0			
55	0.013	0.407	1.0	0.008	0.323	0.943
56	0.003	0.193	1.0			
57	0.006	0.279	0.953			
58	0.003	0.193	1.0			
59	0.004	0.229	1.0			
60	0.003	0.193	1.0			
61	0.005	0.242	1.0			
62	0.146	1.474	0.842	0.115	1.710	0.494
63	0.003	0.193	1.0	0.034	0.694	0.886
64	0.029	0.615	0.977	0.028	0.747	0.628
65	0.025	0.563	0.978			
66	0.016	0.464	0.906			
67	0.004	0.229	1.0			
68	0.009	0.349	0.973			
69	0.012	0.404	0.959	0.012	0.464	0.714
70	0.009	0.349	0.973			
Average Size	0.015	0.378	0.968	0.033	0.678	0.735
Max Size	0.171	1.937	1.0	0.119	1.710	0.943
Min Size	0.002	0.141	0.539	0.006	0.307	0.462

Hexcel Satin Weave - Image 3					
	Hand Painted			Auto Analysis		
Void #	Size (mm^2)	Perimeter (mm)	Circularity	Size (mm^2)	Perimeter (mm)	Circularity
1	0.006	0.265	1.0	0.012	0.353	1.196
2	0.006	0.265	1.0			
3	0.132	1.614	0.638			
4	0.011	0.384	0.974			
5	0.006	0.265	1.0			
6	0.011	0.384	0.974			
7	0.006	0.265	1.0			
8	0.035	0.781	0.719	0.038	0.848	0.664
9	0.011	0.384	0.974	0.006	0.293	0.808
10	0.008	0.316	1.0			
11	0.011	0.384	0.974			
12	0.008	0.316	1.0			
13	0.006	0.265	1.0			
14	0.007	0.301	1.0			
15	0.006	0.265	1.0			
16	0.006	0.265	1.0			
17	0.019	0.509	0.911			
18	0.006	0.265	1.0			
19	0.033	0.692	0.866			
20	0.006	0.265	1.0			
21	0.035	0.685	0.940			
22	0.006	0.265	1.0			
23	0.006	0.265	1.0			
24	0.019	0.509	0.911			
25	0.029	0.612	0.977			
26	0.022	0.570	0.867	0.021	0.555	0.844
27	0.015	0.463	0.907			
28	0.006	0.265	1.0			
29	0.020	0.514	0.948	0.016	0.553	0.648
30	0.023	0.571	0.897			
31	0.008	0.316	1.0	0.008	0.353	0.792
32	0.012	0.389	1.0	0.011	0.412	0.834
33	0.006	0.265	1.0			
34	0.006	0.265	1.0			
35	0.006	0.265	1.0			

36	0.006	0.265	1.0			
37	0.011	0.384	0.974			
38	0.008	0.316	1.0			
39	0.022	0.553	0.885			
40	0.006	0.265	1.0			
41	0.091	1.111	0.921	0.089	1.145	0.849
42	0.023	0.566	0.894			
43	0.011	0.384	0.974			
44	0.008	0.316	1.0			
45	0.006	0.265	1.0			
46	0.011	0.384	0.974			
47	0.011	0.384	0.974	0.007	0.331	0.764
48	0.018	0.509	0.879	0.008	0.397	0.672
49	0.011	0.384	0.974			
50	0.011	0.384	0.974			
51	0.011	0.384	0.974			
52	0.011	0.384	0.974			
53	0.011	0.384	0.974			
54	0.027	0.608	0.928			
55	0.011	0.384	0.974			
56	0.011	0.379	0.994	0.010	0.397	0.792
57	0.006	0.265	1.0			
58	0.006	0.265	1.0			
59	0.007	0.301	1.0			
60	0.029	0.612	0.977			
61	0.009	0.338	0.965			
Average Size	0.016	0.417	0.974	0.020	0.512	0.806
Max Size	0.132	1.614	1.0	0.089	1.145	1.196
Min Size	0.006	0.265	0.638	0.006	0.293	0.648

Hexcel Satin Weave - Image 4

Void #	Hand Painted			Auto Analysis		
	Size (mm^2)	Perimeter (mm)	Circularity	Size (mm^2)	Perimeter (mm)	Circularity
1	0.009	0.349	0.973	0.012	0.506	0.571
2	0.009	0.349	0.973			
3	0.160	1.732	0.668			
4	0.015	0.438	0.961			
5	0.009	0.349	0.973			
6	0.009	0.349	0.973			
7	0.009	0.349	0.973			
8	0.036	0.708	0.900	0.037	1.020	0.448
9	0.012	0.386	0.974			
10	0.026	0.751	0.577			
11	0.029	0.698	0.739			
12	0.013	0.423	0.948			
13	0.014	0.436	0.937			
14	0.025	0.587	0.922			
15	0.009	0.349	0.973			
16	0.025	0.585	0.917			
17	0.025	0.615	0.817			
18	0.030	0.713	0.729			
19	0.016	0.459	0.923	0.005	0.316	0.680
20	0.016	0.459	0.923			
21	0.009	0.349	0.973			
22	0.046	0.886	0.731			
23	0.009	0.349	0.973			
24	0.062	0.976	0.819	0.059	1.087	0.630
25	0.040	0.747	0.896			
26	0.010	0.368	0.972			
27	0.023	0.596	0.809			
28	0.011	0.386	0.967			
29	0.009	0.349	0.973			
30	0.030	0.693	0.772			
31	0.019	0.522	0.878			
32	0.020	0.533	0.865			
33	0.034	0.674	0.934	0.064	1.398	0.409
34	0.028	0.600	0.965			
35	0.022	0.527	0.978			
36	0.009	0.349	0.973			
37	0.022	0.543	0.921			
Average Size	0.024	0.555	0.896	0.035	0.865	0.548
Max Size	0.160	1.732	0.978	0.064	1.398	0.680
Min Size	0.009	0.349	0.577	0.005	0.316	0.409

Hexcel Satin Weave - Image 5					
	Hand Painted			Auto Analysis		
Void #	Size (mm^2)	Perimeter (mm)	Circularity	Size (mm^2)	Perimeter (mm)	Circularity
1	0.009	0.349	0.973	0.006	0.317	0.786
2	0.009	0.349	0.973			
3	0.007	0.291	1.0			
4	0.143	1.790	0.561			
5	0.010	0.362	0.936			
6	0.004	0.229	1.0			
7	0.009	0.354	0.935			
8	0.005	0.255	1.0			
9	0.026	0.600	0.909	0.036	0.885	0.578
10	0.008	0.317	1.0			
11	0.011	0.372	0.990			
12	0.008	0.317	1.0	0.008	0.362	0.815
13	0.008	0.317	1.0			
14	0.002	0.140	1.0			
15	0.004	0.229	1.0			
16	0.038	0.904	0.590			
17	0.008	0.317	1.0			
18	0.008	0.317	0.943			
19	0.030	0.656	0.868	0.016	0.498	0.798
20	0.035	0.743	0.800			
21	0.025	0.624	0.793			
22	0.009	0.349	0.973			
23	0.006	0.266	1.0			
24	0.041	0.749	0.926	0.048	0.826	0.878
25	0.037	0.717	0.898			
26	0.012	0.411	0.918	0.005	0.330	0.561
27	0.006	0.266	1.0			
28	0.011	0.398	0.905	0.004	0.354	0.446
29	0.004	0.229	1.0			
30	0.004	0.229	1.0			
31	0.004	0.229	1.0			
32	0.011	0.404	0.868			
33	0.008	0.315	0.957			
34	0.004	0.229	1.0			
35	0.017	0.495	0.848			

36	0.004	0.229	1.0			
37	0.026	0.592	0.924			
38	0.013	0.422	0.948			
39	0.007	0.297	0.983			
40	0.004	0.229	1.0			
41	0.005	0.247	1.0			
42	0.013	0.439	0.853			
43	0.009	0.349	0.973	0.012	0.468	0.700
44	0.006	0.266	1.0			
45	0.006	0.266	1.0			
46	0.008	0.323	1.0			
47	0.013	0.430	0.910			
48	0.022	0.549	0.909	0.072	1.464	0.421
49	0.018	0.495	0.925	0.008	0.336	0.937
50	0.037	0.712	0.920			
51	0.021	0.542	0.892			
52	0.024	0.605	0.807			
53	0.034	0.719	0.823			
54	0.023	0.562	0.915	0.011	0.427	0.784
55	0.038	0.725	0.914			
56	0.006	0.266	1.0			
57	0.009	0.349	0.973	0.007	0.299	0.921
58	0.016	0.459	0.974			
59	0.010	0.354	0.977			
60	0.018	0.508	0.895	0.009	0.489	0.477
61	0.008	0.321	0.986			
Average Size	0.016	0.432	0.948	0.019	0.543	0.700
Max Size	0.143	1.790	1.0	0.072	1.464	0.937
Min Size	0.002	0.140	0.561	0.004	0.299	0.421

Vector Ply NCF

Vector Ply NCF - Image 1					
	Hand Painted			**Auto Analysis**		
Void #	Size (mm^2)	Perimeter (mm)	Circularity	Size (mm^2)	Perimeter (mm)	Circularity
1	0.012	0.397	0.938	0.009	0.427	0.644
2	0.010	0.358	1.0			
3	0.014	0.456	0.868	0.014	0.477	0.800
4	0.019	0.527	0.869			
5	0.034	0.709	0.848			
6	0.180	2.184	0.475			
7	0.073	1.039	0.850	0.100	1.499	0.561
8	0.020	0.508	0.979			
9	0.101	1.224	0.851	0.070	1.225	0.584
10	0.013	0.418	0.925			
11	0.009	0.335	0.959			
12	0.016	0.456	0.959			
13	0.012	0.394	0.973			
14	0.148	1.483	0.848	0.139	1.512	0.763
15	0.114	1.393	0.737	0.124	1.529	0.668
16	0.152	1.642	0.710			
17	0.010	0.358	1.0			
18	0.050	0.853	0.867			
19	0.181	1.988	0.577			
20	0.644	4.016	0.501	0.591	4.124	0.436
21	0.194	1.980	0.620	0.201	2.129	0.556
22	0.128	1.463	0.749	0.085	1.322	0.612
23	0.041	0.774	0.863			
24	0.052	0.865	0.867	0.010	0.579	0.386
25	0.071	1.047	0.819	0.036	0.732	0.845
26	0.111	1.246	0.902	0.098	1.279	0.749
27	0.319	2.344	0.730	0.257	2.312	0.603
28	0.012	0.394	0.973			
29	0.013	0.415	0.972			
30	0.017	0.458	1.0	0.022	0.597	0.789
31	0.023	0.564	0.909			
32	0.030	0.632	0.935			
33	0.017	0.458	1.0	0.018	0.549	0.742
Average Size	0.086	1.012	0.852	0.118	1.353	0.649
Max Size	0.644	4.016	1.0	0.591	4.124	0.845
Min Size	0.009	0.335	0.475	0.009	0.427	0.386

	Hand Painted			Auto Analysis		
Vector Ply NCF - Image 2						
Void #	Size (mm^2)	Perimeter (mm)	Circularity	Size (mm^2)	Perimeter (mm)	Circularity
1	0.015	0.441	0.974	0.012	0.411	0.915
2	0.142	1.558	0.736			
3	0.015	0.441	0.974			
4	0.019	0.504	0.958			
5	0.021	0.525	0.948			
6	0.174	2.249	0.433			
7	0.088	1.137	0.858			
8	0.015	0.441	0.974			
9	0.112	1.320	0.809	0.087	1.237	0.713
10	0.015	0.441	0.974			
11	0.152	1.497	0.850			
12	0.166	1.647	0.769	0.136	1.556	0.708
13	0.196	1.757	0.797			
14	0.009	0.339	0.959			
15	0.009	0.339	0.959			
16	0.180	2.022	0.554			
17	0.653	4.363	0.431	0.617	4.369	0.406
18	0.242	2.132	0.670	0.214	2.132	0.592
19	0.101	1.479	0.578	0.076	1.268	0.593
20	0.036	0.710	0.897			
21	0.099	1.255	0.790			
22	0.136	1.458	0.803	0.090	1.265	0.705
23	0.314	2.366	0.705	0.292	2.367	0.656
24	0.023	0.542	0.978			
25	0.015	0.441	0.974			
26	0.141	1.419	0.879	0.101	1.516	0.554
27	0.015	0.441	0.974			
28	0.011	0.363	1.0	0.017	0.612	0.585
29	0.024	0.601	0.848			
30	0.057	0.944	0.801	0.073	1.346	0.508
Average Size	0.106	1.172	0.829	0.156	1.644	0.630
Max Size	0.653	4.363	1.0	0.617	4.369	0.915
Min Size	0.009	0.339	0.431	0.012	0.411	0.406

Vector Ply NCF - Image 3					
	Hand Painted			Auto Analysis		
Void #	Size (mm^2)	Perimeter (mm)	Circularity	Size (mm^2)	Perimeter (mm)	Circularity
1	0.028	0.602	0.966	0.011	0.391	0.878
2	0.025	0.588	0.893			
3	0.026	0.628	0.840			
4	0.182	2.342	0.417			
5	0.115	1.292	0.864			
6	0.023	0.540	0.978			
7	0.058	0.897	0.898			
8	0.092	1.179	0.836			
9	0.025	0.581	0.911			
10	0.011	0.361	1.0			
11	0.157	1.625	0.749	0.131	1.662	0.594
12	0.067	0.991	0.863			
13	0.170	1.578	0.857			
14	0.140	2.071	0.410			
15	0.009	0.338	0.959			
16	0.622	4.592	0.370	0.617	4.665	0.356
17	0.248	2.192	0.649	0.213	2.168	0.569
18	0.117	2.005	0.364	0.047	1.046	0.543
19	0.025	0.581	0.911	0.016	0.574	0.606
20	0.072	1.024	0.860	0.062	1.017	0.752
21	0.346	2.336	0.796	0.350	2.560	0.671
22	0.131	1.499	0.731	0.088	1.335	0.624
23	0.023	0.540	0.978	0.022	0.601	0.750
24	0.023	0.540	0.978			
25	0.028	0.602	0.966			
26	0.023	0.540	0.978	0.016	0.521	0.721
Average Size	0.107	1.233	0.809	0.143	1.504	0.642
Max Size	0.622	4.592	1.0	0.617	4.665	0.878
Min Size	0.009	0.338	0.364	0.011	0.391	0.356

Vector Ply NCF - Image 4

Void #	Hand Painted			Auto Analysis		
	Size (mm^2)	Perimeter (mm)	Circularity	Size (mm^2)	Perimeter (mm)	Circularity
1	0.055	0.906	0.841	0.023	0.759	0.511
2	0.059	0.914	0.889			
3	0.094	1.136	0.918	0.041	0.853	0.717
4	0.023	0.541	0.978	0.010	0.377	0.890
5	0.004	0.219	1.0			
6	0.014	0.488	0.734	0.015	0.467	0.852
7	0.150	2.343	0.343			
8	0.103	1.192	0.912			
9	0.020	0.520	0.941			
10	0.071	1.011	0.867			
11	0.083	1.137	0.810			
12	0.011	0.362	1.0			
13	0.013	0.404	1.0			
14	0.011	0.362	1.0			
15	0.009	0.339	0.959			
16	0.074	1.165	0.688	0.068	1.048	0.779
17	0.152	1.623	0.725	0.136	1.587	0.678
18	0.011	0.392	0.896			
19	0.087	1.171	0.793			
20	0.012	0.398	0.973			
21	0.187	2.113	0.526			
22	0.675	4.911	0.352			
23	0.270	2.257	0.667	0.231	2.297	0.549
24	0.025	0.610	0.851			
25	0.156	1.584	0.779	0.130	1.592	0.645
26	0.086	1.249	0.695	0.044	0.923	0.654
27	0.065	1.102	0.675	0.011	0.543	0.475
28	0.032	0.642	0.978	0.036	0.713	0.881
29	0.012	0.383	1.0			
30	0.482	2.722	0.818	0.482	3.217	0.585
31	0.141	1.479	0.812	0.133	1.637	0.625
32	0.040	0.767	0.859	0.059	0.992	0.751
33	0.046	0.818	0.855	0.024	0.621	0.788
34	0.012	0.398	0.973	0.019	0.578	0.708
Average Size	0.097	1.108	0.830	0.091	1.138	0.693
Max Size	0.675	4.911	1.0	0.482	3.217	0.890
Min Size	0.004	0.219	0.343	0.010	0.377	0.475

Vector Ply NCF - Image 5					
	Hand Painted			Auto Analysis		
Void #	Size (mm^2)	Perimeter (mm)	Circularity	Size (mm^2)	Perimeter (mm)	Circularity
1	0.096	1.165	0.889	0.021	0.892	0.328
2	0.035	0.687	0.921			
3	0.036	0.718	0.883			
4	0.017	0.459	1.0	0.009	0.359	0.870
5	0.017	0.459	1.0	0.014	0.456	0.866
6	0.172	2.545	0.333			
7	0.114	1.256	0.906			
8	0.074	0.989	0.945			
9	0.083	1.213	0.708			
10	0.025	0.580	0.924	0.028	0.654	0.813
11	0.018	0.480	0.997			
12	0.017	0.459	1.0			
13	0.009	0.336	0.959			
14	0.009	0.336	0.959			
15	0.017	0.459	1.0			
16	0.097	1.200	0.851	0.075	1.102	0.781
17	0.135	1.522	0.735	0.145	1.598	0.714
18	0.017	0.459	1.0			
19	0.039	0.733	0.917			
20	0.097	1.228	0.812	0.057	1.085	0.614
21	0.193	2.241	0.483			
22	0.557	4.958	0.285			
23	0.022	0.536	0.978			
24	0.335	2.925	0.493	0.298	3.238	0.357
25	0.176	1.811	0.676			
26	0.118	1.580	0.593	0.133	1.696	0.580
27	0.009	0.342	0.971			
28	0.003	0.180	1.0			
29	0.566	3.637	0.538			
30	0.193	2.038	0.583	0.241	2.438	0.509
31	0.110	1.243	0.893	0.089	1.196	0.783
32	0.023	0.542	0.975	0.016	0.480	0.886
33	0.024	0.557	0.967			
34	0.079	1.144	0.754	0.046	0.982	0.604
Average Size	0.104	1.206	0.824	0.090	1.244	0.670
Max Size	0.566	4.958	1.0	0.298	3.238	0.886
Min Size	0.003	0.180	0.285	0.009	0.359	0.328

ImageJ Settings and Effectivity Ratios

Hexcel Satin Weave

	1	2	3	4	5	6	7	8	9	10
Base Image	Blue with enhanced Contrast	Blue with enhanced Contrast	Blue with enhanced Contrast	Blue with enhanced Contrast	Blue with enhanced Contrast	Blue with enhanced Contrast	Blue with no Adjustment	Blue with no Adjustment	Blue with shade correction	Blue with shade correction
Threshold	80	80	100	100	120	120	120	120	100	100
Size Range	50-8000	100-8000	50-8000	100-8000	50-8000	100-8000	50-8000	100-8000	50-8000	100-8000
Circularity	.3-1.0	.3-1.0	.3-1.0	.3-1.0	.3-1.0	.3-1.0	.3-1.0	.3-1.0	.3-1.0	.3-1.0
TOTAL	9	8	10	7	13	7	12	7	9	4
FALSE	37	12	31	6	12	1	20	2	28	6
EFFECTIVITY RATIO	0.151	0.152	0.173	0.145	0.266	0.189	0.224	0.174	0.155	0.076
% Accurate Void ID	13%	11%	14%	10%	19%	10%	17%	10%	13%	6%

	11	12	13	14	15	16	17	18	19	20
Base Image	Blue with shade correction	Blue with shade correction	Enhanced contrast blue	Enhanced contrast blue	Enhanced contrast green	Enhanced contrast green	Enhanced contrast green	Enhanced contrast green	Enhanced contrast green	Enhanced contrast green
Threshold	120	120	240	240	90	90	110	110	130	130
Size Range	50-8000	100-8000	50-8000	100-8000	50-8000	100-8000	50-8000	100-8000	50-8000	100-8000
Circularity	.3-1.0	.3-1.0	.3-1.0	.3-1.0	.3-1.0	.3-1.0	.3-1.0	.3-1.0	.3-1.0	.3-1.0
TOTAL	15	10	10	9	8	14	18	11	13	7
FALSE	24	7	34	3	2	9	16	6	16	2
EFFECTIVITY RATIO	0.281	0.215	0.171	0.218	0.202	0.305	0.371	0.246	0.254	0.174
% Accurate Void ID	21%	14%	14%	13%	11%	20%	26%	16%	19%	10%

	21	22	23	24	25	26	27	28	29	30
Base Image	Green with enhanced contrast	Green with enhanced contrast	Green with enhanced contrast	Green with enhanced contrast	Green with enhanced contrast	Green with enhanced contrast	Green with no adjustment	Green with no adjustment	Green with no adjustment	Green with no adjustment
Threshold	80	80	100	100	120	120	70	70	90	90
Size Range	50-8000	100-8000	50-8000	100-8000	50-8000	100-8000	50-8000	100-8000	50-8000	100-8000
Circularity	.3-1.0	.3-1.0	.3-1.0	.3-1.0	.3-1.0	.3-1.0	.3-1.0	.3-1.0	.3-1.0	.3-1.0
TOTAL	15	9	16	9	14	7	13	10	13	9
FALSE	9	0	16	2	22	2	8	3	12	1
EFFECTIVITY RATIO	0.331	0.273	0.323	0.231	0.263	0.174	0.285	0.246	0.266	0.248
% Accurate Void ID	21%	13%	23%	13%	20%	10%	19%	14%	19%	13%

	31	32	33	34	35	36	37
Base Image	Green with shade correction	Green with shade correction	Green with shade correction	Green with shade correction	Green with shade correction	Enhanced Contrast Green	Enhanced Contrast Green
Threshold	80	80	100	100	110	110	110
Size Range	50-8000	100-8000	50-8000	100-8000	50-8000	53-2000	70-2000
Circularity	.3-1.0	.3-1.0	.3-1.0	.3-1.0	.3-1.0	.4-1.0	.4-1.0
TOTAL	17	11	10	8	7	17	13
FALSE	21	2	21	5	8	4	3
EFFECTIVITY RATIO	0.332	0.289	0.181	0.175	0.138	0.433	0.332
% Accurate Void ID	24%	16%	14%	11%	10%	24%	19%

Vector Ply NCF

	1	2	3	4	5	6	7
Base Image	Blue with enhanced Contrast	Blue with enhanced Contrast	Blue with enhanced Contrast	Blue with no adjustment	Blue with no adjustment	Blue with no adjustment	Blue with shade correction
Threshold	50	100	120	70	80	100	80
Size Range	50-15000	50-15000	50-15000	50-15000	50-15000	50-15000	50-15000
Circularity	.3-1.0	.3-1.0	.3-1.0	.3-1.0	.3-1.0	.3-1.0	.3-1.0
TOTAL	8	9	11	10	11	13	14
FALSE	30	22	17	37	38	12	34
EFFECTIVITY RATIO	0.135	0.160	0.207	0.170	0.188	0.266	0.248
% Accurate Void ID	24%	27%	33%	30%	33%	39%	42%

	8	9	10	11	12	13	14
Base Image	Blue with shade correction	Blue with shade correction	Enhanced contrast blue	Enhanced contrast green	Enhanced contrast green	Enhanced contrast green	Enhanced contrast green
Threshold	90	110	180	50	80	100	120
Size Range	50-15000	50-15000	50-15000	50-15000	50-15000	50-15000	50-15000
Circularity	.3-1.0	.3-1.0	.3-1.0	.3-1.0	.3-1.0	.3-1.0	.3-1.0
TOTAL	11	11	10	14	14	14	15
FALSE	28	15	27	29	43	40	42
EFFECTIVITY RATIO	0.194	0.211	0.175	0.253	0.242	0.244	0.262
% Accurate Void ID	33%	33%	30%	42%	42%	42%	45%

	15	16	17	18	19	20	21
Base Image	Green with enhanced contrast	Green with enhanced contrast	Green with enhanced contrast	Green with no adjustment	Green with no adjustment	Green with shade correction	Green with shade correction
Threshold	35	80	110	30	60	40	80
Size Range	50-15000	50-15000	50-15000	50-15000	50-15000	50-15000	50-15000
Circularity	.3-1.0	.3-1.0	.3-1.0	.3-1.0	.3-1.0	.3-1.0	.3-1.0
TOTAL	10	15	15	14	14	13	17
FALSE	45	35	44	29	13	52	51
EFFECTIVITY RATIO	0.167	0.267	0.260	0.253	0.286	0.219	0.294
% Accurate Void ID	30%	45%	45%	42%	42%	39%	52%

	22	23	24	25	26	27
Base Image	Green with shade correction	Green with shade correction	Green with shade correction	Green with shade correction	Green with enhanced contrast	Green with enhanced contrast
Threshold	100	100	70	70	80	80
Size Range	50-15000	56-5000	60-7000	60-7000	70-8000	70-8000
Circularity	.3-1.0	.4-1.0	.35-1.0	.4-1.0	.4-1.0	.35-1.0
TOTAL	16	15	17	16	14	15
FALSE	10	6	18	13	5	7
EFFECTIVITY RATIO	0.350	0.354	0.340	0.335	0.336	0.345
% Accurate Void ID	48%	45%	52%	48%	42%	45%

Data from Matlab Program

Hexcel Satin Weave

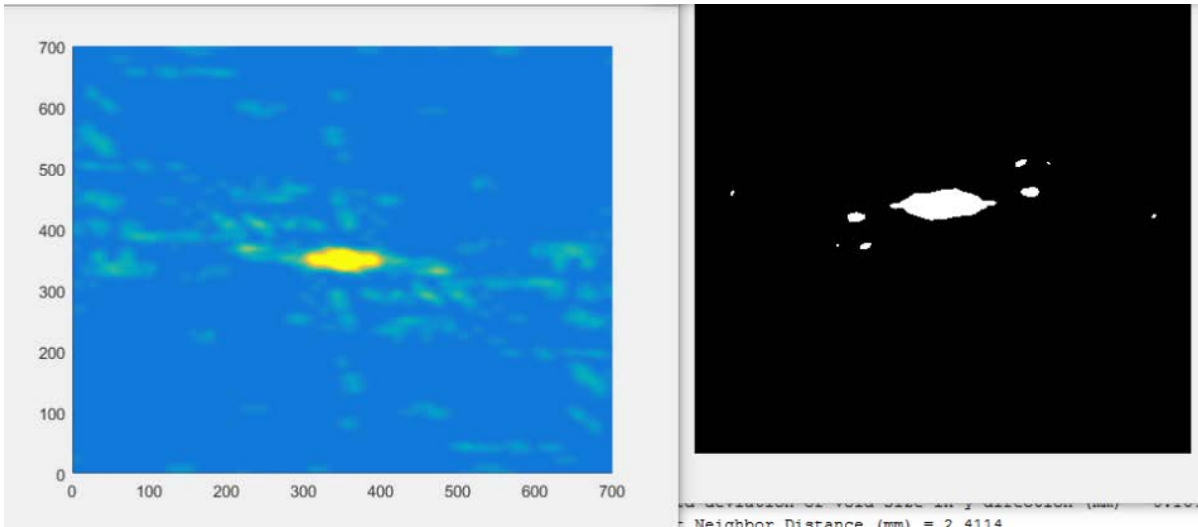| Image 1 |
|---|
| Average void size (mm^2) = 0.015856 |
| Standard deviation of void size (mm^2) = 0.03167 |
| Average void size in x-direction (mm) = 0.12286 |
| Standard deviation of void size in x-direction (mm) = 0.1102 |
| Average void size in y-direction (mm) = 0.10487 |
| Standard deviation of void size in y-direction (mm) = 0.064209 |
| Nearest Neighbor Distance (mm) = 0.77442 |
| Standard Deviation NN Distance (mm) = 0.82329 |
| Betti Numbers = 70   0   0 |
| Max cluster size (mm^2): 0.47264 |
| Ix/Iy for max cluster: 0.31055 |
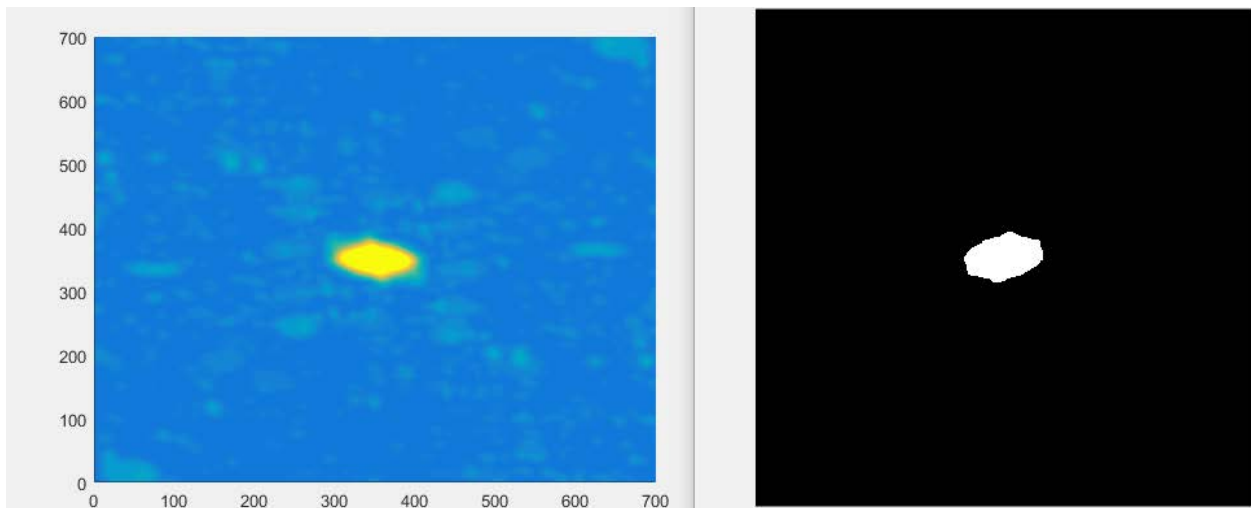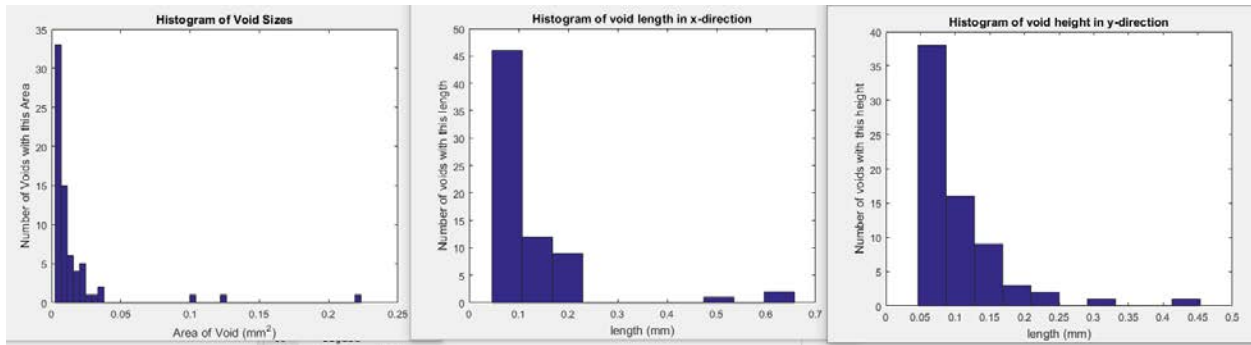
Image 2
Average void size (mm^2) = 0.018703
Standard deviation of void size (mm^2) = 0.032272
Average void size in x-direction (mm) = 0.14651
Standard deviation of void size in x-direction (mm) = 0.13369
Average void size in y-direction (mm) = 0.11471
Standard deviation of void size in y-direction (mm) = 0.072065
Nearest Neighbor Distance (mm) = 1.02
Standard Deviation NN Distance (mm) = 1.0661
Betti Numbers = 46   1   0
Max cluster size (mm^2): 0.44093
Ix/Iy for max cluster: 0.24006
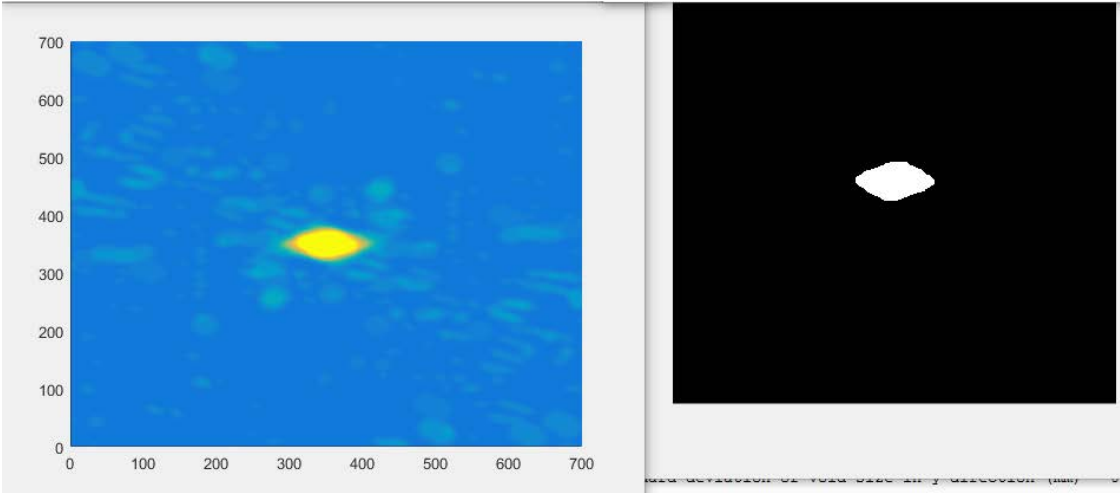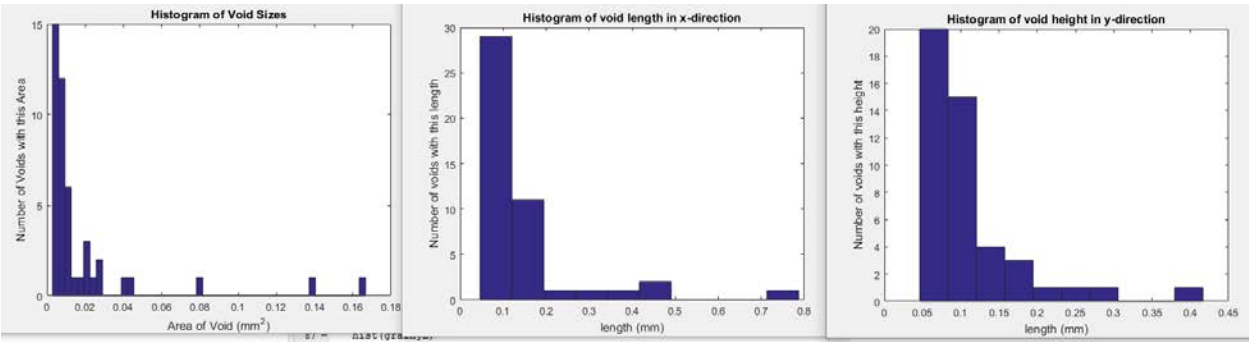
Image 3	
Average void size (mm^2) = 0.013609	
Standard deviation of void size (mm^2) = 0.019326	
Average void size in x-direction (mm) = 0.11731	
Standard deviation of void size in x-direction (mm) = 0.087166	
Average void size in y-direction (mm) = 0.10623	
Standard deviation of void size in y-direction (mm) = 0.05044	
Nearest Neighbor Distance (mm) = 0.79179	
Standard Deviation NN Distance (mm) = 0.99548	
Betti Numbers = 61 0 0	
Max cluster size (mm^2): 0.24536	
Ix/Iy for max cluster: 0.18228	
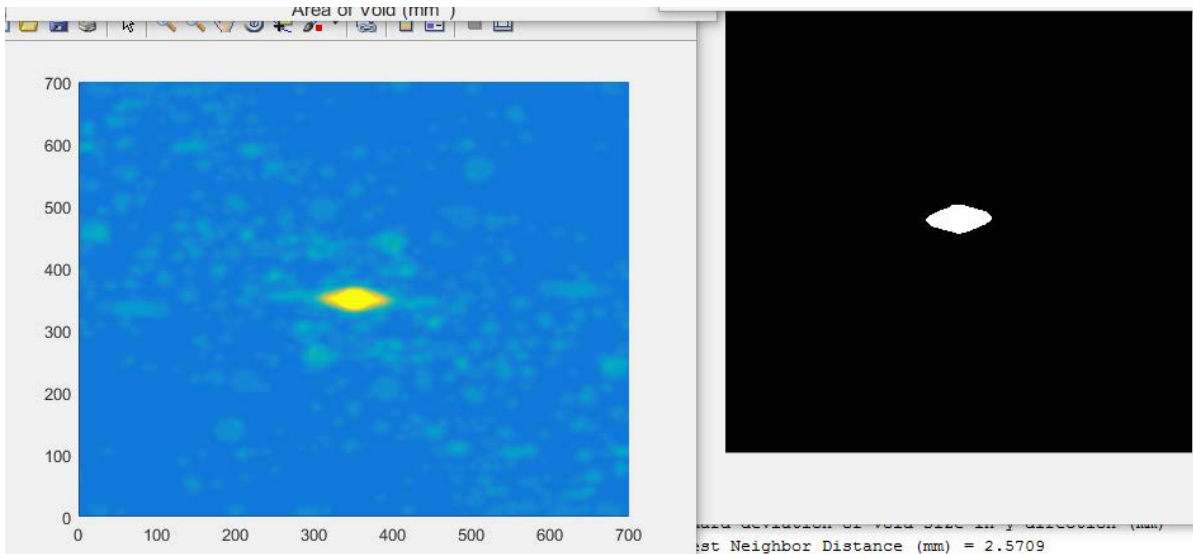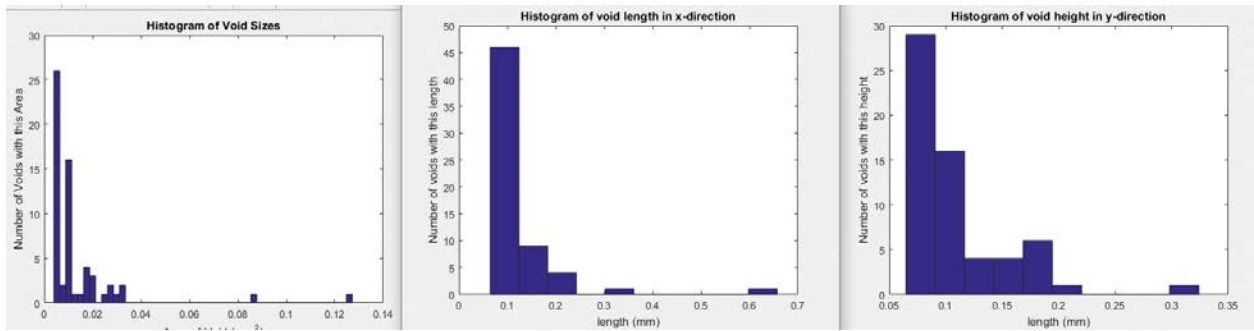
Image 4
Average void size (mm^2) = 0.021606
Standard deviation of void size (mm^2) = 0.024178
Average void size in x-direction (mm) = 0.17364
Standard deviation of void size in x-direction (mm) = 0.10876
Average void size in y-direction (mm) = 0.13136
Standard deviation of void size in y-direction (mm) = 0.050791
Nearest Neighbor Distance (mm) = 0.74268
Standard Deviation NN Distance (mm) = 0.72141
Betti Numbers = 37   0   0
Max cluster size (mm^2): 0.34546
Ix/Iy for max cluster: 0.094091
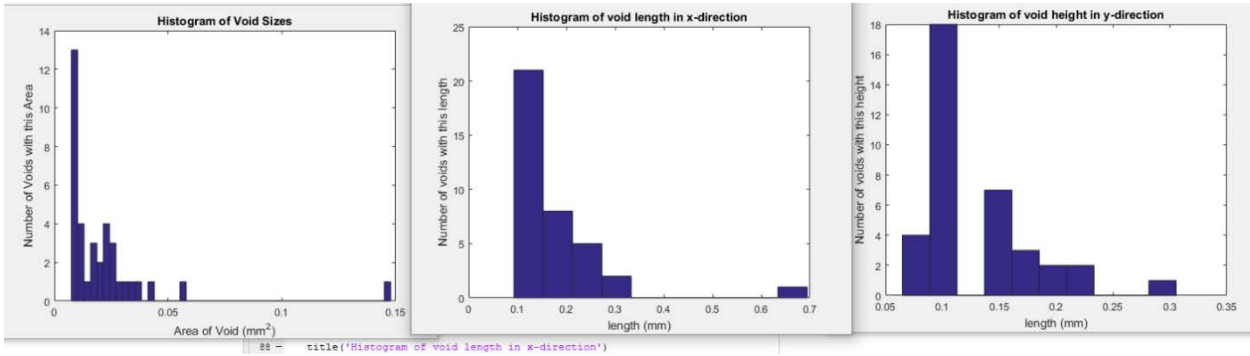
Image 5
Average void size (mm^2) = 0.014156
Standard deviation of void size (mm^2) = 0.018799
Average void size in x-direction (mm) = 0.12744
Standard deviation of void size in x-direction (mm) = 0.10097
Average void size in y-direction (mm) = 0.10445
Standard deviation of void size in y-direction (mm) = 0.04561
Nearest Neighbor Distance (mm) = 0.7879
Standard Deviation NN Distance (mm) = 0.77268
Betti Numbers = 60   0   0
Max cluster size (mm^2): 0.38985
Ix/Iy for max cluster: 0.037409
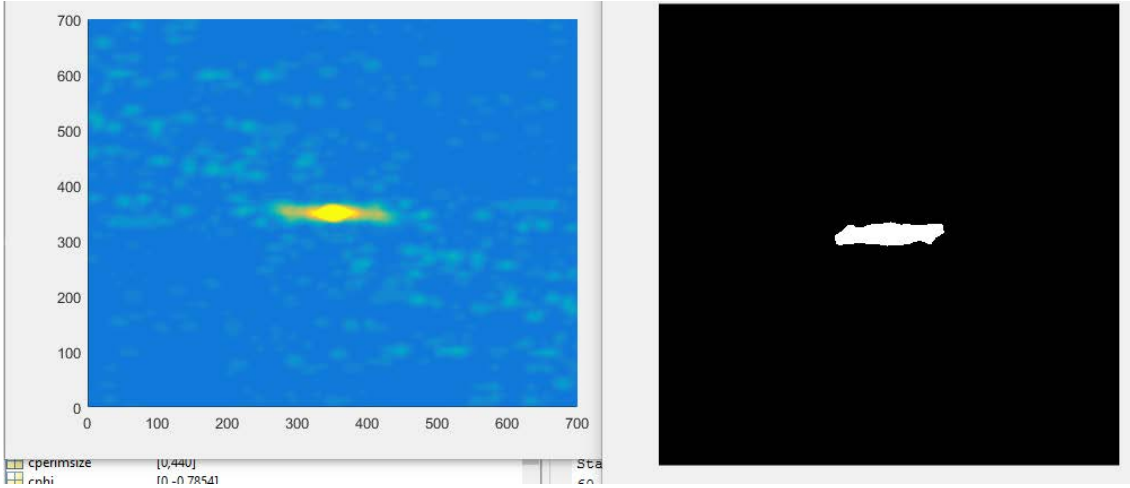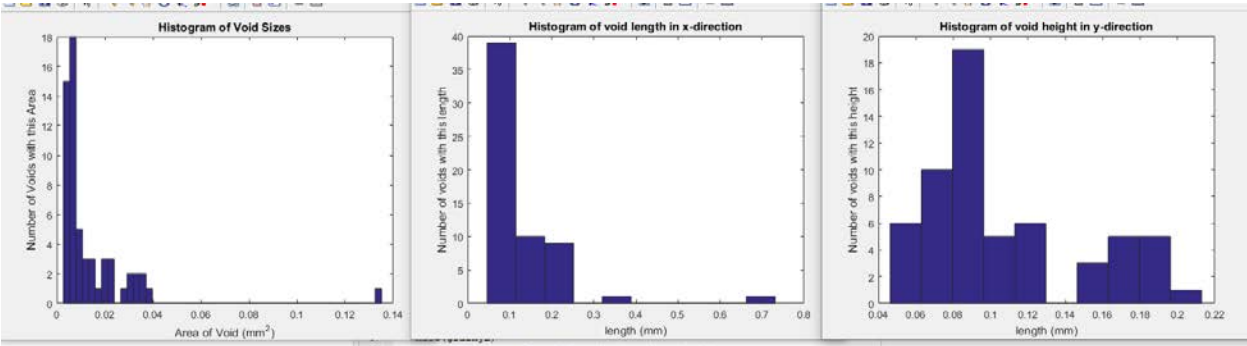
Vector Ply NCF

Image 1
Average void size (mm^2) = 0.091156
Standard deviation of void size (mm^2) = 0.13693
Average void size in x-direction (mm) = 0.31741
Standard deviation of void size in x-direction (mm) = 0.28018
Average void size in y-direction (mm) = 0.31104
Standard deviation of void size in y-direction (mm) = 0.27025
Nearest Neighbor Distance (mm) = 1.3273
Standard Deviation NN Distance (mm) = 0.97575
Betti Numbers = 33   3   0
Max cluster size (mm^2): 1.5994
Ix/Iy for max cluster: 0.067425
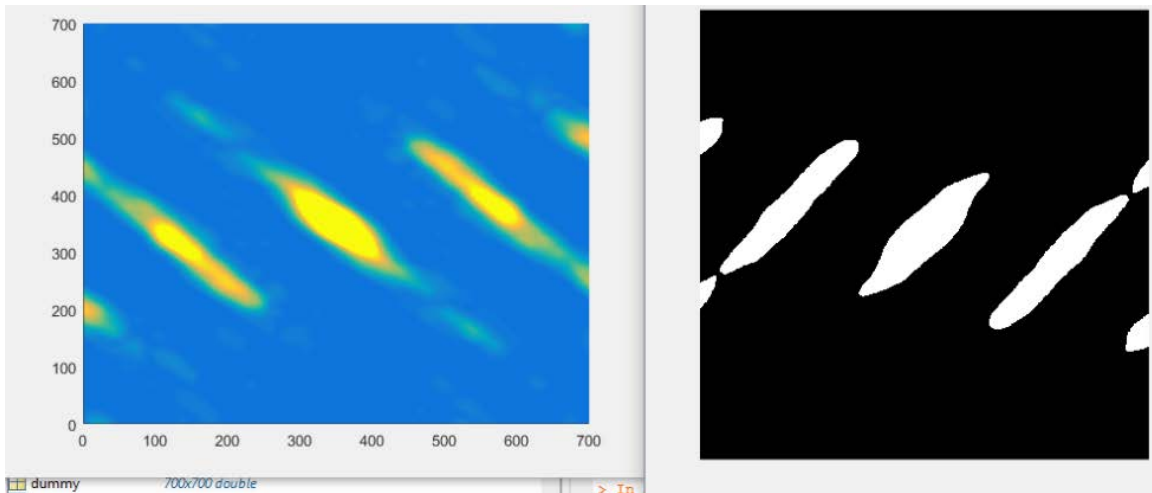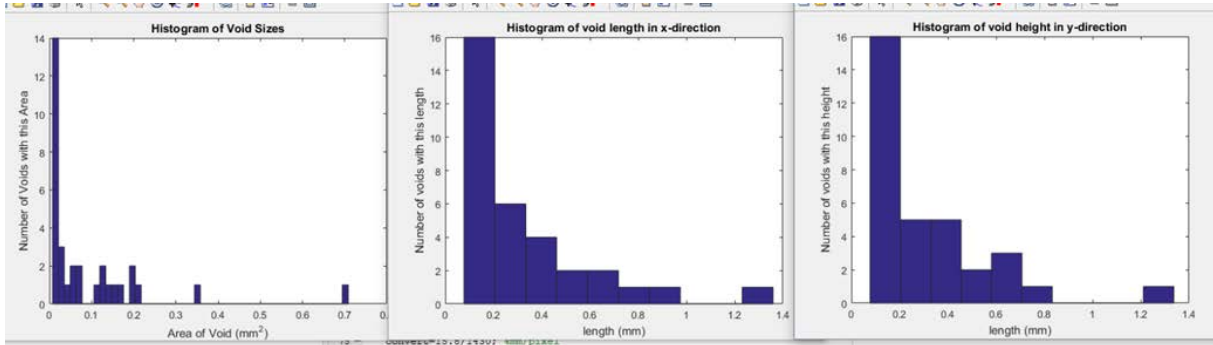
Image 2
Average void size (mm^2) = 0.11036
Standard deviation of void size (mm^2) = 0.14037
Average void size in x-direction (mm) = 0.35946
Standard deviation of void size in x-direction (mm) = 0.30916
Average void size in y-direction (mm) = 0.3613
Standard deviation of void size in y-direction (mm) = 0.29211
Nearest Neighbor Distance (mm) = 1.7673
Standard Deviation NN Distance (mm) = 1.5162
Betti Numbers = 30   6   0
Max cluster size (mm^2): 1.512
Ix/Iy for max cluster: 0.051926
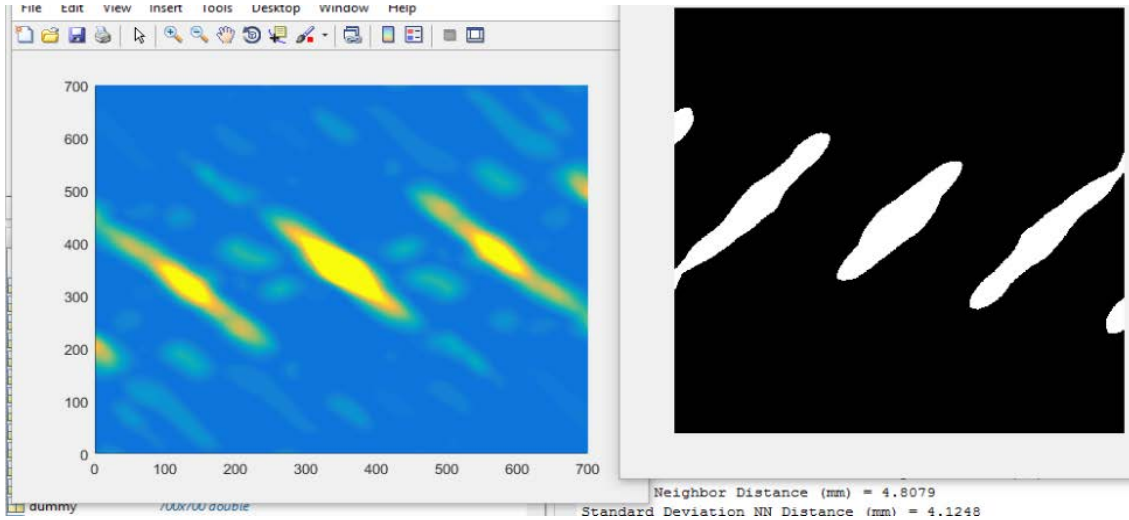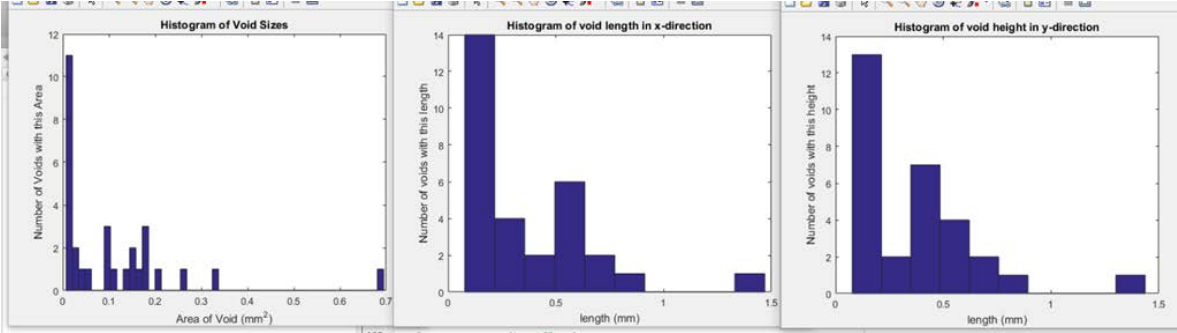
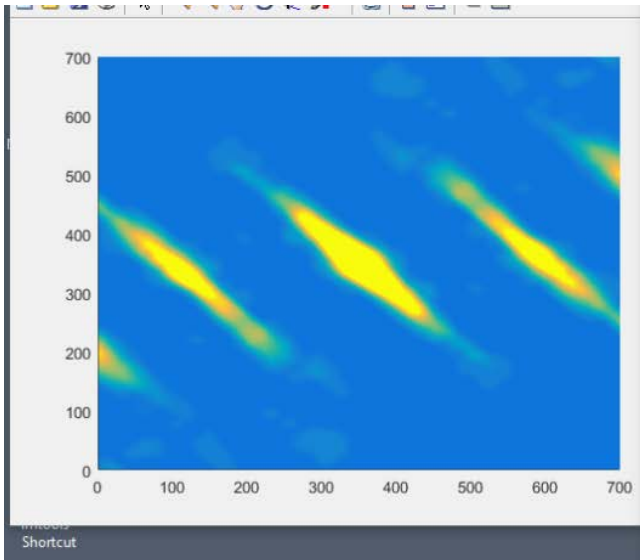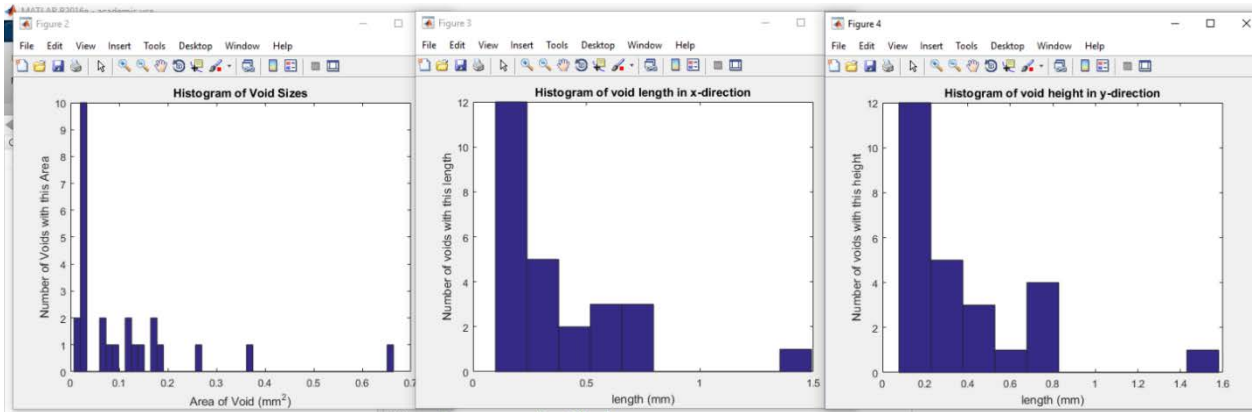| Image 3	
Average void size (mm^2) = 0.11151	
Standard deviation of void size (mm^2) = 0.14372	
Average void size in x-direction (mm) = 0.38076	
Standard deviation of void size in x-direction (mm) = 0.3095	
Average void size in y-direction (mm) = 0.38246	
Standard deviation of void size in y-direction (mm) = 0.33235	
Nearest Neighbor Distance (mm) = 1.715	
Standard Deviation NN Distance (mm) = 1.7521	
Betti Numbers = 26 3 0	
Max cluster size (mm^2): 1.7197	
Ix/Iy for max cluster: 0.037419	

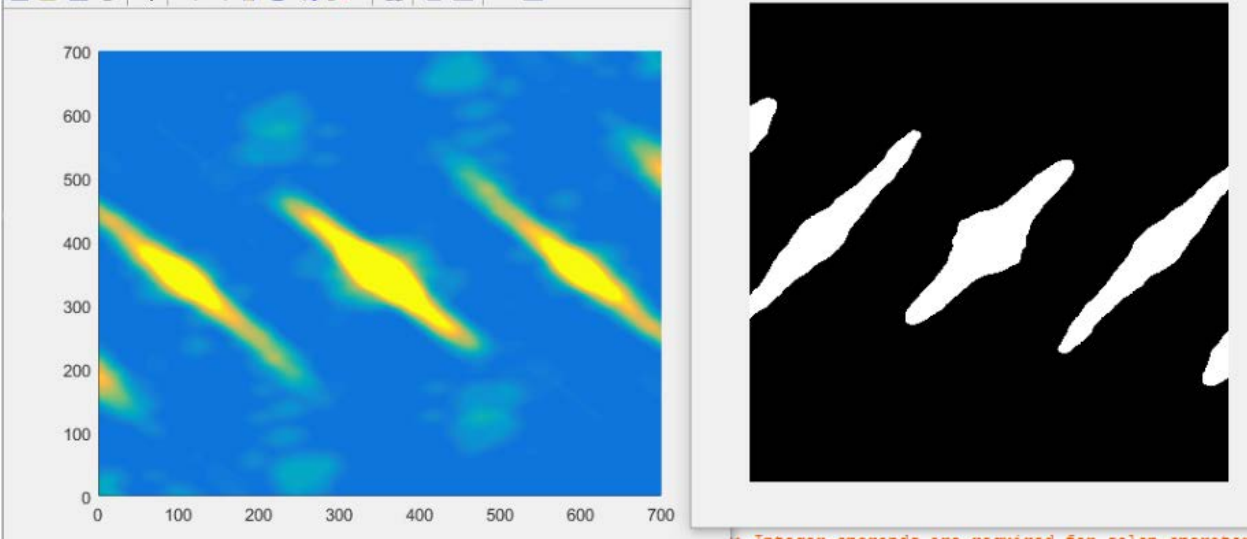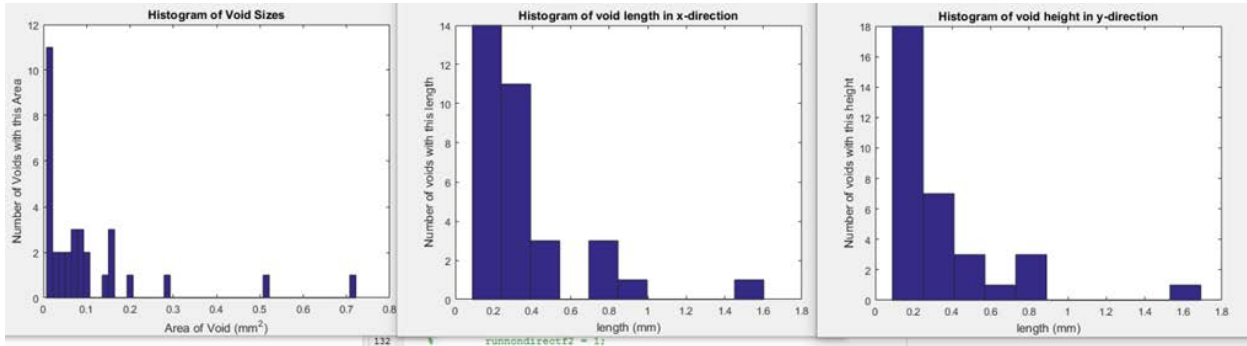| Image 4 |
|---|
| Average void size (mm^2) = 0.10321 |
| Standard deviation of void size (mm^2) = 0.15064 |
| Average void size in x-direction (mm) = 0.35859 |
| Standard deviation of void size in x-direction (mm) = 0.31345 |
| Average void size in y-direction (mm) = 0.34319 |
| Standard deviation of void size in y-direction (mm) = 0.32148 |
| Nearest Neighbor Distance (mm) = 1.2012 |
| Standard Deviation NN Distance (mm) = 0.88127 |
| Betti Numbers = 33   3   0 |
| Max cluster size (mm^2): 2.0711 |
| Ix/Iy for max cluster: 0.057355 |

Image 5
Average void size (mm^2) = 0.11264
Standard deviation of void size (mm^2) = 0.15045
Average void size in x-direction (mm) = 0.40245
Standard deviation of void size in x-direction (mm) = 0.37132
Average void size in y-direction (mm) = 0.38035
Standard deviation of void size in y-direction (mm) = 0.35438
Nearest Neighbor Distance (mm) = 1.1537
Standard Deviation NN Distance (mm) = 0.63723
Betti Numbers = 33   2   0
Max cluster size (mm^2): 2.2381
Ix/Iy for max cluster: 0.16174